Understanding Surface Structure and Interactions of Ionic Liquids for Energy Applications

University of Central Lancashire

by

Zoë Henderson

A thesis submitted in partial fulfilment for the requirements for the degree of Doctor of Philosophy at the University of Central Lancashire

August 2019

STUDENT DECLARATION PAGE

Type of Award　　　　　　Doctor of Philosophy

School　　　　　　　　　School of Physical Sciences and Computing

1.　　　　**Concurrent registration for two or more academic awards**

　　　　*I declare that while registered as a candidate for the research degree, I have not been a registered candidate or enrolled student for another award of the University or other academic or professional institution

2.　　　　**Material submitted for another award**

　　　　*I declare that no material contained in the thesis has been used in any other submission for an academic award and is solely my own work

3.　　　　**Collaboration**

　　　　Where a candidate's research programme is part of a collaborative project, the thesis must indicate in addition clearly the candidate's individual contribution and the extent of the collaboration. Please state below:

　　　　_____

4.　　　　**Use of a Proof-reader**

　　　　*No proof-reading service was used in the compilation of this thesis.

Signature of Candidate　_____

Print name:　　_____

Abstract

Presented within this thesis are four studies into the structure and interactions of ionic liquids (ILs), using X-ray photoelectron spectroscopy (XPS) both in situ and in vacuo, and using other complementary techniques. The findings provide insight into the surface chemistry and ordering of ILs, and are discussed in the context of energy applications.

The water/hydrophilic IL interface was investigated using near-ambient pressure XPS (NAPXPS) using a multilayer IL system (~109 Å) and an ultrathin layer system (~10 Å) on TiO_2 substrates. Results indicate rearrangement of the outermost ions as water molecules adsorb on the IL surface, primarily manifested as intensity changes in the C 1s core level region. The higher binding energy features, associated with the charged parts of the IL (i.e. the anion and the imidazolium ring of the cation) increase in intensity with exposure to water, which infers a reorientation of the cation toward the interface. Because the water molecules were able to adsorb on the IL surface for a significant period under vacuum, this may have negative implications for IL catalysis systems, as water may inhibit the absorption of gaseous reactants.

The interactions between a superbasic IL and water/CO_2 were investigated using NAPXPS. The reaction with CO_2 forms carbamate, as evidenced by peaks in the N 1s core level region at the higher binding energy edge. The reaction is reversible by reducing the surrounding CO_2 pressure. The results show that in each regime where the IL is exposed to CO_2, the molar uptake ratio of CO_2 molecules to IL pairs has an upper limit of 0.5. This indicates that the presence of water does not inhibit the IL's ability to react with CO_2 under near-ambient pressure conditions. Furthermore, it appears that the IL preferentially reacts with CO_2 over water vapour. This has implications for gas capture and separation technology, where complex mixtures of gases, including CO_2 and water, is released from industrial processes.

The structure and interactions at the IL/polar ZnO and IL/non-polar ZnO interfaces were probed using a combination of XPS and near-edge X-ray absorption fine structure (NEXAFS) spectroscopy. Shifts in the core level XPS regions associated with the anion support the idea that the IL interacts more strongly with the polar ZnO than the non-polar ZnO. IL/substrate interactions are thought to be occurring at O-terminated step edges, which is a mechanism involved in other reactions on polar ZnO surfaces described in literature. As evidenced by the NEXAFS spectra, the imidazolium ring of the approximately submonolayer deposition on non-polar ZnO was found to orientate at an angle closer to the surface normal than the surface itself. This has important implications for solar cells, where molecular interactions at a surface can affect the charge transfer across the interface. The polar ZnO substrate appeared to somewhat catalyse IL decomposition at the surface, as determined by XPS measurements taken at different temperatures using an analogous IL on the same substrate. Signs of decomposition began to show at temperatures much lower than those in literature. This has consequences for solar cell applications, where thermal stability is important to maintain device longevity.

The electrochemical influence of ILs on the anodization of Ti was investigated using an IL-based electrolyte, and varying anodization voltages between 5 V and 20 V. Scanning electron microscopy revealed that nanoporous TiO_2, and TiO_2 nanotubes were synthesised. The surface chemistry, determined by XPS, revealed a trend with anodization voltage, which may be linked to electrochemical decomposition of the IL. The introduction of contaminant species into TiO_2 nanotubes has consequences for their application in photocatalytic water splitting, where contamination could inhibit their hydrogen production capabilities.

Table of Contents

Acknowledgements

First and foremost, I thank my supervisor, Karen, for her incredible patience, guidance, and encouragement throughout my time at UCLan. You have been an incredible supervisor, and I can only hope that I have been a good PhD student! Thank you for everything: the laughs, the cat stickers, and for the chocolate/tea/biscuits that fuelled us along the way! Thanks also to my second supervisor, Joe, who introduced me to the surface science group at UCLan, and made me want to be a part of it. It was one of the best decisions I have ever made, so I thank you from the bottom of my heart!

I'd also like to thank all of our collaborators and friends at the University of Manchester. Firstly Tom, for his help and guidance in my work (and for his cooking skills that saved us in Denmark...!). Thanks also to Alex, whose patience and help with the NAPXPS will forever be appreciated, and for keeping us all in line with the X-ray window wall-of-shame! I'd also like to thank Manchester postgrad alumni, Mike Wagstaffe, Maria Torres-Molina and Jack Chun-Ren Ke, for their help in acquiring some of the data presented in this thesis. Additional thanks go to Mike and Maria, for keeping me sane on my first ever beamtime night shift with late-night exploration and the goal of drawing cats on all the whiteboards of Aarhus University. Also, thanks to all of the beamline scientists we have worked with over the course of my PhD: Zheshen, Oier, Hadeel, Federica, and Mattia. I hope we were good users! Additional thanks to Hadeel, for going above and beyond for our nanotubes! Thanks also to all the UCLan workshop technicians who helped to create our electrochemical cell- your patience and expertise was muchly appreciated!

I'd like to thank my fellow basement dwellers; my past and present officemates: Steven, Simon, Jack, and Conor. Thanks to all of you, for the wonderfully bizarre conversations and for making me laugh until I cried. Thanks also to my fellow JHI postgrads (past and present): Tom Kirk, Danny Lee, Chris Kaye, Ben Macfarlane, Adam Knowles, Andrew Walker and Jordan Thirwall; you all made me feel so welcome at the JHI despite my shyness. Additional thanks to honorary basement dwellers Jordan and Cal, whose consistently well-timed two cents always gave us those extra laughs! Congrats on your PhD places, guys, they were well deserved!

Last, but certainly not least, I thank my loved ones: my partner, my family, and my friends, for their incredible, unyielding support and steadfast encouragement. It is to every last one of you that I dedicate this thesis.

Zoë Henderson

List of Tables

List of Figures

Figure 6.12: Atomic concentration (%) of N, F, and C of all samples acquired from the XPS data (i); and the O/Ti atomic ratio of all samples (ii). The dashed line in (ii) represents the stoichiometric Ti/O atomic ratio = 2. For reference, the time taken for each anodization stage for each sample is illustrated in (iii) with an inset table displaying their respective anodization potentials. (227)

Figure 6.13: O 1s (i) and Ti 2p (ii) regions of all samples overlaid. Each spectrum is annotated with the associated sample designation. The binding energy values of the fitted lattice O peak in the O 1s for samples a, c, and d are shown on the right in (i). The binding energy values of the Ti $2p_{3/2}$ peak for samples a, c and d are shown on the right in (ii). On the left side of each spectrum describes the order of samples in atomic concentration of N (determined quantitatively from the XPS), from sample b (with the least concentration) to sample a (with the greatest concentration). (230)

List of Abbreviations

AEY	Auger electron yield
BE	Binding energy
EDX	Energy dispersive X-ray (spectroscopy)
EM	Electromagnetic
FTIR	Fourier transform infrared (spectroscopy)
FWHM	Full width (at) half maximum
GE	Grazing emission
HSA	Hemispherical analyser
ID	Insertion device
IL	Ionic liquid
IMFP	Inelastic mean free path
KE	Kinetic energy
LEED	Low-energy electron diffraction
MEA	Monoethanolamine
NAP	Near-ambient pressure
NAPXPS	Near-ambient pressure X-ray photoelectron spectroscopy
NE	Normal emission
NEXAFS	Near-edge X-ray absorption fine structure (spectroscopy)
NMR	Nuclear magnetic resonance (spectroscopy)
PEY	Partial electron yield
PTFE	Polytetrafluoroethylene
PV	Photovoltaic(s)
PVD	Physical vapour deposition
RF	Radio frequency
RH	Relative humidity
RT	Room temperature
RTIL	Room temperature ionic liquid
SCILL	Solid catalyst (with) ionic liquid layer
SEM	Scanning electron microscope/microscopy
SFG	Sum frequency generation (spectroscopy)
SILP	Supported ionic liquid phase (catalysis)
SR	Synchrotron radiation
STM	Scanning tunnelling microscope/microscopy
TEY	Total electron yield
TGA	Thermal gravimetric analysis
TSIL	Task-specific ionic liquid
UHV	Ultra-high vacuum
VB	Valence band
XAS	X-ray absorption spectroscopy
XPS	X-ray photoelectron spectroscopy

Publications by the Author

Z. Henderson, A. S. Walton, A. G. Thomas, K. L. Syres, Journal of Physics: Condensed Matter, 30 (2018) 334003. DOI: https://doi.org/10.1088/1361-648X/aad24f

Z. Henderson, A. G. Thomas, M. Wagstaffe, S. F. R. Taylor, C. Hardacre, K. L. Syres, Journal of Physical Chemistry C, 123, 12, 7134-7141 (2019). DOI: https://doi.org/10.1021/acs.jpcc.8b11670

Presentations by the Author

<u>Oral presentations:</u>

- *Jeremiah Horrocks Institute Annual CARD Presentations* (University of Central Lancashire, August 2016), title: "Water-Cation Interactions in Ionic Liquid Multilayers: a Near-Ambient Pressure X-ray Photoelectron Spectroscopy Study"
- *Jeremiah Horrocks Institute Annual CARD Presentations* (University of Central Lancashire, August 2017), title: "Reversible CO_2 Reaction with a Superbasic Ionic Liquid"
- *British Federation of Women Graduates North West Academic Presentation Day* (invited) (Hollins Hey Hotel, New Brighton, UK, October 2017), title: "Probing the Surface Structure and Interactions of Ionic Liquids"

<u>Poster presentations:</u>

- *Nanoenergy* (conference) (University of Liverpool, Liverpool, UK, July 2016), title: "Observation of Water-Cation Interactions in Ionic Liquid Multilayers using Near-Ambient Pressure X-ray Photoelectron Spectroscopy"
- *NanoScience@Surfaces* (summer school) (3rd place poster prize) (Cavendish Laboratory, Cambridge, UK, August 2016), title: "Water-Cation Interactions in Ionic Liquid Multilayers: a Near-Ambient Pressure X-ray Photoelectron Spectroscopy Study"
- *UCLan Annual Research Student Conference* (University of Central Lancashire, Preston, UK, September 2016), title: "Water-Cation Interactions in Ionic Liquid Multilayers: a Near-Ambient Pressure X-ray Photoelectron Spectroscopy Study"
- *ISSC 21* (conference) (Northern Royal College of Music, Manchester, UK, April 2017), title: "In Situ Observation of Water-Induced Reordering in Ultrathin Ionic Liquid Films"
- *ECOSS 33* (conference) (TIK Congress Centre, Szeged, Hungary, August 2017), title: "In Situ Observation of Water-Induced Reordering in Ultrathin Ionic Liquid Layers"
- *WEH Seminar on Surfaces and Interfaces of Ionic Liquids* (conference) (Physikzentrum, Bad Honnef, Germany, December 2017), title: "Reversible CO_2 Reaction with a Superbasic Ionic Liquid"
- *Surface Science Day* (conference) (University of Birmingham, Birmingham, UK, December 2018), title: "Reversible CO_2 Reaction with a Superbasic Ionic Liquid"

1 Introduction

1.1 Introduction and motivation

Ionic liquids, or ILs, are salts that are liquid below 100°C, with many being liquid at room temperature. They are composed solely of ions that are held together by a strong Coulomb potential [1]. ILs have only recently gained significant scientific interest, and only in the last few decades have IL-centric publications increased in number significantly, from less than 200 in 1990 to over 40000 by 2018 (according to the Web of Science database). This surge in publications is not surprising: not only are they interesting from an industrial perspective (due their wide range of potential applications for numerous technologies), but they are also interesting from an academic perspective, as they demonstrate some unusual behaviour for liquids (see Section 1.2.3).

The global demand for energy is ever increasing, and discovering more efficient ways of harvesting, storing and using energy are important to maintain our technology-driven lifestyles. This increasing energy demand means we need to improve upon, or invent new light-harvesting technologies; as well as adapt current energy technologies to mitigate the harmful effects of their by-products on the environment.

ILs have a wide variety of potential applications in energy. They have applications in energy production, such as incorporation in photovoltaic technologies for solar energy harvesting [2, 3]. They also have applications in energy storage, as an electrolyte in batteries for example [4]. They also have applications in greenhouse gas emission reduction as CO_2 capture agents [5]. ILs can also be used to synthesise nanoparticles and nanostructures for energy applications, such as titanium dioxide nanotubes for photocatalytic water splitting, which produces hydrogen and oxygen [6, 7].

This thesis presents a variety of surface-sensitive studies with a view toward energy applications. Presented first is an investigation into the interface between a hydrophilic IL and water, using near-ambient pressure X-ray photoelectron spectroscopy (NAPXPS). NAPXPS data was recorded at the

University of Manchester by the author, and colleagues. These data allow some insight into the behaviour of the constituent ions at the IL/water interface from a fundamental perspective, which has implications for gas capture and catalysis applications.

The second study investigates the reversible CO_2 capture behaviour of a superbasic IL. These ILs present superior CO_2 capture capabilities compared to other types of ILs. Using NAPXPS, the IL/CO_2 interface was probed under different gas composition conditions, including CO_2, H_2O vapour, and mixtures of both. Similarly to the first study, these data were taken at the University of Manchester by the author and colleagues. This investigation has allowed a unique insight into the surface chemistry taking place at the surface of the IL under ambient pressure conditions.

The third study is composed of two halves, and investigates the behaviour of IL multilayers on ZnO. ZnO has applications in photovoltaic cells and catalysis. The first half investigates the structure and orientation of the constituent IL ions at the surface of polar and non-polar ZnO using XPS and near-edge X-ray absorption fine structure (NEXAFS) spectroscopy, undertaken by colleagues of the author at the ANTARES beamline of the French synchrotron facility, SOLEIL. Understanding how the ions self-organise at the interface with ZnO has implications for interfacial charge transfer in photovoltaic technologies. The second half investigates the thermal stability of an IL on polar ZnO, monitored at increasing temperatures, from the glass transition, to 200°C. This was investigated using XPS, undertaken by the author and colleagues at AU-MATline beamline of the Danish synchrotron facility, ISA. The thermal stability of ILs at these temperatures has implications for catalysis, including supported ionic liquid phase (SILP) catalysis and solid catalysts with ionic liquid layers (SCILL).

The final study investigates the use of an IL as an electrolyte to synthesise TiO_2 nanotubes via the anodization of Ti, investigated using a combination of scanning electron microscopy and XPS, carried out at the University of Manchester by colleagues of the author. TiO_2 is a versatile material with applications in catalysis. TiO_2 nanotubes in particular have applications in photocatalytic water splitting. Understanding the morphology and surface chemistry of the resultant nanostructures on a fundamental level can contribute

toward a deeper understanding of the influence on the electrochemical conditions on these properties, and even the subsequent effects on photocatalytic performance.

To introduce these experiments, a research context is provided, beginning with a short history of ionic liquids with a discussion of their use in energy applications.

1.2 Ionic liquids

While scientific interest into the properties and potential applications of ionic liquids (ILs) is fairly recent, they do have a rich history. Since the 1960s, a huge variety of ILs have been discovered. In recent years, many of these have been functionalised to alter a particular property or to tailor them for a specific purpose. As mentioned earlier, ILs possess interesting properties, some of which are unusual for liquids. The fact that ILs are able to be functionalised, or 'tuned', means they have potential applications in many different fields. In the context of this thesis, those of particular interest are in gas capture, photovoltaic technologies and catalysis.

1.2.1 Short history of ionic liquids

ILs are thought to have been first discovered in 1914 by Paul Walden, who created an alkylammonium nitrate salt from combining concentrated nitric acid (HNO_3) and ethylamine ($CH_3CH_2NH_2$). The resultant salt was discovered to be a liquid at a relatively low temperature [8]. During the 1960s and 1970s, numerous other liquid salts were discovered under a variety of different names like 'molten salts', and 'liquid clathrates' [9]. However, many of the modern-day ILs originate from research conducted by a group working for the Unites States Air Force Academy in the early 1960s, who were investigating alternative electrolytes for thermal batteries. After testing a variety of unstable compounds, the group uncovered a patent from 1948 that outlined mixtures of aluminium chloride ($AlCl_3$) and 1-ethylpyridinium halides (see Figure 1.1 for the structure of pyridinium cations) that were conductive, non-aqueous and electrochemically stable. Using the patent as a starting point, the group developed a system consisting of 1-butylpyridinium chloride-$AlCl_3$, which proved to be somewhat more stable than its predecessors [10, 11]. These groups of mixtures are often

referred to as chloroaluminate melts [1]. Around a similar time, Swain et al [12] discovered that the salt tetrahexylammonium benzoate (see Figure 1.1 for ammonium cation structure) was liquid at 25°C, and suggested it could potentially be used as a solvent in electrochemistry due to its conductivity.

The next milestone in the history of ILs was during the 1980s and 1990s, when the groups of Seddon and Hussey were studying transition metal complexes and using room temperature chloroaluminate melts as solvents [13-15]. Their investigations were from an electrochemical perspective, and it was from the work of these groups that the modern-day, prototypical ILs (the imidazolium-based ILs, see Figure 1.1) were developed. The imidazolium-based ILs were a little more stable than their pyridinium counterparts, as they did not tend to reduce as easily. Despite their promising behaviour as electrolytes, one of the problems faced by the chloroaluminate materials was their reactivity with water. Research conducted in the early 1990s by Wilkes and Zaworotko [16], based at the United States Air Force Academy, gave way to imidazolium cations paired with water-stable anions. These included tetrafluoroborate and acetate (see Figure 1.1), which produced water- and air-stable salts that were liquid at ambient temperatures.

Since these pioneering works, much of the research endeavour in the synthesis and characterisation of ILs has led to unearthing a wealth of information about their bulk properties, such as electrical conductivity, density, viscosity and thermal stability. While the study of ILs within the material sciences, in general, can be considered fairly young, the study of the surface properties of ILs is even younger. The field of 'ionic liquid surface science' as it is viewed today could be considered to have started with the first XPS studies of ILs carried out by the Licence group in 2005 [17]. Studying behaviour at surfaces and interfaces is important for optimising their integration into technologies, particularly where phenomena at those interfaces is vital for function.

1.2.2 Ionic liquid categorisation

Before detailing the wide array of IL properties, it may be useful to frame them in the context of categories.

A simple categorisation, included in a recent review by Vekariya et al [18], is by generation: the origins of which are chronological by discovery. Generation I ILs

are what are often referred to as the chloroaluminate ILs, developed in the 1980s as electrolytes in batteries [13]. Generation II ILs could be considered some of the more widely-known ILs, and were discovered in the 1990s. These were found to be stable in air and with water, which their chloroaluminate ancestors were not. ILs categorised as Generation III are those that have been functionalised for a specific purpose, and are known as task-specific ILs, or TSILs. TSILs were first developed around the start of the millennium [19], and have since been developed as potential candidates for a wide variety of applications, from heavy metal extraction [20] to superhydrophobic coatings [21].

Figure 1.1: A selection of common cations and anions.

ILs can be more specifically categorised in terms of their cationic or anionic structure, and often in literature, a group of ILs may be identified as '-based', referring to a common cation or anion. Figure 1.1 displays a small collection of ions that make up a variety of ILs. Those selected are some of the more common cations and anions, and the ILs composed of these ions have been studied with relative rigour.

Among some of the most well-studied ILs in the research community are the imidazolium-based ILs. These are ILs that contain the imidazolium cation (Figure 1.1, top left). The imidazolium cation consists of an aromatic ring that contains two nitrogen atoms: one which is positively charged, and one which is protonated (bonded to a hydrogen atom, and is neutral). This structure is therefore called an imidazolium ring. As seen in Figure 1.1, other atoms or small molecular groups can be bonded to the nitrogen atoms in the imidazolium cation. In chemistry, these other atoms or molecular groups are typically referred to as R-groups or functional groups. The most common functional group for imidazolium cations is the alkyl functional group (hydrocarbon chains with length of n carbon atoms, terminating with CH_3). These alkyl chains can be bonded to either nitrogen in the imidazolium ring, and are hydrophobic functional groups. Other functional groups include amine, hydroxyl and carboxyl groups.

Other cations containing aromatic ring structures include pyrrolidinium and pyridinium cations (shown in Figure 1.1). While both pyrrolidinium and pyridinium cations contain aromatic structures with only one nitrogen atom, pyridinium cations consist of a benzene ring where one of the carbon atoms is replaced by a nitrogen atom. Pyrrolidinium, on the other hand, has a similar structure to imidazolium, but consists of a cyclopentane structure with one carbon atom replaced by a nitrogen atom. Again, much like imidazolium cations, functional groups may be bonded at the nitrogen atoms in pyrrolidinium and pyridinium cations. Typical functional groups include alkyl chains and hydroxyl groups, and even heavier molecules such as a benzene ring. Of course, cations do not necessarily need to contain ring structures. Ammonium, phosphonium, and sulphonium (shown in Figure 1.1) are just three examples of such ring-less cations. While ring-structured functional groups can bond to these cations, the charge-carrying moiety of these cations is the 'central' atom, which in the case

of ammonium, phosphonium and sulphonium is nitrogen, phosphorus, and sulphur respectively. One of the more common functional groups of these cations are long alkyl chains, some of which can be up to $n = 14$ carbons in length [22].

Anions, much like cations, can range in size, from halide monoatomic anions (such as chloride, bromide and iodide- see Figure 1.1, top right), to relatively bulky anions containing large functional groups such as long alkyl chains or aromatic rings. While many cations are organic, anions can be either organic or inorganic. Inorganic anions include monoatomic halide anions and others, such as tetrafluoroborate ($[BF_4]^-$) and hexafluorophosphate ($[PF_6]^-$, see inorganic section of Figure 1.1). Larger inorganic anions exist, with bis(trifluoromethyl-sulphonyl)imide ($[NTf_2]^-$) being a prototypical example. Other organic cations include imidazolide (see Figure 1.1) and triazolide. Imidazolide is an anion with a similar structure to the imidazolium cation, but the charge carrier is a negatively charged nitrogen atom instead of a positively charged nitrogen atom. It is negatively charged as it is not doubly bonded to either of its neighbouring carbon atoms. Meanwhile triazolide is similar in structure to imidazolide, but one or more of the remaining carbon atoms are replaced by nitrogen atoms. These, too, can include functional groups, including alkyl chains of various lengths and heavier structures like benzene.

The composite cations and anions influence different properties of an IL- as will any functional groups that are attached to the cation or anion. For the sake of brevity, the effect of non-TSIL cationic and anionic constituents on IL properties will be considered here, using the ILs made up of the ions in Figure 1.1 as examples.

1.2.3 Ionic liquid properties

The tuneable nature of ILs is one attribute among many that make them so uniquely interesting. A simple 'swap' of cation or anion in order to change a property (or properties) for a particular function is a core aspect of their usefulness. As such, the physicochemical properties of a vast array of ILs have been, and are still being, investigated and documented.

<u>Liquidus range</u>

One of the fundamental properties of ILs are their liquidus range, which is defined as the temperature range in which they are in the liquid phase. The property that defines the lower limit of this range is the melting point of the IL. The upper limit is usually defined by the thermal decomposition temperature of the IL rather than vaporisation temperature. Many thermally-stable ILs can be evaporated under extremely low-pressure conditions and at substantially high temperatures [1].

The melting point of most ILs will not describe an absolute crystalline-to-liquid phase change, but rather a glassy solid-to-liquid (and vice versa). Thus, for most ILs, the lower limit of the liquidus range is actually defined by the glass transition temperature- typically denoted T_g. The temperature of the lower limit is influenced by the constituent cation or anion, more specifically the sizes of the ions. An increase in ion size will reduce the Coulombic attraction experienced between the cation and anion. The size difference between cations and anions also affect how well they can pack together, and a large discrepancy in size reduces the packing efficiency. This effect is particularly obvious in alkylammonium and alkylphosphonium ILs (ammonium and phosphonium cations functionalised with four alkyl chains, typically three are of equal lengths), where the long alkyl chains will often shield the charge-carrying nitrogen or phosphorus from the anion, reducing the Coulombic attraction. Large anions have a similar effect to large cations, where bulky, neutral functional groups cause a similarly steric effect on the anion charge. The subsequent reduction in cation-anion interactions means smaller ions (such as 1-methyl-3-methylimidazolium cations, or monoatomic halide anions) produce ILs with higher melting points than those with larger ions (such as trihexyl-tetradecylphosphonium cations or bis(trifluoromethylsulphonyl)imide anions).

The upper limit of the liquidus range of an IL is not as easily definable as its lower limit. Decomposition temperatures depend on the experimental conditions, including IL purity [23], heating rate [24], and even the sample pans used [25]. However, under the same experimental conditions, it has been shown that the decomposition temperature depends on the anion, where weakly nucleophilic anions (such as bis(trifluoromethylsulphonyl)imide) are more thermally stable [26, 27].

Conductivity and electrochemical window

The origins of IL research are rooted in electrochemistry, so a discussion of IL properties will naturally include two key electrochemical properties: the electrical conductivity, and the electrochemical window. The electrochemical window of an IL is defined as the voltage range between which the IL is neither reduced nor oxidised. It is also known as the electrochemical stability. It is typically measured using cyclic voltammetry, which contains a three-electrode system: a working electrode (composing of glassy carbon, platinum or tungsten), a counter electrode (made of platinum, or a carbon rod), and a reference electrode (typically silver or platinum wire). In this method, the potential across the working electrode and the reference electrode is varied to extreme positive/negative potentials until background currents (which are measured between the working and counter electrodes) rise due to oxidation of the anion/reduction of the cation [1]. In neat ILs, the 'width' of the electrochemical window depends on how resistant the constituent cations are to reduction, and how resistant the constituent anions are to oxidation. For example if the reduction potential of a cation is measured at 2 V, and the oxidation potential of an anion at -3.5 V, the electrochemical window of that particular IL would be 5.5 V. The electrochemical windows for common ILs span a range between 2.1 eV and 6.4 V [1, 28].

The conductivity of ILs is dependent on a number of factors. ILs conduct electricity via ion mobility, and their electrical conductivity is, therefore, influenced by the mobility of their constituent ions. The conductivity, denoted by the symbol κ, of ILs range between 10 S cm^{-1} (Siemens per centimetre) to 300 S cm^{-1} [29]. To put into context, the conductivity of water can range between 50 and 400 S cm^{-1} depending on the temperature and the presence of ions [30, 31]. The relationship with temperature follows a linear Arrhenius trend above room temperature, but as the temperature decreases toward the glass transition temperature (T_g), the relationship is similar to other glass-forming liquids, according to the Vogel-Tamman-Fulcher equation [1]:

$$\kappa = AT^{-\frac{1}{2}} \exp\left(-\frac{B}{(T-T_0)}\right) \qquad (1.01)$$

where κ is the electrical conductivity in S cm^{-1}, T is temperature in K, A and B

are empirically-derived constants, and T_0 is the temperature at which the conductivity goes to zero (also in K). Therefore, as $T \rightarrow T_0$, $\kappa \rightarrow 0$. An Arrhenius plot illustrating temperature dependency of the electrical conductivities (and the line of best fit for each set calculated using Equation (*1.01*) [32, 33]) of 1-ethyl-3-methylimidazolium tetrafluoroborate (denoted (A)(C)), 1-ethyl-3-methylimidazolium bis(trifluoromethylsulfonyl)imide (denoted (A)(D)), and 1,2-dimethyl-3-propylimidazolium bis(trifluoromethylsulfonyl)imide (denoted (B)(D)) are shown in Figure 1.2 [1].
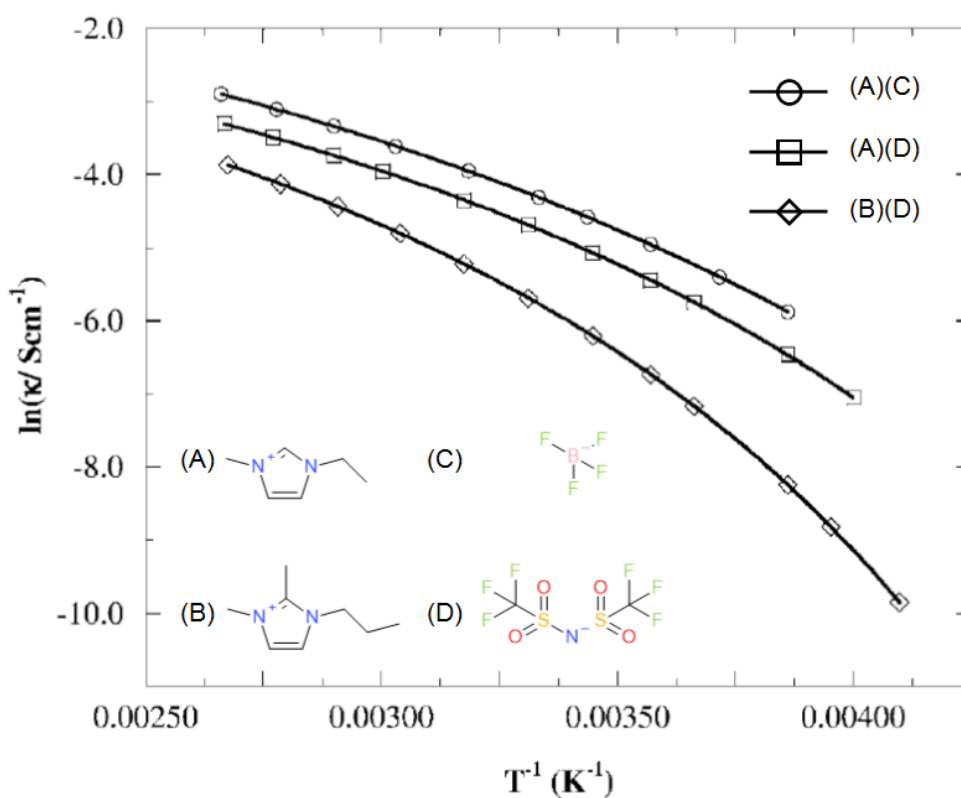
Figure 1.2: Arrhenius plots of the temperature-dependent conductivity for three ILs. (A) is the 1-ethyl-3-methylimidazolium cation, (B) is the 1,2-dimethyl-3-propylimidazolium cation, (C) is the tetrafluoroborate anion, and (D) is the bis(trifluoromethylsulfonyl)imide anion. The (X)(Y) label format signifies the cation (X) and anion (Y) pairing of each IL. Figure adapted from [1].

For liquids and solutions, particularly those used in electrolytes, it is sometimes useful to use molar conductivity, denoted by the symbol Λ, which is defined as the conductivity of an electrolyte solution divided by the electrolyte concentration of the solution. The molar conductivity of ILs varies between 0.01 and 16.0 S cm^2 mol^{-1} [1]. Molar conductivity of an IL is given by the following [1]:

$$\Lambda = \frac{\kappa \, M_{IL}}{\rho} \qquad (1.02)$$

where κ is the conductivity of the IL in S cm^{-1}, M_{IL} is the molecular weight of an IL pair in g mol^{-1}, and ρ is the density of the IL in g cm^{-3}. The molar conductivity and viscosity of ILs are related via a quantity known as Walden's Product [1, 34]:

$$\Lambda\eta = \text{constant} \qquad\qquad (1.03)$$

where η is the viscosity (often expressed in units of Poise, or P) of the IL. Ideally, Walden's Product should be a constant for a given IL, irrespective of temperature. With that in mind, an increase in IL viscosity results in a decreased molar conductivity, and vice versa. So, as shown by Equation (1.02) and Equation (1.03), key electrochemical properties of ILs are influenced by their viscosity and density.

<u>Viscosity and density</u>

ILs are more viscous than other molecular solvents, and are non-Newtonian fluids [1]. Non-Newtonian fluids are differentiated from Newtonian fluids by a viscosity that changes with applied strain. As mentioned in the previous subsection, viscosity is in units of P, and quite often for ILs, cP, or centipoise. At room temperature, the viscosity of ILs spans a range of 10 cP to 500 cP, which is considerably more viscous than water, which is 0.890 cP at room temperature [35]. Like many other materials, the viscosity of ILs shares an inversely-proportional relationship with temperature; but the viscosity also depends on the anionic component, where there appears to be a loose correlation with size [1]. However, much like the liquidus range, an increase in IL viscosity may be due to the ability to form hydrogen bond networks within the IL, i.e. the IL is more likely to be viscous if hydrogen networks are easy to form [36].

The measurement of IL viscosity is difficult to determine absolutely, since a small amount of contaminant species can result in rather large discrepancies in viscosity. For example, Seddon et al [37] measured the viscosities of a variety of ILs, and found that the viscosities varied depending upon the contaminant chloride (Cl$^-$) content (originating from preparation procedures), as well as water content (originating from absorption of ambient water vapour). They found that residual chloride content (which varied between 1.5 wt% and 6 wt%) could

increase the viscosity by as much as 600%. The ILs that absorbed water when exposed to atmosphere experienced a decrease in viscosity, in the case of 1-butyl-3-methylimidazolium tetrafluoroborate, to less than 50% of the original viscosity. There is also a relationship between viscosity and length of alkyl chains in imidazolium-based ILs, where ILs containing imidazolium cations with longer alkyl chains are more viscous than imidazolium-based ILs with shorter alkyl chains [1]. As mentioned earlier, symmetry of constituent ions impact the melting point of an IL. In a similar fashion, symmetry of the organic cation has shown to impact the viscosity in alkylimidazolium and dialkylimidazolium ILs [38]. Asymmetrical cations (with one alkyl chain shorter than the other) displayed greater viscosities than their symmetrical counterparts [38].

The SI unit for density is $kg\,m^{-3}$, but the density of ILs is usually quoted in $g\,cm^{-3}$ or $g\,ml^{-1}$. Most ILs are denser than water (which is approximately $1\,g\,cm^{-3}$), with densities ranging from $1.12\,g\,cm^{-3}$ to $2.40\,g\,cm^{-3}$ [1]. There is also a trend between alkyl chain length and density of ILs. Generally, ILs with longer alkyl chains are less dense than those with shorter alkyl chains, as longer chains are more difficult to pack together [26]. There is also a relationship between density and anion mass, where anions with larger masses tend to result in denser ILs [26, 39]. The density values of ILs are not as significantly affected by temperature as their viscosity values are [1], but as shown by Tariq et al [40], the density decreases as a function of increasing temperature. Similarly to their viscosities, the densities of ILs are known to decrease with increasing water content, approaching the density of water with greater dilution, as shown in Figure 1.3 [26].
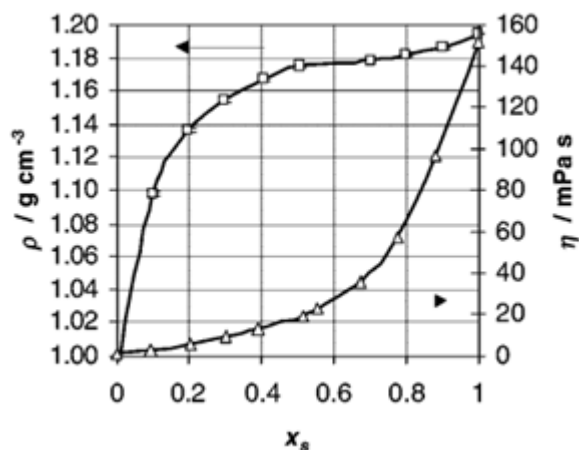
Figure 1.3: Density (squares) and viscosity (triangles) changes in the IL, 1-butyl-3-methylimidazolium tetrafluoroborate. The molar fraction of IL is denoted by x_s (so pure IL corresponds to $x_s = 1$ and pure water corresponds to $x_s = 0$). The viscosity is displayed in mPa, which is equal to cP. Figure adapted from [37].

Hydrophilicity

ILs can be categorised as hydrophobic or hydrophilic depending on their bulk miscibility of water (i.e. whether or not water is stable in the bulk of the IL; if they can 'mix together'). If the IL is water-miscible, it is considered hydrophilic; and if water-immiscible, it is considered hydrophobic. These definitions, however, are rather loose: some ILs that have been classified as hydrophobic can hold onto a significant amount of water in the bulk, for example the IL [C_4C_1Im][Tf_2N], which can hold up to a water mole fraction of approximately 0.26 (equivalent to ~1.5% by mass) [41]. Some ILs absorb water vapour from exposure to ambient conditions, and are referred to as hygroscopic. The length of the alkyl chain on the cation influences the extent to which an imidazolium-based IL is hygroscopic (hygroscopicity). A study into the change in mass through exposure to ambient humidities by Cuadrado-Prado et al [42] found that, out of four imidazolium-based ILs ([C_nC_1Im], where n = 2, 4, 6, 8) with the same anion (tetrafluoroborate), the IL with the shortest alkyl chain on the cation experienced the largest increase in mass after 24 hours in 100% humidity atmosphere. With increased chain length, the ILs experienced a smaller increase in mass, as shown in Figure 1.4. Of the four ILs, the cations with chain lengths of $n = 2$ and $n = 4$, were classified as miscible. Those with chain lengths of $n = 6$ and $n = 8$, however, were categorised by the authors as partially miscible and immiscible to water under ambient conditions respectively, yet they still experienced a mass increase upon exposure to extremely humid conditions.
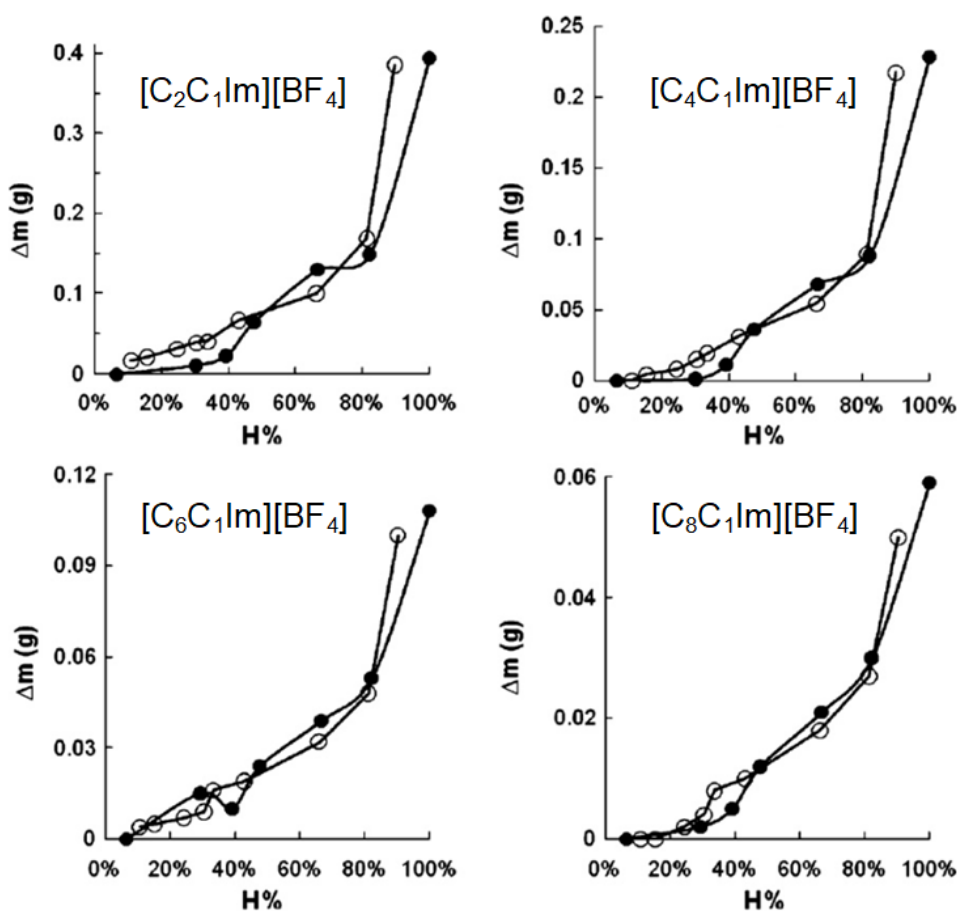
Figure 1.4: Increase in mass (Δm in g) measured as a function of humidity (H%) for four imidazolium-based ILs of the same anion. Figure adapted from [42].

Vapour pressure

One of the most intriguing properties of ILs is their vapour pressures. The vapour pressure of a liquid is defined as the pressure (force per unit area) exerted by a vapour in thermodynamic equilibrium with its liquid form at a given temperature. While gases can exist purely in the gas phase, a finite value of vapour pressure means that liquids do not exist solely in the liquid phase. So rather than a well-defined boundary separating the surface of a liquid and its surrounding environment, there is a gradient of phase: from solely bulk liquid, to a vapour (or mixed vapour if surrounded by a gas or air), to vacuum (or gaseous) environment surrounding the liquid.

At room temperature, many ILs possess very low, practically negligible, vapour pressures. For comparison, the vapour pressure of water at room temperature is 30 mbar [43], while for the IL 1-butyl-3-methylimidazolium hexafluorophosphate, is of the order of 10^{-12} mbar [44]. Vapour pressures of liquids, including ILs, increase with increasing temperature, and various groups

have measured the vapour pressures at a range of temperatures for numerous imidazolium-based ILs [1, 45-48]. Figure 1.5 shows the change in vapour pressure as a function of temperature for two non-ionic liquids (NILs), three room temperature ILs (RTILs), and two inorganic fused salts (IFSs).
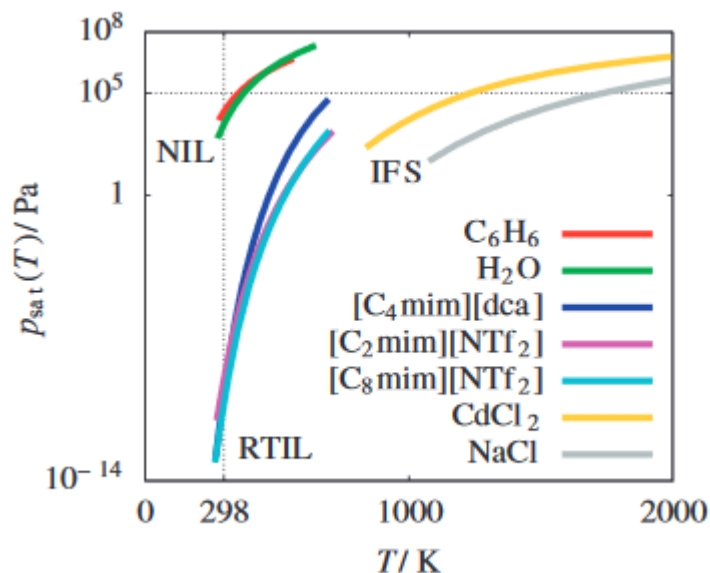
Figure 1.5: Vapour pressures (p_{sat}) for two NILs, three RTILs, and two IFSs. The two NILs are benzene and water (red and green lines respectively). The three RTILs are 1-butyl-3-methylimidazolium dicyanamide, 1-ethyl-3-methylimidazolium bis(trifluoromethylsulfonyl)imide, and 1-octyl-3-methylimidazolium bis(trifluoromethylsulfonyl)imide (blue, violet, and cyan lines respectively). The two IFSs are cadmium chloride and sodium chloride (yellow and grey lines respectively). Figure adapted from [46].

Techniques exist that can probe the IL surface in ambient conditions, but certain kinds of information can only be gathered using surface-sensitive methods. Access to this information requires the use of sub-molecular-sized probes such as photons, electrons, and ions. These kinds of techniques require extremely low-pressure conditions, also known as ultra-high vacuum, or UHV (see Chapter 2 for more detailed information). In order for a material to be investigated in UHV, it must be stable under extremely low-pressure conditions and therefore have a low or negligible vapour pressure. It follows that ILs, with their negligible vapour pressures, can be studied using UHV techniques.

1.3 Ionic liquids in surface science

While the bulk properties of ILs have been studied relatively extensively, research into their surface properties is still relatively recent, tracing back only a couple of decades. Studying bulk systems can only yield so much information, until an understanding of kinetics and chemistry at IL surfaces and interfaces at

a fundamental level is required, particularly for applications where surface/interfacial phenomena is important. Surface studies of ILs did not begin with low-pressure methods, but rather with techniques that can be used under ambient conditions, such as sum frequency generation spectroscopy [49, 50], and X-ray reflectometry [51, 52]. While they have revealed important information regarding the surface properties of ILs, exploiting the advantages provided by low vapour pressures of ILs is what has allowed the field of ionic liquid surface science to grow exponentially.

1.3.1 Introduction

One of the most well established techniques for investigating chemical composition at surfaces is X-ray photoelectron spectroscopy, or XPS. Like many other surface-sensitive techniques, XPS is typically conducted under very low pressure conditions: in the range of 10^{-8} to 10^{-11} mbar, which is classified as ultra-high vacuum, or UHV (see Chapter 2.2 for more details about vacuum classification). ILs are stable in UHV because of their low vapour pressures, and can, therefore, be investigated using XPS and other techniques. XPS can provide much insight into the chemical composition at the surface of ILs, particularly information regarding cation-anion interactions, and interactions at the interface between ILs and solid media [53, 54]. This can then provide insight into other aspects, such as structure and ordering at the interface. XPS studies of liquid media are few, due to many liquids being unsuitable for vacuum, but recent advancements in electron transfer optics have brought about the development of near-ambient pressure XPS (see Chapter 2.4), which allows the interface between ILs (and even other liquids [55, 56]) and gaseous media to be investigated with equal surface sensitivity as regular XPS.

In the context of ILs, a 'monolayer' refers to the substrate surface covered by a 'single layer' of cations and anions, where the thickness of the layer is approximately equal to the 'thickness' of an IL pair. A simple estimate can be made of the 'thickness' of an IL pair using Equation (*1.04*) [57, 58], given by:

$$d = \sqrt[3]{\frac{M_{IL}}{\rho \, N_A \times 10^{-21}}} \qquad (1.04)$$

where *d* is the 'thickness' of one IL pair in nm, M_{IL} is the molecular mass of the

IL in g mol^{-1}, ρ is the density of the IL in g cm^{-3}, and N_A is Avogadro's constant. By extension, 'sub-monolayer' coverage is incomplete coverage of a substrate surface. The term 'multilayers' therefore refers to several 'monolayers' on top of one another. Studies of the interface between an IL and a solid or gaseous medium can be done using a surface-sensitive technique and a thin or ultrathin film (which can also be referred to as multilayer, monolayer or sub-monolayer coverage on solid substrates), or by using a penetrative technique that can observe an interface buried within a medium.

1.3.2 IL/vacuum interface

ILs demonstrate stronger ordering than most molecular liquids, and their ability to self-assemble distinguishes IL ordering from the ordering displayed by molten salts [59]. The molecular structure at the surface or interface is different from the bulk of the IL, since interactions between the IL and a medium are different from the interactions within the IL itself. ILs will arrange themselves in a particular orientation as a way of 'balancing out' forces at the interface. This is the case for the IL/gas, IL/solid, and even the IL/vacuum interface.

The composition and molecular structure of the IL/vacuum interface has been studied using various UHV methods, namely XPS [53]. XPS is inherently surface-sensitive due to the short inelastic mean free path of photoelectrons (see Chapter 2.3). This surface sensitivity has allowed insight into the comparative differences between surface and bulk compositions of ILs, highlighting the so-called enrichment of IL surfaces [60]. Generally speaking, ILs arrange such that the neutral components of ions are located at the outermost surface of an IL, while the charged components are contained beneath the neutral components. The surface ions in imidazolium-based ILs arrange such that the alkyl chains face outward, creating a 'charged underlayer' that contains the anion and the charged imidazolium ring of the cation [61-64]. As mentioned in Section 1.2.3, the density of an IL is dependent on the size of the composite ions and alkyl chain length. The density of the outer surface also depends on these factors. Using an alkylimidazolium-based IL as an example, when the anions are small, the alkyl chains can pack closer together, and will orient approximately perpendicular to the IL surface, creating a denser outer layer [65, 66]. With larger composite anions (such as [BF$_4$]$^-$, [PF$_6$]$^-$, [NTf$_2$]$^-$), the anion pushes the alkyl chains apart, and with a sufficiently long alkyl chain, can

develop a layer where the chains are approximately parallel to the IL surface, lying across the anions [67, 68]. For $[C_nC_1Im][X]$, where X is a large anion, with $n < 4$, the alkyl chains will orient upright, just as they would in an IL with a small anion. For the alkyl chain to lie approximately parallel to the IL surface, the length typically corresponds to $n > 8$ [67, 68]. Although the alkyl chains display a preferential orientation toward vacuum (regardless of chain length), the outer layer is not dense enough to completely shield the charged components beneath, meaning that all components of the composite ions can be probed with XPS [69].

The preferential orientation of alkyl chains toward vacuum is also seen in functionalised ILs, such as the terminating Cl moiety of the anion in 1-methyl-3-octylimidazolium 4-chlorobutylsulphonate (or $[C_8C_1Im][ClC_4H_8SO_3]$). Using angle-resolved XPS (i.e. measurements taken at different emission angles), it was found that the anion preferred to orient with its Cl-terminated alkyl chain toward vacuum, with its charge-carrying SO_3^- group oriented toward the bulk IL [70]. Furthermore, much like other imidazolium-based ILs, the alkyl chain of the $[C_8C_1Im]^+$ cation oriented toward vacuum, and the charge-carrying imidazolium ring oriented toward the bulk. The behaviour is different, however, when functional groups are located throughout the chain, rather than at the end. A theoretical study into the arrangement of the IL/vacuum interface for the IL 1-methyl-3-octylimidazolium octylsulfate (or $[C_8C_1Im][C_8H_{17}SO_4]$), which has an anion consisting of alkyl chain with a penultimate linking ether group, making $CH_3-(CH_2)_7-O-SO_3^-$. In the study, the IL displayed a lamellar morphology (i.e. alternating layers of charged and neutral components) at the IL/vacuum interface, whereas the bulk of the IL was more 'sponge-like' [71]. The lamellar behaviour extended to almost tens of nanometres in the simulations, and it was speculated that it could continue on even larger length scales. Another theoretical study was done by the same research group with a similar IL, but with chains containing ether groups (which are structured as R-O-R') rather than purely alkyl chains. This study, contrastingly, showed that the arrangement in the IL/vacuum interfacial region only extended a few nanometres [72].

1.3.3 IL/gas interface

The ordering of the outermost surface of ILs, as determined by the composite ions, is thought to govern their gas capture and uptake behaviour. Studying the

interactions between ILs and gases is important for a number of reasons. An understanding of the adsorption and absorption phenomena at a molecular level provides a foundation for tailoring ILs for future gas capture applications. There is much interest in the interactions between ILs and greenhouse gases, as ILs show great promise as candidates for industrial gas capture applications.

As discussed in the previous section, there is an enrichment of alkyl chains at the 'free' surface (i.e. at the interface with vacuum) of ILs whereby the chains of the cation face out toward vacuum, and the imidazolium ring and the anion are located beneath. This also appears to be the case at the IL/air interface, as confirmed by various techniques that are carried out under ambient conditions. This includes sum frequency generation (SFG) spectroscopy [73], which provides information about the structure of the topmost layer of an IL. Of particular interest for the work in this thesis is the IL/water interface, which has also been studied using SFG by various research groups. For example, SFG measurements of the IL, 1-butyl-3-methylimidazolium bis(trifluoromethylsulphonyl)imide at low pressures of water vapour ($< 10^{-4}$ mbar) reveal that the imidazolium ring orientates parallel to the IL surface. Upon increased pressure, however, the imidazolium ring is orientated at an angle of approximately 35° to 50° from the IL surface [74], indicating a preferential orientation in the presence of water vapour. Other SFG studies of the same IL [75] reveal that the SO_2 groups of the anion are oriented more toward the water phase, which indicates that the anion also experiences a preferential orientation at the interface with water. Other techniques include X-ray reflectometry [51, 76], which provides density profile information of the topmost few layers of an IL. Lauw et al [51], for example, used a combination of X-ray reflectometry and molecular dynamics simulations to study the interfacial structure of the IL 1-butyl-1-methylpyrrolidinium bis(trifluoromethylsulphonyl)imide with water. Their findings revealed layering at the interface with water, where a 'net positive' layer of water and cations composed the topmost layer, which swelled with increasing water exposure. A 'net negative' layer was located beneath the 'net positive' layer, composed of anions. This has consequences for applications involving IL electrolytes, where ionic arrangement at electrodes and presence of water impact the electrochemical performance.

Studying the IL/gas interface using ultra-high vacuum techniques is a little more difficult, requiring preparation of all media so that they will agree with the low-pressure conditions. This involves 'freezing' a gas onto the IL surface, followed by heating in situ and monitoring changes as the gas desorbs from the IL [77, 78]. This procedure was carried out for a combined XPS and temperature programmed desorption investigation into the adsorption of water on 1-octyl-3-methylimidazolium tetrafluoroborate [79]. They found that multilayers of water desorbed at approximately 185 K, but a monolayer coverage of water on the IL surface was present until the IL was heated to approximately 245 K. XPS has a lot of information to offer with regards to surface chemistry of IL/gas systems, and recent technological advancements in electron transfer optics means that XPS can now be conducted under near-ambient conditions through the use of differential pumping. Near-ambient pressure XPS (see Chapter 2.5 for more information) is being used to investigate the IL/gas interface by a number of groups. Broderick et al [80], investigated the IL/water interface using the hydrophobic IL, 1-hexyl-3-methylimidazolium chloride, and found that there was a build-up of interfacial water under low relative humidity compared to absorption in the bulk IL. The same group has investigated the IL/gas interface of relatively thick films of other ILs, such as 1-butyl-3-methylimidazolium acetate [81, 82]. NAPXPS has also been used by Niedermaier et al [83] to investigate the IL/CO_2 interface using the amine-functionalised IL, dihydroxyethyl-dimethylammonium taurinate. They found that, in combination with infrared spectroscopy measurements of the bulk IL, the surface composition of the IL during exposure to relatively low pressures of CO_2 (< 1 mbar) differed to the bulk composition, where carbamic acid (CH_3NO_2) dominated the near-surface region, while carbamate (N-COO$^-$) dominated in the bulk of the IL.

Many questions remain about the mechanics of adsorption and absorption of gases in ILs, and studying their sorption behaviour is vital if they are to be used in gas capture applications.

1.3.4 IL/oxide interface

One of the ways in which the IL/solid interface can be investigated is using thin and ultrathin films of IL on a solid substrate. Numerous XPS studies have used this method to investigate the ordering and interactions on various substrates, including gold [84], nickel [85], copper [86], mica [77] and glass [87]. More

recently, with a view toward energy and catalysis applications, thin and ultrathin IL film/oxide systems have been studied.

Sobota et al [88] investigated the structure and ordering of 1-butyl-3-methylimidazolium bis(trifluoromethylsulphonyl)imide on alumina (Al_2O_3), using a combination of XPS, density functional theory (DFT), and infrared reflection absorption spectroscopy (IRAS). The IRAS measurements, which were recorded during the IL deposition onto the alumina surface, revealed the composite anion displayed a preferential orientation, which was confirmed and quantified by DFT. At submonolayer coverage, the anion adsorbs slightly tilted with respect to the surface, with the sulphonyl (R-SO_2-R') groups interacting with the alumina substrate. Mezger et al [89] investigated the layering geometry displayed by three ILs with the tris(pentafluoroethyl)trifluorophosphate anion in common. Using X-ray reflectometry, they determined two different kinds of layering arrangements: checkerboard-type arrangement (where cation and anion arrange side-by-side, forming a checkerboard pattern of charge), and double layer-type (where either cations or anions arrange preferentially at the surface, followed by a second layer of the oppositely-charged ion).

With a view toward photovoltaic applications, investigation of the structure and interactions of ILs at oxides, particularly those used in dye-sensitised solar cells (see Section 1.4.2), is extremely useful. One example is the interactions of an IL, 1-benzyl-3-methylimidazolium chloride, with tin dioxide (SnO_2), studied by Tran et al [90] as part of coated-glass electrodes in dye-sensitised solar cells. The XPS analysis showed a shift in binding energy of the peaks associated with the SnO_2 substrate toward lower binding energy, attributed to the presence of the electronegative chloride anion on the substrate surface. The band gap of the SnO_2 film was reduced after IL deposition, as revealed by ultraviolet photoelectron spectroscopy, resulting in better conduction and improved interfacial charge transfer. Wagstaffe et al [91] investigated the surface chemistry and cationic arrangement of the IL 1-butyl-3-methylimidazolium tetrafluoroborate on anatase TiO_2. The structural information, acquired by carrying out near-edge X-ray absorption fine structure (NEXAFS) spectroscopy measurements, revealed the cation arranged itself at the IL/TiO_2 interface such that the imidazolium ring was orientated at approximately 32° relative to the surface. They used XPS to study the surface chemistry of approximately

monolayer and multilayer coverage of the IL on anatase TiO_2, and found that there is an interaction between the anion and the substrate, where Ti-F bonds form most likely at O-vacancy sites. Both the structure and interaction of the ions with the TiO_2 substrate could impact the charge transfer across the interface, and thus the device performance.

Double layer-type arrangements of ILs at oxide interfaces are useful for electrochemical applications for ILs in contact with electrodes in electrochemical systems [92]. Furthermore, understanding the arrangement of ILs at oxide interfaces is important for applications involving charge transfer across interfaces, such as battery and photovoltaic applications. Many studies into IL/oxide systems take an empirical approach, while few studies have investigated the structure and interactions at the interface.

1.4 Energy-based applications of ionic liquids

The tuneable nature of ILs insinuates a vast array of potential uses, and since their discovery from research into battery electrolytes, this has proven to be true. While ILs are interesting from a fundamental perspective, they have gained a significant amount of interest from an industrial perspective, particularly for their potential applications in catalysis, lubrication and energy storage.

As mentioned earlier in this chapter, many ILs are electrochemically stable, making them desirable as non-aqueous electrolytes in batteries. Much research has explored the possibility of their integration into lithium ion battery technologies [93]. Ionic liquids as part of other energy storage applications includes supercapacitors [94], which are electrochemical capacitors that deliver high energy for short time periods (up to a few seconds).

It is from the initial research by the US Air Force into IL-based battery technology that has brought forth their potential applications in a wide variety of energy technologies, which encompasses harvesting as well as storage. This is particularly important in the context of two main problems facing humanity in the modern age: climate change and the global demand for energy.

1.4.1 Gas capture

Climate change, the long-term and large-scale shift of global weather patterns and average temperatures, is one of the most pressing issues we face. It is also probably one of the most widely recognised, with many countries implementing legislation in an effort to mitigate the human impact on climate change [95, 96]. The human impact is defined as our direct contribution as a species to the natural climate change process. The global temperature naturally increases and decreases over long periods of time, but there is overwhelming evidence to support that humans are accelerating the rate of global temperature via greenhouse gas emissions.

Greenhouse gas effect and related gas emissions

Greenhouse gases are gases in the atmosphere that absorb radiation, particularly infrared radiation. Greenhouse gases include carbon dioxide (CO_2), methane (CH_4), and nitrous oxide (N_2O). Visible light from the Sun is reemitted by the Earth as infrared radiation, which is absorbed by the greenhouse gases in the atmosphere. The presence of greenhouse gases in the atmosphere are required to raise the temperature of the Earth in order to support life, but an excess of greenhouse gases in the atmosphere will result in more absorption of infrared radiation and an overall rise in global temperature [97]. In an effort to slow down the increase in global temperatures and adhere to current legislation to reduce emissions, technologies that capture and store greenhouse gases, namely CO_2, have been implemented in industry to minimise emissions.

CO_2 capture and CO_2 scrubbing

Industrial processes release multiple gases in a mixture (called flue gas), so in order to remove CO_2 from the mixture, a material that reacts with CO_2 is required. One of the most commonly employed CO_2 capture technologies is CO_2 scrubbing [98, 99]. This kind of CO_2 scrubbing technology consists of a liquid solvent that reacts with CO_2, and a stripper that removes the CO_2 from the solvent so it can be reused.
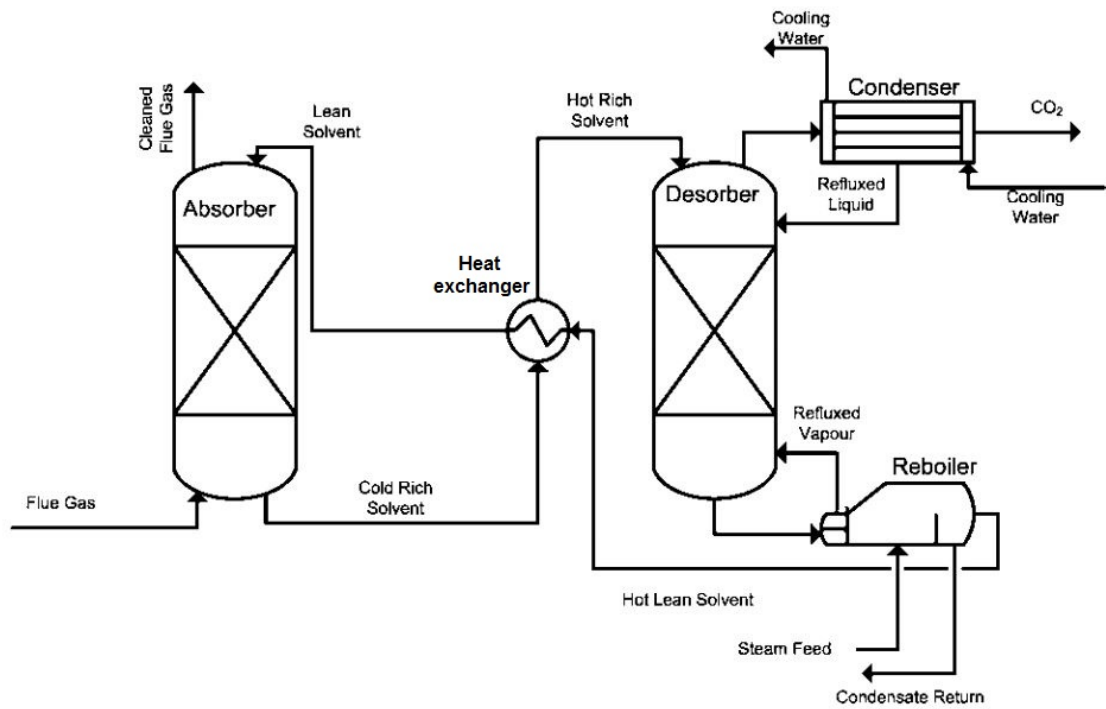
Figure 1.6: Schematic diagram of an absorber-stripper system. The stripper system consists of a desorber equipped with a condenser and reboiler. The condenser removes the CO_2, and the reboiler regulates the temperature of the solvent inside the desorber. The terms 'rich' and 'lean' refer to the CO_2 content of the solvent. Figure adapted from [100].

The generic process, as shown in Figure 1.6, begins with flue gas entering the system through a flue gas inlet, located at the bottom of the absorber. The CO_2 within the flue gas reacts with the solvent, and as the flue gas travels up through the system, more CO_2 is removed from it. Solvent that is saturated with CO_2 (used solvent) is transferred from the system to the stripper, where the CO_2 is removed from the solvent via heating. The used solvent enters at the top of the column in the stripper system, and travels down toward the bottom of the column, which is heated using steam. When the solvent reaches the bottom, the solvent is at a sufficient temperature to release the CO_2. Some of the solvent will transform to into the gas phase, and rise back up to the top of the column. The gas-phase solvent condenses back into a liquid phase inside a condenser, and returned to the absorber system as regenerated solvent. The CO_2 is cooled inside the condenser and compressed for transport [98].
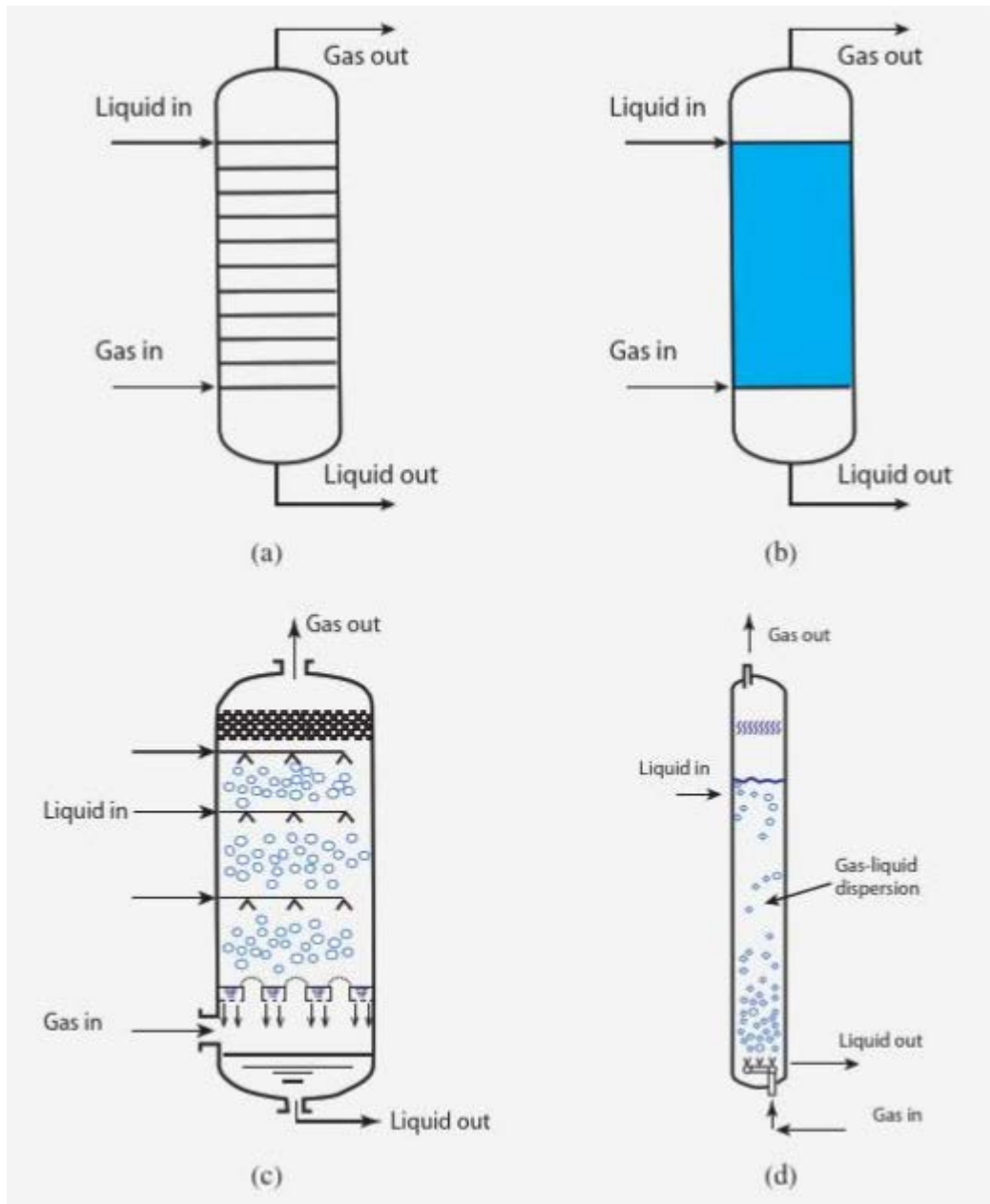
Figure 1.7: Diagrams of the plate tower (a), packed column (b), spray tower (c), and bubble column (d) absorber setups. In each setup, the flue gas inlet and used solvent outlet are located toward the bottom of the system. The cleaned gas outlet and regenerated solvent inlet are located toward the top of the system. Figure adapted from [98].

Figure 1.7 illustrates various absorber setups for CO_2 scrubbing. The plate tower design increase the surface area between the liquid solvent and the flue gas with equidistantly stacked plates. These plates have holes small enough to retain the solvent, but allow gas to pass through them. The packed column design is filled with 'packing material' that resembles material used in packaging. The spray column design increases the surface area between the solvent and flue gas by distributing the solvent as liquid droplets, much like running water from a showerhead. The bubble column works in a similar way,

but rather than the flue gas surrounding the solvent, flue gas is bubbled through, and surrounded by, the solvent.

The most popular industrial solvents for CO_2 scrubbing are amine-based, and one such example is monoethanolamine (MEA). Amines are derivatives of ammonia (NH_3), and consist of a nitrogen atom and up to three non-hydrogen R-groups. MEA consists of NH_2 with a single ethanol functional group, hence monoethanolamine (see Scheme 1.1 for chemical structure of MEA). MEA is popular as it is relatively cheap as a bulk solvent [101].
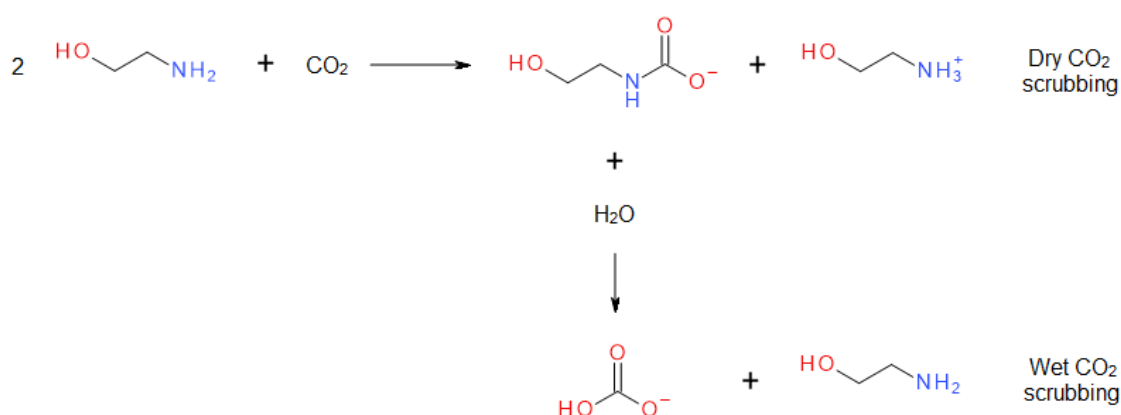
Scheme 1.1: Reaction between MEA and CO_2. Dry CO_2 scrubbing results in the formation of 2-hydroxyethylcarbamate and ammonium, while wet CO_2 scrubbing results in the formation of bicarbonate and MEA, allowing a net molar uptake ratio n_{CO2}:n_{MEA} of 1:1.

The reaction between CO_2 and MEA requires two MEA molecules for every one molecule of CO_2, which can also be expressed in terms of a molar uptake ratio, n_{CO2}:n_{MEA}, of 0.5:1. The reaction forms a carbamate group (N-COO⁻), whereby a bond is formed between the carbon atom in the CO_2 and the nitrogen in one of the MEA molecules. The second MEA molecule becomes protonated (bonds to a 'spare' hydrogen), and forms ammonium (NH_3^+). The addition of water to the solvent can improve the ratio of CO_2 molecules to MEA molecules, reducing the amount of solvent to process the same amount of CO_2. This is known as wet CO_2 scrubbing, and relies on a proportion of the carbamate groups to react with water to form bicarbonate (see Scheme 1.1). This reaction removes the CO_2 from the MEA molecule without regeneration through heating, which increases n_{CO2}:n_{MEA} to a ratio of 1:1.

While MEA and other amine-based solvents can store large quantities of CO_2, the regeneration process to 'strip' the CO_2 requires a relatively large amount of energy. The heat of absorption for primary amines (those containing only one

non-hydrogen R-group, such as the ethanol group in MEA) and secondary amines (which contain two non-hydrogen R-groups) is approximately -80 kJ mol^{-1} [98], which means the reaction takes a significant amount of energy to reverse, and culminates in an expensive process in the long-term. This aspect is vitally important from an industrial perspective, where costs for creation, implementation and maintenance of any potential CO_2 capture material will increase overall costs. For various gas energy applications, separation of CO_2 from other gases is also important for equipment maintenance, since its presence can cause pipeline corrosion [102-104].

Ionic liquids and CO_2 capture

Owing to their tuneable nature and thermal stability, ILs have emerged as potential future CO_2 capture materials [105-108]. Within the last two decades, much research has been carried out into the interactions between ILs and CO_2, beginning with the Davis group [109] who synthesised ILs with the purpose of CO_2 chemisorption. CO_2 that is chemically absorbed by ILs is generally easier to release, which consequently decreases the energy required for regeneration to below that of traditional scrubbing [110]. Numerous investigations into the CO_2 uptake capabilities of ILs have involved functionalised ILs [107, 110]. This includes ILs with carboxylate (O=C-O$^-$) and amine functional groups.

Carboxylate-functionalised ILs can hold onto a molar ratio of water to IL, n_{H2O}:n_{IL}, of 2:1. [111]. CO_2 is absorbed by the IL, and reacts with water to form bicarbonate, as it does in aqueous amine solvents mentioned previously. However, with current global water shortages, and potential further shortages induced by climate change [112], a process requiring an equimolar quantity of water to capture and process CO_2 is problematic. Amine-functionalised ILs react with CO_2 directly to form carbamate. While a number of research groups have found that amine-functionalised ILs can successfully capture CO_2, their absorption capabilities are somewhat limited by their viscosities, which increase when they react with CO_2 [113], in some cases as much as 200-fold [114]. This inhibits further absorption of CO_2 into the IL. Furthermore, while the addition of water can somewhat alleviate the viscosity problem [113], this increases the energy required to regenerate the IL. In the interest of gas separation, supported ionic liquid membranes, or SILM, systems have been investigated using various different ILs [115, 116]. In the last few years, research has been

conducted into the synthesis and performance of ILs with CO_2 capture ability without specific functionalisation, and without the necessity for water. This includes imidazolide-based ILs (see Figure 1.1 under organic anions), which are typically paired with phosphonium cations with long alkyl chains [22, 101, 117]. The heat of absorption of CO_2 for these ILs is typically greater than -65 kJ mol^{-1} [113, 117], making them a more energy-efficient alternative to MEA.

In order to gain insight into the sorption mechanics at the interface between ILs and gases, surface-sensitive methods are of vital importance. While gas sorption can be investigated under the low-pressure conditions required by many surface science techniques, it is also important to be able to investigate sorption behaviour under more realistic pressure and temperature conditions. One such technique is near-ambient pressure X-ray photoelectron spectroscopy (NAPXPS, see Chapter 2.4 or more information about this technique), which combines surface-sensitive measurements with near-ambient pressures and ambient temperatures. Gaining an understanding of the interactions at the IL/gas interface will provide a solid foundation for development and optimisation of task-specific ILs for potential applications in gas capture and separation. The interface between ILs and water, and ILs and CO_2, are particularly important for industrial gas capture applications. Chapters 3 and 4 report NAPXPS data of the IL/water and IL/CO_2 interfaces, and provide insight into the influence of these gases on the structure and interactions of the IL ions.

1.4.2 Photovoltaics

As mentioned previously in Section 1.4, the global energy demand is ever increasing, which is unsurprising as the planet sustains a growing population and a prevalence of technology in modern-day life. In 2017, the total amount of electricity generated by all nations on Earth amounted to approximately 2.6 $\times10^4$ terawatt hours, which is equivalent to a total of 9×10^{19} J [118].

The majority of the energy consumed globally is generated from coal, natural gas, and petroleum via combustion processes. These sources, collectively known as fossil fuels, are non-renewable, which means they are a foreseeably finite resource. To keep up with global energy demand, the consumption of fossil fuels has increased, as well as brought about the development and usage

of energy technologies utilising renewable resources. This includes solar harvesting technologies, such as photovoltaics.

Over the span of a year, approximately 4×10^{24} J of energy reaches the surface of Earth [97]. This is five orders of magnitude greater than the energy consumed in 2017. While not all the solar energy incident on Earth is harvestable, the sheer excess of energy available provides strong justification for the research and development into new and innovative photovoltaic (PV) technologies.

Photovoltaic effect and related technologies

The photovoltaic effect is defined as the generation of an electromotive force through the absorption of a photon. As part of generating the electromotive force, negative and positive charge must be generated, separated, and recombined much like in a conventional battery.

There are many different types of photovoltaic cell, as illustrated by the sheer variety of types presented in the National Renewable Energy Laboratory (NREL) PV efficiencies graph [119] (see Figure 1.8), which have developed over many years. All PV cells are built around the same principle of photo-induced electron promotion, but the range of materials that comprise PV technologies is relatively varied.

Figure 1.8: Best research-cell efficiencies graph, collated and published by the National Renewable Energy Laboratory [113].

Some of the PV technologies listed on the left side in Figure 1.8 show a sharp rise in efficiencies over a short period of time (with their efficiencies labelled on the right side), including some of the thin film PV, and many of the emerging PV. Thin film PV cells, such as cadmium telluride (CdTe) and copper indium gallium selenide (CIGS) technologies consist of additional layers than those of traditional silicon solar cells, including transparent conducting oxide layers as electrical contacts.
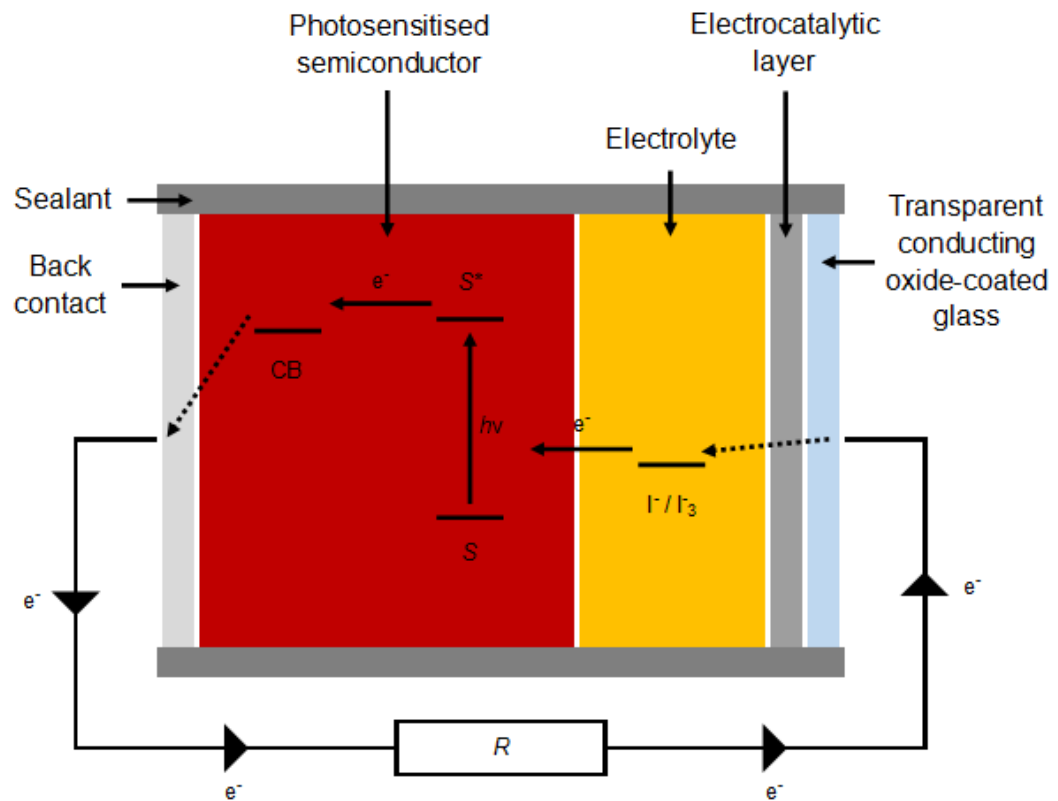
Figure 1.9: Schematic diagram of a dye-sensitised solar cell. The incident visible light photon promotes an electron from the valence band of the dye (S) to the conduction band (CB) of the semiconductor, leaving the dye molecule in an excited state (S*). The electron travels around the circuit, doing useful work through a load, R. The electron continues through the circuit, eventually transferring to the electrolyte, where the redox couple allows the previously oxidised dye molecule to be reduced through the transfer of electrons [120, 121].

Those of particular interest to the work in this thesis are dye-sensitised solar cells (DSSCs), a schematic diagram of which is shown in Figure 1.9. They are electrochemical in nature, unlike typical semiconductor devices, and are significantly cheaper to manufacture than semiconductor-based systems. The dye (typically ruthenium-based) sensitises the cell to visible light. In DSSCs under illumination, the electrons in the dye are excited from the valence band in

the dye to unoccupied states in the conduction band. The electrons are then injected into the conduction band of the semiconductor, where they then drift through to a back contact. The electrons in the dye are 'replenished' by electrons from the electrolyte. Typical electrolytes in DSSCs consist of a redox (reduction-oxidation) active component, such as iodide (I^-), in an organic solvent. The redox-active component forms a redox couple. Using iodide as an example, electrons from the iodide are transferred to several dye molecules, and forms triiodide (I_3^-) as a result. Additionally, electrons that are on their way to completing the circuit transfer to triiodide, forming iodide once again. The semiconductor in DSSCs is typically a large band gap semiconductor (3 eV < E_g < 3.5 eV) such as titanium dioxide (TiO_2) or zinc oxide (ZnO). The highest efficiency DSSC reported to date was reported by Komiya et al [122, 123] with an efficiency of (11.9 ± 0.4)%.

One of the issues facing layered PV technologies is electron injection across each of the composite layers. For ZnO-based technologies in particular, slow processes (of the order of picoseconds) can dominate the electron transfer across the interface between the active layer and the ZnO [124, 125]. This can be mitigated through band gap engineering and reducing the contact resistance between layers [126]. Another issue specific to DSSCs is the use of volatile organic solvents in the electrolyte, which have high vapour pressures and evaporate over time. Electrolyte evaporation is accelerated by solar heating, and thus heavily impedes the longevity of the DSSC [127, 128].

<u>Ionic liquids in photovoltaics</u>

As mentioned in Section 1.2.3, ILs are thermally stable and have good electrical conductivities. They are also non-volatile, unlike the conventional electrolytes currently used in DSSCs (such as acetonitrile) [129]. This makes them desirable as potential electrolytes in DSSCs. Typical IL-based electrolytes consist of a mixture of a low-viscosity IL and a salt capable of taking part in a redox reaction (also known as a redox-active salt). The low viscosity of the IL allows superior diffusion rates (over higher viscosity ILs) for the redox couple generated by the redox-active salt [121]. While the more efficient IL-based DSSCs have <10% efficiency, they are still versatile in practical applications. For example, IL electrolytes have been successfully printed using inkjet technology, making them viable for flexible DSSCs [130]. This is also possible with ZnO-based

DSSCs, since a number of research groups have developed ZnO electrodes on plastic substrates for the same application [131-133].

ILs are not restricted to DSSCs, and have been implemented into solid-state devices, such as hybrid organic-inorganic solar cells [126], perovskite solar cells [134], and quasi-solid state devices that contain IL-based gel-polymer electrolytes [135]. Studying ILs on oxide surfaces using surface-sensitive techniques will provide insight into their structure and interactions at the interface, which is vital when investigating electronic, electrochemical, and catalytic properties of IL-modified oxide systems. In order to be able to tailor the components of future photovoltaic devices to incorporate ILs, an intimate understanding of the IL/oxide interface is required. Chapter 5 of this thesis features a combined XPS and NEXAFS study into the surface ordering and interactions of ILs at polar and non-polar ZnO surfaces with a view toward DSSC and catalysis applications. Chapter 6 features XPS data of TiO_2 nanotubes to gain an insight into the influence of their growth conditions on their surface chemistry with a view toward photocatalytic water splitting applications.

1.4.3 Catalysis

ILs are useful in catalysis, both as solvents for catalysts and for synthesis of catalysts. There is little solvent loss during reactions due to their low vapour pressures, and their good thermal stabilities, solvation abilities, and electrical conductivities make them desirable catalysis solvents. ILs can be used to synthesise a wide variety of materials, both chemically and electrochemically [1]. Of particular interest is electrochemical nanoparticle and nanostructure synthesis, particularly of transition metal oxide photocatalysts used for water splitting.

Supported ionic liquid phase and solid catalyst with ionic liquid layer systems

IL-based catalysis systems have the benefits of homogeneous catalysis (catalysis involving a soluble catalyst in a solvent), which include high specificity and selectivity of the catalyst. They also have the benefits of heterogeneous catalysis (where the phase of the reactants are different to that of the catalyst), which include the products and the catalyst are easily separable, and large interfacial area for the reactions to take place [60].

Supported ionic liquid phase (SILP) catalysis involves a thin film of IL, which contains the homogeneous catalyst, on a high surface area support material (see Figure 1.10 for a schematic diagram). The system is useful for reactions involving gas-phase reactants, where the low vapour pressure of the IL film allows for continuous reaction via easy sorption of reactants and desorption of products. Example reactions using the SILP system include rhodium-catalysed hydrogenation [136, 137] and rhodium-, palladium- and zinc-catalysed hydroamination [138].
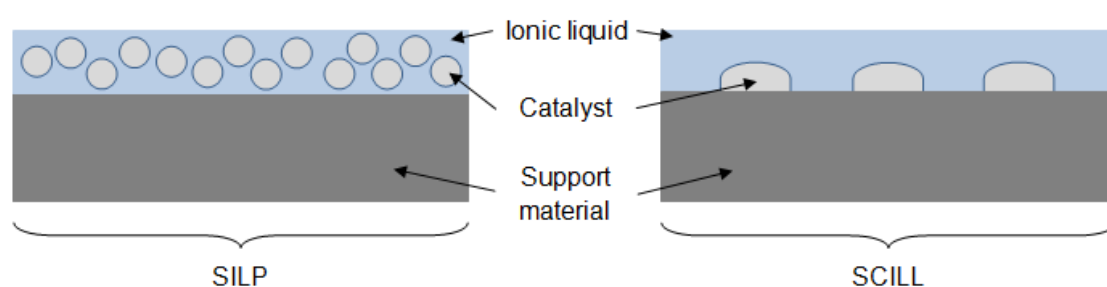
Figure 1.10: Schematic diagrams of the SILP (left) and SCILL (right) catalysis systems.

Another IL-modified catalysis concept is solid catalysts with ionic liquid layer (SCILL, see Figure 1.10), where catalysts are immobilised on a support beneath a thin layer of IL. Compared to their non-IL counterparts, the SCILL catalysis systems exhibit superior selectivity of products, as demonstrated experimentally with hydrogenation reactions using nickel [139] and palladium [140] catalysts.

<u>Nanostructure synthesis and photocatalytic water splitting</u>

ILs have been used to successfully electrochemically synthesise nanoparticles for catalysis applications [141]. Examples include noble metal nanoparticles, such as silver [142], transition metal nanoparticles, such as iridium [143] and palladium [144], and semiconductor catalysts, such as germanium [145]. ILs have also been used to electrochemically synthesise transition metal oxide nanostructures, such as TiO_2 nanotubes [146] (see Chapter 6).

TiO_2 is one of the most photocatalytically active materials due to the position of its conduction and valence bands in aqueous environments [147]. TiO_2 nanotubes are useful for a variety of energy applications, but of particular relevance to this thesis is their application in photocatalytic water splitting. Photocatalytic water splitting involves photogeneration of electron-hole pairs, which react with water to form H_2 and O_2 [148]:

$$TiO_2 \xrightarrow{h\nu} e^- + h^+ \qquad (1)$$

$$2H_2O + 4h^+ \rightarrow O_2 + 4H^+ \qquad (2)i$$

$$2H^+ + 2e^- \rightarrow H_2 \qquad (2)ii$$
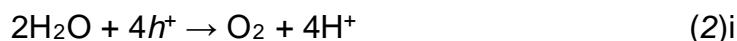
Where e^- and h^+ are electrons and holes respectively. There are competing reactions involving an excited electron, where the electron becomes part of an O_2 molecule to form O_2^-. Charge exchange between a water molecule and a vacancy in the valence band can result in a hydroxyl radical ($OH\cdot$), and charge exchange at the conduction band can generate O_2^- from O_2 [147]:

$$2H_2O + 2h^+ \rightarrow 2OH\cdot + H_2 \qquad (2)iii$$

$$O_2 + e^- \rightarrow O_2^- \qquad (2)iv$$
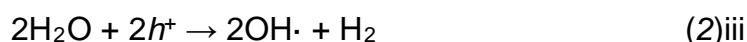
TiO_2 nanotubes are particularly favourable for water splitting, since reaction rates can be increased through the maximisation of surface area. The electrochemical synthesis of TiO_2 nanotubes via anodization of Ti allows control over various morphological properties, and the use of ILs has proven to produce good quality nanotube arrays without the need for dangerous materials like hydrofluoric acid [149]. In order to fully understand the extent of customisability of TiO_2 nanotubes, the relationship between the anodization conditions and the resultant nanotubes must be explored with techniques that can provide morphological and chemical information. Chapter 6 features a study into the influence of anodization conditions on electrochemically synthesised TiO_2 nanotubes. It includes scanning electron microscopy data, which provides morphological information, as well as XPS data for insight into the surface chemistry of the nanotubes. The data is discussed in the context of TiO_2 nanotubes for photocatalytic water splitting applications.

Chapter 1 References

[1] P. Wasserscheid, T. Welton, *Ionic Liquids in Synthesis*, 2nd ed., John Wiley & Sons, (2008).

[2] D.R. MacFarlane, N. Tachikawa, M. Forsyth, J.M. Pringle, P.C. Howlett, G.D. Elliott, J.H. Davis, M. Watanabe, P. Simon, C.A. Angell, *Energy Applications of Ionic Liquids*, Energy & Environmental Science, 7 (2014) 232-250, D.O.I.: 10.1039/C3EE42099J

[3] J.F. Wishart, *Energy Applications of Ionic Liquids*, Energy & Environmental Science, 2 (2009) 956-961, D.O.I.: 10.1039/B906273D

[4] M. Armand, F. Endres, D.R. MacFarlane, H. Ohno, B. Scrosati, *Ionic-Liquid Materials for the Electrochemical Challenges of the Future*, Nature Materials, 8 (2009) 621-629, D.O.I.: 10.1038/nmat2448

[5] S. Zeng, X. Zhang, L. Bai, X. Zhang, H. Wang, J. Wang, D. Bao, M. Li, X. Liu, S. Zhang, *Ionic-Liquid-Based CO2 Capture Systems: Structure, Interaction and Process*, Chemical Reviews, 117 (2017) 9625-9673, D.O.I.: 10.1021/acs.chemrev.7b00072

[6] A. Fujishima, K. Honda, *Electrochemical Photolysis of Water at a Semiconductor Electrode*, Nature, 238 (1972) 37-38, D.O.I.: 10.1038/238037a0

[7] H. Wender, A.F. Feil, L.B. Diaz, C.S. Ribeiro, G.J. Machado, P. Migowski, D.E. Weibel, J. Dupont, S.R. Teixeira, *Self-Organized TiO2 Nanotube Arrays: Synthesis by Anodization in an Ionic Liquid and Assessment of Photocatalytic Properties*, ACS Applied Materials & Interfaces, 3 (2011) 1359-1365, D.O.I.: 10.1021/am200156d

[8] P.I. Walden, *Ueber die Molekulargrösse und elektrische Leitfähigkeit einiger geschmolzenen Salze*, Bulletin de l'Académie Impériale des Sciences (St. Petersbourg), (1914) 405-422

[9] J.L. Atwood, J.D. Atwood, Advances in Chemistry Series, American Chemical Society, Washington DC, United States, 1976, pp. 112-127.

[10] R.J. Gale, B. Gilbert, R.A. Osteryoung, *Raman Spectra of Molten Aluminum Chloride: 1-Butylpyridinium Chloride Systems at Ambient Temperatures*, Inorganic Chemistry, 17 (1978) 2728-2729, D.O.I.: 10.1021/ic50188a008

[11] J.C. Nardi, C.L. Hussey, L.A. King, U. S. Patent 4 122 245, 1978.

[12] C.G. Swain, A. Ohno, D.K. Roe, R. Brown, T. Maugh, *Tetrahexylammonium Benzoate, a Liquid Salt at 25°, a Solvent for Kinetics or*

Electrochemistry, Journal of the American Chemical Society, 89 (1967) 2648-2649, D.O.I.: 10.1021/ja00987a025

[13] J.S. Wilkes, J.A. Levisky, R.A. Wilson, C.L. Hussey, *Dialkylimidazolium Chloroaluminate Melts: A New Class of Room-Temperature Ionic Liquids for Electrochemistry, Spectroscopy and Synthesis*, Inorganic Chemistry, 21 (1982) 1263-1264, D.O.I.: 10.1021/ic00133a078

[14] T.M. Laher, C.L. Hussey, *Copper(I) and Copper(Ii) Chloro Complexes in the Basic Aluminum Chloride-1-Methyl-3-Ethylimidazolium Chloride Ionic Liquid*, Inorganic Chemistry, 22 (1983) 3247-3251, D.O.I.: 10.1021/ic00164a016

[15] T.B. Scheffler, C.L. Hussey, K.R. Seddon, C.M. Kear, P.D. Armitage, *Molybdenum Chloro Complexes in Room-Temperature Chloroaluminate Ionic Liquids: Stabilization of Hexachloromolybdate(2-) and Hexachloromolybdate(3-)*, Inorganic Chemistry, 22 (1983) 2099-2100, D.O.I.: 10.1021/ic00157a001

[16] J.S. Wilkes, M.J. Zaworotko, *Air and Water Stable 1-Ethyl-3-Methylimidazolium Based Ionic Liquids*, Journal of the Chemical Society, Chemical Communications, (1992) 965-967, D.O.I.: 10.1039/C39920000965

[17] E.F. Smith, I.J.V. Garcia, D. Briggs, P. Licence, *Ionic Liquids in Vacuo; Solution-Phase X-Ray Photoelectron Spectroscopy*, Chemical Communications, (2005) 5633-5635, D.O.I.: 10.1039/B512311A

[18] R.L. Vekariya, *A Review of Ionic Liquids: Applications Towards Catalytic Organic Transformations*, Journal of molecular liquids, 227 (2017) 44-60, D.O.I.: 10.1016/j.molliq.2016.11.123

[19] J.H. Davis, *Task-Specific Ionic Liquids*, Chemistry letters, 33 (2004) 1072-1077, D.O.I.: 10.1246/cl.2004.1072

[20] A. Stojanovic, B.K. Keppler, *Ionic Liquids as Extracting Agents for Heavy Metals*, Separation Science and Technology, 47 (2012) 189-203, D.O.I.: 10.1080/01496395.2011.620587

[21] J.J. Tindale, K.L. Mouland, P.J. Ragogna, *Thiol Appended, Fluorinated Phosphonium Ionic Liquids as Covalent Superhydrophobic Coatings*, Journal of molecular liquids, 152 (2010) 14-18, D.O.I.: 10.1016/j.molliq.2009.05.005

[22] M. Mercy, S.F.R. Taylor, J. Jacquemin, C. Hardacre, R.G. Bell, N.H. De Leeuw, *The Addition of CO2 to Four Superbase Ionic Liquids: A DFT Study*, Physical Chemistry Chemical Physics, 17 (2015) 28674-28682, D.O.I.: 10.1039/C5CP05153C

[23] D.M. Fox, J.W. Gilman, H.C. De Long, P.C. Trulove, *TGA Decomposition Kinetics of 1-Butyl-2,3-Dimethylimidazolium Tetrafluoroborate and the Thermal Effects of Contaminants*, Journal of Chemical Thermodynamics, 37 (2005) 900-905, D.O.I.: 10.1016/j.jct.2005.04.020

[24] K.J. Baranyai, G.B. Deacon, D.R. MacFarlane, J.M. Pringle, J.L. Scott, *Thermal Degradation of Ionic Liquids at Elevated Temperatures*, Australian Journal of Chemistry, 57 (2004) 145-147, D.O.I.: 10.1071/CH03221

[25] H.L. Ngo, K. LeCompte, L. Hargens, A.B. McEwen, *Thermal Properties of Imidazolium Ionic Liquids*, Thermochimica Acta, 357-358 (2000) 97-102, D.O.I.: 10.1016/S0040-6031(00)00373-7

[26] J.G. Huddleston, A.E. Visser, W.M. Reichert, H.D. Willauer, G.A. Broker, R.D. Rogers, *Characterization and Comparison of Hydrophilic and Hydrophobic Room Temperature Ionic Liquids Incorporating the Imidazolium Cation*, Green Chemistry, 3 (2001) 156-164, D.O.I.: 10.1039/B103275P

[27] J. D. Holbrey, K. R. Seddon, *The Phase Behaviour of 1-Alkyl-3-Methylimidazolium Tetrafluoroborates; Ionic Liquids and Ionic Liquid Crystals*, Journal of the Chemical Society, Dalton Transactions, (1999) 2133-2140, D.O.I.: 10.1039/A902818H

[28] M.C. Buzzeo, R.G. Evans, R.G. Compton, *Non-Haloaluminate Room-Temperature Ionic Liquids in Electrochemistry—a Review*, Chemphyschem, 5 (2004) 1106-1120, D.O.I.: 10.1002/cphc.200301017

[29] M. Galiński, A. Lewandowski, I. Stępniak, *Ionic Liquids as Electrolytes*, Electrochimica Acta, 51 (2006) 5567-5580, D.O.I.: 10.1016/j.electacta.2006.03.016

[30] T.S. Light, S. Licht, A.C. Bevilacqua, K.R. Morash, *The Fundamental Conductivity and Resistivity of Water*, Electrochemical and Solid-State Letters, 8 (2005) E16-E19, D.O.I.: 10.1149/1.1836121

[31] Tables of Physical and Chemical Constants (16th Edition 1995) 3.9.2 Conductivities. Kaye & Laby Online. Version 1.0 (2005).

[32] A.B. McEwen, H.L. Ngo, K. LeCompte, J.L. Goldman, *Electrochemical Properties of Imidazolium Salt Electrolytes for Electrochemical Capacitor Applications*, Journal of the Electrochemical Society, 146 (1999) 1687-1695, D.O.I.: 10.1149/1.1391827

[33] A. Noda, K. Hayamizu, M. Watanabe, *Pulsed-Gradient Spin−Echo 1H and 19F NMR Ionic Diffusion Coefficient, Viscosity, and Ionic Conductivity of Non-*

Chloroaluminate Room-Temperature Ionic Liquids, The Journal of Physical Chemistry B, 105 (2001) 4603-4610, D.O.I.: 10.1021/jp004132q

[34] S.I. Smedley, *The Interpretation of Ionic Conductivity in Liquids*, Springer Science & Business Media, (2012).

[35] Tables of Physical and Chemical Constants (16th Edition 1995) 2.2.3 Viscosities. Kaye & Laby Online. Version 1.0 (2005).

[36] P. Bonhôte, A.-P. Dias, N. Papageorgiou, K. Kalyanasundaram, M. Grätzel, *Hydrophobic, Highly Conductive Ambient-Temperature Molten Salts*, Inorganic Chemistry, 35 (1996) 1168-1178, D.O.I.: 10.1021/ic951325x

[37] K.R. Seddon, A. Stark, M.-J. Torres, *Influence of Chloride, Water, and Organic Solvents on the Physical Properties of Ionic Liquids*, Pure and Applied Chemistry, 72 (2000) 2275-2287, D.O.I.: 10.1351/pac200072122275

[38] W. Zheng, A. Mohammed, L.G. Hines, D. Xiao, O.J. Martinez, R.A. Bartsch, S.L. Simon, O. Russina, A. Triolo, E.L. Quitevis, *Effect of Cation Symmetry on the Morphology and Physicochemical Properties of Imidazolium Ionic Liquids*, The Journal of Physical Chemistry B, 115 (2011) 6572-6584, D.O.I.: 10.1021/jp1115614

[39] S.V. Dzyuba, R.A. Bartsch, *Influence of Structural Variations in 1-Alkyl(Aralkyl)-3-Methylimidazolium Hexafluorophosphates and Bis(Trifluoromethylsulfonyl)imides on Physical Properties of the Ionic Liquids*, Chemphyschem, 3 (2002) 161-166, D.O.I.: 10.1002/1439-7641(20020215)3:2<161::aid-cphc161>3.0.co;2-3

[40] M. Tariq, P.A.S. Forte, M.F.C. Gomes, J.N.C. Lopes, L.P.N. Rebelo, *Densities and Refractive Indices of Imidazolium- and Phosphonium-Based Ionic Liquids: Effect of Temperature, Alkyl Chain Length, and Anion*, The Journal of Chemical Thermodynamics, 41 (2009) 790-798, D.O.I.: 10.1016/j.jct.2009.01.012

[41] M.G. Freire, P.J. Carvalho, R.L. Gardas, I.M. Marrucho, L.M.N.B.F. Santos, J.A.P. Coutinho, *Mutual Solubilities of Water and the [Cnmim][Tf2N] Hydrophobic Ionic Liquids*, The Journal of Physical Chemistry B, 112 (2008) 1604-1610, D.O.I.: 10.1021/jp7097203

[42] S. Cuadrado-Prado, M. Domínguez-Pérez, E. Rilo, S. García-Garabal, L. Segade, C. Franjo, O. Cabeza, *Experimental Measurement of the Hygroscopic Grade on Eight Imidazolium Based Ionic Liquids*, Fluid Phase Equilibria, 278 (2009) 36-40, D.O.I.: 10.1016/j.fluid.2008.12.008

[43] Tables of Physical and Chemical Constants (16th Edition 1995) 3.4.5 Vapour Pressures. Kaye & Laby Online. Version 1.0 (2005).

[44] Y.U. Paulechka, G.J. Kabo, A.V. Blokhin, O.A. Vydrov, J.W. Magee, M. Frenkel, *Thermodynamic Properties of 1-Butyl-3-Methylimidazolium Hexafluorophosphate in the Ideal Gas State*, Journal of Chemical & Engineering Data, 48 (2003) 457-462, D.O.I.: 10.1021/je025591i

[45] D.H. Zaitsau, G.J. Kabo, A.A. Strechan, Y.U. Paulechka, A. Tschersich, S.P. Verevkin, A. Heintz, *Experimental Vapor Pressures of 1-Alkyl-3-Methylimidazolium Bis(Trifluoromethylsulfonyl)imides and a Correlation Scheme for Estimation of Vaporization Enthalpies of Ionic Liquids*, The Journal of Physical Chemistry A, 110 (2006) 7303-7306, D.O.I.: 10.1021/jp060896f

[46] M. Bier, S. Dietrich, *Vapour Pressure of Ionic Liquids*, Molecular Physics, 108 (2010) 211-214, D.O.I.: 10.1080/00268971003604609

[47] Y.U. Paulechka, D.H. Zaitsau, G.J. Kabo, A.A. Strechan, *Vapor Pressure and Thermal Stability of Ionic Liquid 1-Butyl-3-Methylimidazolium Bis(Trifluoromethylsulfonyl)amide*, Thermochimica Acta, 439 (2005) 158-160, D.O.I.: 10.1016/j.tca.2005.08.035

[48] J.O. Valderrama, L.A. Forero, *An Analytical Expression for the Vapor Pressure of Ionic Liquids Based on an Equation of State*, Fluid Phase Equilibria, 317 (2012) 77-83, D.O.I.: 10.1016/j.fluid.2011.12.021

[49] S. Rivera-Rubero, S. Baldelli, *Influence of Water on the Surface of Hydrophilic and Hydrophobic Room-Temperature Ionic Liquids*, Journal of the American Chemical Society, 126 (2004) 11788-11789, D.O.I.: 10.1021/ja0464894

[50] S. Rivera-Rubero, S. Baldelli, *Influence of Water on the Surface of the Water-Miscible Ionic Liquid 1-Butyl-3-Methylimidazolium Tetrafluoroborate: A Sum Frequency Generation Analysis*, Journal of Physical Chemistry B, 110 (2006) 15499-15505, D.O.I.: 10.1021/jp062694p

[51] Y. Lauw, M.D. Horne, T. Rodopoulos, N.A.S. Webster, B. Minofar, A. Nelson, *X-Ray Reflectometry Studies on the Effect of Water on the Surface Structure of [C(4)mpyr][NTf2] Ionic Liquid*, Physical Chemistry Chemical Physics, 11 (2009) 11507-11514, D.O.I.: 10.1039/b916046a

[52] N. Nishi, T. Uruga, H. Tanida, T. Kakiuchi, *Temperature Dependence of Multilayering at the Free Surface of Ionic Liquids Probed by X-Ray Reflectivity Measurements*, Langmuir, 27 (2011) 7531-7536, D.O.I.: 10.1021/la200252z

[53] H.-P. Steinrück, *Recent Developments in the Study of Ionic Liquid Interfaces Using X-Ray Photoelectron Spectroscopy and Potential Future Directions*, Physical Chemistry Chemical Physics, 14 (2012) 5010-5029, D.O.I.: 10.1039/C2CP24087D

[54] K.R.J. Lovelock, I.J. Villar-Garcia, F. Maier, H.-P. Steinrück, P. Licence, *Photoelectron Spectroscopy of Ionic Liquid-Based Interfaces*, Chemical Reviews, 110 (2010) 5158-5190, D.O.I.: 10.1021/cr100114t

[55] S. Axnanda, E.J. Crumlin, B. Mao, S. Rani, R. Chang, P.G. Karlsson, M.O.M. Edwards, M. Lundqvist, R. Moberg, P. Ross, Z. Hussain, Z. Liu, *Using "Tender" X-Ray Ambient Pressure X-Ray Photoelectron Spectroscopy as a Direct Probe of Solid-Liquid Interface*, Scientific Reports, 5 (2015) 9788, D.O.I.: 10.1038/srep09788

[56] S. Ghosal, J.C. Hemminger, H. Bluhm, B.S. Mun, E.L.D. Hebenstreit, G. Ketteler, D.F. Ogletree, F.G. Requejo, M. Salmeron, *Electron Spectroscopy of Aqueous Solution Interfaces Reveals Surface Enhancement of Halides*, Science, 307 (2005) 563, D.O.I.: 10.1126/science.1106525

[57] Y. Khalifa, A. Broderick, J.T. Newberg, *Water Vapor Electron Scattering Cross-Section Measurements Using a Hydrophobic Ionic Liquid*, Journal of Electron Spectroscopy and Related Phenomena, 222 (2018) 162-166, D.O.I.: 10.1016/j.elspec.2017.06.002

[58] B. McLean, H. Li, R. Stefanovic, R.J. Wood, G.B. Webber, K. Ueno, M. Watanabe, G.G. Warr, A. Page, R. Atkin, *Nanostructure of [Li(G4)] TFSI and [Li(G4)] NO3 Solvate Ionic Liquids at HOPG and Au(111) Electrode Interfaces as a Function of Potential*, Physical Chemistry Chemical Physics, 17 (2015) 325-333, D.O.I.: 10.1039/C4CP04522J

[59] R. Hayes, G.G. Warr, R. Atkin, *Structure and Nanostructure in Ionic Liquids*, Chemical Reviews, 115 (2015) 6357-6426, D.O.I.: 10.1021/cr500411q

[60] H.P. Steinrück, J. Libuda, P. Wasserscheid, T. Cremer, C. Kolbeck, M. Laurin, F. Maier, M. Sobota, P. Schulz, M. Stark, *Surface Science and Model Catalysis with Ionic Liquid-Modified Materials*, Advanced Materials, 23 (2011) 2571-2587, D.O.I.: 10.1002/adma.201100211

[61] R.M. Lynden-Bell, M. Del Popolo, *Simulation of the Surface Structure of Butylmethylimidazolium Ionic Liquids*, Physical Chemistry Chemical Physics, 8 (2006) 949-954, D.O.I.: 10.1039/b514848k

[62] K. Lovelock, C. Kolbeck, T. Cremer, N. Paape, P. Schulz, P. Wasserscheid, F. Maier, H.-P. Steinruck, *Influence of Different Substituents on the Surface Composition of Ionic Liquids Studied Using ARXPS*, The Journal of Physical Chemistry B, 113 (2009) 2854-2864, D.O.I.: 10.1021/jp810637d

[63] C. Kolbeck, T. Cremer, K.R.J. Lovelock, N. Paape, P.S. Schulz, P. Wasserscheid, F. Maier, H.P. Steinrück, *Influence of Different Anions on the Surface Composition of Ionic Liquids Studied Using ARXPS*, The Journal of Physical Chemistry B, 113 (2009) 8682-8688, D.O.I.: 10.1021/jp902978r

[64] F. Maier, T. Cremer, C. Kolbeck, K.R.J. Lovelock, N. Paape, P.S. Schulz, P. Wasserscheid, H.P. Steinrück, *Insights into the Surface Composition and Enrichment Effects of Ionic Liquids and Ionic Liquid Mixtures*, Physical Chemistry Chemical Physics, 12 (2010) 1905-1915, D.O.I.: 10.1039/B920804F

[65] T. Iwahashi, T. Miyamae, K. Kanai, K. Seki, D. Kim, Y. Ouchi, *Anion Configuration at the Air/Liquid Interface of Ionic Liquid [bmim]OTf Studied by Sum-Frequency Generation Spectroscopy*, The Journal of Physical Chemistry B, 112 (2008) 11936-11941, D.O.I.: 10.1021/jp8021908

[66] M. Reichelt, T. Hammer, H. Morgner, *Influence of Water on the Surface Structure of 1-Hexyl-3-Methylimidazolium Chloride*, Surface Science, 605 (2011) 1402-1411, D.O.I.: 10.1016/j.susc.2011.05.001

[67] B. Wu, J. Zhang, T.K. Minton, K.G. McKendrick, J.M. Slattery, S. Yockel, G.C. Schatz, *Scattering Dynamics of Hyperthermal Oxygen Atoms on Ionic Liquid Surfaces: [emim][NTf2] and [C12mim][NTf2]*, The Journal of Physical Chemistry C, 114 (2010) 4015-4027, D.O.I.: 10.1021/jp910641s

[68] T. Iwahashi, T. Nishi, H. Yamane, T. Miyamae, K. Kanai, K. Seki, D. Kim, Y. Ouchi, *Surface Structural Study on Ionic Liquids Using Metastable Atom Electron Spectroscopy*, The Journal of Physical Chemistry C, 113 (2009) 19237-19243, D.O.I.: 10.1021/jp9056797

[69] A.S. Pensado, M.F.C. Gomes, J.N.C. Lopes, P. Malfreyt, A.A.H. Pádua, *Effect of Alkyl Chain Length and Hydroxyl Group Functionalization on the Surface Properties of Imidazolium Ionic Liquids*, Physical Chemistry Chemical Physics, 13 (2011) 13518-13526, D.O.I.: 10.1039/C1CP20563C

[70] I. Niedermaier, C. Kolbeck, N. Taccardi, P.S. Schulz, J. Li, T. Drewello, P. Wasserscheid, H.-P. Steinrück, F. Maier, *Organic Reactions in Ionic Liquids Studied by in Situ XPS*, Chemphyschem, 13 (2012) 1725-1735, D.O.I.: 10.1002/cphc.201100965

[71] W.D. Amith, J.J. Hettige, E.W. Castner, C.J. Margulis, *Structures of Ionic Liquids Having Both Anionic and Cationic Octyl Tails: Lamellar Vacuum Interface Vs Sponge-Like Bulk Order*, The Journal of Physical Chemistry Letters, 7 (2016) 3785-3790, D.O.I.: 10.1021/acs.jpclett.6b01763

[72] J.J. Hettige, W.D. Amith, E.W. Castner, C.J. Margulis, *Ionic Liquids with Symmetric Diether Tails: Bulk and Vacuum-Liquid Interfacial Structures*, The Journal of Physical Chemistry B, 121 (2017) 174-179, D.O.I.: 10.1021/acs.jpcb.6b09148

[73] C.S. Santos, S. Baldelli, *Gas–Liquid Interface of Room-Temperature Ionic Liquids*, Chemical Society Reviews, 39 (2010) 2136-2145, D.O.I.: 10.1039/B921580H

[74] S. Baldelli, *Influence of Water on the Orientation of Cations at the Surface of a Room-Temperature Ionic Liquid: A Sum Frequency Generation Vibrational Spectroscopic Study*, The Journal of Physical Chemistry B, 107 (2003) 6148-6152, D.O.I.: 10.1021/jp027753n

[75] T. Iwahashi, Y. Sakai, D. Kim, T. Ishiyama, A. Morita, Y. Ouchi, *Nonlinear Vibrational Spectroscopic Studies on Water/Ionic Liquid([Cnmim]TFSA: n = 4, 8) Interfaces*, Faraday Discussions, 154 (2012) 289-301, D.O.I.: 10.1039/C1FD00061F

[76] Y. Jeon, J. Sung, W. Bu, D. Vaknin, Y. Ouchi, D. Kim, *Interfacial Restructuring of Ionic Liquids Determined by Sum-Frequency Generation Spectroscopy and X-Ray Reflectivity*, Journal of Physical Chemistry C, 112 (2008) 19649-19654, D.O.I.: 10.1021/jp807873j

[77] A. Deyko, R.G. Jones, *Adsorption, Absorption and Desorption of Gases at Liquid Surfaces: Water on [C 8 C 1 Im][BF 4] and [C 2 C 1 Im][Tf 2 N]*, Faraday Discussions, 154 (2012) 265-288, D.O.I.: 10.1039/C1FD00062D

[78] M. Buckley, K.L. Syres, R.G. Jones, *Interactions and Stabilisation of Acetone, Sulfur Dioxide and Water with 1-Octyl-3-Methylimidazolium Tetrafluoroborate at Low Temperatures*, Faraday Discussions, 206 (2017) 475-495, D.O.I.: 10.1039/C7FD00146K

[79] K.R.J. Lovelock, E.F. Smith, A. Deyko, I.J. Villar-Garcia, P. Licence, R.G. Jones, *Water Adsorption on a Liquid Surface*, Chemical Communications, (2007) 4866-4868, D.O.I.: 10.1039/B711680B

[80] Y. Khalifa, A. Broderick, J.T. Newberg, *Surface Enhancement of Water at the Ionic Liquid–Gas Interface of [HMIM][Cl] under Ambient Water Vapor*,

Journal of Physics: Condensed Matter, 30 (2018) 325001, D.O.I.:
10.1088/1361-648X/aad102

[81] A. Broderick, Y. Khalifa, M.B. Shiflett, J.T. Newberg, *Water at the Ionic Liquid–Gas Interface Examined by Ambient Pressure X-Ray Photoelectron Spectroscopy*, Journal of Physical Chemistry C, 121 (2017) 7337-7343, D.O.I.:
10.1021/acs.jpcc.7b00775

[82] A. Broderick, M.A. Rocha, Y. Khalifa, M.B. Shiflett, J.T. Newberg, *Mass Transfer Thermodynamics through a Gas–Liquid Interface*, The Journal of Physical Chemistry B, 123 (2019) 2576-2584, D.O.I.: 10.1021/acs.jpcb.9b00958

[83] I. Niedermaier, M. Bahlmann, C. Papp, C. Kolbeck, W. Wei, S. Krick Calderón, M. Grabau, P.S. Schulz, P. Wasserscheid, H.-P. Steinrück, *Carbon Dioxide Capture by an Amine Functionalized Ionic Liquid: Fundamental Differences of Surface and Bulk Behavior*, Journal of the American Chemical Society, 136 (2013) 436-441, D.O.I.: 10.1021/ja410745a

[84] T. Cremer, M. Stark, A. Deyko, H.-P. Steinrück, F. Maier, *Liquid/Solid Interface of Ultrathin Ionic Liquid Films:[C1C1Im][Tf2N] and [C8C1Im][Tf2N] on Au (111)*, Langmuir, 27 (2011) 3662-3671, D.O.I.: 10.1021/la105007c

[85] T. Cremer, L. Wibmer, S.K. Calderón, A. Deyko, F. Maier, H.-P. Steinrück, *Interfaces of Ionic Liquids and Transition Metal Surfaces—Adsorption, Growth, and Thermal Reactions of Ultrathin [C 1 C 1 Im][Tf 2 N] Films on Metallic and Oxidised Ni (111) Surfaces*, Physical Chemistry Chemical Physics, 14 (2012) 5153-5163, D.O.I.: 10.1039/C2CP40278E

[86] K.L. Syres, R.G. Jones, *Adsorption, Desorption, and Reaction of 1-Octyl-3-Methylimidazolium Tetrafluoroborate, [C8C1Im][BF4], Ionic Liquid Multilayers on Cu (111)*, Langmuir, 31 (2015) 9799-9808, D.O.I.:
10.1021/acs.langmuir.5b02932

[87] T. Cremer, M. Killian, J.M. Gottfried, N. Paape, P. Wasserscheid, F. Maier, H.P. Steinruck, *Physical Vapor Deposition of [EMIM][Tf(2)N]: A New Approach to the Modification of Surface Properties with Ultrathin Ionic Liquid Films*, Chemphyschem, 9 (2008) 2185-2190, D.O.I.: 10.1002/cphc.200800300

[88] M. Sobota, I. Nikiforidis, W. Hieringer, N. Paape, M. Happel, H.P. Steinruck, A. Gorling, P. Wasserscheid, M. Laurin, J. Libuda, *Toward Ionic-Liquid-Based Model Catalysis: Growth, Orientation, Conformation, and Interaction Mechanism of the [Tf2N](-) Anion in [BMIM][Tf2N] Thin Films on a Well-Ordered Alumina Surface*, Langmuir, 26 (2010) 7199-7207, D.O.I.: 10.1021/la904319h

[89] M. Mezger, S. Schramm, H. Schröder, H. Reichert, M. Deutsch, E.J. De Souza, J.S. Okasinski, B.M. Ocko, V. Honkimäki, H. Dosch, *Layering of [BMIM]+-Based Ionic Liquids at a Charged Sapphire Interface*, Journal of Chemical Physics, 131 (2009) 094701, D.O.I.: 10.1063/1.3212613

[90] V.-H. Tran, R. Khan, I.-H. Lee, S.-H. Lee, *Low-Temperature Solution-Processed Ionic Liquid Modified SnO2 as an Excellent Electron Transport Layer for Inverted Organic Solar Cells*, Solar Energy Materials and Solar Cells, 179 (2018) 260-269, D.O.I.: 10.1016/j.solmat.2017.12.013

[91] M. Wagstaffe, M.J. Jackman, K.L. Syres, A. Generalov, A.G. Thomas, *Ionic Liquid Ordering at an Oxide Surface*, Chemphyschem, 17 (2016) 3430-3434, D.O.I.: 10.1002/cphc.201600774

[92] H. Yuan, H. Shimotani, A. Tsukazaki, A. Ohtomo, M. Kawasaki, Y. Iwasa, *Hydrogenation-Induced Surface Polarity Recognition and Proton Memory Behavior at Protic-Ionic-Liquid/Oxide Electric-Double-Layer Interfaces*, Journal of the American Chemical Society, 132 (2010) 6672-6678, D.O.I.: 10.1021/ja909110s

[93] J.B. Goodenough, K.-S. Park, *The Li-Ion Rechargeable Battery: A Perspective*, Journal of the American Chemical Society, 135 (2013) 1167-1176, D.O.I.: 10.1021/ja3091438

[94] D.R. MacFarlane, M. Forsyth, P.C. Howlett, J.M. Pringle, J. Sun, G. Annat, W. Neil, E.I. Izgorodina, *Ionic Liquids in Electrochemical Devices and Processes: Managing Interfacial Electrochemistry*, Accounts of Chemical Research, 40 (2007) 1165-1173, D.O.I.: 10.1021/ar7000952

[95] United Nations (1998), Kyoto Protocol. Available at: https://unfccc.int/resource/docs/convkp/kpeng.pdf Accessed [25/02/2019].

[96] United Nations (2015), Paris Agreement. Available at: https://unfccc.int/sites/default/files/english_paris_agreement.pdf Accessed [25/02/2019].

[97] A.W. Brinkman, *Physics of the Environment*, Imperial College Press, (2008).

[98] B. Smit, I.C. Bourg, C.M. Oldenburg, J.R. Reimer, *Introduction to Carbon Capture and Sequestration*, Imperial College Press, (2014).

[99] D.A. Eimer, *Gas Treating : Absorption Theory and Practice*, John Wiley & Sons, Incorporated, (2014).

[100] N. MacDowell, N. Florin, A. Buchard, J. Hallett, A. Galindo, G. Jackson, C.S. Adjiman, C.K. Williams, N. Shah, P. Fennell, *An Overview of CO2 Capture Technologies*, Energy & Environmental Science, 3 (2010) 1645-1669, D.O.I.: 10.1039/C004106H

[101] S.F.R. Taylor, C. McCrellis, C. McStay, J. Jacquemin, C. Hardacre, M. Mercy, R.G. Bell, N.H. de Leeuw, *CO2 Capture in Wet and Dry Superbase Ionic Liquids*, Journal of Solution Chemistry, 44 (2015) 511-527, D.O.I.: 10.1007/s10953-015-0319-z

[102] G. George, N. Bhoria, S. AlHallaq, A. Abdala, V. Mittal, *Polymer Membranes for Acid Gas Removal from Natural Gas*, Separation and Purification Technology, 158 (2016) 333-356, D.O.I.: 10.1016/j.seppur.2015.12.033

[103] K. Huang, X.-M. Zhang, Y. Xu, Y.-T. Wu, X.-B. Hu, Y. Xu, *Protic Ionic Liquids for the Selective Absorption of H2S from CO2: Thermodynamic Analysis*, AIChE Journal, 60 (2014) 4232-4240, D.O.I.: 10.1002/aic.14634

[104] I.S. Molchan, G.E. Thompson, P. Skeldon, R. Lindsay, J. Walton, E. Kouvelos, G.E. Romanos, P. Falaras, A.G. Kontos, M. Arfanis, E. Siranidi, L.F. Zubeir, M.C. Kroon, J. Klöckner, B. Iliev, T.J.S. Schubert, *Microscopic Study of the Corrosion Behaviour of Mild Steel in Ionic Liquids for CO2 Capture Applications*, RSC Advances, 5 (2015) 35181-35194, D.O.I.: 10.1039/C5RA01097G

[105] X. Zhang, X. Zhang, H. Dong, Z. Zhao, S. Zhang, Y. Huang, *Carbon Capture with Ionic Liquids: Overview and Progress*, Energy & Environmental Science, 5 (2012) 6668-6681, D.O.I.: 10.1039/C2EE21152A

[106] S.D. Kenarsari, D. Yang, G. Jiang, S. Zhang, J. Wang, A.G. Russell, Q. Wei, M. Fan, *Review of Recent Advances in Carbon Dioxide Separation and Capture*, RSC Advances, 3 (2013) 22739-22773, D.O.I.: 10.1039/C3RA43965H

[107] C. Chiappe, C.S. Pomelli, *Point-Functionalization of Ionic Liquids: An Overview of Synthesis and Applications*, European Journal of Organic Chemistry, 2014 (2014) 6120-6139, D.O.I.: 10.1002/ejoc.201402093

[108] S. Babamohammadi, A. Shamiri, K. Aroua Mohamed, Reviews in Chemical Engineering, 2015, pp. 383.

[109] E.D. Bates, R.D. Mayton, I. Ntai, J.H. Davis, *CO2 Capture by a Task-Specific Ionic Liquid*, Journal of the American Chemical Society, 124 (2002) 926-927, D.O.I.: 10.1021/ja017593d

[110] M.E. Boot-Handford, J.C. Abanades, E.J. Anthony, M.J. Blunt, S. Brandani, N. Mac Dowell, J.R. Fernández, M.-C. Ferrari, R. Gross, J.P. Hallett, R.S. Haszeldine, P. Heptonstall, A. Lyngfelt, Z. Makuch, E. Mangano, R.T.J. Porter, M. Pourkashanian, G.T. Rochelle, N. Shah, J.G. Yao, P.S. Fennell, *Carbon Capture and Storage Update*, Energy & Environmental Science, 7 (2014) 130-189, D.O.I.: 10.1039/C3EE42350F

[111] A. Brandt, J. Gräsvik, J.P. Hallett, T. Welton, *Deconstruction of Lignocellulosic Biomass with Ionic Liquids*, Green Chemistry, 15 (2013) 550-583, D.O.I.: 10.1039/C2GC36364J

[112] M. Howells, S. Hermann, M. Welsch, M. Bazilian, R. Segerström, T. Alfstad, D. Gielen, H. Rogner, G. Fischer, H. van Velthuizen, D. Wiberg, C. Young, R.A. Roehrl, A. Mueller, P. Steduto, I. Ramma, *Integrated Analysis of Climate Change, Land-Use, Energy and Water Strategies*, Nature Climate Change, 3 (2013) 621, D.O.I.: 10.1038/nclimate1789

[113] B.F. Goodrich, J.C. de la Fuente, B.E. Gurkan, Z.K. Lopez, E.A. Price, Y. Huang, J.F. Brennecke, *Effect of Water and Temperature on Absorption of CO2 by Amine-Functionalized Anion-Tethered Ionic Liquids*, Journal of Physical Chemistry B, 115 (2011) 9140-9150, D.O.I.: 10.1021/jp2015534

[114] B. Gurkan, B.F. Goodrich, E.M. Mindrup, L.E. Ficke, M. Massel, S. Seo, T.P. Senftle, H. Wu, M.F. Glaser, J.K. Shah, E.J. Maginn, J.F. Brennecke, W.F. Schneider, *Molecular Design of High Capacity, Low Viscosity, Chemically Tunable Ionic Liquids for CO2 Capture*, The Journal of Physical Chemistry Letters, 1 (2010) 3494-3499, D.O.I.: 10.1021/jz101533k

[115] L.C. Tomé, I.M. Marrucho, *Ionic Liquid-Based Materials: A Platform to Design Engineered CO2 Separation Membranes*, Chemical Society Reviews, 45 (2016) 2785-2824, D.O.I.: 10.1039/C5CS00510H

[116] K. Huang, X.-M. Zhang, Y.-X. Li, Y.-T. Wu, X.-B. Hu, *Facilitated Separation of CO2 and SO2 through Supported Liquid Membranes Using Carboxylate-Based Ionic Liquids*, Journal of Membrane Science, 471 (2014) 227-236, D.O.I.: 10.1016/j.memsci.2014.08.022

[117] C. Wang, X. Luo, H. Luo, D.e. Jiang, H. Li, S. Dai, *Tuning the Basicity of Ionic Liquids for Equimolar CO2 Capture*, Angewandte Chemie International Edition, 50 (2011) 4918-4922, D.O.I.: 10.1002/anie.201008151

[118] BP Statistical Review of World Energy 2018, 67th edition. Available at: https://www.bp.com/content/dam/bp/business-

sites/en/global/corporate/pdfs/energy-economics/statistical-review/bp-stats-review-2018-full-report.pdf, Accessed [13/03/2019].

[119] NREL, Best Research-Cell Efficiency Chart https://www.nrel.gov/pv/cell-efficiency.html, Accessed [13/03/2019].

[120] B. O'Regan, M. Grätzel, *A Low-Cost, High-Efficiency Solar Cell Based on Dye-Sensitized Colloidal TiO2 Films*, Nature, 353 (1991) 737-740, D.O.I.: 10.1038/353737a0

[121] J.M. Pringle, V. Armel, *The Influence of Ionic Liquid and Plastic Crystal Electrolytes on the Photovoltaic Characteristics of Dye-Sensitised Solar Cells*, International Reviews in Physical Chemistry, 30 (2011) 371-407, D.O.I.: 10.1080/0144235X.2011.638450

[122] M.A. Green, Y. Hishikawa, E.D. Dunlop, D.H. Levi, J. Hohl-Ebinger, A.W.Y. Ho-Baillie, *Solar Cell Efficiency Tables (Version 52)*, Progress in Photovoltaics: Research and Applications, 26 (2018) 427-436, D.O.I.: 10.1002/pip.3040

[123] R. Komiya, A. Fukui, N. Murofushi, N. Koide, R. Yamanaka, H. Katayama, 21st International Photovoltaic Science and Engineering Conference, ICS Convention Design, Fukuoka, Japan, 2011.

[124] N.A. Anderson, T. Lian, *Ultrafast Electron Injection from Metal Polypyridyl Complexes to Metal-Oxide Nanocrystalline Thin Films*, Coordination Chemistry Reviews, 248 (2004) 1231-1246, D.O.I.: 10.1016/j.ccr.2004.03.029

[125] Q. Zhang, C.S. Dandeneau, X. Zhou, G. Cao, *ZnO Nanostructures for Dye-Sensitized Solar Cells*, Advanced Materials, 21 (2009) 4087-4108, D.O.I.: 10.1002/adma.200803827

[126] B.R. Lee, H. Choi, J. SunPark, H.J. Lee, S.O. Kim, J.Y. Kim, M.H. Song, *Surface Modification of Metal Oxide Using Ionic Liquid Molecules in Hybrid Organic-Inorganic Optoelectronic Devices*, Journal of Materials Chemistry, 21 (2011) 2051-2053, D.O.I.: 10.1039/c0jm03688a

[127] F. Fabregat-Santiago, J. Bisquert, E. Palomares, L. Otero, D.B. Kuang, S.M. Zakeeruddin, M. Gratzel, *Correlation between Photovoltaic Performance and Impedance Spectroscopy of Dye-Sensitized Solar Cells Based on Ionic Liquids*, Journal of Physical Chemistry C, 111 (2007) 6550-6560, D.O.I.: 10.1021/jp066178a

[128] R. Harikisun, H. Desilvestro, *Long-Term Stability of Dye Solar Cells*, Solar Energy, 85 (2011) 1179-1188, D.O.I.: 10.1016/j.solener.2010.10.016

[129] M. Grätzel, *Conversion of Sunlight to Electric Power by Nanocrystalline Dye-Sensitized Solar Cells*, Journal of Photochemistry and Photobiology A: Chemistry, 164 (2004) 3-14, D.O.I.: 10.1016/j.jphotochem.2004.02.023

[130] S.G. Hashmi, M. Ozkan, J. Halme, K.D. Misic, S.M. Zakeeruddin, J. Paltakari, M. Grätzel, P.D. Lund, *High Performance Dye-Sensitized Solar Cells with Inkjet Printed Ionic Liquid Electrolyte*, Nano Energy, 17 (2015) 206-215, D.O.I.: 10.1016/j.nanoen.2015.08.019

[131] C.Y. Jiang, X.W. Sun, K.W. Tan, G.Q. Lo, A.K.K. Kyaw, D.L. Kwong, *High-Bendability Flexible Dye-Sensitized Solar Cell with a Nanoparticle-Modified ZnO-Nanowire Electrode*, Applied Physics Letters, 92 (2008) 143101, D.O.I.: 10.1063/1.2905271

[132] S.K. Hau, H.-L. Yip, N.S. Baek, J. Zou, K. O'Malley, A.K.Y. Jen, *Air-Stable Inverted Flexible Polymer Solar Cells Using Zinc Oxide Nanoparticles as an Electron Selective Layer*, Applied physics letters, 92 (2008) 253301, D.O.I.: 10.1063/1.2945281

[133] G.-J. Chang, S.-Y. Lin, J.-J. Wu, *Room-Temperature Chemical Integration of ZnO Nanoarchitectures on Plastic Substrates for Flexible Dye-Sensitized Solar Cells*, Nanoscale, 6 (2014) 1329-1334, D.O.I.: 10.1039/C3NR05267B

[134] Q. Wu, W. Zhou, Q. Liu, P. Zhou, T. Chen, Y. Lu, Q. Qiao, S. Yang, *Solution-Processable Ionic Liquid as an Independent or Modifying Electron Transport Layer for High-Efficiency Perovskite Solar Cells*, ACS Applied Materials & Interfaces, 8 (2016) 34464-34473, D.O.I.: 10.1021/acsami.6b12683

[135] H.M. Ng, S. Ramesh, K. Ramesh, *Efficiency Improvement by Incorporating 1-Methyl-3-Propylimidazolium Iodide Ionic Liquid in Gel Polymer Electrolytes for Dye-Sensitized Solar Cells*, Electrochimica Acta, 175 (2015) 169-175, D.O.I.: 10.1016/j.electacta.2015.01.076

[136] C.P. Mehnert, E.J. Mozeleski, R.A. Cook, *Supported Ionic Liquid Catalysis Investigated for Hydrogenation Reactions*, Chemical Communications, (2002) 3010-3011, D.O.I.: 10.1039/B210214E

[137] A. Wolfson, I.F.J. Vankelecom, P.A. Jacobs, *Co-Immobilization of Transition-Metal Complexes and Ionic Liquids in a Polymeric Support for Liquid-Phase Hydrogenations*, Tetrahedron Letters, 44 (2003) 1195-1198, D.O.I.: 10.1016/S0040-4039(02)02843-5

[138] S. Breitenlechner, M. Fleck, T.E. Müller, A. Suppan, *Solid Catalysts on the Basis of Supported Ionic Liquids and Their Use in Hydroamination Reactions,*

Journal of Molecular Catalysis A: Chemical, 214 (2004) 175-179, D.O.I.: 10.1016/j.molcata.2003.12.032

[139] U. Kernchen, B. Etzold, W. Korth, A. Jess, *Solid Catalyst with Ionic Liquid Layer (SCILL) – a New Concept to Improve Selectivity Illustrated by Hydrogenation of Cyclooctadiene*, Chemical Engineering & Technology, 30 (2007) 985-994, D.O.I.: 10.1002/ceat.200700050

[140] J. Arras, M. Steffan, Y. Shayeghi, D. Ruppert, P. Claus, *Regioselective Catalytic Hydrogenation of Citral with Ionic Liquids as Reaction Modifiers*, Green Chemistry, 11 (2009) 716-723, D.O.I.: 10.1039/B822992A

[141] Z. Li, Z. Jia, Y. Luan, T. Mu, *Ionic Liquids for Synthesis of Inorganic Nanomaterials*, Current Opinion in Solid State and Materials Science, 12 (2008) 1-8, D.O.I.: 10.1016/j.cossms.2009.01.002

[142] Y. Li, Q. Qiang, X. Zheng, Z. Wang, *Controllable Electrochemical Synthesis of Ag Nanoparticles in Ionic Liquid Microemulsions*, Electrochemistry Communications, 58 (2015) 41-45, D.O.I.: 10.1016/j.elecom.2015.05.020

[143] J. Dupont, G.S. Fonseca, A.P. Umpierre, P.F.P. Fichtner, S.R. Teixeira, *Transition-Metal Nanoparticles in Imidazolium Ionic Liquids: Recycable Catalysts for Biphasic Hydrogenation Reactions*, Journal of the American Chemical Society, 124 (2002) 4228-4229, D.O.I.: 10.1021/ja025818u

[144] J.-H. Cha, K.-S. Kim, S. Choi, S.-H. Yeon, H. Lee, C.-S. Lee, J.-J. Shim, *Size-Controlled Electrochemical Synthesis of Palladium Nanoparticles Using Morpholinium Ionic Liquid*, Korean Journal of Chemical Engineering, 24 (2007) 1089-1094, D.O.I.: 10.1007/s11814-007-0126-3

[145] F. Endres, S.Z. El Abedin, *Electrodeposition of Stable and Narrowly Dispersed Germanium Nanoclusters from an Ionic Liquid*, Chemical Communications, (2002) 892-893, D.O.I.: 10.1039/B110716J

[146] I. Paramasivam, J. Macak, T. Selvam, P. Schmuki, *Electrochemical Synthesis of Self-Organized TiO2 Nanotubular Structures Using an Ionic Liquid (BMIM-BF 4)*, Electrochimica Acta, 54 (2008) 643-648, D.O.I.: 10.1016/j.electacta.2008.07.031

[147] P. Roy, S. Berger, P. Schmuki, *TiO2 Nanotubes: Synthesis and Applications*, Angewandte Chemie-International Edition, 50 (2011) 2904-2939, D.O.I.: 10.1002/anie.201001374

[148] M. Sankir, N.D. Sankir, *Hydrogen Production Technologies*, John Wiley & Sons, (2017).

[149] V. Zwilling, M. Aucouturier, E. Darque-Ceretti, *Anodic Oxidation of Titanium and TA6V Alloy in Chromic Media. An Electrochemical Approach*, Electrochimica Acta, 45 (1999) 921-929, D.O.I.: 10.1016/s0013-4686(99)00283-2

2 Theory, Techniques and Instrumentation in Surface Science

2.1 Introduction

By its very nature, surface science is an interdisciplinary field. The techniques used in surface science typically require incredibly low pressures (also known as ultra-high vacuum) in order to investigate surfaces with nanoscale accuracy. Some of these techniques have been adapted in recent years, engineered to gain the same information while operating at higher pressures. There are a number of surface science techniques that can be performed using a laboratory kit, but some require synchrotron facilities.

All of the data in this thesis has been collected using surface-sensitive techniques that are usually carried out under vacuum conditions. Chapters 3 and 4 use X-ray photoelectron spectroscopy, carried out under both ultra-high vacuum (UHV) and near-ambient pressure conditions. Chapter 5 features X-ray photoelectron spectroscopy data taken at UHV, which were recorded at two different synchrotron facilities (SOLEIL, ASTRID2 (ISA)), and X-ray absorption data, specifically near-edge X-ray absorption fine structure spectroscopy data, also recorded at a synchrotron facility (SOLEIL). Chapter 6 uses X-ray photoelectron spectroscopy, scanning electron microscopy, and energy-dispersive X-ray spectroscopy. These techniques are outlined below, explaining their physical principles and experimental setups.

2.2 Vacuum systems

A vacuum is characterised by the pressure within a particular region. While the international system (SI) unit of pressure is the Pascal (Pa), in vacuum science the units of millibar (mbar) or Torr are usually used. There are different regions of vacuum, which start at rough vacuum (typically defined as $>10^{-4}$ mbar), and go up to ultra-high vacuum (UHV) (defined as $<10^{-8}$ mbar) [1].

Surface science techniques that characterise surfaces using particles require UHV conditions. This is because longer mean free paths are necessary for use and/or detection of particles in these systems. The lower the pressure in the system, the longer the mean free path of these particles, and thus fewer scattering events occur and minimises the loss of information contained within those particles.

2.2.1 Achieving vacuum

Vacuum systems consist of various pumps, valves, plumbing (tubing) and pressure gauges. Reducing the pressure inside a system to UHV must be done in stages.

First, the pressure in the system must be brought down from atmospheric to $\sim 10^{-3}$ mbar using a roughing pump. For UHV systems, roughing pumps are also used as 'forepumps' for those that require rough vacuum to function (see turbomolecular and entrapment pumps below). The most commonly used roughing pumps are rotary pumps and scroll pumps. Rotary pumps (see Figure 2.1) remove gas in a chamber through vanes mounted onto a rotor. The vanes move back and forth, creating a motion that captures and compresses gas in the interior of the pump. The trapped gas is then expelled through an exhaust valve to atmosphere [2]. Scroll pumps, on the other hand, remove gas using two nested Archimedean screws. These screws are made by mounting spiral-shaped walls on a circular base plate. Each of these screws are called scrolls. The scrolls rotate, and trap gas between the spiral walls (see Figure 2.2). The continued rotation moves the trapped gas along the pump toward the outlet to atmosphere [3].
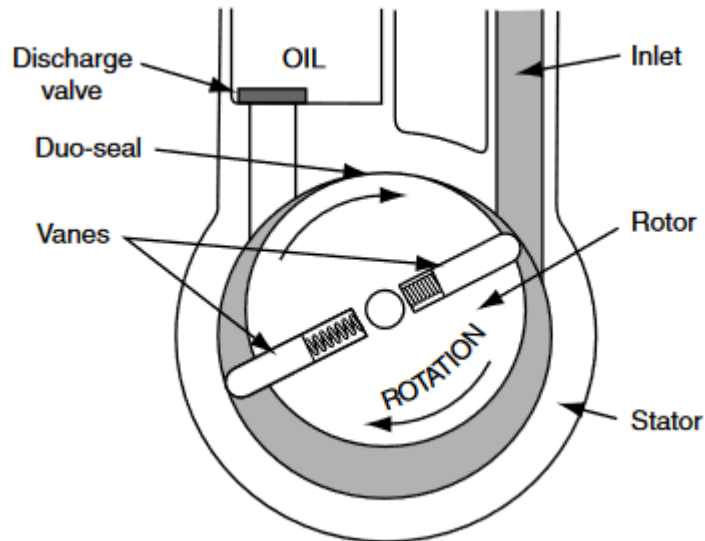
Figure 2.1: Schematic diagram of a rotary vane pump [3].

Figure 2.2: Diagram of the scrolls inside a scroll pump. The shaded area illustrates the path of gas as it is trapped in the scrolls inside a scroll pump [4].

Once a chamber is in the 10^{-3} to 10^{-4} mbar range, a turbomolecular pump (sometimes simply referred to as a turbo-pump) is used to reduce the pressure to ~10^{-6} mbar and below (a schematic diagram is featured in Figure 2.3). Using rapidly spinning, circular rotor blades (that can reach up to $3{\times}10^4$ revolutions per minute), residual gas molecules travel downward to the lower section of the pump. The blade design is such that molecules impinging upon them gain momentum in the downward direction. The gas is compressed in the lower section, and then expelled to an auxiliary pump [2]. For many systems, the use of turbomolecular pumps (supported by roughing pumps) is enough to reduce the pressure to 10^{-9} to 10^{-10} mbar range. However, the pressure in a chamber can be reduced even further with the use of entrapment pumps.
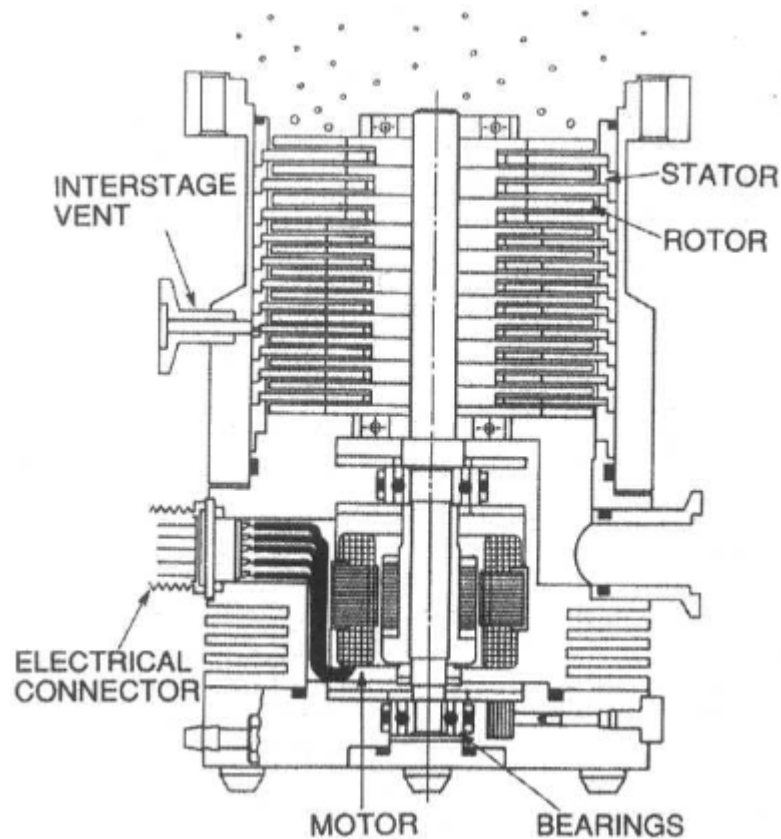
Figure 2.3: Schematic of a turbomolecular pump [2].

Reducing the pressure from $<10^{-10}$ mbar to the order of 10^{-12} mbar requires an entrapment pump. These pumps 'trap' remaining molecules by various means. Commonly used entrapment pumps include cryopumps, sputter ion pumps, and titanium sublimation pumps. Cryopumps, as the name suggests, trap molecules on surfaces cooled to temperatures below -150°C. Gas molecules bind to these cooled surfaces via van der Waals forces. In a sputter ion pump, gas is ionised between a Ti cathode and a stainless steel anode that generate a strong electric field between them (of the order of several kV). The gaseous ions, accelerate to the cathode by the strong electric field, which then sputter Ti atoms. This forms a Ti film on the inner walls of the pump (as shown in Figure 2.4) which reacts with residual gases in the chamber, such as oxygen, nitrogen and hydrogen. The gases (or compounds formed from the reaction) are subsequently trapped beneath layers of further sputtered Ti. A Ti sublimation pump uses a combination of cryopump and sputter ion pump technology. In these pumps, Ti is evaporated (or sublimed) from a filament onto cooled surfaces, where gases condense due to the low temperatures. The gases then

react with the Ti, leading to irreversible gas entrapment. Entrapment pumps can bring the pressure down to as low as 10^{-11} mbar.
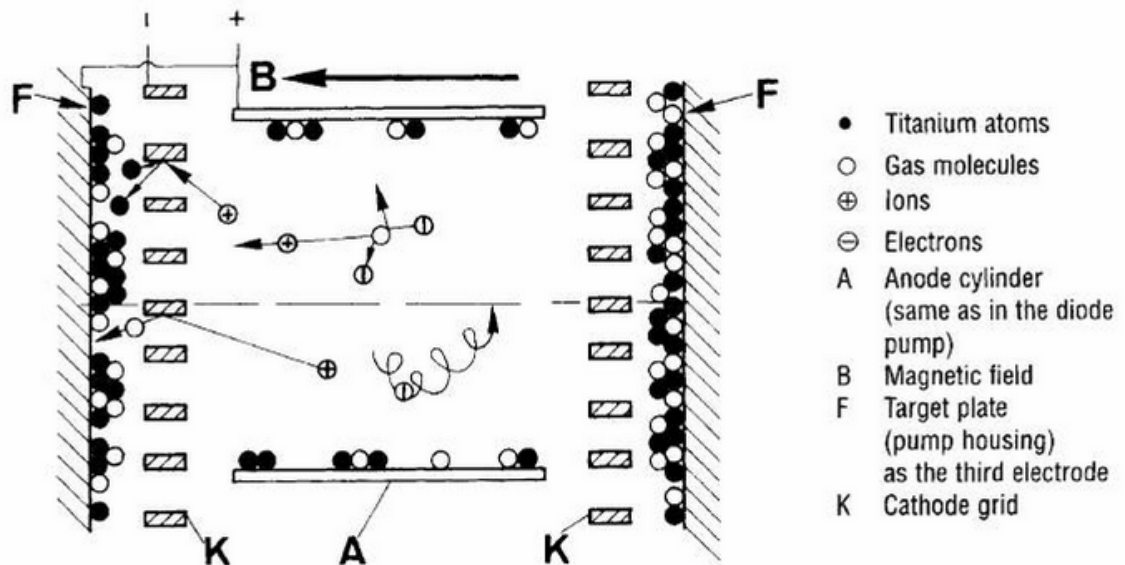
Figure 2.4: Schematic diagram illustrating components within a sputter-ion pump and the process of ionising and trapping stray gas molecules to maintain UHV [5].

2.2.2 Maintaining vacuum

Part of attaining a good vacuum is a process known as a bakeout, executed prior to an experiment. This is when the chamber is heated between 150°C and 200°C for approximately 24 hours to remove atoms or molecules that have adsorbed on the internal surfaces of the equipment. These atoms or molecules desorb and are subsequently pumped away.

The pressure inside a vacuum system can be monitored using pressure gauges specifically catered for monitoring the quality of vacuum. The most common type for monitoring pressure from atmosphere to 10^{-2} mbar is the Pirani gauge, which measures the pressure via heat lost from a thin metal wire to its surroundings. At high pressures, heat is transferred from the wire to gas molecules that collide with the wire. As the pressure decreases, thermal conduction decreases and the wire loses heat at a slower rate [6].

Ionisation gauges are used to monitor the pressure from ~10^{-3} mbar pressure to UHV. These work with the use of electrons accelerated from a cathode filament to a cylindrical wire mesh anode. Running down the middle of the anode mesh is a negatively-charged thin metal wire. A portion of the gas molecules ionised

by the accelerated electrons are 'collected' by the wire. The current through the wire is proportional to the number density of gas molecules inside the chamber and therefore proportional to pressure [5, 6].

Attaching external components to a vacuum system requires a tight seal- this is so that there is no leaking of atmosphere into the system. These seals are usually made of metal, and are known as gaskets. The gasket is 'sandwiched' between two flanges (one belonging to the component being attached). Once the component is attached securely with nuts and bolts onto the system, the knife-edges in both flanges 'bite' into the gasket and creates an air-tight seal. Copper gaskets are most widely used, but other materials used include gold and aluminium.

UHV can be sustained in a system of chambers with the use of valves. Chambers that are vented and pumped down again often (such as load lock chambers), can be closed off from sample preparation/sample analysis chambers using valves. That way, the load lock chamber can be exposed to atmosphere, while the UHV conditions are maintained in the sample preparation/sample analysis chamber. There are a variety of valves that will be suitable depending on the vacuum system (such as size, manual/computer-controlled, etc), and where they are located in the system (backing valve between a mechanical pump and a backing pump, for example) but all serve the same purpose [2, 7]. Gas canisters attached to a chamber (containing argon for sputtering, or oxygen for annealing purposes (see Chapter 5 for an example of this)), may be separated from the chamber by a needle valve, which allows for control of the gas flow into a chamber.

2.3 X-ray photoelectron spectroscopy (XPS)

2.3.1 Introduction

X-ray photoelectron spectroscopy, or XPS, is a technique based on the photoelectric effect, where illumination of a sample with electromagnetic (EM) radiation results in photoelectrons being ejected from the sample surface. For XPS, the EM radiation is usually soft X-rays (defined as X-rays with energies in the region of 200 eV- 2000 eV). It can be used to probe the occupied electronic

states in materials, and explore the chemical composition of, and chemical environments within, the surface of a sample.

2.3.2 Theory

Core electrons are bound to the nucleus of an atom in discrete energy levels, known as orbitals, or stationary states. The energies of the electron orbitals are element-specific and are influenced by the chemical environments of said element. These interactions alter the energies of the core electrons and therefore alter the electron density of the atom.

Orbitals are denoted using spectroscopic notation, which is of the form nl_j where n, l, and j are quantum numbers that define the orbital. The principal quantum number, n, is proportional to the energy of the orbital, and so larger values of n correspond to higher energy orbitals. The orbital angular momentum is described by the orbital angular momentum quantum number l, and can have any integer value between 0 and n - 1, where n is the principal quantum number. The quantum number l describes the type of orbital the electron is in (when l = 0, 1, 2, 3,…; this corresponds to the s, p, d, f,… orbitals respectively). The total angular momentum (described by the total angular momentum quantum number, j) factors in both the orbital angular momentum (l) and the electron spin (s), where $j = l \pm s$. The spin quantum number, s, for an electron is equal to ½, and the projection of the spin relative to the orbital angular momentum, s_p, takes the value ± ½, depending on whether it is parallel (positive) or antiparallel (negative). This results in two values of j for all core orbitals apart from s orbitals.

In XPS, X-ray photons of a fixed-energy (hv) are directed at the sample, which results in the emission of electrons from the sample surface- from both the core and valence states. The process is outlined in Figure 2.5. The electrons emitted (or photoelectrons) have a particular kinetic energy (E_K), which can then be used to obtain the binding energy (E_B) of the state the photoelectron once occupied. This requires the equation for Einstein's photoelectric effect, given by Equation (*2.01*):

$$hv = E_K - E_B - \varphi \qquad\qquad (2.01)$$

Where φ is the work function. The work function is defined as the energy

necessary to remove an electron from the Fermi level to the vacuum level [8], i.e. to a position where the electron is no longer influenced by the system it came from. The binding energy is usually scaled to the Fermi level rather than vacuum level (i.e. defining the Fermi level as the zero point).
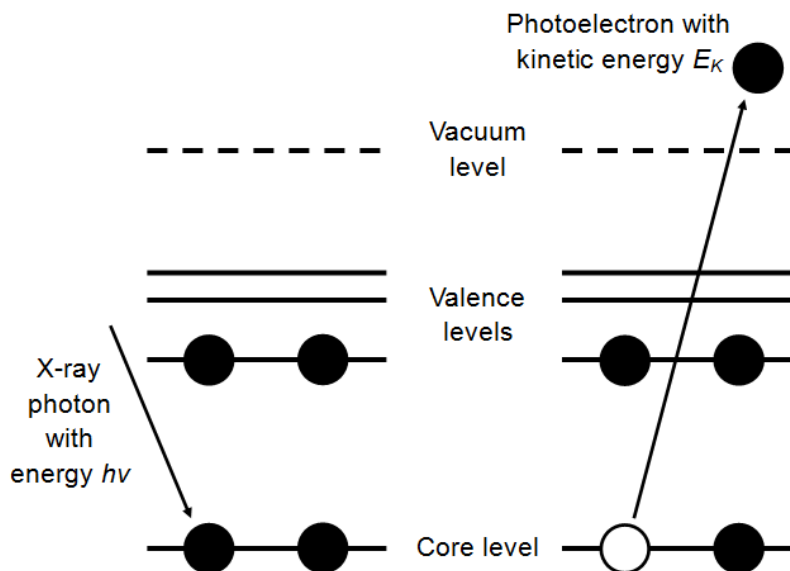
Figure 2.5: Energy level diagram describing the process of X-ray photoemission.

The work function in most cases is largely due to the electron energy analyser used and is not the inherent work function of the sample. The difference in work function is due to the electrical contact between the sample being analysed and the analyser itself [9].

The assumption can be made that the core hole left behind by the ejected photoelectron is not immediately filled by another electron, meaning the energies required to remove the electrons from their orbits are representative (equal to the negative of) of the energy of the orbitals from which they were ejected. The approximation that these other electrons are 'fixed' is known as Koopmans' theorem. While in actuality rearrangement of electrons will occur (also known as relaxation), this is only significant for valence electrons. When considering core levels, the electrons surrounding the core hole are insensitive and the approximation holds [10].

2.3.3 Experimental setup for XPS

The necessary components of XPS include an X-ray source, a monochromator, and a hemispherical analyser (HSA). The HSA houses a detector (either a

channeltron or a multichannel plate) which allows an XPS spectrum to be generated.

X-ray source

For laboratory-based XPS, the most popular choices of X-ray sources are Al K_α and Mg K_α sources. X-rays are produced when the anode (which for the aforementioned sources are made of aluminium and magnesium respectively) is bombarded with high-energy electrons, ionising atoms within the anode. The electrons bombarding the anode are of a high enough energy to ionise a core shell, resulting in a K_α electronic transition (transition of an electron from an L shell orbital ($n = 2$) to an orbital in the K shell ($n = 1$)). Because there are two 2p levels ($2p_{3/2}$ and $2p_{1/2}$), there are two K_α transitions, and so produces a doublet. For Al K_α sources, the width of this doublet is narrow enough as to not limit the resolution (0.85 eV), and the X-rays are of high enough energy (1486.6 eV) to cause core-level photoemission in the sample.

Monochromator
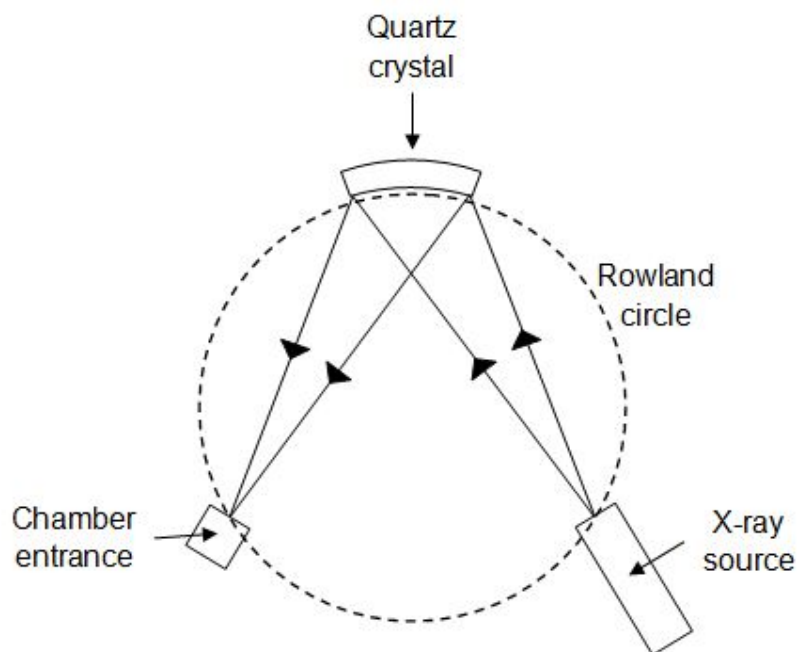
Figure 2.6: Schematic diagram showing the setup for monochromatic X-rays, whereby the X-ray source, the concave quartz crystal and the target chamber entrance are in position on a Rowland circle.

When X-rays are emitted from the source, the K_α emission needs to be separated from radiation produced by Bremsstrahlung processes (radiation emitted by electrons decelerating due to electromagnetic interaction with the

60

nucleus), and from weaker radiation produced by other transitions (such as K$_\beta$ transitions). This is done using a monochromator, which is composed of a concave quartz crystal. The quartz crystal diffracts the incoming radiation according to Bragg's law:

$$n\lambda = d\sin\theta \qquad (2.02)$$

Where n is the order of diffraction, λ is the wavelength of the X-rays, d is the lattice spacing in the crystal and θ is the Bragg angle. The sample is placed in a position where the diffracted X-rays (those with characteristic energy of Al K$_\alpha$ or Mg K$_\alpha$ transition) are able to be refocussed. The position where this can occur is on a Rowland circle, which is a circle whose diameter is equal to the radius of curvature of the grating (assuming the X-ray source also lies on the Rowland circle, see Figure 2.6) [11].

Hemispherical analyser (HSA)
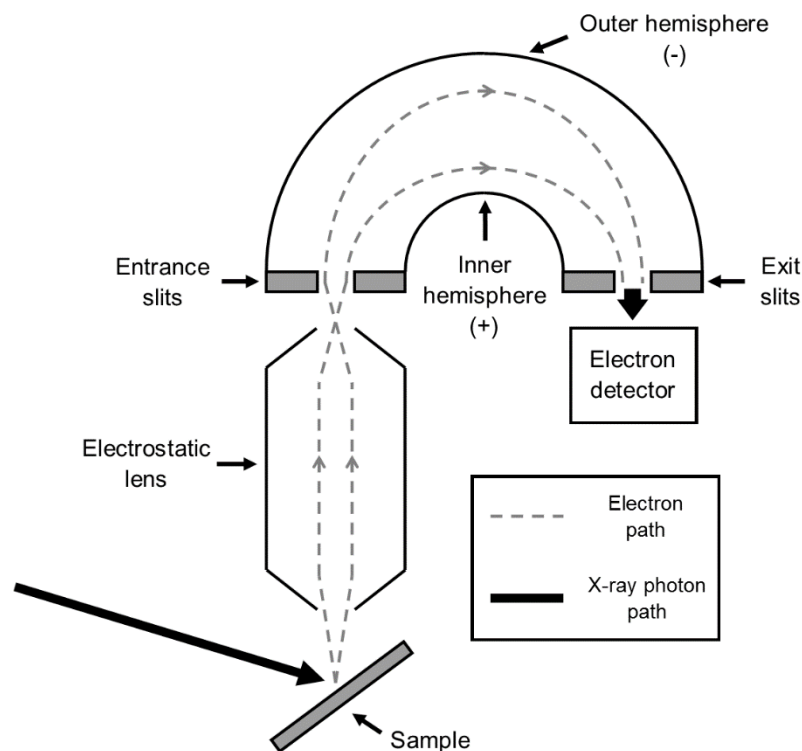
Figure 2.7: Schematic diagram of a hemispherical analyser. The path of the photoelectron is represented by a grey dashed line and the incident X-ray photon is represented by a solid black arrow.

The X-rays, travelling from the crystal monochromator to the sample surface, generate photoelectrons with a range of kinetic energies. Before entering the HSA, they pass through an electrostatic lens (see Figure 2.7) designed to slow

the electrons down to an energy known as the pass energy. They also focus the electrons into a beam of dimensions comparable to the entrance slit of the HSA. Upon entering the slits, the electrons are then subject to an electric field generated by the hemispheres (a negative voltage is applied to the outer hemisphere, and a positive voltage is applied to the inner hemisphere). Electrons that are more energetic than the pass energy are deflected less by the field, and into the outer hemisphere. Electrons that are less energetic than the pass energy are deflected more by the field, and into the inner hemisphere. This means that only the electrons with the required energy arrive at the exit slits and into the detector, which typically houses a channeltron or microchannel plate.

Detector

The detector, either a channeltron or microchannel plate, amplifies the signal through the generation of secondary electrons. In the case of a channeltron, a curved tube is used, which is coated in an insulating material with a low work function. A potential difference is applied across the ends of the tube, accelerating incoming electrons. The incoming electrons impinge on the material inside the tube, generating secondary electrons. In turn, those electrons impinge the material and generate more electrons, and so on. This amplifies the output by approximately 10^6. The sample principle is applied in a microchannel plate, but rather than one single tube, an array of smaller tubes are used, where the entrance of the tubes are angled in such a way that incoming electrons hit the tube walls. Both types of detector are illustrated in Figure 2.8.
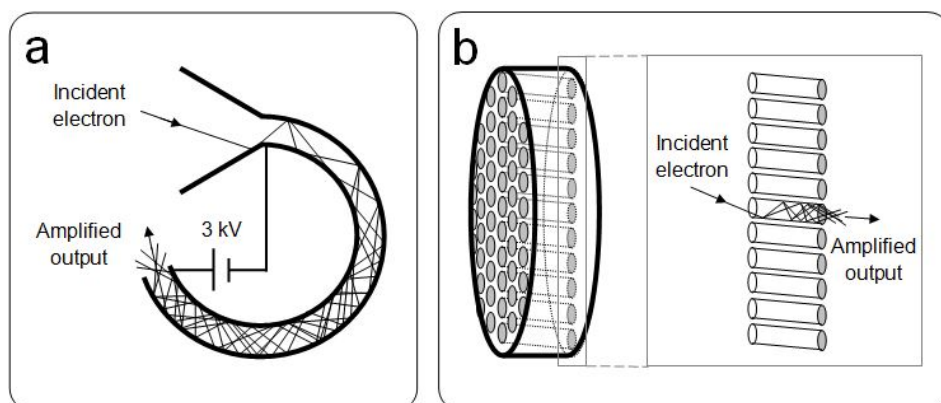
Figure 2.8: Schematic diagrams of a channeltron (a) and a microchannel plate (b). The inset of (b) shows the path of a photoelectron through one of the microchannels.

2.3.4 Core level photoelectron spectra
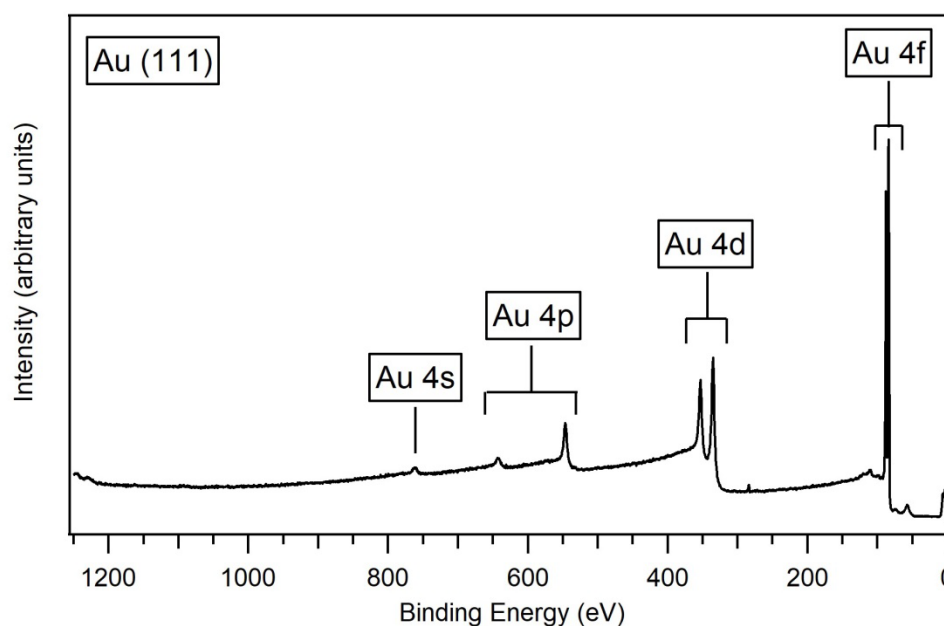
Figure 2.9: Example XPS survey spectrum recorded from Au (111) single crystal. Some of the more intense core level peaks have been annotated.

Figure 2.9 displays a typical XPS spectrum, taken from a clean sample of gold, specifically an Au (111) single crystal. Plotted on the x-axis is binding energy (often abbreviated to BE), and plotted on the y-axis is intensity. This particular spectrum is known as a survey spectrum, as it spans a wide binding energy range. Spectra that span a narrower energy range (in order to obtain a spectrum of a particular peak with better resolution) are known as narrow scans or region scans. Most peaks in XPS can be fitted with mixed Gaussian-Lorentzian line shapes (also known as a Voigt line shape), typically of a 70:30 ratio of Gaussian:Lorentzian. The Lorentzian profile originates from the lifetime broadening of states, and the Gaussian profile originates from instrumental broadening [1, 12]. Peaks arising from orbitals other than s orbitals are doublets, due to the interaction between orbital angular momentum and electron spin. The respective degeneracies of the orbitals ($2j$ + 1) give the relative intensities of the doublet peaks.

Peaks in XPS are superimposed on a background that increases toward higher binding energies. The background is comprised of signals arising from secondary electrons. These secondary electrons are the result of inelastic photoemission (whereby an ejected photoelectron experiences an energy loss, or multiple energy losses, on its way out of a sample). Inelastic photoemission

can be caused by phonon excitation, plasmon excitation, and/or inter and intra-atomic transitions.

Background corrections, normalisation, and spectra calibration
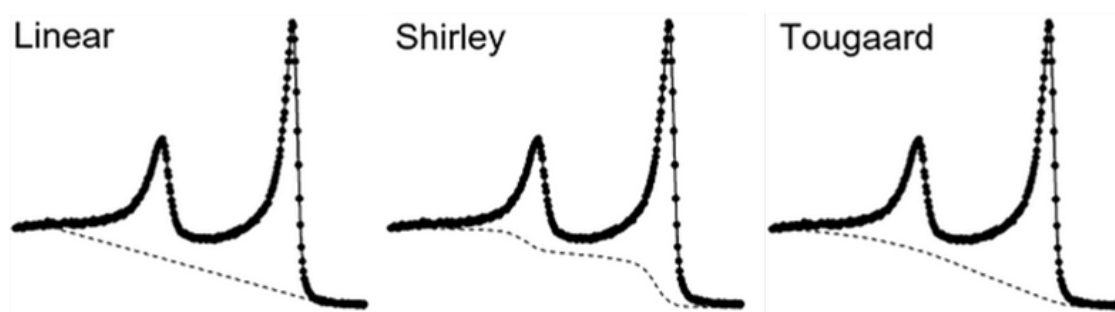
Figure 2.10: Linear, Shirley, and Tougaard background correction types displayed on an example Fe 2p spectrum. Figure adapted from [9].

A number of different background corrections can be made to XPS spectra. The most commonly used are a linear background; a Shirley background algorithm, or a Tougaard algorithm [9]. These background correction methods are shown using an example Fe 2p spectrum in Figure 2.10. Linear backgrounds are a simple approximation, and while they can alter the total peak area depending on the start and end points, are useful for data with numerous overlapping peaks. The Tougaard algorithm corrects for the background by simulation of the inelastic scattering over an energy range, but can be problematic for use in analysing complex samples with overlapping peaks in the spectra. The Shirley background algorithm corrects an S-shaped background for each peak in a spectrum, with the shape of the S dependent on the intensity of the start and end points. Because of its simplicity and accuracy, it is the most popular choice.
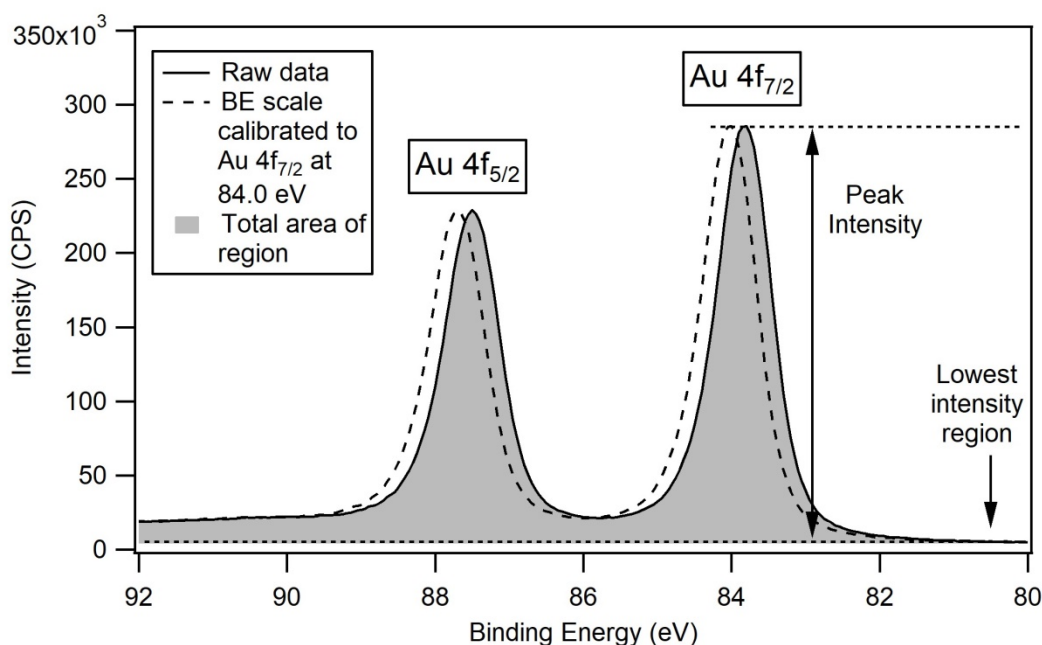
Figure 2.11: Example region spectrum, taken of the Au 4f region. The figure shows two sets of data: the raw data (solid line) and the data BE-calibrated to the Au $4f_{7/2}$ peak to 84.0 eV, showing a shift of approximately 0.2 eV to lower BE. Also annotated are the lowest intensity region (where the dotted horizontal line represents the intensity value of the lowest intensity data point), and the peak intensity. The grey shaded area represents the area of the whole region.

Spectra are typically normalised in one of two ways. They can be normalised to a particular peak, which means a specific feature maintains the same intensity, allowing for comparison of intensity changes in other peaks. First, the lowest intensity part of the spectrum needs to be at zero intensity (the lowest intensity region is annotated at the right side of Figure 2.11). The spectrum is then divided by the intensity of the peak to which the region is being normalised (see Figure 2.11), and thus the intensity of the peak is equal to unity. Chapters 3, 4, 5, and 6 contain spectra where this type of normalisation has been used. Spectra may also be normalised to the total area of a particular region (given by the shaded area in Figure 2.11 in this example). This involves the same procedure as normalisation to a specific peak, but instead the spectrum is divided by the area of the whole region. This allows intensity comparison of multiple peaks, and is particularly useful when comparing peaks of vastly differing peak intensities (i.e. a region containing both quite low-intensity and high-intensity peaks). Chapter 4 features normalisation of this kind.

Calibration of spectra is important when comparing spectra with binding energy shifts. As mentioned earlier, binding energies would normally be calibrated to the Fermi edge of the sample (fixing the Fermi edge to 0 eV), but this is not

feasible for fixed-energy X-ray sources. Instead, a particular peak must be chosen for calibration. This involves assigning a particular peak to a specific binding energy, usually one that is featured in all spectra and is least likely to experience a shift. The shift between the 'experimental' binding energy of the peak and the 'true' binding energy value is then applied to all other regions (the shift in the Au 4f region can be seen in Figure 2.11). Quite often substrate peaks are chosen for calibration (this could include Au $4f_{7/2}$ at 84.0 eV, for example), but a popular choice in XPS spectra of imidazolium- or phosphonium-based ionic liquids is calibration to the alkyl chain (C-C) peak in the C 1s region.

Chemical shifts

As mentioned earlier, region scans in XPS measure the number of electrons over a relatively narrow binding energy range. The exact range will vary from region to region (and depending on the core level peak/doublet of interest). Photoelectrons from the same element, but in non-equivalent atoms, will produce peaks at slightly different binding energies. This is known as chemical shift. The direction of the shift (i.e. to higher or lower binding energy) depends on the nature of the difference between atoms. For example, the O 1s signal in nitrogen-doped TiO_2 is lower in binding energy than that of undoped TiO_2 [13].

Sample charging

In samples with poor electrical conductivity (such as insulator materials or viscous ionic liquids), charge can gather in the sample and cause artefacts in the XPS spectra. These include unusual binding energy shifts (usually of several to tens of eV) and peak broadening. Sample charging can be offset using an electron flood gun or reducing the thickness of the sample material.

Surface sensitivity of XPS

While X-ray photons can penetrate deep into a sample, the depth from which photoelectrons can escape the sample is limited by their inelastic mean free path (IMFP). The intensity of photoelectrons are attenuated according to the Beer-Lambert law:

$$I = I_0 \exp\left(\frac{-d}{\lambda \sin \alpha}\right) \qquad (2.03)$$

Where λ is the inelastic mean free path length, α is the angle at which the

photoelectrons exit the sample (relative to the surface), I_0 is the initial intensity and I is the intensity of the photoelectrons after travelling through a vertical distance d through the sample. Using Equation (2.03), the angle at which electrons escape from the sample can be used to determine the vertical distance they have traversed in the sample (i.e. sampling depth). 95% of the photoelectrons measured in XPS will have been produced approximately 3λ distance into the sample. The smaller (more grazing) the photoemission angle probed ($0° < \alpha < 90°$), the more surface-sensitive the resultant XPS measurements.
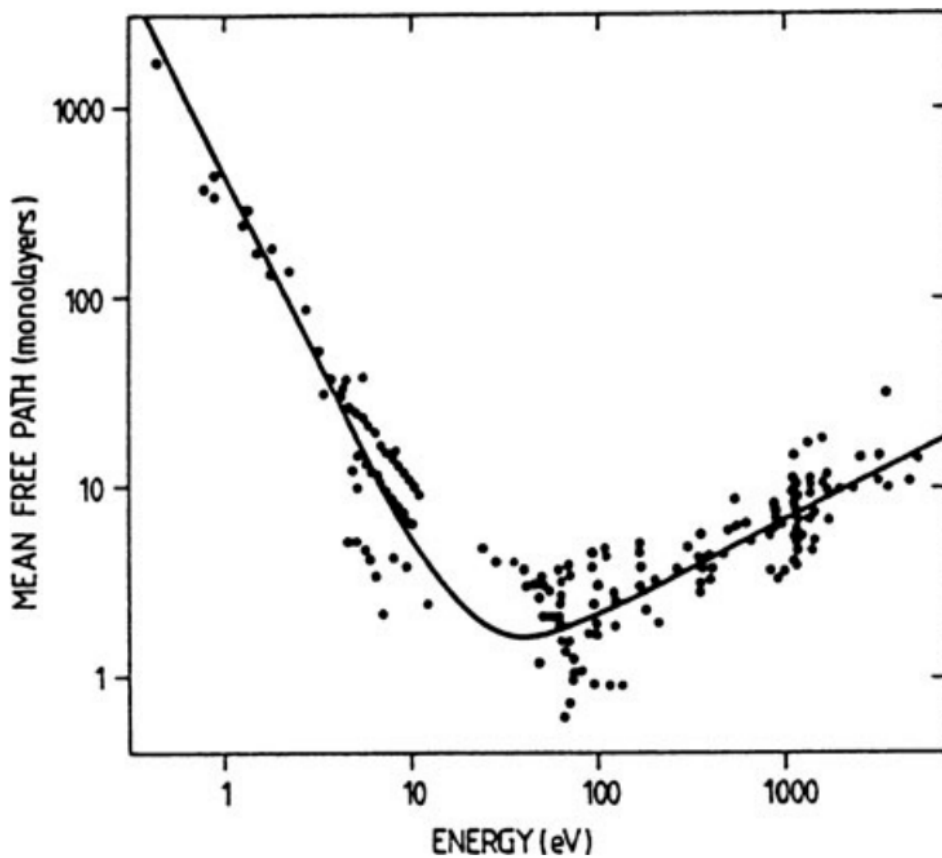
Figure 2.12: Mean free path (in monolayers) for the inelastic scattering of photoelectrons as a function of their kinetic energy [14].

The inelastic mean free path of an electron is dependent on its kinetic energy, which is illustrated by the IMFP curve shown in Figure 2.12. This is the IMFP, plotted on the y-axis in monolayers, as a function of electron energy in eV. The curve has a minimum at ~100 eV, where the mean free path is only a few monolayers. To obtain the most surface-sensitive information, electrons with a kinetic energy of ~100 eV (and thus with a minimum value of IMFP) are ideal. Therefore, for variable X-ray sources, such as synchrotrons (see Section 2.9 for

more details about synchrotron radiation and synchrotron facilities), photon energies should be selected that will produce photoelectrons with kinetic energies of ~100 eV.

2.4 Near-ambient pressure X-ray photoelectron spectroscopy (NAPXPS)

2.4.1 Introduction

At the basic level, near-ambient pressure XPS (NAPXPS) and XPS carried out in UHV operate on the same physical principles. The technique still involves X-rays incident on a sample, and photoelectrons are still emitted from the sample surface, but in NAPXPS, this process no longer requires vacuum conditions to be measured. While the idea of NAPXPS has been around for several decades, it is only because of the comparatively recent advancement of transfer optics that allows NAPXPS hemispherical analysers to acquire feasible electron signals.

2.4.2 Experimental setup for NAPXPS

The key differences between XPS in UHV and XPS under NAP conditions lie in the experimental set up. The components that allow NAPXPS to be carried out are the NAP cell and the transfer optics.
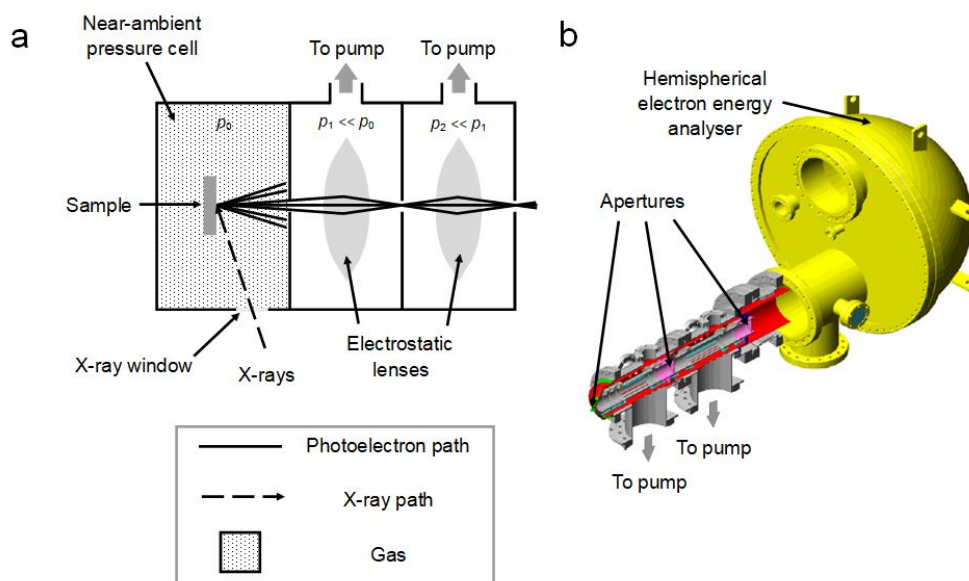
Figure 2.13: A schematic diagram of a NAP cell and differential pumping is shown in (a) with the sample surrounded by gas. The apertures are annotated inside the differential pumping system that is attached to the HSA in the schematic diagram shown in (b). Figure adapted from [15].

<u>NAP cell</u>

For NAPXPS measurements, the sample is housed inside a NAP cell, where a near-ambient pressure gas surrounds the sample, as shown in Figure 2.13. Incident X-rays enter the NAP cell through an X-ray window. The X-ray window is typically coated in a Si_3N_4 membrane 50 μm or 100 μm in thickness. The window serves to prevent gas leakage from the NAP cell to the X-ray source, which is under UHV. The X-ray housing is mounted on bellows (with the X-ray window at the end of the bellows) for ease of alignment. The source is typically positioned ~10 mm away from the sample.

Photoelectrons emitted from the sample can experience both elastic and inelastic collisions with the gas molecules as they travel through the gas. The mean free path of photoelectrons is proportional to their kinetic energy and is inversely proportional to the gas pressure inside the NAP cell. This requires the first aperture to be at a suitable distance from the sample in order to maximise the photoelectron yield (typically in the range of tens of μm). The first aperture is conical, and has a diameter of 1 mm or less (the conical apertures are detachable and are available in different sizes). Photoelectrons that have successfully exited the NAP cell through the first aperture travel through a series of differentially pumped chambers.

<u>Transfer optics</u>

In the first two chambers after leaving the NAP cell, the photoelectrons are focussed by two sets of electrostatic lenses into the third chamber. These first two chambers are pumped by turbomolecular pumps to bring them down to lower pressures extremely quickly. As illustrated in Figure 2.13a, the second chamber has a lower pressure than the first. In the third chamber, a quadrupole directs the photoelectrons toward the entrance of the HSA. The third chamber is pumped using an ion pump bring the pressure down even further, to the extremely low-pressure conditions required by the HSA. This differential pumping system allows the NAP cell to sustain a comparatively high pressure while the HSA is under UHV.

2.4.3 Near-ambient pressure photoelectron spectra
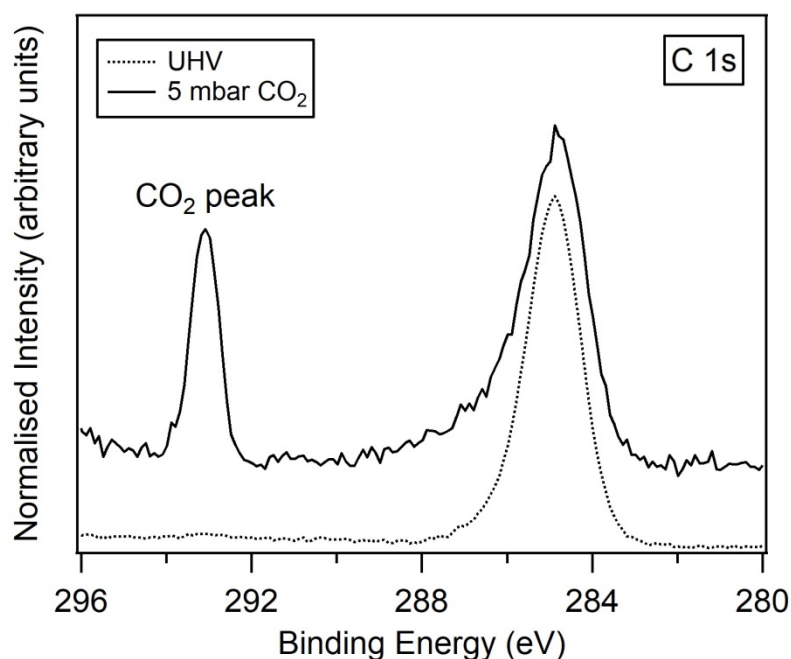
Figure 2.14: C 1s NAPXPS spectrum, featuring a sample of trihexyl-tetradecyl phosphonium benzimidazolide under UHV conditions (dotted line) and under 5 mbar of CO_2 (solid line). The CO_2 peak, appearing at ~293.1 eV, is annotated.

The spectra produced by NAPXPS are much the same as those produced by XPS under UHV (and thus can usually be background-corrected, normalised and BE calibrated in the same way), but possess some differences. Gas molecules surround the sample and are, too, illuminated by incident X-rays. Like the atoms in the sample, a transfer of energy occurs from the X-rays to the electrons in the constituent atoms of the gas molecules, which results in photoemission. This produces a signal, or multiple signals depending on the composition of the NAP environment, known as gas-phase features.

Gas-phase features

Peaks produced by the gas inside the NAP cell are typically separated from other features by several eV. This is demonstrated by the CO_2 peak in the example spectrum in Figure 2.14. The intensity of the gas-phase features is dependent on the gas pressure surrounding the sample, so a greater gas pressure results in a more intense the gas-phase peak.

Gas-induced attenuation

The counts per second measured for NAPXPS are much lower than that of ordinary XPS because of the short mean free path of electrons at high pressures, meaning a proportion of electrons are lost before they even enter the first aperture. However, as mentioned previously, electrostatic lenses that are in place between the apertures focus the electrons and maximise the photoelectron yield. Fewer electrons reaching the detector results in lower counts, and spectra with reduced signal-to-noise ratio. This is evident in the example spectrum in Figure 2.14.

2.5 X-ray absorption spectroscopy (XAS)

2.5.1 Introduction

X-ray absorption spectroscopy (XAS) probes the unoccupied electronic states of atoms. In XAS and related spectroscopies, electrons are excited rather than ejected from the surface, which differentiates it from XPS. It can be used to investigate the chemical environments of a sample, as well as the structure and arrangement of resonant structures on a sample.

2.5.2 Theory

An incident X-ray photon with energy $h\nu$ excites a core electron into an unoccupied state. The greater the incident X-ray photon energy, the greater the energy of the unoccupied states that can be probed. The incident X-ray photon will be attenuated by the material it is probing according to the Beer-Lambert equation (see Equation (*2.04*)), where I_0 is the initial intensity of the incident X-ray, μ is the X-ray linear absorption coefficient, x is the thickness of the sample, and I is the attenuated intensity of the X-ray photon. The X-ray linear absorption coefficient is therefore defined as the reciprocal of the sample thickness (*x*) to reduce the intensity of the incident X-ray by a factor of $1/e$. The coefficient increases with atomic number (approximately Z^4), and, generally, decreases with increasing X-ray photon energy (approximately E^{-3}) [16].

$$I = I_0 \exp(-\mu x) \qquad (2.04)$$

At particular energies, there is a drastic increase in the absorption coefficient of a sample, distinguished by a discontinuity, or sharp 'dip' in the absorption coefficient as a function of X-ray energy (see Figure 2.15). This increase in

absorption is known as the absorption edge and occurs when the incident X-ray photon is of a sufficient energy to result in an electron transition from a core state to an unoccupied state. The absorption edges are denoted as K-, L-, M-edges which correspond to transitions involving electrons from K ($n = 1$), L ($n = 2$), M ($n = 3$) subshells.
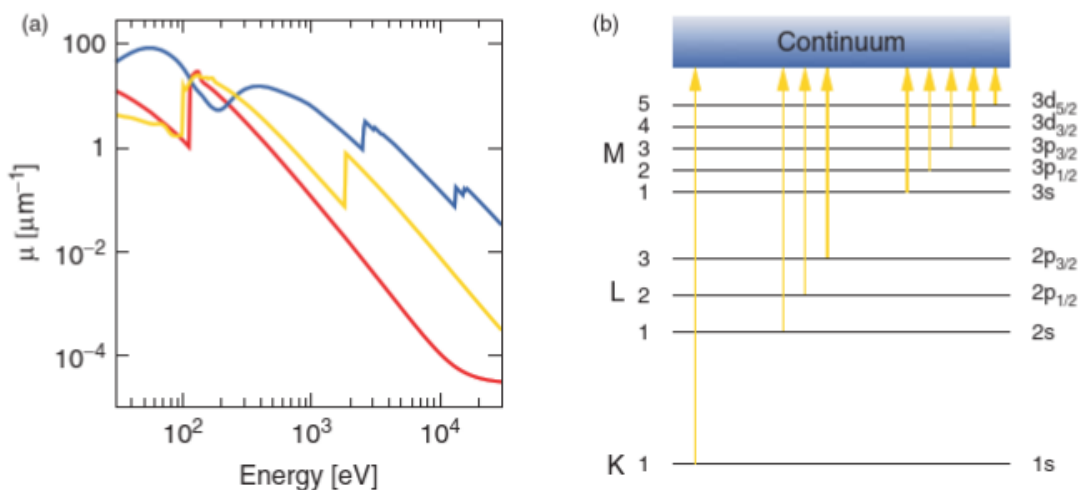
Figure 2.15: Absorption coefficient (in μm^{-1}) as a function of photon energy in eV (a) for beryllium (red), silicon (yellow), and lead (blue). The absorption edges arise from electron transitions with just sufficient energy to liberate an electron from a core orbital to a continuum state. Example transitions are shown in (b) with X-ray notation on the left and spectroscopic notation on the right (see Section 2.6.2 for more information about these notations) [16].

When the hole that is left behind by the excited electron is filled, this results in the loss of energy (de-excitation) via either the emission of an X-ray (X-ray fluorescence) or emission of an Auger electron (see Figure 2.16). In XAS, either X-rays or Auger electrons can be collected to gain information about the surface (corresponding to fluorescence yield XAS and electron yield XAS respectively). Because of the relatively short mean free path of electrons (see Section 2.3.4), Auger yield XAS can be considered more surface-sensitive than fluorescence yield XAS.
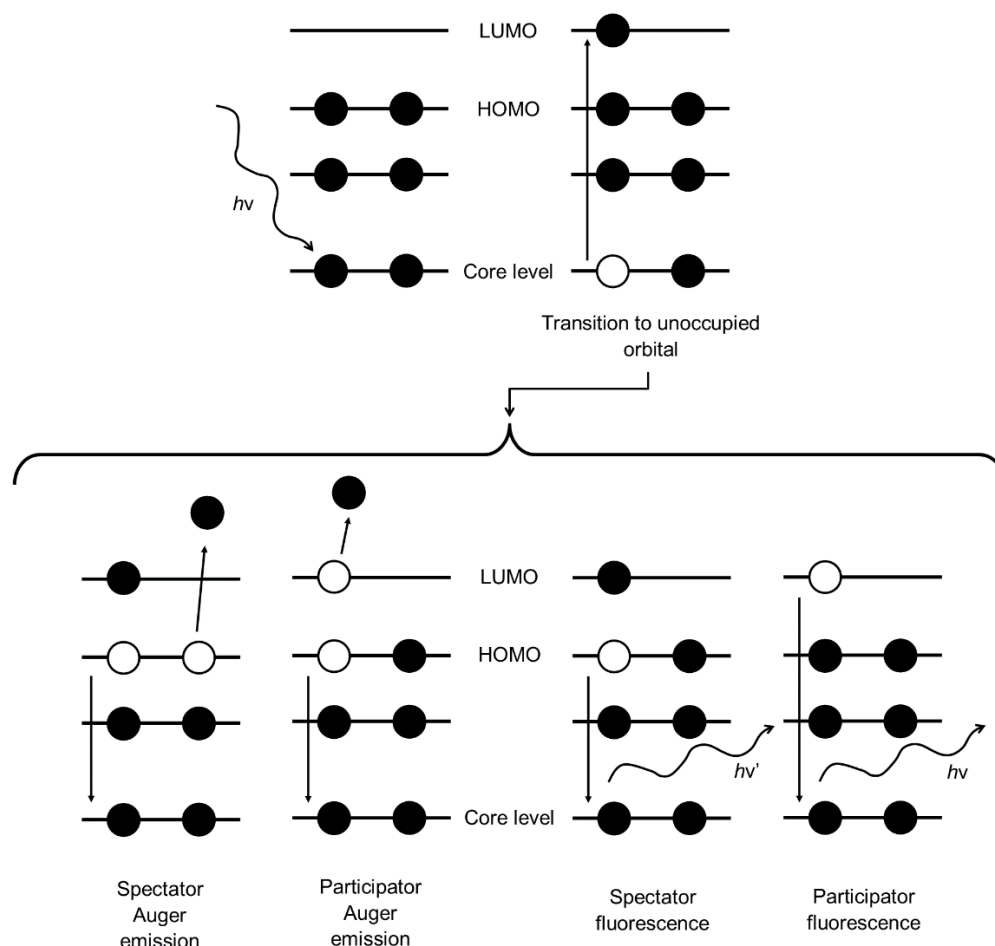
Figure 2.16: Schematic diagram demonstrating the spectator and participator decay processes as a result of electronic transition to an unoccupied orbital. The spectator and participator Auger electrons are emitted with a unique kinetic energy independent of the energy of incident X-ray photon, $h\nu$. The energy of the X-ray photon emitted via spectator fluorescence is given by $h\nu'$ and is less than that of the incident X-ray photon, while the X-ray photon emitted via participator fluorescence is the same as the incident X-ray photon. The labels HOMO and LUMO stand for highest occupied molecular orbital and lowest unoccupied molecular orbital respectively.

In Auger electron emission, an electron from a valence state fills the core hole. The energy released by the newly-filled core hole is transferred to another electron. If the energy transferred is enough to liberate that electron, it is then emitted as an Auger electron with a specific kinetic energy. For molecules consisting of lighter atoms (atoms with low atomic number, Z), Auger emission is the most dominant energy-loss method. For organic molecules, the absorption edges of interest require soft X-rays (<1000 eV). It is also worth noting that the kinetic energy of an Auger electron is independent of incident X-ray photon energy. Auger features often appear in XPS spectra depending on the energy of the incident X-ray photons. If a binding energy spectrum is taken at different photon energies, the Auger peaks will shift but the photoemission peaks will not (an example of this is featured in Chapter 5).

2.6 Near-edge X-ray absorption fine structure (NEXAFS) spectroscopy

2.6.1 Introduction
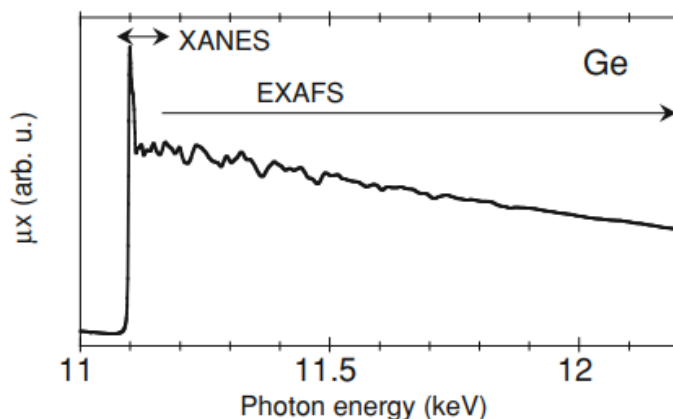
Figure 2.17: XAS spectrum (absorption cross section as a function of photon energy in keV) over the K absorption edge of germanium, highlighting the energy regions covered by near-edge X-ray absorption fine structure (NEXAFS) spectroscopy (labelled XANES in the figure due to the use of hard X-rays) and extended X-ray absorption fine structure (EXAFS) spectroscopy. Adapted from [8].

Studying XAS features near absorption edges is known as near-edge X-ray absorption fine structure (or NEXAFS) spectroscopy, where significant variations in the X-ray absorption coefficient of a material occur at energies close to an absorption edge (and usually in the soft X-ray range, somewhat distinguishing it from its hard X-ray sibling, X-ray absorption near-edge spectroscopy, or XANES). Therefore, the scanned energy range is only around 30 eV to 50 eV above the absorption edge. On the other hand, extended X-ray absorption fine structure, or EXAFS; investigates regions in the range of 50 eV to 1000 eV above the absorption edge. Example energy ranges are displayed in Figure 2.17 for EXAFS and XANES spectrum of germanium.

2.6.2 Theory

Spectroscopic notation versus X-ray notation

Both spectroscopic and X-ray notation describe electronic transitions. In X-ray photoelectron spectroscopy (XPS), spectroscopic notation is often employed, and reflects the origin of photoelectrons collected during measurements. As mentioned previously in Section 2.3.2, the spectroscopic notation is of the form nl_j, where n is the principal quantum number, l is the orbital angular momentum

quantum number and j is the total angular momentum quantum number, which incorporates the orbital angular momentum and spin quantum numbers.

X-ray notation, on the other hand, uses capital letters K, L, M, N, O etc. to denote the principal quantum number (i.e. K corresponds to $n = 1$, L corresponds to $n = 2$, and so on), and are sometimes known as shells. These are sometimes followed by a subscripted number to denote a specific state within the shell (and thus states within the shells are called subshells), which increases according to how closely bound the electrons are within the subshell. For example, the 2s level is denoted in X-ray notation as L_1, $2p_{1/2}$ as L_2, $2p_{3/2}$ as L_3, and so on. Core states, such as those within the K or L shell, are sometimes represented by C for simplicity. Valence states are often represented by the letter V due to their closeness in energy to one another, as the energy of one valence state difficult to distinguish from another and assumed to be of the same energy and one state.

While spectroscopic notation is favoured in XPS, X-ray notation is particularly useful when considering Auger electrons, since multiple electronic transitions can be expressed in a much simpler way. For example, the generation of a 1s core hole in an aluminium atom followed by the transition of an electron from the $2p_{3/2}$ orbital to fill the core hole would be denoted in spectroscopic notation in two parts: the production of the ionised Al, and the electronic transition from $2p_{3/2}$ to 1s:

$$\text{Ionisation: } 1s^2 2p^6 \rightarrow 1s^1 2p^6$$

$$\text{Transition: } 1s^1 2p^6 \rightarrow 1s^2 2p^5$$
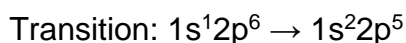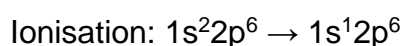
In X-ray notation, the transition would be represented as a KL_3 transition. If this transition results in an Auger emission from the $2p_{1/2}$ orbital, the electron would be referred to, in X-ray notation, as a KL_3L_2 Auger electron [9].

Ionisation potential and dipole selection rule

The ionisation potential is defined as the energy required to liberate an electron from a core level to the continuum of free states (located above vacuum level, as shown in Figure 2.15b). The X-ray absorption cross section of an atom or molecule is defined as the number of electrons excited per unit time divided by the number of incident X-ray photons per unit time per unit area. This quantity,

therefore, has the units of cm^2 or barn (where 1 barn = 1×10^{-28} m). This is an important aspect in X-ray absorption spectra in general, but is also important in understanding the shape of NEXAFS spectra. When the excitation energy approaches that of the ionisation potential, the absorption cross section approaches the value for electron transition to continuum states, rather than bound states [17]. At the ionisation potential, it follows that the cross section is then equal to that of the continuum cross section. The absorption cross section, derived from Fermi's 'Golden Rule', incorporates a number of approximations in order to simplify quantum mechanically. One important approximation is the electric dipole approximation, which at its core is the dipole selection rule, which, among others, is given by:

$$\Delta l = \pm 1 \tag{2.05}$$

Of relevance to this thesis are X-ray absorption spectra above the K-edge. So, this rule implies that, for K shell excitations (with an electron initially in an s orbital, and $l = 0$), the final state must contain a p orbital (where $l = 1$). Transitions forbidden by the dipole selection rules (such as s-s or p-p transitions) have implications for NEXAFS spectra, and may provide non-negligible contributions [8].

Molecular orbitals

Atomic orbitals consist of the culmination of all electron orbitals. Each orbital is the solution of a Schrödinger equation, where the potential arises from both attraction to the nucleus and repulsion from neighbouring electrons in their own orbitals. Molecular orbitals can be considered a linear combination of atomic orbitals. Using a homonuclear diatomic molecule (such as molecular hydrogen, or H_2) as an example, the molecular orbitals are formed from a combination of 1s atomic orbitals by addition or subtraction [18]. In the case of a heteronuclear diatomic molecule (i.e. a molecule made up of two different atoms), the relative energy of the atomic orbitals results in the molecular orbitals located more on one atom than the other. This causes a net charge transfer across the molecule if electrons populate the orbital. Bonding molecular orbitals have a lower energy than the atomic orbitals that combine to create them. Antibonding molecular orbitals have a higher energy than the atomic orbitals that combine to create

them. This is illustrated in Figure 2.18. Therefore ψ_1 is an antibonding molecular orbital and ψ_2 is a bonding molecular orbital.
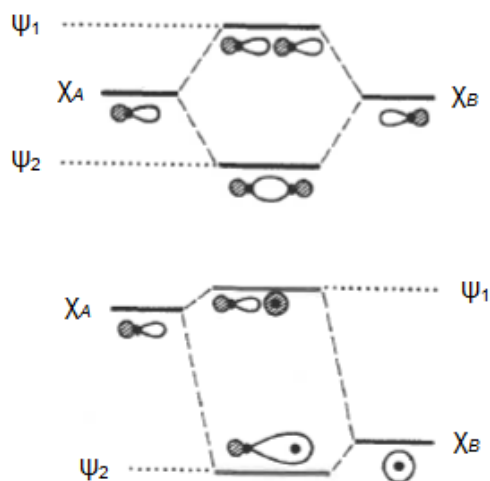
Figure 2.18: Schematic energy level diagram illustrating the interaction of two atomic orbitals inside a homonuclear molecule (top) and a heteronuclear molecule (bottom), each combining together to form molecular orbitals in the linear combination method. The shapes represent the probability distribution of electron position in each atom/molecule. Figure adapted from [17].

Wavefunctions associated with atomic orbitals describe the probability amplitudes of the position of an electron in that orbital. The wavefunctions correspond to an energy and a shape which determines how atomic orbitals interact. The shapes of atomic s- and p-orbitals are shown in Figure 2.19. Atomic s-orbitals have a 'spherical' symmetry, and atomic p-orbitals can have symmetry in either the x, y, or z axis; and thus these p-orbitals can be distinguished from one another by a subscript x, y, or z to denote their symmetry.

s

p_x p_y p_z
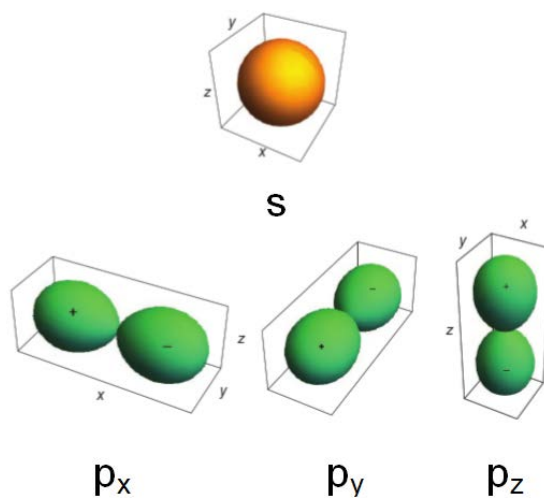
Figure 2.19: Shape of probability distribution for s- and p-orbitals. Figure adapted from [18].

Origin of bonding and antibonding σ and π molecular orbitals

The combination of atomic orbitals influences the shape and energy of the resultant molecular orbitals and the bonding between atoms [18]. Example combinations using 2p atomic orbitals of two homonuclear atoms are shown in Figure 2.20.
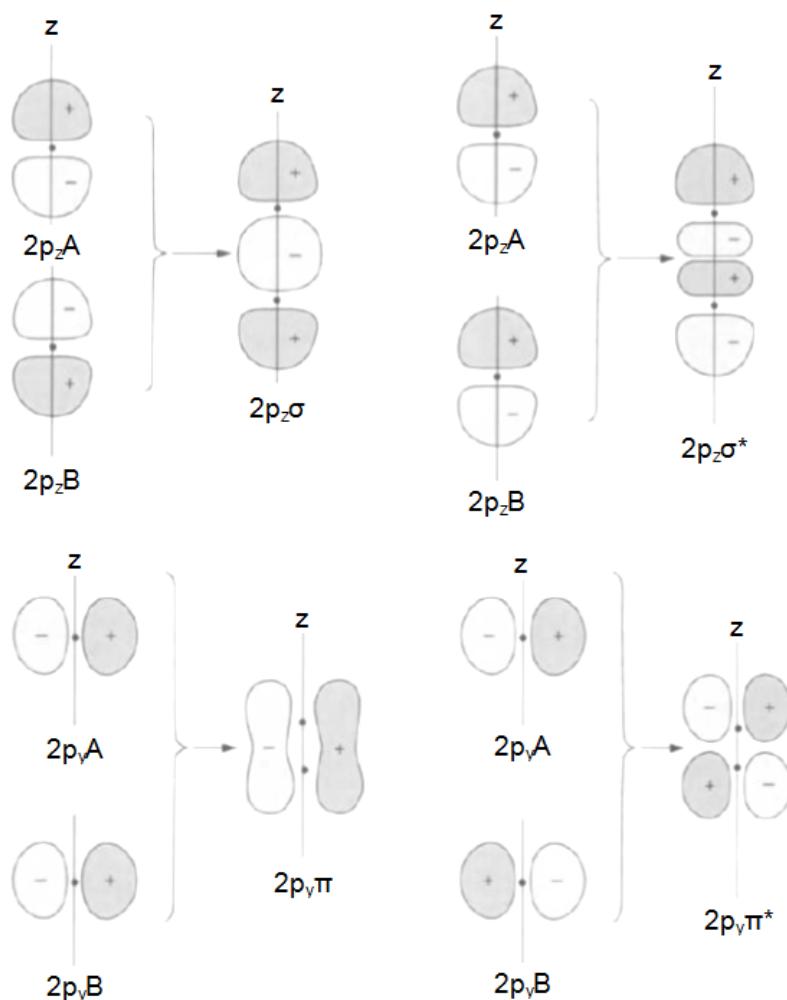
Figure 2.20: Example combinations of atomic $2p_z$ and $2p_y$ orbitals of two atoms, A and B, to generate bonding and antibonding σ and π molecular orbitals. Figure adapted from [19].

An asterisk as a suffix denotes antibonding molecular orbitals. Molecular orbitals that are involved in K shell excitations are the σ* and π* orbitals, which are unoccupied antibonding σ and π orbitals. Features observed in K-edge NEXAFS spectra correspond to a dipole-allowed electronic transition from a 1s orbital to an unoccupied π or σ antibonding orbital [17]. Molecular σ orbitals arise from s-s or p_z-p_z atomic orbital interaction. Molecular π orbitals arise from p_x-p_x or p_y-p_y atomic orbital interaction. The bonds that form from σ and π

orbitals are known as σ- and π-bonds respectively. Examples are shown in benzene in Figure 2.24.
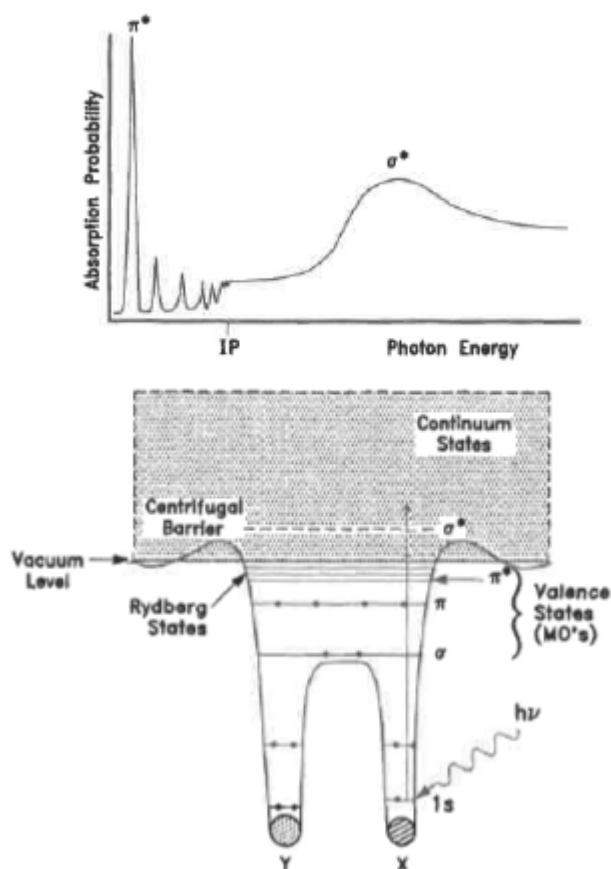
Figure 2.21: Schematic potential (bottom) and the resultant K-edge NEXAFS spectrum (top) of a diatomic molecule. The potential wells of each atom in the molecule combine, where the molecular orbitals reside, labelled as valence states. Beyond the Rydberg states and the vacuum level lie the continuum states, and the centrifugal barrier (the magnitude of which depends on the angular momentum quantum number l of the atom or molecule) separates the inner potential wells (which includes the core and valence levels) from the shallower outer wells. In the spectrum (top), the π* features appear below the ionisation potential (IP), and the σ* features appear above the IP. Figure adapted from [17].

Figure 2.21 shows a potential well diagram of a generic diatomic molecule (bottom) and the K-shell spectrum of the molecule (top). Above the vacuum level are continuum states. In a neutral molecule, the π* and σ* orbitals are above vacuum level, but ionisation/excitation of an electron from a core level (and thus the generation of a core hole) leads to an increase in Coulomb potential between the nucleus and the remaining electrons. Consequently there is a shift toward higher binding energy for the outer orbitals, and thus the excitation energy required for a transition from a 1s orbital to a π* orbital is below the ionisation potential. Rydberg states arise from bound state transitions

involving states below the vacuum level. Transitions to Rydberg states are responsible for the sharp features below the IP in the spectrum [17].

2.6.3 Experimental setup for NEXAFS

The experimental setup for NEXAFS depends on the yield detection method. Two types exist: electron yield and fluorescence yield. As mentioned in the introduction to this Chapter, Auger electron-yield NEXAFS was used in Chapter 5.

Electron yield NEXAFS can be measured in three ways: Auger electron yield (AEY), partial electron yield (PEY), and total electron yield (TEY). PEY and TEY are often taken in tandem with AEY, but have different window settings (kinetic energy ranges) to one another, as shown in Figure 2.22.
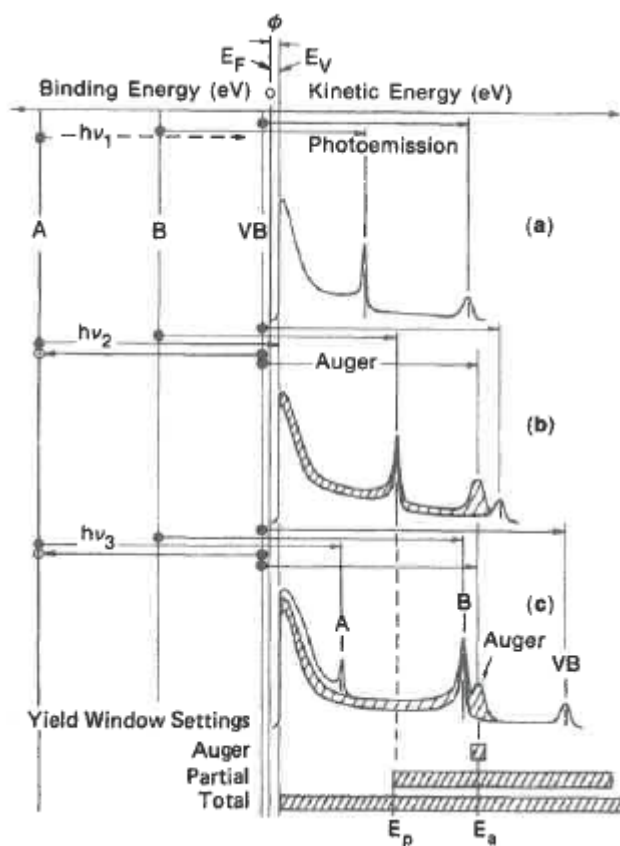
Figure 2.22: A combined energy level diagram (left to right) and example photoemission spectra at different incident photon energies (right side). In (a), the photon energy is below the excitation energy of the core level A, but is above the excitation energy for photoemission from the core level of B. In (b), the photon energy is sufficiently above the absorption threshold of A, which results in an Auger peak and a shift in the photoemission spectrum. In (c), the photon energy is beyond the threshold, and results in a photoemission peak from A and B, as well as the emergence of the valence band, VB. The Auger peak, independent of incident photon energy, appears at the same kinetic energy as it does in (b). The yield window settings (bottom) illustrate the energy window that is probed in Auger yield, partial yield, and total yield detection. Figure adapted from [17].

As the name suggests, in AEY, the window selected spans a narrow range around the Auger peak of interest. In PEY, the detector detects electrons with a kinetic energy above a threshold kinetic energy limit, E_p (see Figure 2.22), and uses a biased grid to decelerate electrons below that limit. For a specific value of E_p, photoemission peaks from the substrate can be omitted from the spectrum. While the count rate is higher for PEY than AEY, the signal-to-noise ratio is reduced. In TEY, all electrons are detected via the drain current using an ammeter. An inelastic 'tail' (a convolution of signals from low energy electrons of kinetic energy < 20 eV) dominates the resultant spectrum. Although the count rates of TEY spectra are high, their signal-to-background ratios are typically very small [17]. Of all the electron-yield methods, TEY is less surface sensitive than AEY and PEY due to the wide range of electron energies.

2.6.4 NEXAFS spectra
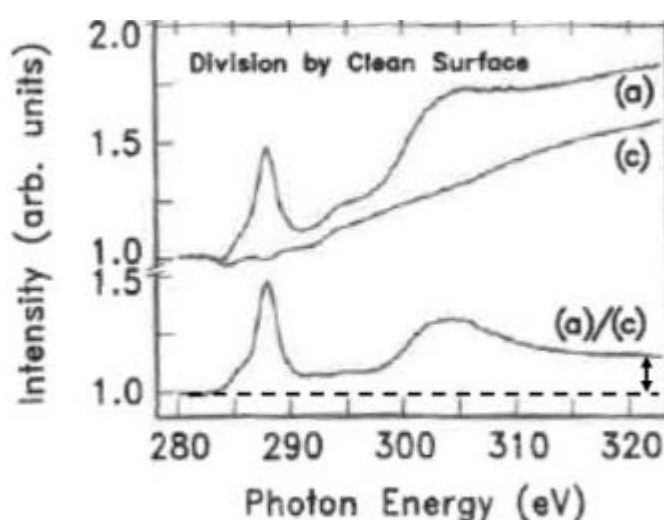
Figure 2.23: Example partial-yield C-K edge NEXAFS spectrum recorded from a sample of carbon monoxide on a molybdenum (110) single crystal (a), illustrating background correction using a spectrum recorded from the clean Mo (110) single crystal (c). The corrected spectrum is annotated with the label (a)/(c). Also illustrated is the spectrum 'step', shown by the double-headed arrow in the bottom panel. Figure adapted from [17].

Figure 2.23 shows an example K-edge NEXAFS spectrum for carbon monoxide on a molybdenum (110) single crystal surface. In order to quantify the angular direction of resonant structures at the surface of a substrate, the spectra need to be background-corrected and normalised.

Background correction and normalisation

Correcting the background of a NEXAFS spectrum requires a NEXAFS spectrum recorded of the clean substrate over the same photon energy range, ideally with the same energy step size. The clean spectrum should have a similar shape and 'step' as the general background of the spectrum or spectra taken from the sample. The background correction is done by dividing the NEXAFS spectrum of the sample by the NEXAFS spectrum of the clean substrate. This has multiple benefits: dividing by the clean spectrum compensates for aberrations in the monochromator and the detector. However, any instabilities in the X-ray source will remain in the spectrum if not compensated for through multiple measurements [17].

Following substrate correction, the baseline of the sample spectrum is then shifted to zero intensity. The spectrum can then be normalised to the size of the spectrum 'step' (see Figure 2.23). This allows relative changes in the intensity of the π^* and σ^* features to be observed.

Identifying orientation of molecules on surfaces
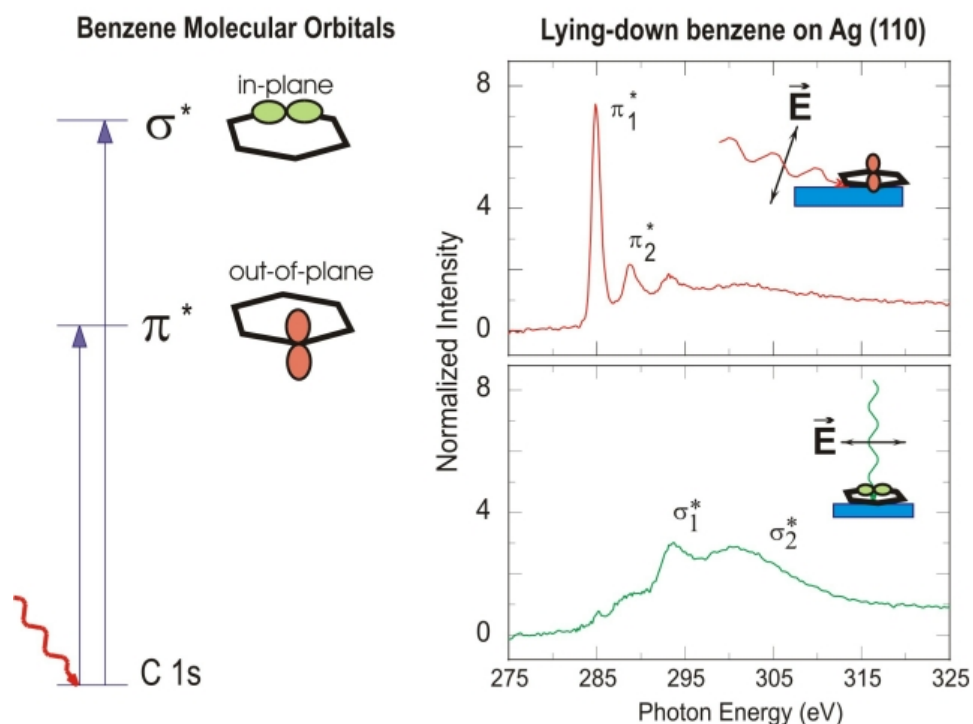
Figure 2.24: Example NEXAFS spectra demonstrating the dependence of the alignment of electric field vector of the incident X-ray beam in determining the direction of the molecular orbital vector relative to the sample surface. On the left shows transitions of an electron from the C 1s core level to either the π^* or σ^* orbital in benzene (ring structure of carbon and hydrogen). On the right shows the resultant C K-edge NEXAFS spectra. The top spectrum is with the electric field vector aligned 'out-of-plane' of the benzene ring, and thus displaying π^* features. The bottom spectrum is with the electric field vector aligned 'in-plane' of the benzene ring, displaying σ^* features [20].

X-rays are EM radiation, and are, therefore, made up of an electric field and a magnetic field, which are perpendicular to one another, and are perpendicular to the direction of travel. The electric field of the incident X-ray will interact with the π* and σ* orbitals of the adsorbed molecule on the surface of the substrate. The electric field vector will be more closely aligned to either the σ* or π* orbital (see Figure 2.24), and, therefore, NEXAFS spectra must be recorded at various angles (ideally one with the incident X-rays 90° to the substrate surface, and one at a more grazing incidence angle). Measurements recorded at different angles will result in concomitant intensity changes in the features associated with the σ* and π* orbitals, as the electric field interacts more strongly with one orbital more than another.

2.7 Scanning electron microscopy (SEM) and energy-dispersive X-ray (EDX) spectroscopy

2.7.1 Introduction

Scanning electron microscopes use electrons to map out the morphology of sample surfaces. Because they use electrons to image samples, they require vacuum conditions to operate. The advantage of an electron microscope is a small wavelength allowing for nanoscale (of the order of nanometres (nm), or 10^{-9} m) resolution, allowing supported nanostructures (i.e. nanostructures immobilised on a substrate) to be imaged with ease. Energy-dispersive X-ray spectroscopy often accompanies SEM analysis. This involves analysing X-rays of characteristic energies emitted by the samples studied, which gives an insight into the chemical composition of the sample.

2.7.2 Theory

In SEM, electrons are emitted from a filament and accelerated via an electric field toward an anode. The wavelength, λ (in m), of the electron is given by the de Broglie equation:

$$\lambda = \frac{h}{mv} \qquad (2.07)$$

Where h is Planck's constant (6.62×10^{-34} kgm^{2}s^{-1}), m is the mass of the electron (9.11×10^{-31} kg), and v is the velocity of the electron. The velocity can be

determined by the acceleration voltage (V), and the electron charge (q, and is - 1.6×10^{-19} C):

$$v^2 = \frac{2qV}{m}$$

(2.08)

Equation (2.08) can be rearranged and inserted into the de Broglie equation, which gives:

$$\lambda = \frac{h}{\sqrt{2qVm}}$$

(2.09)

Electrons in the range of 10-30 keV are typically used, which corresponds to wavelengths in the range of 0.01 Å to 0.1 Å.
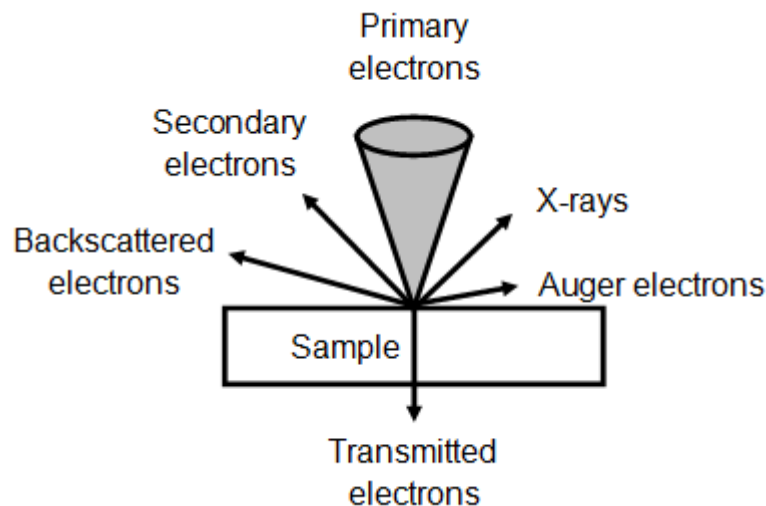
Figure 2.25: Diagram showing the resultant particles from the interaction between the primary electrons and a sample in SEM/EDX.

A narrow beam of electrons is created by focusing the electrons using electrostatic or magnetic lenses. The beam then traverses a given area of a sample. Electrons in the electron beam (also known as primary electrons) produce secondary electrons or backscattered electrons in the sample (see Figure 2.25). Secondary electrons are produced as a result of the primary electrons colliding inelastically with electrons in the atoms of the sample. The energy transferred from the primary to the secondary electrons needs to be greater than that of the work function of the sample in order for emission to occur. Backscattered electrons are produced by elastic collisions between the primary electrons and the nuclei of the sample atoms. Backscattered electrons are emitted from the surface with the same energy as the primary electrons,

and are emitted at a variety of angles [21]. Depending on the desired image, either the secondary or backscattered electrons are collected by a detector.

EDX analysis, on the other hand, detects X-rays generated via de-excitation of core electrons. Primary electrons transfer energy to core electrons, causing excitation. The core electron loses energy via de-excitation, which can result in the emission of a photon in the X-ray energy range. This is fluorescence, similar to that described in Section 2.5.2, but with electrons causing excitation rather than X-ray photons. The energy of the emitted X-ray is element-specific, and is detected as a pulse in a multichannel analyser. The information then forms a spectrum.

2.7.3 Experimental setup for SEM/EDX

A scanning electron microscope is a single vertical column system, with EDX and electron detector attachments (see Figure 2.26). Inside the column is an electron gun, several sets of electrostatic lenses, and scanning coils. The electrons are produced in the electron gun by applying a high voltage across a specially coated tungsten filament. Electrons emitted by the filament are focussed by the lenses, generating a beam of electrons (primary electrons), with a diameter between tens and hundreds of nanometres. The primary electrons pass through a series of scanning coils that direct the beam with nanoscale precision using electrically induced magnetic fields. The electrons exit the column and enter the sample chamber, where they impinge on the sample surface. Secondary/ backscattered electrons are collected separately to X-rays.
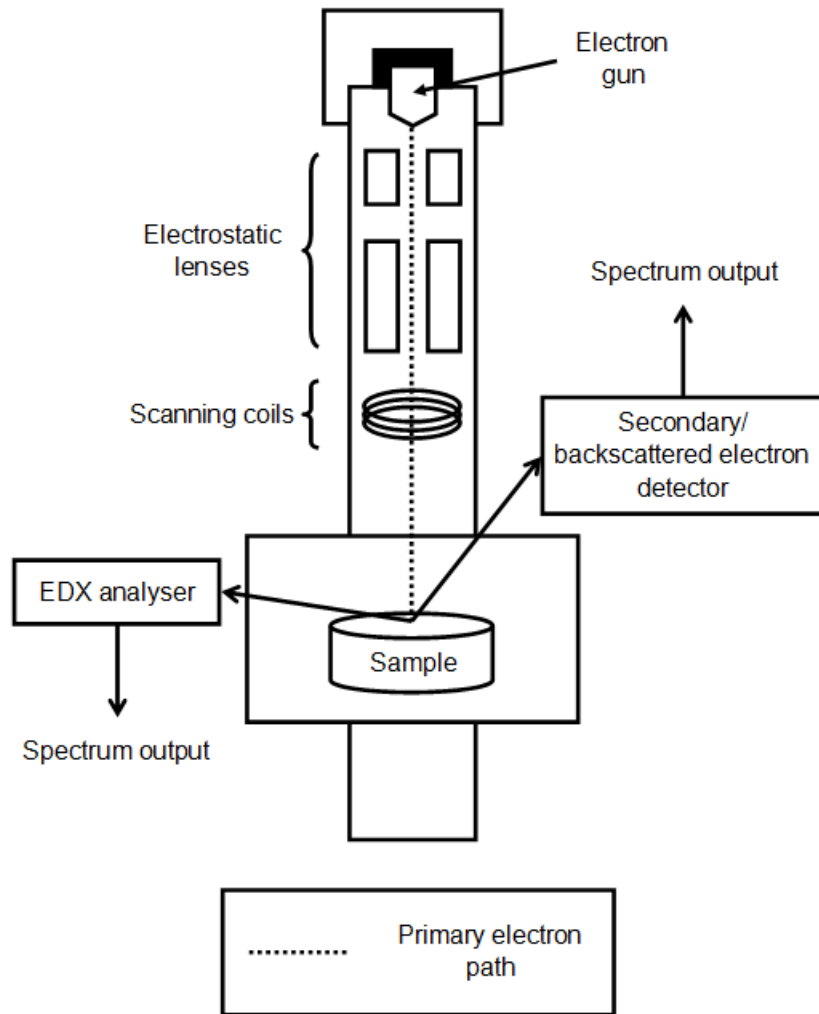
Figure 2.26: Schematic diagram of a typical scanning electron microscope. The dotted line represents the path of the primary electrons.

Secondary/backscattered electrons are collected by the detector in slightly different ways. Secondary electrons are typically weaker than backscattered electrons, and in order to produce an image using information gathered from secondary electrons, they must be separated from others by applying a small negative bias to the transducer housing.
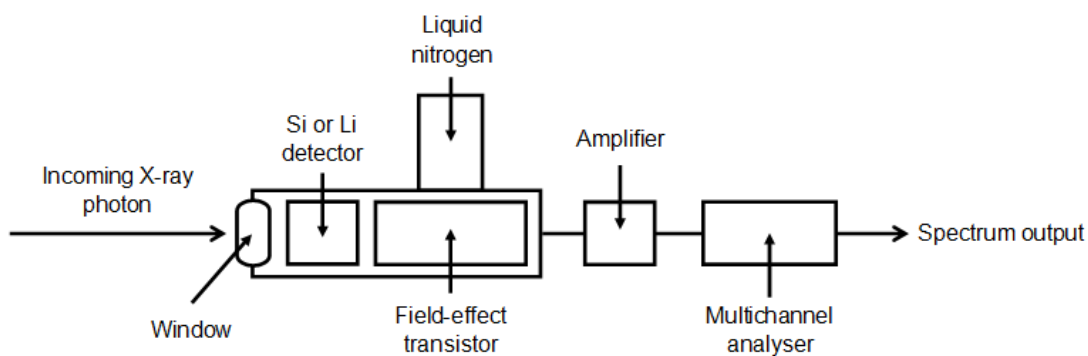
Figure 2.27: Schematic diagram illustrating the components inside an EDX analyser.

X-ray photons that are emitted from the sample are collected by the EDX detector (a schematic diagram of which is shown in Figure 2.27). The incoming X-ray photons enter first through a window. While contemporary EDX instruments are windowless or have ultrathin windows, some older instruments are equipped with beryllium windows, which can impede the low energy X-rays and stop them from reaching the analyser. This can limit in-depth quantitative analysis of organic materials, including ionic liquids. Once the X-ray enters, it hits the detector, which houses a silicon/lithium wafer. Inside the Si or Li wafer, the X-ray photon is absorbed, and transfers enough energy to promote several thousand electrons into the conduction band. These electrons are detected as a pulse, with a current proportional to the energy of the incident X-ray photon. The pulse is converted to a voltage and amplified by a field effect transistor that is cooled with liquid nitrogen, and an amplifier. The signals produced by the field effect transistor are sorted according to energy and stored in a corresponding channel in a multichannel analyser. A spectrum of counts as a function of energy is then outputted.

2.8 Low energy electron diffraction (LEED)

2.8.1 Introduction

Low-energy electron diffraction (LEED), as the name suggests, uses low-energy electrons (typically in the range of tens of eV) to study the surface structure of a sample, in particular the crystallographic structure. It is a useful tool in determining the cleanliness of single-crystal substrates.

2.8.2 Theory and experimental setup for LEED

An electron beam of variable energy is generated by an electron gun, with energy between 20 eV and 200 eV. The incident electrons hit the sample and are backscattered onto a grid (see Figure 2.28).
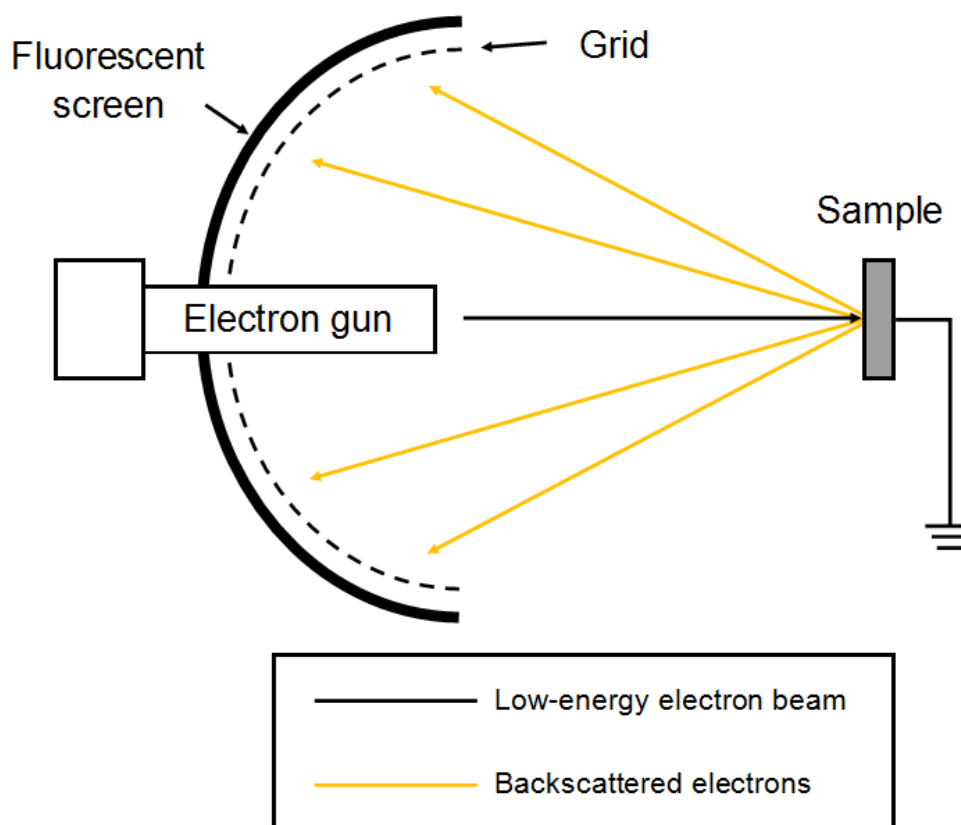
Figure 2.28: Example setup for LEED. The low energy electrons incident on the sample are backscattered. Elastically backscattered electrons make it through the grid, while inelastically scattered electrons do not. The electrons that make it through the grid and hit the fluorescent screen generate a LEED pattern.

The electrons that scatter elastically produce a pattern on a fluorescent screen beyond the grid. As expressed in de Broglie's equation (Equation (*2.07*)), the wavelength of these low energy electrons is comparable to atomic spacing. This is a prerequisite for diffraction to occur from the sample atoms.

The pattern produced by the elastically-scattered electrons illustrates the sample lattice in reciprocal space, which can be used to elucidate the lattice in real space. Since the energy of these electrons is low, LEED is a surface-sensitive technique (see Section 2.3.4 for more about the surface sensitivity of electrons). Samples with few surface defects and long-range order produce LEED patterns with sharp, clear diffraction spots [1, 22]. Samples with a heavily

defective surface will produce LEED patterns with diffuse and blurry diffraction spots [23].

2.9 Synchrotron radiation

2.9.1 Introduction

Synchrotron radiation (SR) is EM radiation emitted from an accelerated charged particle in a circular orbit. At synchrotron facilities, SR is typically produced by electrons accelerated at close to the speed of light in a circular storage ring. SR can produce radiation from the infrared (λ ~10^{-5} m) to the hard X-ray region (λ ~10^{-10} m), and is thus considered a tuneable source of radiation. SR is useful for techniques utilising soft X-rays, since SR is more intense than that produced by typical laboratory sources, particularly in the X-ray region. It is also particularly useful for a technique like NEXAFS where a range of X-ray photon energies is necessary to carry out the measurements. It is also beneficial for XPS since a desired surface sensitivity can be achieved by tuning the energy of the incident X-ray photons, which affects the kinetic energy and IMFP of the photoelectrons, and therefore the depth from which they can originate and successfully escape the sample.

2.9.2 Production of synchrotron radiation

Electrons are accelerated in a circular orbit in the storage ring, directed by dipole magnets, in order to produce SR. The acceleration of the electrons in a circular orbit under the influence of a magnetic field can be expressed using the Lorentz equation:

$$\frac{d\bar{p}}{dt} = e\left(\bar{E} + \frac{\bar{v} \times \bar{B}}{c}\right) \tag{2.10}$$

Where $\bar{p}$, e, and $\bar{v}$ are the momentum, charge and velocity of the electrons, c is the speed of light, and $\bar{B}$ and $\bar{E}$ are the magnetic and electric fields respectively. The power radiated (P) by the electrons moving with a radius of curvature R, at relativistic velocities is proportional to E^4, $1/R^2$ and $1/m_e^4$, where E is the energy of the electrons and m_e is the electron rest mass (which is 0.511 MeV). This therefore means that, to produce higher energy electrons, the radius of the storage ring must decrease. This, in turn, means more SR emitted by the

electrons. In order to keep the electrons at a constant energy, their energy can be replenished using radio frequency (RF) cavities. Inside the RF cavity is a longitudinal electric field that accelerates the electrons [8].

The main features of a SR facility are outlined below, starting with how the electrons are generated, followed by the SR generation process using a linear accelerator (linac), a booster ring, and a storage ring. Also described are beamlines and end stations, which utilise the SR emitted by the electrons in the storage ring.
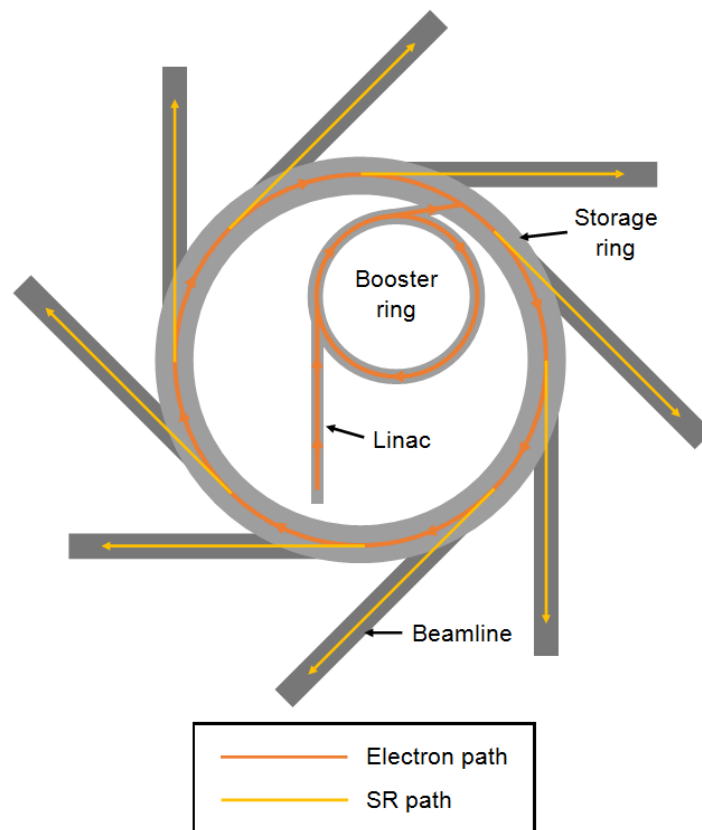
Figure 2.29: Schematic diagram of a typical synchrotron radiation (SR) facility. The orange lines inside the linac, booster ring, and storage ring represent the path of the accelerated electrons. The yellow lines inside the beamlines represent the path of the SR emitted by the accelerated electrons inside the storage ring.

Electron generation and linear accelerator

A schematic diagram of a synchrotron facility is shown in Figure 2.29. Before electrons enter any kind of circular orbit, they first need to be produced by heating a filament. These electrons are then accelerated along a linear accelerator (linac) to approximately 100 MeV where they are then injected into a booster ring.

Booster ring

Electrons in the booster ring are brought up to an energy where they can be periodically injected into the storage ring. Modern SR facilities 'top up' the electrons in the storage ring by frequent injections of a small number of electrons from the booster ring. This simultaneously maintains a steady current in the storage ring, which means continuous user operation without the need for suspending experiments, or risking damage to X-ray optical components from SR intensity changes [16].

Storage ring

Once electrons are injected into the storage ring, they are accelerated for a number of hours under high vacuum. The storage ring directs the electrons in a circular orbit with a network of magnets. Dipole magnets direct and bend the beam to generate the circular trajectory (they are also known as bending magnets). Quadrupole magnets are used to compensate for Coloumb repulsion and focus the beam of electrons. Sextupole magnets correct any aberrations caused by the quadrupole focusing of the electrons [16]. The energy of the electrons in the storage ring is of the order of GeV. The storage ring also contains insertion devices (see Section 2.9.3) which produce more intense SR than the bending magnets.

Beamlines and end stations

The electrons lose energy in the form of SR tangentially to the direction of orbit. SR is harnessed on beamlines that are tactically positioned, tangentially to the storage ring. On a typical beamline, the SR traverses through a series of optics (with specifications relevant to the experiments conducted on the beamline) and a monochromator, filtering the desired SR toward the end station. At the end station, specialist equipment that utilises the desired SR is set up, where users conduct experiments. The 'front end' of the beamline (i.e. the part attached to the storage ring) is heavily shielded with lead-lined concrete walls to protect from high-energy photons (such as γ photons) or high-energy neutrons produced by any collisions between the electrons in the storage ring and gas molecules.

2.9.3 Insertion devices

Insertion devices (IDs) are composed of periodic magnetic arrays and are designed to increase the intensity and brightness of the SR. When an electron passes through the alternating magnetic field, it emits radiation with every transverse oscillation.

There are two main types of IDs: wigglers and undulators. These are both outlined below.
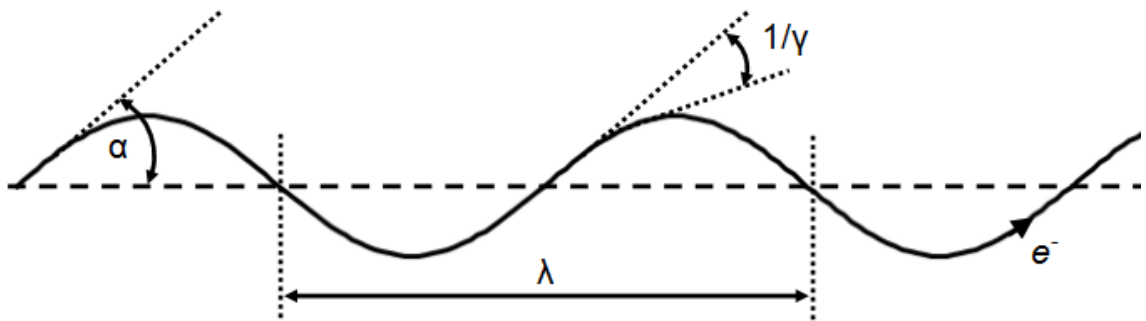
Figure 2.30: Electron path inside an insertion device. The parameters α and 1/γ (and thus λ according to Equation (*2.11*)) vary depending on whether the insertion device is a wiggler or an undulator.

Wigglers are composed of a periodic series of magnets, which generate an alternating magnetic field in the vertical direction (see Figure 2.30). This then causes sinusoidal motion of electrons in the horizontal plane (but perpendicular to their direction of motion), and the electron then follows a "wiggling" path. The magnets in a wiggler are stronger than the dipole magnets used in the storage ring, which increases the spectral range of the SR toward higher energies.

The differences between a wiggler and an undulator are usually expressed in terms of a dimensionless parameter, *K*, which is simply defined as the ratio of the wiggling angle, α, and the natural photon emission angle of the SR, 1/γ:

$$K = \alpha\gamma \qquad\qquad (2.11)$$

In a wiggler, this parameter $K \gg 1$. This means that the amplitudes of the transverse oscillations of the electrons are large (and thus α is large), and in this case, the interference effects from each pole can be considered negligible. Thus, the intensity of the SR emitted due to the wiggler is simply the summation of the individual SR contributions at each pole.

Undulators are similar to wigglers, but α is closer to the photon natural emission angle 1/γ, and therefore $K < 1$. The amplitudes of the transverse oscillations of the electrons are smaller, and interference effects cannot be ignored, and is evidenced in the flux of the beamline. The resultant SR has a much higher photon flux than SR emitted from wigglers and bending magnets [8, 16].

2.10 Instrumentation and synchrotron facilities

The following subsections outline and describe instrumentation used throughout this thesis. Chapters 3 and 4 feature NAPXPS data that was taken using the NAPXPS system at the Photon Science Institute of the University of Manchester. Chapter 5 uses XPS and NEXAFS data collected at the ANTARES beamline at SOLEIL synchrotron facility in France, and at the AU-Matline beamline at ASTRID in Denmark. Chapter 6 features XPS data taken on a standard Kratos XPS system at the University of Manchester.

2.10.1 NAPXPS at the University of Manchester

The near-ambient pressure X-ray photoelectron spectroscope is located at the Photon Science Institute at the University of Manchester. It is a custom-built SPECS system, and comprises of a monochromated Al K_α X-ray source (of photon energy 1486.6 eV) and PHOIBOS 150 NAP hemispherical analyser. The system is equipped with a load lock chamber, preparation chamber, analysis chamber, and NAP cell.
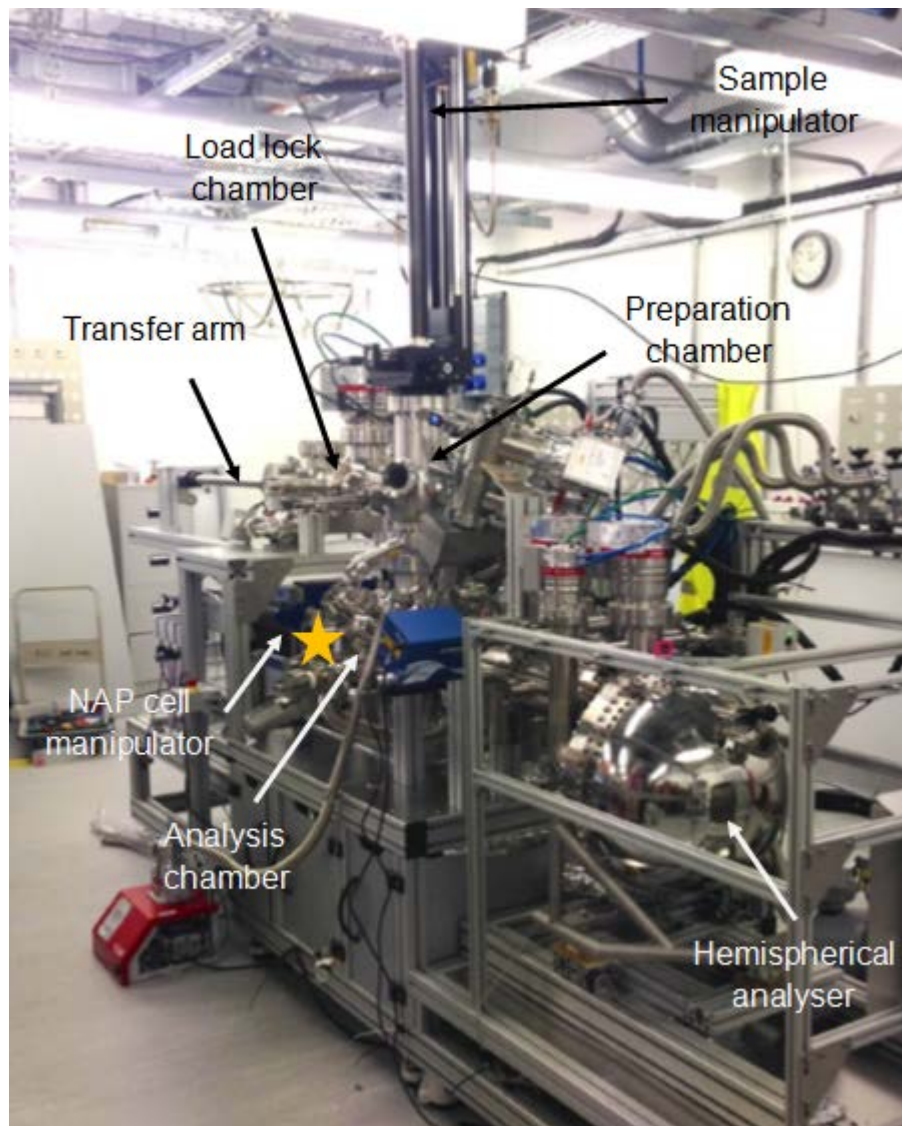
Figure 2.31: Photograph of the SPECS NAPXPS kit at the University of Manchester. The yellow star (between the arrows that point to the NAP cell manipulator and the analysis chamber) shows where the wobble stick is attached to the analysis chamber.

The load lock chamber is equipped with a transfer arm for sample transfers from the load lock chamber to the preparation chamber. Inside the preparation chamber is a sample manipulator to transfer samples between the preparation chamber and the analysis chamber. Attached onto the preparation chamber is a modified Knudsen cell (see Figure 2.32) for deposition of ionic liquid. The sample manipulator is equipped with a k-type thermocouple attached to the sample holder, and spans a sample temperature range of -150°C to 800°C.
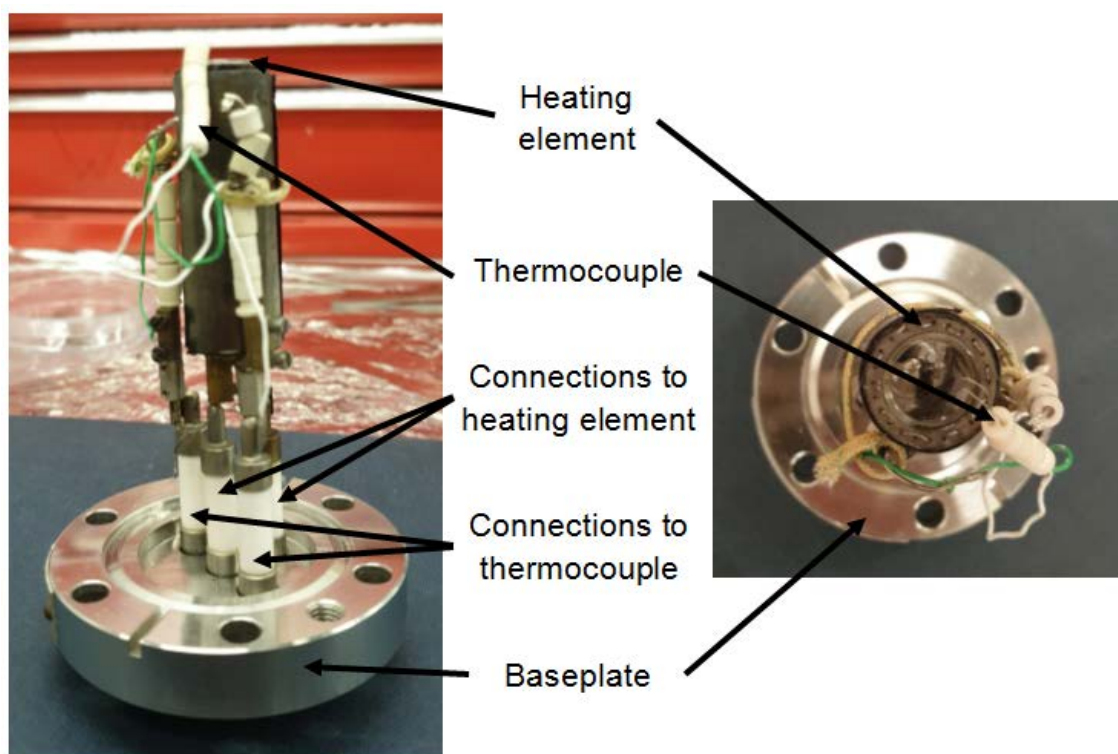
Figure 2.32: Side view (left) and top-down view (right) of the modified Knudsen cell. Prior to being bolted onto the vacuum chamber, a small amount (typically <1 ml) of IL is placed into a small quartz vial (not shown) which fits down the central column. The vial is inserted at an angle to prevent leaking. The heating element consists of tantalum wire weaved through the column wall. The thermocouple, fixed to the column wall by silver epoxy, measures the temperature of the column wall.

The analysis chamber is equipped to perform a variety of measurements on a sample including regular (UHV) XPS, ultraviolet photoelectron spectroscopy (UPS), mass spectrometry and low energy electron diffraction. The NAP cell is brought into the analysis chamber using the sample manipulator (see Figure 2.33) and 'docks' with the PHOIBOS 150 NAP analyser. The wobble stick (indicated by a star in Figure 2.31) is used to open the cell initially before taking the sample from the manipulator and placing it inside the cell (see Figure 2.34 for a photograph of the NAP cell inside the analysis chamber). Once the sample is securely inside, the NAP cell is then closed up and sealed.
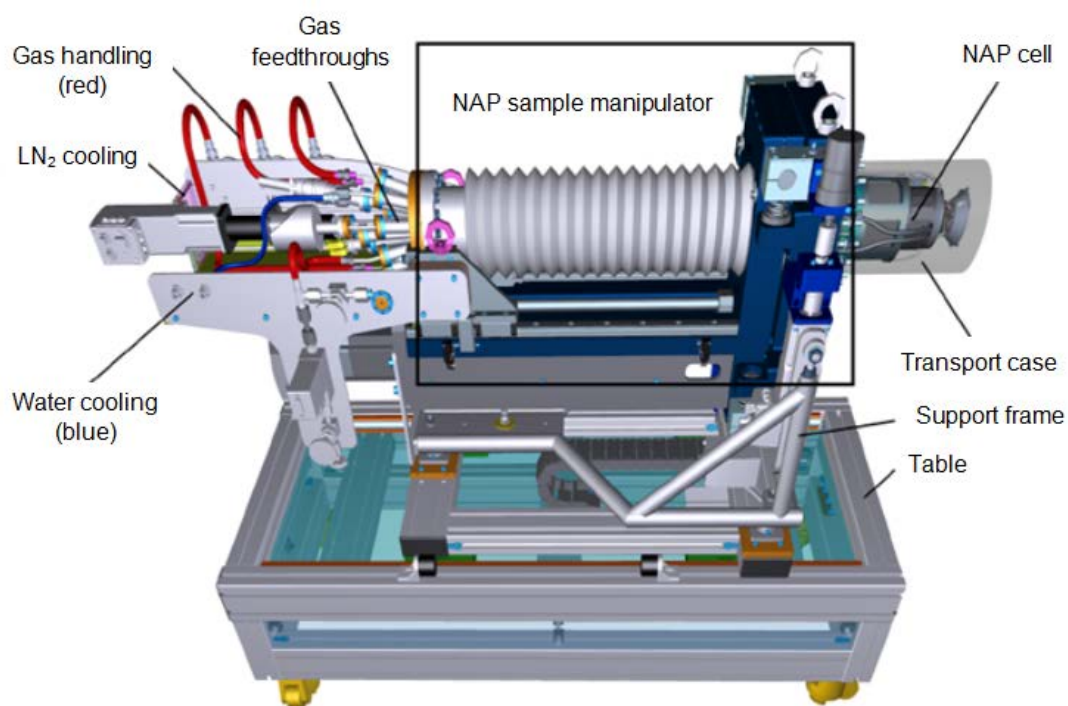
Figure 2.33: Model of the NAP cell, with components annotated. Rather than being housed in a transport case, the NAP cell resides inside the analysis chamber.

The PHOIBOS 150 NAP analyser has a mean radius of 150 mm, a nozzle with a half-angle of 35° and post-lens apertures of radius 0.4 mm. The lenses, analyser and detector are coated in μ-metal to screen external magnetic fields.
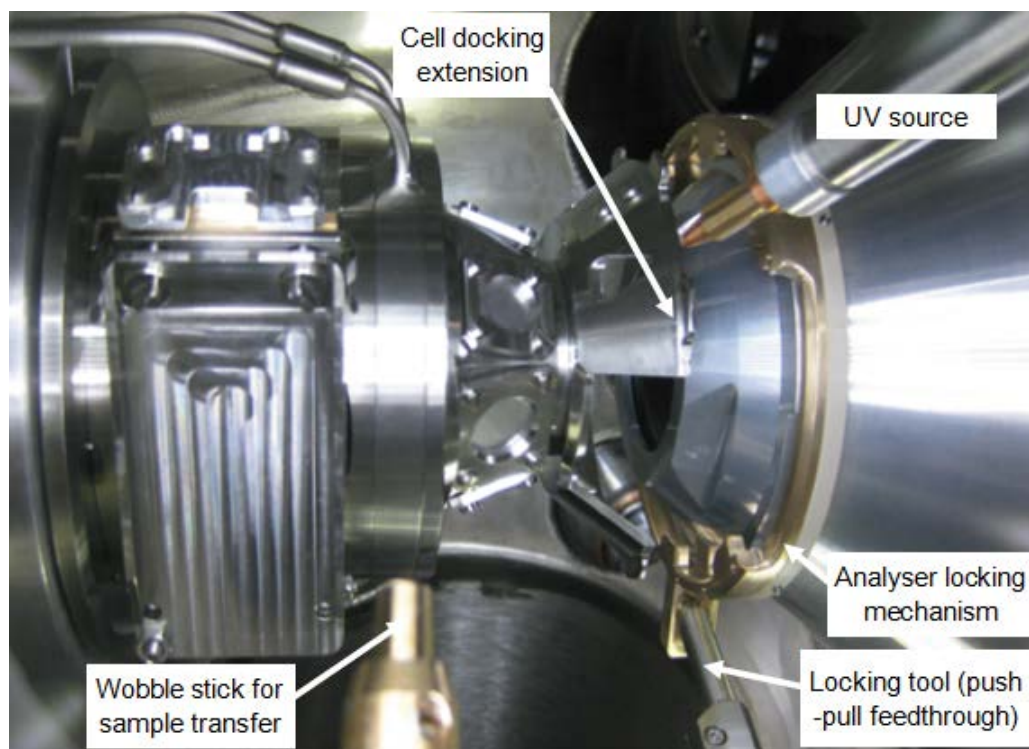
Figure 2.34: Photograph showing the NAP cell extended out into the analysis chamber and docked to the PHOIBOS 150 NAP analyser.

The NAPXPS system can achieve up to 25 mbar in pressure, and available gases include H_2O, O_2, CO, CO_2, and NH_3.

2.10.2   XPS at the University of Manchester

The X-ray photoelectron spectroscopy kit operated under solely ultra-high vacuum conditions is located at the Photon Science Institute of the University of Manchester. It is a standard Kratos system, comprising of an Al k_α X-ray source ($h\nu$ = 1486.6 eV) and a hemispherical analyser.

2.10.3   ANTARES beamline (SOLEIL)

The ANTARES beamline (A New Tailored Angle REsolved Spectroscopy beamline) is located at the SOLEIL synchrotron facility in France. The storage ring of SOLEIL has a circumference of 354.1 m, a maximum stored current of 430 mA, and electron energy of 2.75 GeV. The ANTARES beamline is an undulator beamline and provides photons in the energy range of 10 eV to 1000 eV with energy resolution $\Delta E/E$ >1×10^5 and a photon flux of 1.2×10^{15} s^{-1}.
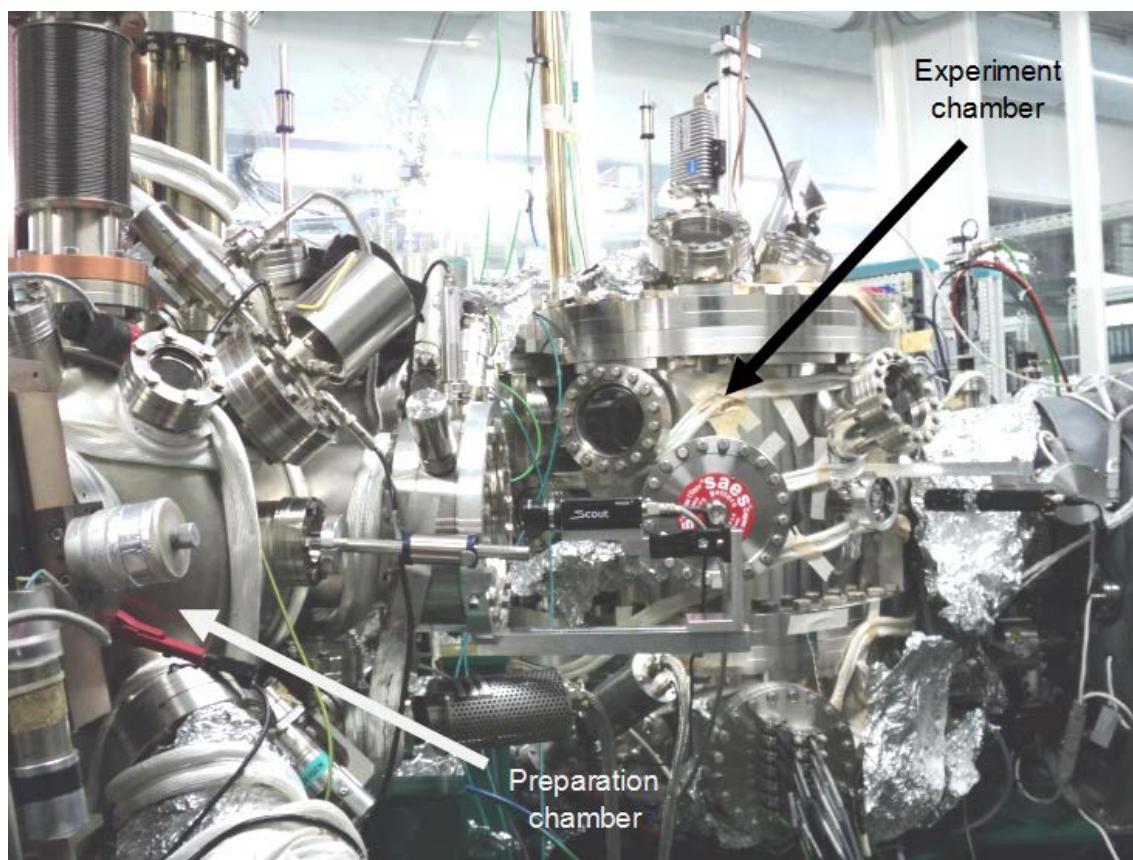
Figure 2.35: Annotated photograph of the ANTARES beamline at the SOLEIL synchrotron facility in France.

The end station on the ANTARES beamline (Figure 2.35) is equipped with a SM-PGM monochromator and a Scienta R4000 hemispherical analyser. Various techniques can be carried out on the ANTARES beamline, including angle-resolved XPS, X-ray absorption spectroscopy, low-energy electron diffraction, photoelectron diffraction and resonant photoemission.

2.10.4 AU-MATline beamline (ASTRID2)

AU-MATline (Aarhus University MATerial science beamLINE) is located at the 3rd generation synchrotron ASTRID2, part of ISA, in Denmark. ASTRID2 has a circumference of 45.7 m, a current of 200 mA, and an electron energy of 580 MeV. AU-MATline is a wiggler beamline able to provide a photon energy range of 20 eV to 700 eV, and a typical photon flux of 1×10^{11} s^{-1}.
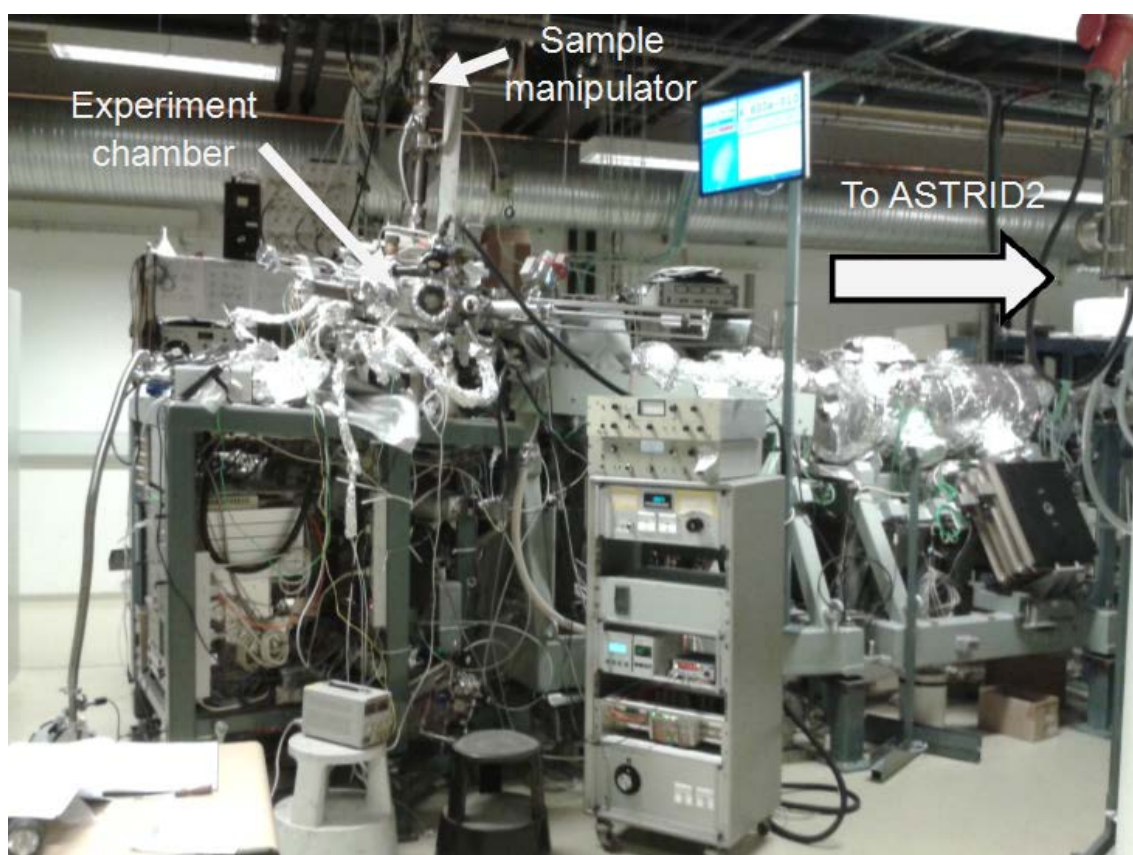
Figure 2.36: Photograph of the endstation at the AU-MATline beamline of ASTRID2 (ISA) in Denmark. The arrow on the rightmost side shows the direction of the storage ring (out of the frame, beyond concrete walls).

The end station (featured in Figure 2.36) is equipped with a SX-700 monochromator and a Scienta hemispherical analyser. Techniques that can be carried out on this beamline include X-ray photoelectron spectroscopy, low-

energy electron diffraction, ultraviolet photoelectron spectroscopy, near-edge X-ray absorption fine structure spectroscopy, and photoelectron diffraction.

2.11 Experimental considerations in ionic liquid surface science

Experiment-based investigations into the structure and interactions of ILs at surfaces and interfaces require a number of factors to be taken into consideration.

2.11.1 Handling ionic liquids and sample preparation

Most imidazolium-based ILs are skin irritants and serious eye irritants, requiring the use of basic personal protective equipment (which comprises of a laboratory coat, nitrile gloves and safety goggles) during handling. Due to their low vapour pressures at room temperatures there is minimal risk of inhalation of IL vapours; however, ingestion of any kind is acutely toxic. They are also toxic to aquatic life with long-lasting effects.

Because ILs have low vapour pressures, they are capable of being deposited on a substrate and degassed under vacuum. However, physical vapour deposition (PVD) of ILs onto substrates in vacuo is becoming more popular. This involves heating the IL to its evaporation temperature and exposing the vapour to the desired substrate. This method is desirable, since the IL can be easily treated prior to deposition to remove contaminant species and impurities (such as water). This involves heating the IL to a temperature below their vaporisation temperature (which for some imidazolium-based ILs is approximately 120°C to 180°C) for several hours prior to deposition.

2.11.2 Contamination

Contamination is always a consideration in surface science. Just as contamination can influence the surface chemistry of solid samples (such as blocking active sites on catalysts), the same principle can apply to ILs. As mentioned previously, hygroscopic ILs (such as 1-butyl-3-methylimidazolium tetrafluoroborate) tend to absorb some water from the surrounding air [24, 25]. Contamination can also originate from the preparation and synthesis of ILs, such as silicon grease contamination from glassware sealant [26]. As

mentioned in the previous section, most contaminants can be removed from ILs via heating before vapour deposition.

2.11.3 Damage from prolonged exposure to X-rays

XPS is sensitive to the chemical environments in samples, which includes contaminant species, and species that manifest as a result of damage from prolonged exposure to the X-ray beam. In studies using thin films of imidazolium-based ILs [27, 28], peaks appeared in the N 1s region at a lower binding energy than the imidazolium nitrogen peak. It can be seen in Chapter 3.4.1 of this thesis that the features associated with beam damage species become more intense with longer exposure time, and it is known that thin and ultrathin IL depositions are particularly susceptible to X-ray beam damage. This can be somewhat mitigated by taking rastered scans (see Chapter 3.4.3 for more information).

Chapter 2 References

[1] K.W. Kolasinski, *Surface Science: Foundations of Catalysis and Nanoscience*, John Wiley & Sons, (2012).

[2] M. Ohring, *Materials Science of Thin Films*, 2nd ed., Academic Press, (2002).

[3] N. Yoshimura, *Vacuum Technology*, Springer Science & Business Media, (2008).

[4] K. Jousten, C.B. Nakhosteen, *Handbook of Vacuum Technology*, John Wiley & Sons, (2016).

[5] D.J. Hucknall, A. Morris, *Vacuum Technology: Calculations in Chemistry*, Royal Society of Chemistry, (2003).

[6] H. Ibach, *Physics of Surfaces and Interfaces*, Springer Science & Business Media, (2006).

[7] D.M. Hoffman, B. Singh, J.H. Thomas III, *Handbook of Vacuum Science and Technology*, Elsevier Science & Technology, (1997).

[8] S. Mobilio, F. Boscherini, C. Meneghini, *Synchrotron Radiation: Basics, Methods and Applications*, Springer Science & Business Media, (2015).

[9] P. van der Heide, *X-Ray Photoelectron Spectroscopy: An Introduction to Principles and Practices*, John Wiley & Sons, (2011).

[10] Y.B. Band, Y. Avishai, *Quantum Mechanics with Applications to Nanotechnology and Information Science*, Elsevier Science & Technology, (2012).

[11] J.M. Hollas, *Modern Spectroscopy*, 4th ed., John Wiley & Sons, (2004).

[12] N. Fairley, *CasaXPS Manual 2.3.15 Introduction to XPS and AES*, Casa Software, (2009).

[13] F. Peng, L. Cai, H. Yu, H. Wang, J. Yang, *Synthesis and Characterization of Substitutional and Interstitial Nitrogen-Doped Titanium Dioxides with Visible Light Photocatalytic Activity*, Journal of Solid State Chemistry, 181 (2008) 130-136, D.O.I.: 10.1016/j.jssc.2007.11.012

[14] M.P. Seah, W. Dench, *Quantitative Electron Spectroscopy of Surfaces: A Standard Data Base for Electron Inelastic Mean Free Paths in Solids*, Surface and Interface Analysis, 1 (1979) 2-11, D.O.I.: 10.1002/sia.740010103

[15] M. Salmeron, R. Schlogl, *Ambient Pressure Photoelectron Spectroscopy: A New Tool for Surface Science and Nanotechnology*, Surface Science Reports, 63 (2008) 169-199, D.O.I.: 10.1016/j.surfrep.2008.01.001

[16] P. Willmott, *An Introduction to Synchrotron Radiation: Techniques and Applications*, John Wiley & Sons, (2011).

[17] J. Stöhr, *NEXAFS Spectroscopy*, Springer Science & Business Media, (2013).

[18] K.W. Kolasinski, *Physical Chemistry: How Chemistry Works*, John Wiley & Sons, (2016).

[19] R.G. Mortimer, *Physical Chemistry*, Elsevier Science & Technology, (2000).

[20] J. Stöhr, NEXAFS Spectroscopy, https://www.ssrl.slac.stanford.edu/stohr/nexafs.htm, Accessed [27/02/2019].

[21] E.A. Clark, I. Fritsch, S. Nasrazadani, C.S. Henry, *Analytical Techniques for Materials Characterization*, 2nd ed., John Wiley & Sons, (2006).

[22] C. Hammond, *The Basics of Crystallography and Diffraction*, Oxford University Press, (2009).

[23] O. Dulub, L.A. Boatner, U. Diebold, *STM Study of the Geometric and Electronic Structure of ZnO (0001)-Zn,(0001)-O,(1010), and (1120) Surfaces*, Surface Science, 519 (2002) 201-217, D.O.I.: 10.1016/S0039-6028(02)02211-2

[24] J.G. Huddleston, A.E. Visser, W.M. Reichert, H.D. Willauer, G.A. Broker, R.D. Rogers, *Characterization and Comparison of Hydrophilic and Hydrophobic Room Temperature Ionic Liquids Incorporating the Imidazolium Cation*, Green Chemistry, 3 (2001) 156-164, D.O.I.: 10.1039/B103275P

[25] V.-H. Tran, R. Khan, I.-H. Lee, S.-H. Lee, *Low-Temperature Solution-Processed Ionic Liquid Modified SnO2 as an Excellent Electron Transport Layer for Inverted Organic Solar Cells*, Solar Energy Materials and Solar Cells, 179 (2018) 260-269, D.O.I.: 10.1016/j.solmat.2017.12.013

[26] K.R.J. Lovelock, E.F. Smith, A. Deyko, I.J. Villar-Garcia, P. Licence, R.G. Jones, *Water Adsorption on a Liquid Surface*, Chemical Communications, (2007) 4866-4868, D.O.I.: 10.1039/B711680B

[27] T. Cremer, M. Stark, A. Deyko, H.-P. Steinrück, F. Maier, *Liquid/Solid Interface of Ultrathin Ionic Liquid Films:[C1C1Im][Tf2N] and [C8C1Im][Tf2N] on Au (111)*, Langmuir, 27 (2011) 3662-3671, D.O.I.: 10.1021/la105007c

[28] M. Wagstaffe, M.J. Jackman, K.L. Syres, A. Generalov, A.G. Thomas, *Ionic Liquid Ordering at an Oxide Surface*, Chemphyschem, 17 (2016) 3430-3434, D.O.I.: 10.1002/cphc.201600774

3 Water-Induced Reordering in Ultrathin Ionic Liquid Films

Studying the interface between ionic liquids (ILs) and gases is important for a variety of capture, separation and catalysis applications involving gaseous materials. The bulk and interfacial structure of ILs are both determined by their composite ions, and thus their structure at the IL free interface (i.e. IL/gas, IL/vacuum). Since the sorption behaviour of ILs is dependent on this ordering, it is imperative to understand how the adsorption of gas molecules influences the outer surface of the IL.

Any IL application that could be potentially used in ambient conditions will, of course, be exposed to water vapour. The mechanics of water adsorption on ILs are still largely a mystery. There have been a number of studies that have tried to answer some of the questions that remain about the IL/water interface, and with a variety of techniques of varying surface sensitivities.

Presented in this chapter is a study of the IL/water interface using an ultrathin IL film and a surface sensitive technique that can be operated under ambient pressure. This has the dual benefit of realistic pressure and temperature conditions and surface sensitivity that is vital for observing phenomena at surfaces and interfaces.

3.1 Introduction

The natural ionic state and characteristic non-volatility of ILs make them promising alternative solvents for homogeneous catalysis [1, 2]. In fact, ILs are an integral part of two catalysis concepts: Supported Ionic Liquid Phase (SILP) and Solid Catalyst with Ionic Liquid Layer (SCILL) [3, 4]. As described in Chapter 1.4.3, SILP catalysis consists of a thin layer of IL containing the catalyst

is spread over an inert support material that is high-area and porous [5]. SCILL is similar, but the catalyst is either a solid material, or is immobilised on the support material [6]. The reactions between the catalyst and the gaseous

reactants and products take place near the IL/gas interface, so the thin film provides the necessary environment and minimises wastage of both the IL and the catalyst. SCILL and SILP catalysis are therefore attractive due to their cost-effectiveness.

ILs are more structured than most molecular liquids, and their ordering and structure is governed by the structure of their constituent ions. Interactions (and subsequent structure and ordering) at the IL/substrate interface have been investigated previously using ultrathin IL films. A study by Cremer et al [7] showed that imidazolium-based ILs display a different morphology at sub-monolayer coverages on Ni (111) compared to O-precovered Ni (111) (specifically Ni (111) with an O($\sqrt{3}\times\sqrt{3}$)R30° superstructure). They observed that on O-precovered Ni, the cation and anion were both in direct contact with the substrate, arranged in a checkboard arrangement at the IL/substrate interface. However, on Ni (111) the ILs demonstrated a bilayer-type ordering, with only the cation in direct contact with the substrate and the anion sat on top of the imidazolium ring of the cation. The arrangement of the IL on the Ni surface was quite different to that observed for the same IL on Au (111) at similar coverages, which instead arranged in a checkerboard formation [3]. Cremer et al also observed that the IL tended to couple more strongly to the metallic Ni surface than the O-covered Ni surface.

At the IL/vacuum interface, it has been seen in imidazolium-based ILs that the ions order such that the alkyl chains of the cations face out toward vacuum [8-11], creating a charged under-layer that contains the anions and the imidazolium ring of the cations. It is this ordering that is believed to govern the gas adsorption and uptake by ionic liquids [12, 13] including that of water vapour. One obstacle that has yet to be overcome for the use of ILs in industrial applications is their tendency for water capture and uptake. Water has been shown to affect the physical properties of ILs [14-16], so this hygroscopic behaviour is often problematic. Many of their potential industrial applications will be subject to ambient conditions and thus will be, naturally, subject to water vapour. While the effect of water on the bulk properties of ILs has been studied relatively extensively, there have been few studies into the IL/water interface. There are two key concepts associated with the interface that still have yet to be understood: transport of water molecules on and through the surface, and the

influence of water on IL surface structure. Understanding the mechanics of water adsorption at the IL/water interface is not only vital for a first model of gas capture in ILs, it is also important to understand the implications the addition of water creates for IL thin film applications in ambient conditions.

In order to observe the IL/water interface in a more realistic environment, in situ measurements with high surface sensitivity must be taken. The emergence of near-ambient pressure X-ray photoelectron spectroscopy (NAPXPS) facilities allows the IL/water interface to be studied with the necessary surface sensitivity under more realistic conditions. Discussed in this Chapter are NAPXPS measurements of water with a multilayer deposition and and an ultrathin film of the water-miscible IL, 1-butyl-3-methylimidazolium tetrafluoroborate, or $[C_4C_1Im][BF_4]$.

3.2 Experimental section

Two experiments were conducted to investigate the $[C_4C1Im][BF_4]$/water interface. The first was an IL deposition on anatase TiO_2 (101), where the IL/water interface was investigated using two different relative humidities. The second was an ultrathin IL deposition on rutile TiO_2 (110), where the IL/water interface was investigated under one relative humidity, but with multiple measurements after exposure in order to study the interactions between adsorbed water molecules and the IL surface.
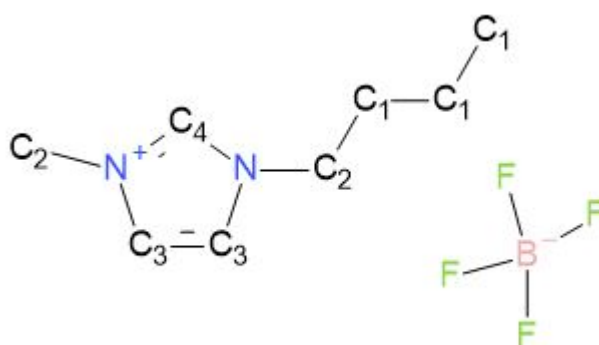
Figure 3.1: Chemical structure diagram of 1-butyl-3-methylimidazolium tetrafluoroborate, or $[C_4C_1Im][BF_4]$. The different carbon environments in the $[C_4C_1Im]^+$ cation are labelled C_1 to C_4.

3.2.1 Water/IL on anatase TiO_2 (101)

The IL, $[C_4C_1Im][BF_4]$ (>97%, Sigma Aldrich), was degassed in a modified Knudsen cell by heating to 393 K for three hours to remove water and other impurities (the chemical structure of the IL is shown in Figure 3.1). The substrate, an anatase TiO_2 (101) single crystal (5 mm × 5 mm, PI-KEM), was mounted onto a Ta sample plate using spot-welded Ta strips. The anatase TiO_2 crystal was cleaned via Ar^+ sputter/anneal cycles until the preliminary ultra-high vacuum (UHV) XPS spectra showed no contamination. To deposit the IL it was heated to 460 K and deposited via vapour deposition on the crystal surface, at room temperature under UHV conditions, for 30 minutes.

Before

Water inlet
opened ↓

20% RH

Water inlet closed;
system pumped
overnight ↓

20% RH

↓ Sample
cooled

60% RH

Water inlet closed;
system pumped
overnight ↓
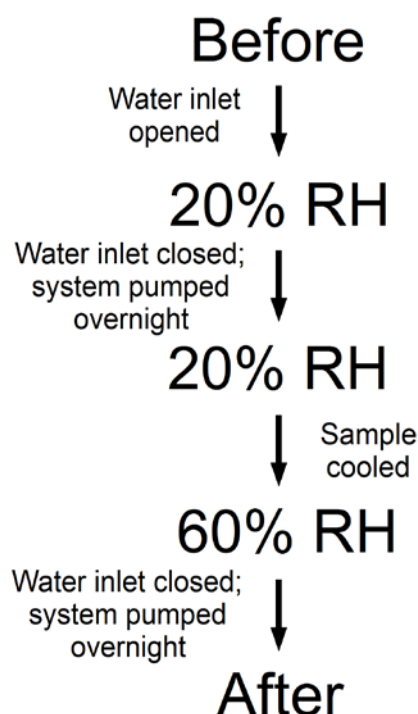
After

Scheme 3.1: Regimes as part of the investigation into water/$[C_4C_1Im][BF_4]$ on anatase TiO_2 (101).

Using the intensity of the O 1s peak before and after deposition, it was calculated that the IL deposition was 109 Å thick, corresponding to approximately 27 layers of IL (assuming the 'thickness' of a single $[C_4C_1Im][BF_4]$ ion pair to be ~4 Å [17] and an electron mean free path of 2.60 nm [18]). The calculation for IL deposition thickness can be found in Appendix A. The room temperature sample was exposed to 6 mbar of water vapour (which corresponds to 20% relative humidity) in the NAP cell (see Chapter 2.10.1) and XPS spectra recorded. The NAP cell was then pumped overnight to

allow the pressure to recover to UHV. The IL multilayers were then exposed to water vapour at 6 mbar again, and spectra recorded once the sample plate had cooled to 280 K (which corresponds to approximately 60% relative humidity). Further XPS measurements were taken once the NAP cell had recovered to UHV. The stages are shown in Scheme 3.1.

The binding energies (BEs) of all core level XPS peaks are calibrated to the C 1s component that corresponds to the alkyl chain of the IL cation at 285.5 eV [19] and quoted to ± 0.1 eV. All spectra have been fitted with a Shirley background and 30:70 (Gaussian:Lorentzian) Voigt line shapes in the absence of sample charging or analyser artefacts. Peak fitting was performed using CasaXPS software.

3.2.2 Water/IL on rutile TiO_2 (110)

The IL, $[C_4C_1Im][BF_4]$ (>97%, Sigma Aldrich), was degassed in a modified Knudsen cell by heating to 393 K for three hours to remove water and other impurities. The substrate, a rutile TiO_2 (110) single crystal (10 mm × 10 mm, 99.9%, PI-KEM), was mounted onto a Ta sample plate using spot-welded Ta strips. The rutile TiO_2 crystal was cleaned via Ar^+ sputter/anneal cycles until the preliminary UHV XPS spectra showed no contamination. The IL was then heated to 460 K for vapour deposition onto the room temperature rutile TiO_2 substrate for approximately 30 minutes under UHV conditions. The ultrathin deposition of IL was then transferred to the NAP cell, and exposed to water vapour at a pressure of 7 mbar and a temperature of 283 K (relative humidity of ~70%).
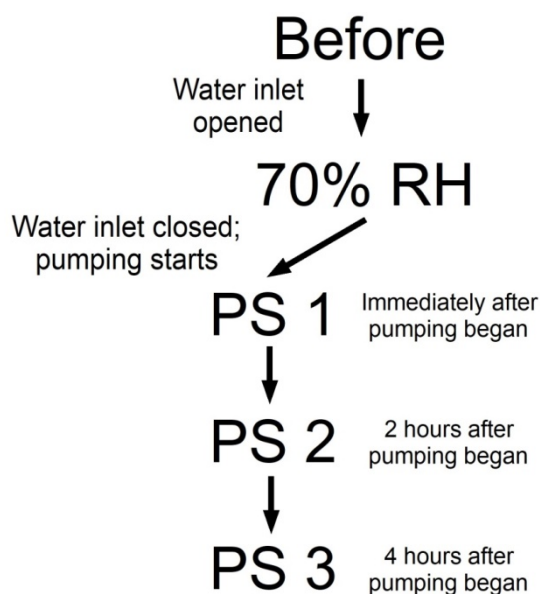
Scheme 3.2: Regimes as part of the investigation into water/[C$_4$C$_1$Im][BF$_4$] on rutile TiO$_2$ (110).

Measurements were taken on a SPECS NAPXPS system (see Chapter 2.10.1) in three regimes: one before water exposure, one during water exposure and one after water exposure (see Scheme 3.2). Three measurements were taken during the regime after water exposure (named Pump Stage 1, 2 and 3; shortened to PS 1, PS 2 and PS 3), while only one was taken in the other regimes. Each measurement took approximately one hour, and each of the measurements after water exposure were separated by one hour. PS 1 was immediately after water vapour was closed off, and the NAP cell was opened to pumping. PS 2 was approximately two hours after pumping began, and PS 3 was approximately four hours after pumping began. These stages are outlined in Scheme 3.2.

Using the intensity of the O 1s peak associated with the lattice O in the TiO$_2$, and using the 'thickness' of a single [C$_4$C$_1$Im][BF$_4$] of ~4 Å [17] and mean free path of 2.60 nm [18], we calculated the thickness of IL to be (10 ± 1) Å, corresponding to three IL layers (the calculation for IL deposition thickness can be found in Appendix A). One of the advantages of using an ultrathin film in this case allowed the IL/water interface to be observed directly without the need for more surface-sensitive grazing emission XP spectra (which is not possible on the NAPXPS system used for these measurements).

All spectra for the study of water/IL on rutile TiO$_2$ (110) are the result of merged raster scans (short scans taken at equally spaced points, specifically 0.6 mm part in a 6×5 grid on the sample, then merged). In each regime, scans of the C 1s, O 1s, N 1s and F 1s regions were recorded, all at normal emission.

The binding energies (BEs) were referenced to the C 1s component that corresponds to the alkyl chain of the IL cation at 285.5 eV [19] and quoted to ± 0.1 eV. All spectra have been fitted with a Shirley background and 30:70 (Gaussian:Lorentzian) Voigt line shapes in the absence of sample charging or analyser artefacts. Peak fitting was performed using CasaXPS software.

3.3 Water/IL on anatase TiO$_2$ (101)

3.3.1 XPS analysis at UHV

Figure 3.2 shows the anatase TiO$_2$ (101) crystal before the IL deposition (Figure 3.2a) and after IL deposition (Figure 3.2b). It can be seen that the IL multilayer deposition is thick enough to attenuate the O 1s and Ti 2p regions significantly. In the O 1s region (Figure 3.2c), there appears to be a shoulder at the higher BE edge, attributed to Ti-OH [20, 21]. The Ti 2p region (Figure 3.2d) is consistent with that of an anatase TiO$_2$ (101) crystal surface with minimal defects [19].
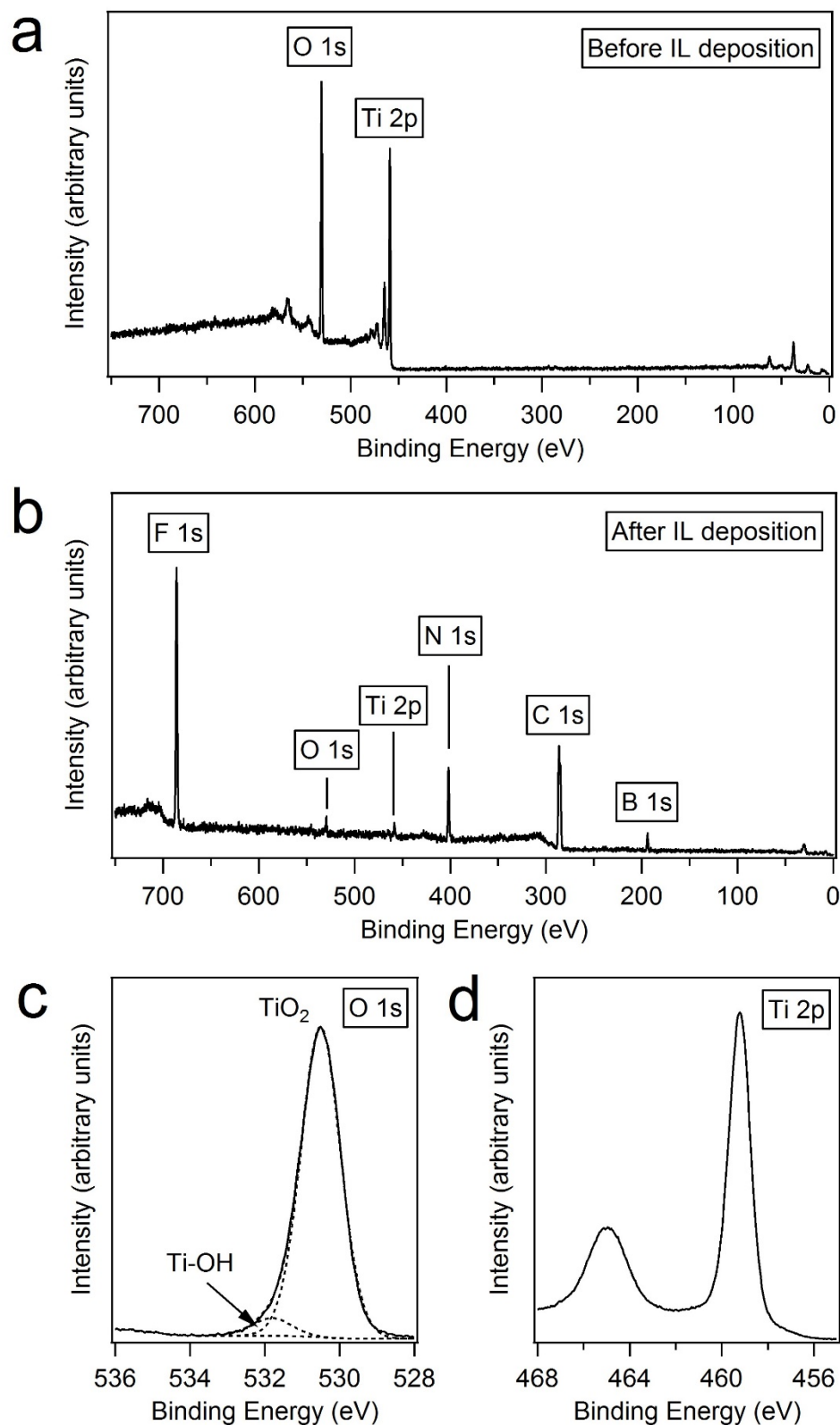
Figure 3.2: Survey spectrum before (a) and after (b) the [C_4C_1Im][BF_4] multilayer deposition on anatase TiO_2 (101). Peaks associated with the substrate (Ti 2p, O 1s) and the IL (C 1s, N 1s, F, 1s, B 1s) are labelled. The O 1s and Ti 2p regions prior to IL deposition are shown in (c) and (d) respectively.

3.3.2 NAPXPS analysis
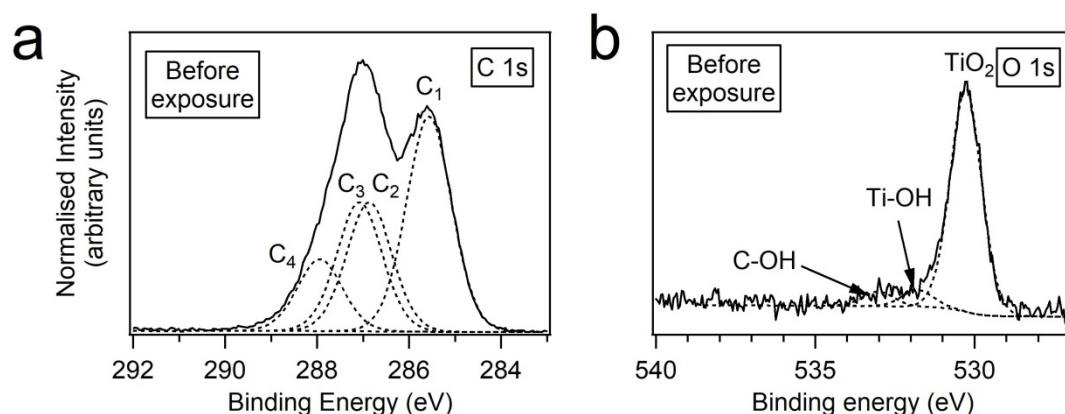
Figure 3.3: C 1s region (a) and O 1s region (b) taken of the IL multilayer deposition on anatase TiO_2 before exposure to water. The annotations in (a) correspond to the carbon labels in Figure 3.1.

Figure 3.3 shows the C 1s and O 1s regions of the IL multilayer deposition on anatase TiO_2 (101) before exposure to water, under UHV conditions. The C 1s region (Figure 3.3a) is fitted with four peaks. The peak at 285.5 eV is attributed to the alkyl chain carbon atoms in the $[C_4C_1Im]^+$ cation (labelled C_1 in Figure 3.1). The peaks at 286.8 eV and 287.0 eV are attributed to the C_2 carbon atoms (just outside of the imidazolium ring) and C_3 carbon atoms (inside the imidazolium ring) respectively. The peak at 287.9 eV is attributed to the C_4 carbon atoms between the nitrogen atoms inside the imidazolium ring. The area ratio of the C 1s composite peaks, $C_1:C_2:C_3:C_4$ is 3:2:2:1, which is the same as that predicted by stoichiometry, and that previously observed for a thick IL film on anatase TiO_2 [19]. The O 1s region (Figure 3.3b) is fitted with three peaks. The dominant peak at 530.3 eV is attributed to lattice O of the anatase TiO_2 substrate [19, 22]. The peaks at 531.9 eV and 533.2 eV are attributed to hydroxyl groups, specifically Ti-OH and contaminant C-OH groups [23] respectively. Table 3.1 summarises all peak assignments, together with their BE values, throughout the investigation of water/IL on anatase TiO_2.
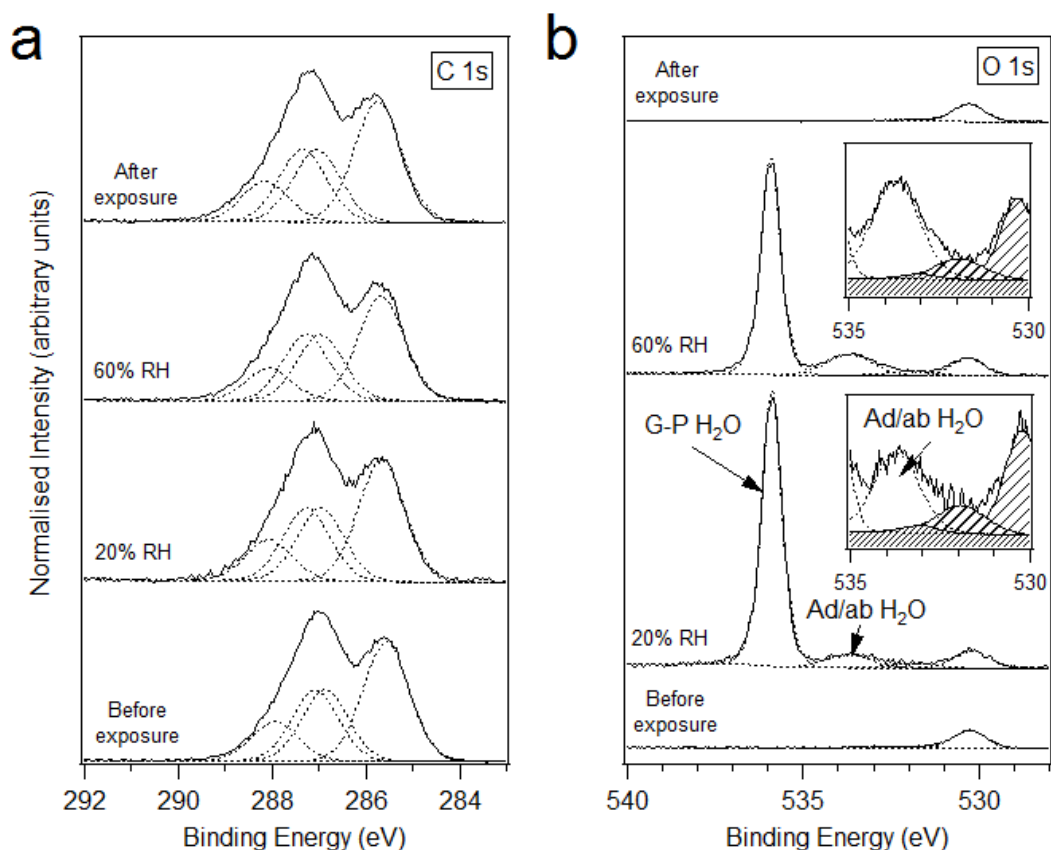
Figure 3.4: C 1s region (a) and O 1s region (b) recorded from the water/IL anatase TiO_2 (101) system. Each feature the region before exposure to water vapour (where the NAP cell was under UHV conditions), at 20% relative humidity, at 60% relative humidity, and after exposure to water vapour (once the NAP cell returned to UHV conditions). The inset figures in (b) display a 15× magnification of the O 1s region between 535 eV and 530 eV. The annotations 'Ad/ab H_2O' and 'G-P H_2O' refer to adsorbed/absorbed water and gas-phase water respectively. In the inset figures, the broad-hatched area is the TiO_2 peak, the thick line-hatched area is the Ti-OH peak, and the fine-hatched area is the C-OH peak.

Figure 3.4 shows the C 1s and O 1s region of the IL deposition on anatase TiO_2 (101), recorded before exposure to water (bottom), at 20% RH, at 60% RH, and after water exposure (top). No new peaks appear in the C 1s region, but there is a slight change in the peak area ratio, C_1/C_4 (see Figure 3.1 for carbon assignments), with pressure. As the relative humidity increases, the ratio decreases. The intensity of the peak attributed to C_4 increases relative to that attributed to the alkyl chain carbons. When the water vapour is removed and the system is allowed to return to UHV overnight, this ratio decreases (the relative intensity of the C_4 peak decreases relative to the C_1 peak), but does not return to its original value, the value prior to any water exposure. The change in shape of the region is easier to see in Figure 3.5a, where the C 1s region at 60% RH and after exposure to water are overlaid. The increase in this ratio with increasing RH could indicate that the imidazolium ring of the IL cation becomes more prominent at the surface of the IL as water molecules are

113

adsorbed/absorbed, indicating interaction between the charged head of the imidazolium cation and ad/absorbed water molecules. The fact that the ratio does not return to its original value may indicate that some water still remains trapped in the IL, even after the system has returned to UHV. This effect is more apparent in the C 1s region of the ultrathin film system in Section 3.4.
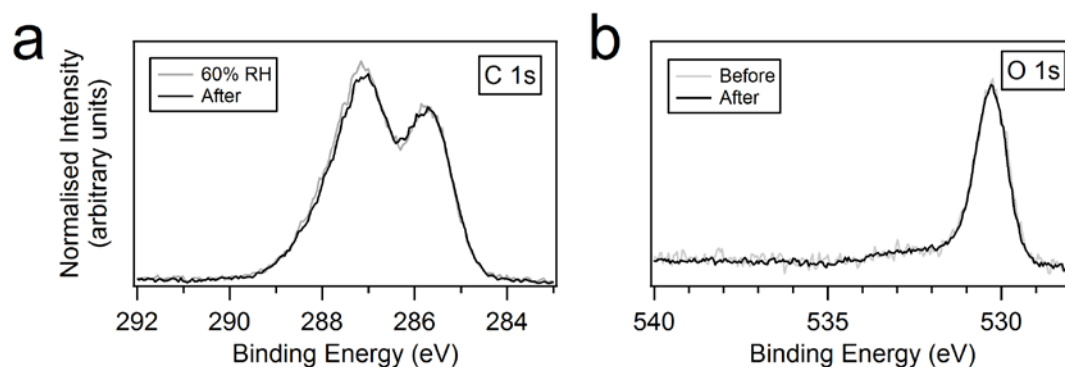
Figure 3.5: The C 1s spectra taken at 60% RH and after exposure to water are shown in (a), represented by a grey solid line and black solid line respectively. The O 1s spectra taken before and after water exposure (represented by a grey solid line and black solid line respectively) are shown in (b).

The O 1s spectra recorded for the IL deposition on anatase TiO_2 are displayed in Figure 3.4b. During exposure to water vapour, two new peaks appear. The peak at 536.0 eV is attributed to gas-phase water vapour [24, 25]. The peak that appears at 533.8 eV is attributed to adsorbed/absorbed water [25, 26]. At 60% RH, the adsorbed/absorbed water peak is more intense relative to the lattice O peak than it is at 20% RH. While the pressure of the water vapour is the same, the cooler temperature of the sample corresponds to a greater relative humidity. This therefore corresponds to a greater water uptake, shown by the increase in relative intensity of the ad/absorbed water peak. The O 1s region recorded after exposure to water (after pumping overnight) is a similar shape to that recorded before exposure (see Figure 3.5b). This would suggest that all water desorbs from the IL. However, it has been shown that peaks attributed to adsorbed water can shift to a lower BE with decreasing coverage [25, 26]. It may be the case here that the coverage (in the case of adsorption) or concentration (in the case of absorption) of water is very low, which could mean that the peak attributed to ad/absorbed water and the peak attributed to C-OH groups in the O 1s region overlap one another. This would account for the peak area ratio C_1/C_4 not returning to the value prior to exposure to water vapour, as well as the disappearance of the ad/absorbed water feature at 533.8 eV. Rivera-Rubero et

al [14] used sum frequency generation (SFG) spectroscopy, to determine how the presence of water affects the surface ordering of imidazolium-based ILs. They suggest that the surfaces of hydrophobic (water-immiscible) ILs are more affected by the addition of water than those of hydrophilic (water-miscible) ILs. They propose that, in the bulk of the hydrophilic IL, the water molecules are stabilised by intermolecular interactions, such as hydrogen bonding and dipole-dipole forces. It is therefore possible that a small amount of water has been allowed to stabilise within the IL multilayers.
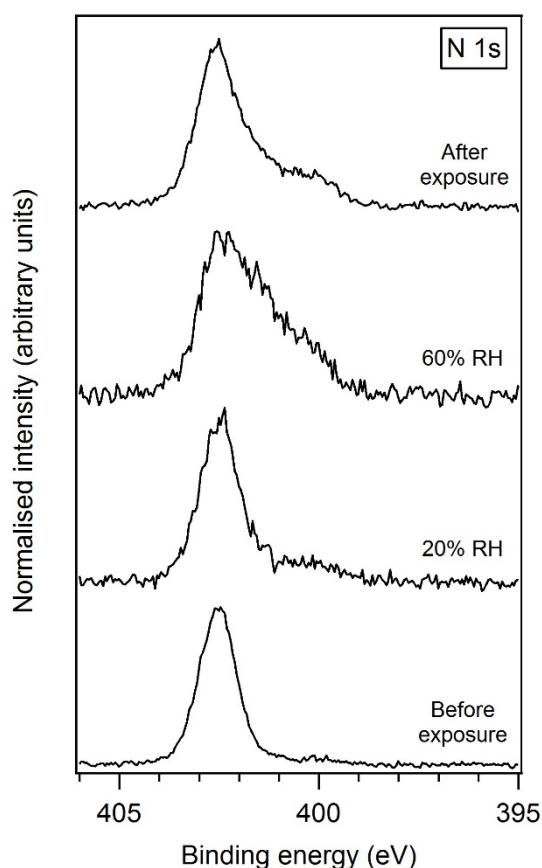
Figure 3.6: The N 1s spectrum recorded before exposure to water vapour (where the NAP cell was under UHV conditions), at 20% RH, at 60% RH, and after exposure to water vapour (once the NAP cell had returned to UHV conditions).

Figure 3.6 shows the N 1s region before exposure to water vapour, at 20% RH, at 60% RH, and after exposure to water vapour. Before exposure to water, there is a single dominant peak at 402.6 eV, which can be attributed to imidazolium nitrogen atoms in the $[C_4C_1Im]^+$ cation. Both nitrogen atoms are considered chemically equivalent, and thus appear as a single peak in the N 1s region. As the relative humidity increases, the N 1s region changes shape significantly. At 20% RH, a shoulder appears at a lower BE than the

imidazolium N peak, and increases in intensity at 60% RH. When the water vapour is removed and the system pumped overnight, the intensity of this shoulder decreases, but is more intense (relative to the imidazolium N peak) than before exposure to water vapour. Lovelock et al [27] showed that thin depositions of IL are susceptible to damage from prolonged X-ray exposure-damage which manifests peaks on the lower BE edge of the N 1s region. From this data, it appears that water may exacerbate this beam damage. One way that could minimise beam damage is the use of raster scanning, where a short measurement is taken at a number of places on the sample, rather than a few longer measurements taken on one area of the sample. The short measurements would be merged together to produce a smooth spectrum. This method was explored and is detailed in Chapter 3.4.1.
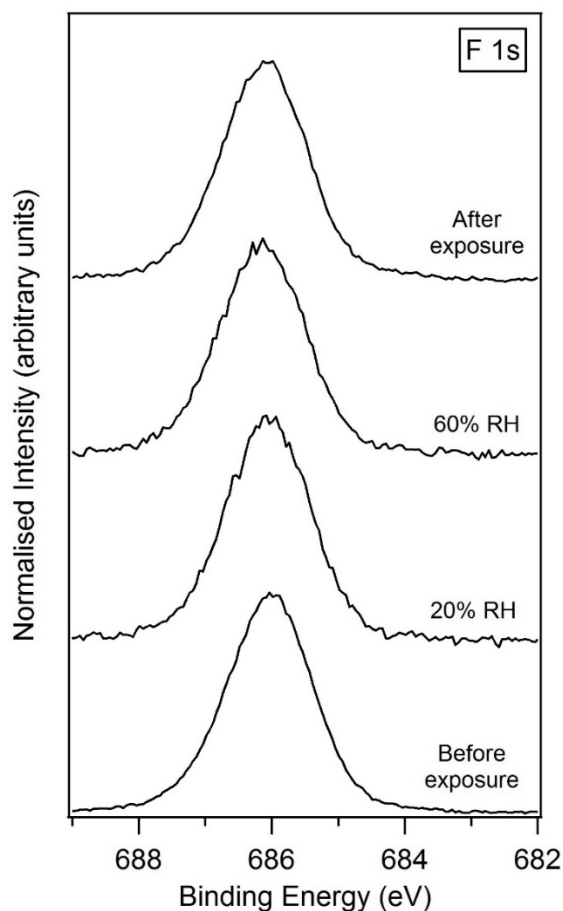
Figure 3.7: The F 1s spectrum recorded before exposure to water vapour (where the NAP cell was under UHV conditions), at 20% RH, at 60% RH, and after exposure to water vapour (once the NAP cell had returned to UHV conditions).

Figure 3.7 shows the F 1s before exposure to water vapour, at 20% RH, at 60% RH, and after exposure to water vapour. At all stages, the region is composed of a single peak at 686.0 eV. The peak is attributed to fluorine in the $[BF_4]^-$

anion, as the BE is consistent with those quoted in literature [19, 28]. In previous works of multilayer and approximately monolayer depositions of the same IL on anatase TiO_2 [19], a feature appears at the lower BE edge of the F 1s region for the monolayer deposition, which is suggested by Wagstaffe et al to be Ti-F interactions. This feature is not present in the F 1s region for the data presented here, which suggests the IL deposition here is too thick to observe a signal from the interactions between the IL and the TiO_2 surface. In order for this peak to appear in the F 1s region for a $[C_4C_1Im][BF_4]/TiO_2$ system (and, therefore, for these interactions to be observed), a much thinner deposition of IL is required. Ultrathin films are highly structured, and are also known to have an alkyl enrichment at their surface, where alkyl chains face outward toward vacuum, just like the IL/vacuum interface of thick IL films [12, 13, 29]. A sufficiently thin film may also allow for interactions at the IL/water interface to be investigated without significant water absorption. Therefore, a second investigation into the IL/water interface was conducted using an ultrathin deposition of the same IL on rutile TiO_2. The results from this experiment are outlined in Chapter 3.4.2.

Table 3.1: Assignments of all fitted core level XPS peaks for the water/IL on anatase TiO_2 (101) system, together with their respective binding energies.

Region	Binding Energy (± 0.1 eV) (eV)	Assignment
C 1s	285.5	C_1, alkyl chain
	286.8	C_2, imidazolium
	287.0	C_3, imidazolium
	287.9	C_4, imidazolium
O 1s	530.3	TiO_2 substrate
	531.9	Hydroxyl (Ti-OH)
	533.2	Hydroxyl (C-OH)
	533.8	Ad/absorbed H_2O
	536.0	Gas-phase H_2O
F 1s	686.0	F, $[BF_4]^-$

3.4 Water/IL on rutile TiO_2 (110)

Because the IL deposition on anatase TiO_2 (101) sustained significant beam damage, a short investigation was carried out on the effects of prolonged X-ray exposure under comparable conditions.

3.4.1 Short investigation into sample beam damage
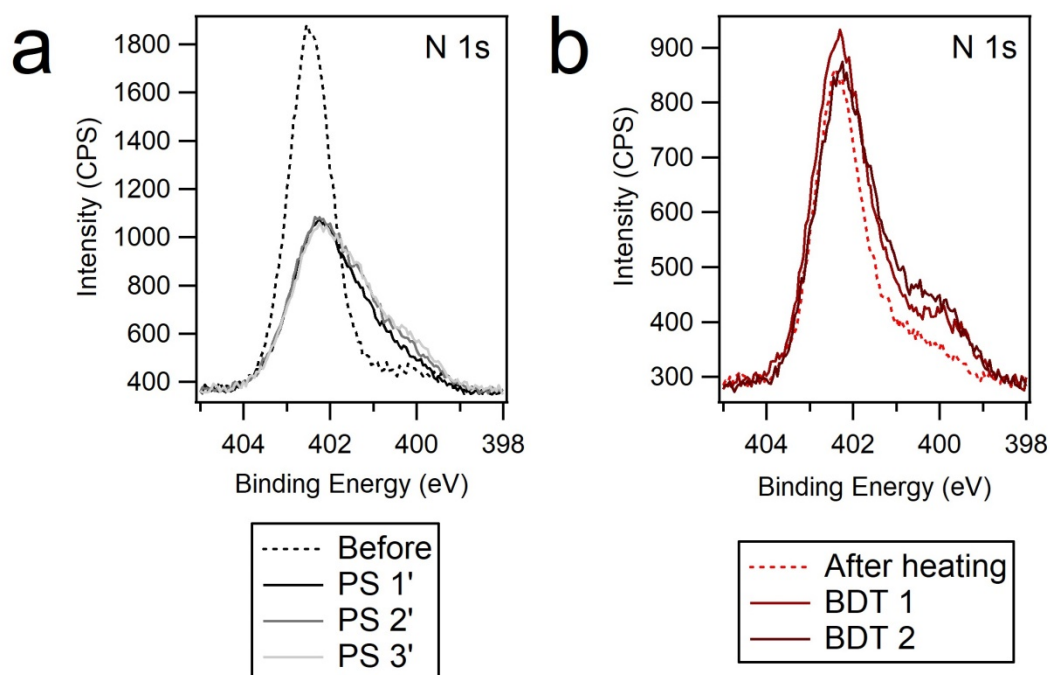
Figure 3.8: N 1s region before and after exposure to water, and (b) N 1s region after heating in UHV and subject to two further scans. The labels in (a) have been differentiated from the labels used in the main data with '. The label BDT stands for 'beam damage test'.

An IL film was deposited onto the rutile TiO_2 substrate in the same manner as the water/IL on rutile TiO_2 experiment (also dosed for 30 minutes). Similarly, measurements were taken in three regimes: before exposure to water, during water exposure (at a pressure of 8 mbar and 285 K, which corresponds to a relative humidity of ~70%, not shown in Figure 3.8) and after water exposure. The regime after water exposure was seceded into three measurements, named here Pump Stages 1' to 3', (similarly abbreviated to PS 1' to PS 3' in Figure 3.8a). These scans were not rastered, and were taken on the same part of the sample surface each time. After these measurements, the sample was then gently heated in UHV conditions to remove some of the beam-damage species (spectrum labelled 'After heating' in Figure 3.8b). To observe only the effects of prolonged X-ray exposure on the ultrathin IL film (i.e. with no water vapour), two more non-rastered measurements were taken under UHV conditions only. These data are labelled as "beam damage test", or BDT, in Figure 3.8b. Each measurement took approximately one hour, and with additional time compensating for sample heating, the experiment overall took eight hours. The shoulder at the lower BE edge of the N 1s spectra recorded

with exposure only to X-rays displays a noticeable increase in intensity. However, the change in shape of the N 1s region is the most dramatic in Figure 3.8a. The shape of the N 1s region only changes slightly throughout PS 1' to PS 3', but it is not as significant as the change between the measurement taken before exposure and immediately after exposure to water vapour (PS 1'). Therefore, it can be concluded that water vapour has a significantly exacerbating effect on the beam damage of IL samples. Subsequently, measurements of the water/IL system on rutile TiO_2 (110) were rastered to minimise sample beam damage.

3.4.2 XPS analysis at UHV
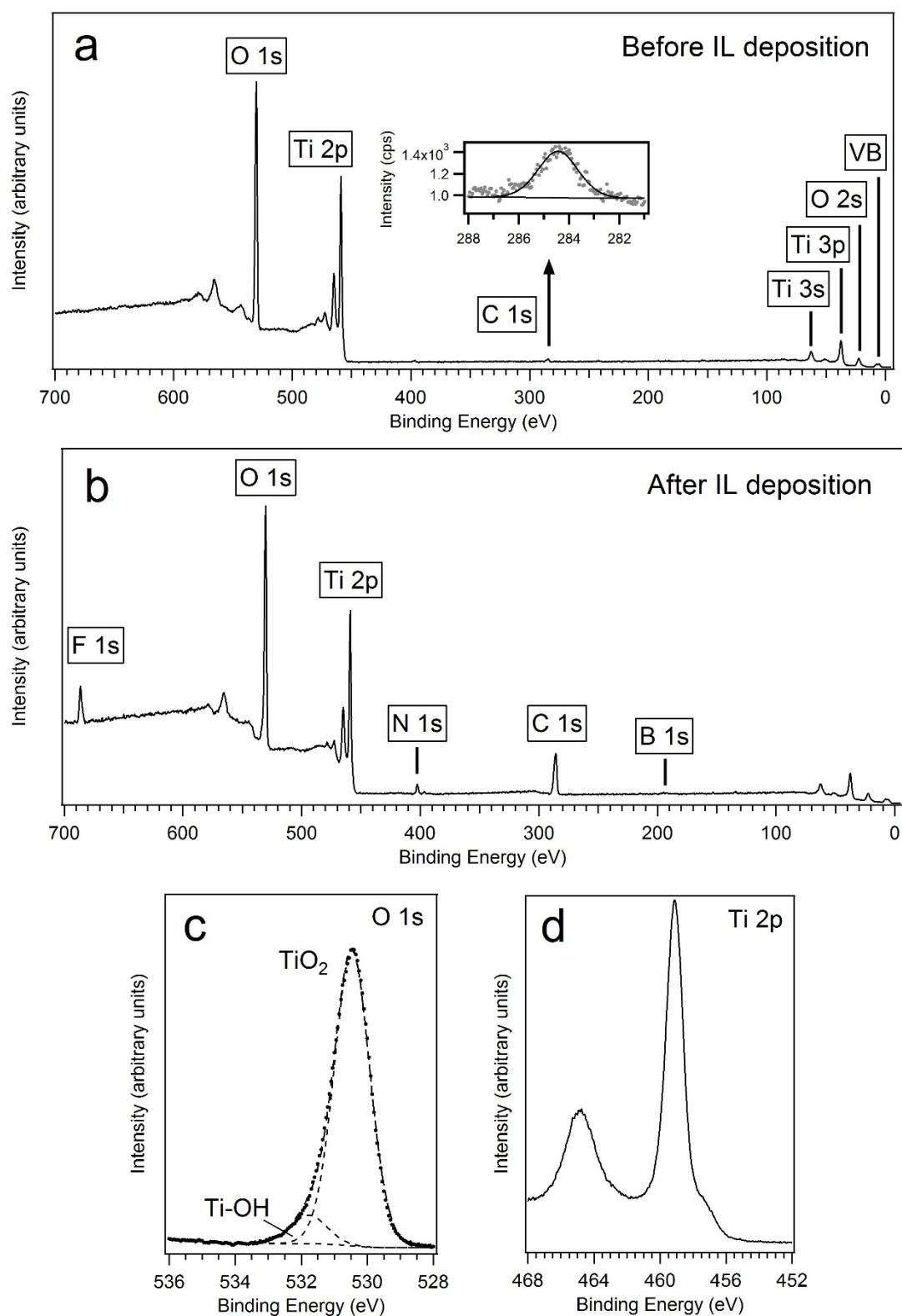
Figure 3.9: Survey spectra of the TiO$_2$ substrate before (a) and after (b) in UHV. All relevant peaks have been labelled in both survey spectra. The inset figure in (a) shows the C 1s spectrum of the TiO$_2$ region prior to IL deposition. The O 1s and Ti 2p regions prior to IL deposition are shown in (c) and (d) respectively.

After the investigation into beam damage, the rutile TiO_2 (110) crystal was cleaned via Ar^+ sputter/anneal cycles until the XPS spectra showed minimal contamination. These XPS spectra are displayed in Figure 3.9. Figure 3.9a shows the survey spectra of the TiO_2 substrate in UHV before the ultrathin IL deposition, and Figure 3.9b shows the survey spectrum after IL deposition. The O 1s and Ti 2p region of the TiO_2 surface in UHV before IL deposition are shown in Figure 3.9c and Figure 3.9d respectively. The inset of Figure 3.9a shows the C 1s region taken of the TiO_2 substrate prior to IL deposition, demonstrating there is some carbon contamination of the surface. The O 1s region appears to have a slight shoulder toward higher BE, indicating the presence of hydroxyl groups, and is labelled Ti-OH (see Table 3.2 for a summary of all peak assignments for water/IL on rutile TiO_2). The surface of the TiO_2 also contains defects, as shown by the shoulder at the lower BE edge of the Ti 2p region (Figure 3.9c). The significance of these observations are discussed in the following subsections.

3.4.3 NAPXPS analysis
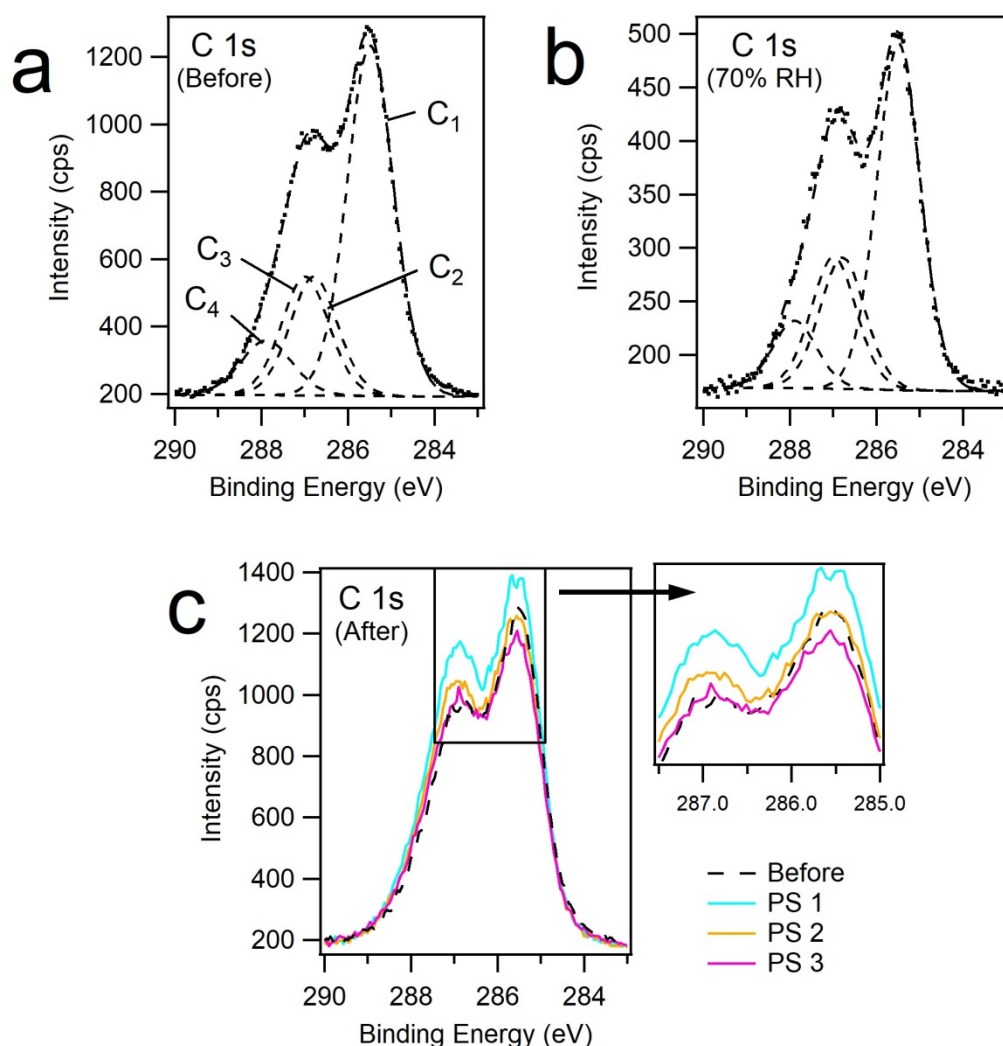
Figure 3.10: C 1s region before exposure to water (a), C 1s region at 70% RH (b), and the C 1s spectrum from PS 1 to PS 3 (represented by the cyan, amber and magenta lines respectively) (c), together with the C 1s spectrum taken before exposure (represented by the black dashed line).

Figure 3.10 shows the C 1s spectrum for the sample prior to water exposure. It can be fitted with four composite peaks, (corresponding to the numbered carbon atoms in Figure 3.1) and in good agreement with literature [19]. The peak at 285.5 eV corresponds to that of the alkyl chain carbons. The peak at 286.8 eV corresponds to the C_2 carbons just outside of the imidazolium ring, the peak at 287.0 eV corresponds to the C_3 carbons inside the imidazolium ring and the peak at 287.9 eV corresponds to the C_4 carbon, between the two N atoms in the imidazolium ring. The alkyl carbon peak and the imidazolium carbon peaks together create the characteristic two-peak shape of the C 1s region. A study by Wagstaffe et al [19] of multilayer and approximately monolayer coverages of

[C$_4$C$_1$Im][BF$_4$] on anatase TiO$_2$ (101) highlighted distinct differences between the C 1s regions of the bulk and monolayer IL films. More specifically, the component associated with the alkyl chain and two of the three components associated with the imidazolium group were found to shift to a lower binding energy (BE) for the thin film. This observation is consistent with findings reported by Cremer et al with analogous ILs [3]. As expected, the binding energies of the components of the C 1s region in our study are more in line with those of a thin film. However, the alkyl chain component dominates the region, which is not consistent with the shape of the C 1s observed by Wagstaffe et al. The film studied here is indeed thicker than the monolayer film studied by Wagstaffe et al, and while it is known that alkyl chains face outward toward vacuum in imidazolium-based ILs, the strength of the alkyl chain signal here may be explained by a contribution from carbon contamination.

Table 3.2: Assignments of all fitted core level XPS peaks for the water/IL on rutile TiO$_2$ (110) system, together with their respective binding energies.

Region	Binding Energy (±0.1 eV) (eV)	Assignment
C 1s	285.5	C$_1$, alkyl chain
	286.8	C$_2$, imidazolium
	287.0	C$_3$, imidazolium
	287.9	C$_4$, imidazolium
O 1s	530.2	TiO$_2$ substrate
	531.5	Hydroxyl (Ti-OH)
	533.0	Hydroxyl (C-OH)
	533.3	Adsorbed H$_2$O
	535.9	Gas-phase H$_2$O
N 1s	399.6	Beam damage
	400.9	Beam damage
	402.3	N, imidazolium
F 1s	684.3	F-Ti
	686.4	F, [BF$_4$]$^-$

ILs have a tendency to become contaminated via external sources: such as the introduction of adventitious carbon from exposure to atmosphere [30, 31], or even Si contamination due to grease present in the IL from synthesis [27, 32]. It is possible that the vapour-deposited IL contained impurities, but we believe it is more likely that the contamination of the IL film in this study originates from the background vacuum of the NAP cell. Quantification of the C 1s, O 1s and Ti 2p regions prior to IL deposition reveals (2.3 ± 0.6)% carbon contamination present

on the TiO_2 surface (see Table 3.3). The nature of the carbon contamination is not clear (i.e. whether it is flat coverage, island-like growth, etc.), but the presence of carbon prior to IL deposition could explain the strength of the alkyl chain signal in the C 1s region. Deyko et al [33] studied the influence of carbon coverage on the growth mechanisms of 1-ethyl-3-methylimidazolium bis(trifluoromethylsulfonyl)imide (or $[C_2C_1Im][Tf_2N]$) on mica. They found that, on mica surfaces with minimal carbon coverage, the IL demonstrated 3D growth in the form of islands at sub-monolayer IL coverage (i.e. complete dewetting of the mica surface). On mica surfaces with partial or complete carbon coverage, the IL demonstrated 2D layer-by-layer growth on the contaminated areas, and 3D growth on the non-contaminated areas (i.e. partial or complete wetting of the mica surface). This illustrates that carbon contamination can play a rather significant role on the growth of ILs on oxide surfaces. The rutile TiO_2 used in our study appears to have minimal carbon coverage prior to IL deposition. Therefore, the IL itself (rather than the TiO_2 substrate) may have become contaminated when introduced to the NAP cell. One possible way to remove contamination from ILs is through gentle Ar^+ sputtering [27, 30], but this was not possible with the sample in the NAP cell.

Table 3.3: Composition (in atomic percentage) of C, Ti and O on the rutile TiO_2 (110) single crystal substrate prior to ionic liquid deposition. The relative sensitivity factor (RSF) is shown for each element.

Element	RSF	Composition (at%)
C	1.00	2.3±0.6
O	2.93	70.4±0.6
Ti	7.81	27.3±0.3

Another noteworthy observation made by Wagstaffe et al [19] is that the IL adsorbed well-ordered on the anatase TiO_2, which was corroborated by X-ray absorption measurements. Although it cannot be determined whether the IL film in our study has grown in a 2D or 3D configuration with these data alone, it is likely that the IL film is highly ordered by both the TiO_2 and vacuum interfaces. Also reported by Wagstaffe and colleagues was that $[C_4C_1Im][BF_4]$ chemically interacts with TiO_2 via the F in the anion bonding with Ti, possibly at O-vacancy sites [19]. This statement is supported in the literature by a peak in the F 1s region, with a BE consistent with that of Ti-F bond formation. Because the IL layer studied was approximately a monolayer, this peak was the majority signal

in the F 1s region. A similar peak has been observed in the F 1s region in our study (see Figure 3.13), which we also attribute to F-Ti bonding. Since it is only the first IL layer that bonds to the Ti surface the F-Ti peak in our study makes up a smaller percentage of the F 1s signal than that presented by Wagstaffe et al. This therefore corroborates our assessment of the film thickness in our study.

Table 3.4: Composition (in atomic percentage) of C, N and F in the sample before exposure to water and at PS 1. The relative sensitivity factor (RSF) is shown for each element.

Element	RSF	Composition (at%)		
		Before	PS 1	Bulk IL*
C	1.00	73 ± 2	70 ± 1	55.6
N	1.80	9.4 ± 0.3	10.3 ± 0.4	13.2
F	4.43	17 ± 1	19.7 ± 0.4	31.2

* Indicates values adapted from Ref [13] for bulk $[C_4C_1Im][BF_4]$ for comparison to values from this work.

Upon exposure to water, the contribution from the imidazolium ring increases relative to the contribution from the alkyl chain. This indicates a rearrangement of the cations at the surface of the IL, where the imidazolium ring becomes more prominent. We suggest that water adsorbed on the IL causes the cations to rearrange such that the imidazolium ring (the hydrophilic part) is orientated toward the adsorbed water, and the hydrophobic alkyl chain orientates away from the adsorbed water. This water-induced rearrangement of the surface ions could be explained by a dipole-dipole interaction between the imidazolium ring and water lone pair, an interaction previously proposed for water in the bulk of imidazolium-based ILs and water [28]. In addition, the concentrations of C, N and F have been calculated for the regions before exposure to water and at PS 1 (as the reordering was most prevalent at this stage than at 70% RH) and compared. The concentrations were calculated using the total area of each region (see Table 3.4). At PS 1, there is a decrease in the concentration of C and an increase in the concentration of N and F. In each case, the concentration decrease/increase is beyond the range of the uncertainty boundaries calculated for the regime before water exposure. This change in composition of the surface further reiterates the idea that the charged parts of the IL, i.e. the anion and the charged head of the cation, become more prominent at the IL/water interface than at the IL/vacuum interface. Previous work into the surface interactions between water and ILs by Deyko and Jones

[34] suggest that water present on the surface of the analogous [C_8C_1Im][BF_4] experiences greater interaction with itself than with the IL surface, behaving as though it were adsorbed on a hydrophobic surface. While this may be consistent with our proposition of water adsorbing on the surface of the IL, the system used by Deyko and Jones had been cooled prior to measurements, so was in fact a glassy solid rather than a liquid film. As water vapour is removed from the NAP cell, the shape of the C 1s peak begins to change again (see Figure 3.10c). The contribution from the alkyl chain now increases relative to the contribution from the imidazolium ring, and the C 1s region begins to resemble the shape of the region prior to water exposure, but the data does not show a complete reversal. This indicates that the ions at the surface begin to return to their original structure as the pressure in the cell returns to high vacuum.
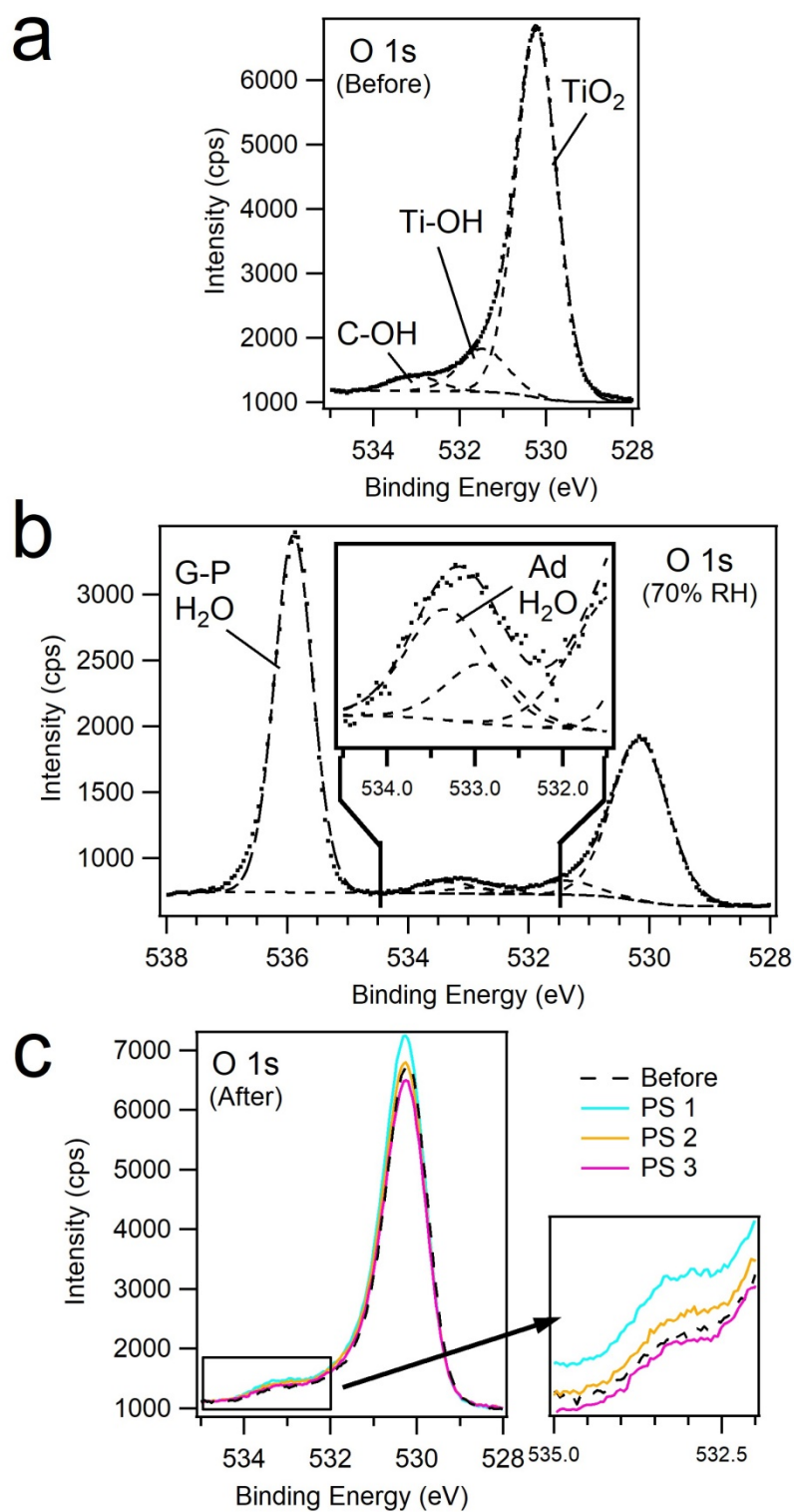
Figure 3.11: O 1s region before exposure to water (a), O 1s region at 70% RH (b), and the O 1s spectrum from PS 1 to PS 3 (represented by the cyan, amber and magenta lines respectively) (c), together with the O 1s spectrum taken before exposure (represented by the dashed black line).

Figure 3.11a and Figure 3.11b show the O 1s spectrum for the IL/rutile TiO_2 sample before and during exposure to water respectively. Before exposure to water, the region can be fitted with three distinct component peaks. At the lower

BE edge, the peak at 530.2 eV is assigned to the TiO_2 lattice oxygen peak [19, 22]. Numerous hydroxyl species can manifest peaks at higher binding energies than the lattice O, including C-OH groups [23] and bridging hydroxyls on the rutile TiO_2 (110) surface [20], some of which can arise from water in the background vacuum even at high vacuum pressures [21]. Thus, the peaks at 531.5 eV and 533.0 eV are assigned as Ti-OH and C-OH species, respectively. Upon exposure to water, two new peaks appear at the higher BE edge of the O 1s spectrum. The peak at 535.9 eV is attributed to gas-phase water, i.e. water vapour surrounding the sample [24, 35]. The peak at 533.3 eV (0.2 eV higher BE than that arising from C-OH), has been assigned to molecular water adsorbed on the IL film [25, 26]. Although the peaks assigned to hydroxyl species and molecular water are close in BE, two separate peaks were needed to properly fit the spectrum. Furthermore, in the NAPXPS measurements recorded of the water/IL system on anatase TiO_2 (101) the peak assigned to molecular adsorbed water is more prominent in the O 1s spectrum due to less attenuation of the signal by gas-phase water. The O 1s assignments from those measurements further support the BE assignments here. When water is evacuated from the NAP cell, the gas-phase water peak disappears whereas the adsorbed water peak is present until the final scan (which was recorded at a background pressure of $\leq 1 \times 10^{-7}$ mbar). While the corresponding changes in the O 1s region are small, they can be seen in the raw data presented in Figure 3.11c. The prolonged presence of the molecular water peak through PS 1 and 2 indicates water becomes trapped on top of the IL layers for some time. Furthermore, this indicates that the ultrathin IL deposition can stabilise a small amount of water at its surface even in UHV for a period of time.
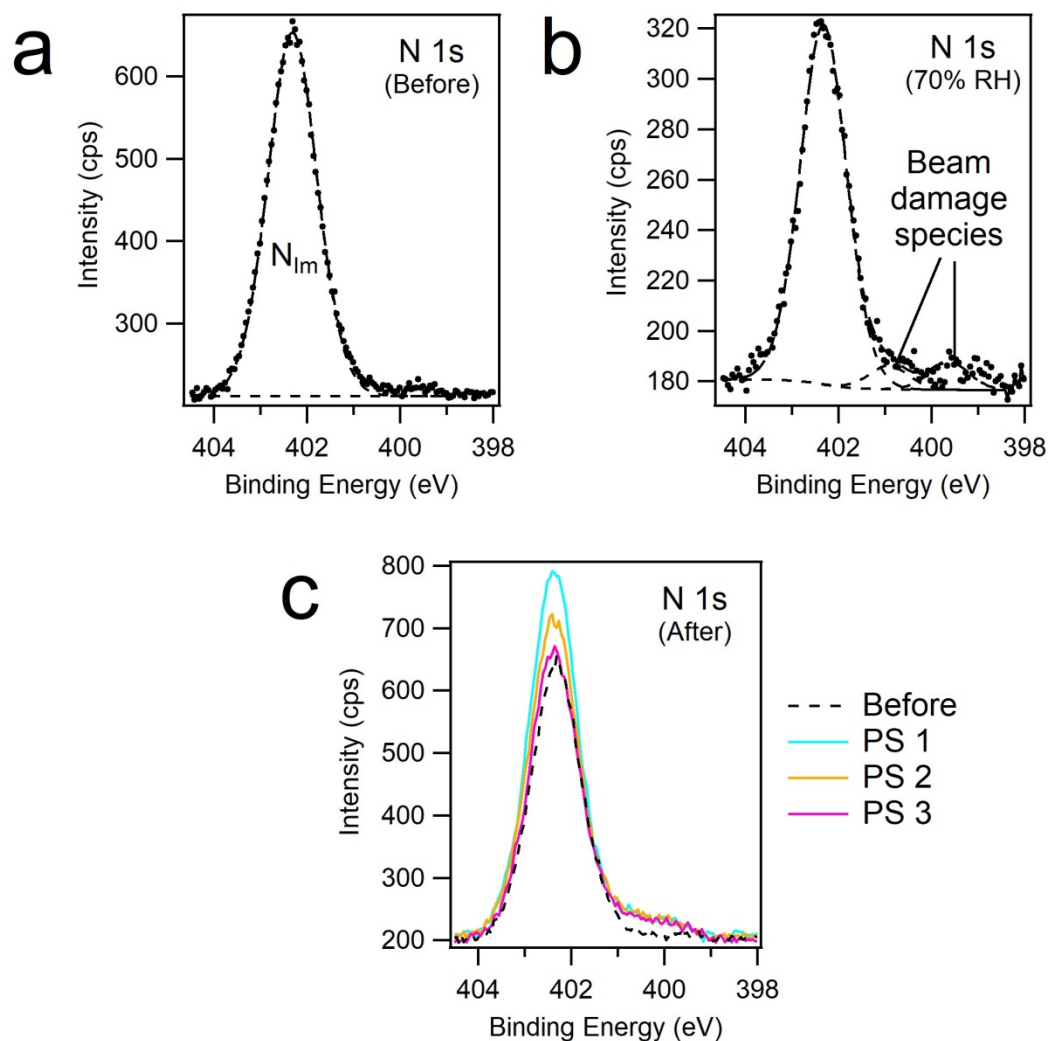
Figure 3.12: N 1s region before exposure to water (a), N 1s region at 70% RH (b), and the N 1s spectrum from PS 1 to PS 3 (represented by the cyan, amber and magenta lines respectively) (c), together with the N 1s spectrum taken before exposure (represented by the dashed black line).

Figure 3.12a shows the N 1s spectrum before exposure to water, and is dominated by a peak at 402.3 eV. This peak is assigned to N in the imidazolium ring of the cations [19][6]. There appears to be a slight shoulder on the lower BE edge, which, as also discussed for the IL multilayers on anatase TiO_2 (101), is attributed to beam damage species.

Figure 3.12b shows the N 1s spectrum at 70% RH. Two peaks appear at 400.9 eV and 399.6 eV. These are attributed to beam damage, and are labelled as 'Beam damage species' in Figure 3.12b. The peaks in the N 1s spectrum do not show any indication of returning to their original intensity values during PS 1 to PS 3. This confirms that these peaks are a result of damage to the sample from prolonged X-ray exposure. Rastered measurements were taken to minimise

sample beam damage, and it can be seen from the N 1s spectra that no extra peaks appear to manifest in the region throughout the experiment. This demonstrates that rastered measurements do somewhat reduce beam damage to IL films. In addition, the peak associated with the N in the imidazolium ring dominates the region throughout the experiment, which shows that that the vast majority of the $[C_4C_1Im]^+$ cations of the IL film remain intact.
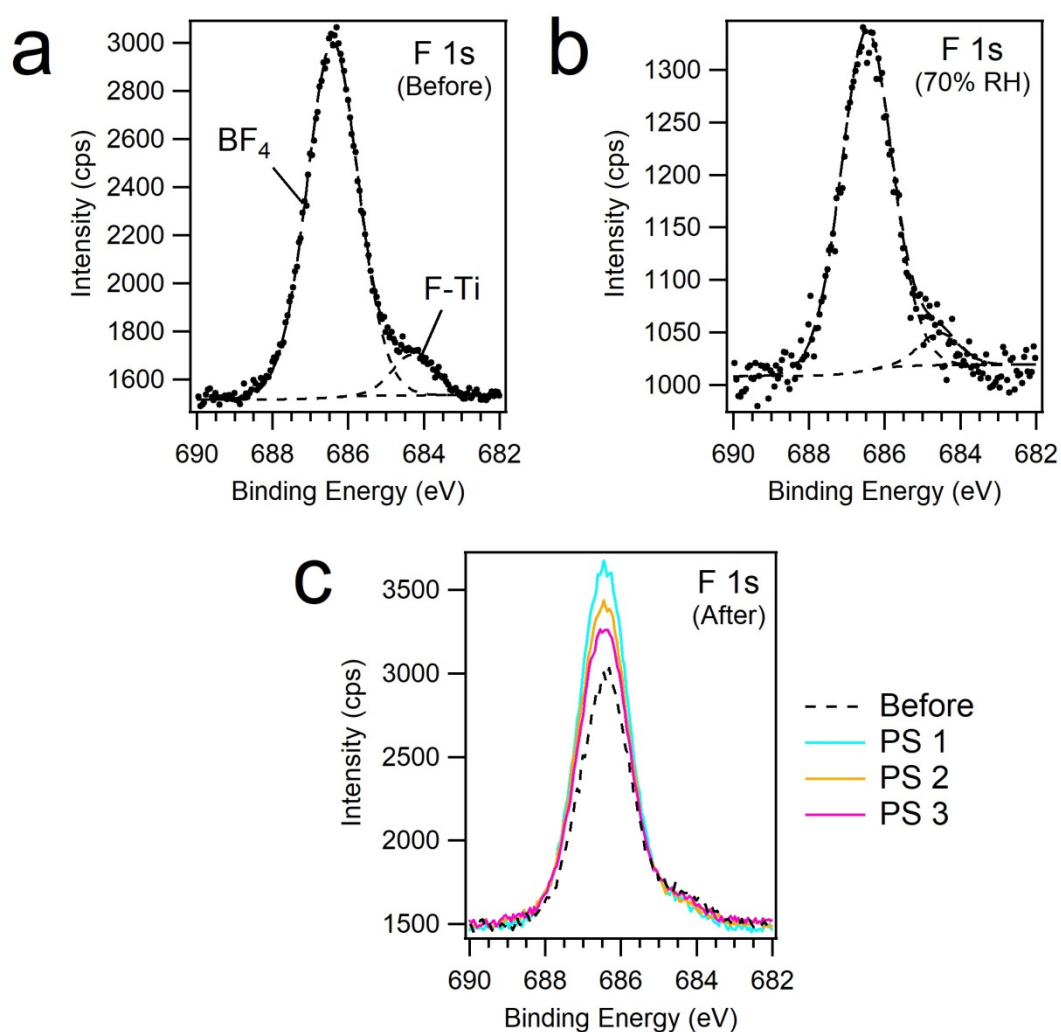
Figure 3.13: F 1s region before exposure to water (a), F 1s region at 70% RH (b), and the F 1s spectrum from PS 1 to PS 3 (represented by the cyan, amber and magenta lines respectively) (c), together with the F 1s spectrum taken before exposure (represented by the black dashed line).

Figure 3.13 shows the F 1s spectrum before exposure to water, and can be fitted with two peaks: the peak at 686.4 eV arises from the F in the tetrafluoroborate ion [19, 28]. As mentioned previously, the smaller peak at 684.3 eV is thought to arise from F-Ti bonding at the IL/TiO$_2$ interface [19]. In the work by Wagstaffe et al with the same IL on anatase TiO$_2$ (101) [19], the peak associated with F-Ti bonding makes up approximately 56% of the F 1s

signal. In our study, this peak only makes up approximately 9% of the F 1s signal, which emphasises that the thickness of our IL film is greater than the (approximately) monolayer IL film studied by Wagstaffe.

Upon water exposure, the relative intensity of the peak associated with the anion increases (from 91% to 93%), while the peak associated with the F-Ti bonding decreases (from 9% to 7%). The decreased relative intensity could be the result of an attenuation effect, whereby the adsorbed water has increased the depth of the sample, resulting in an attenuation of the F-Ti signal from the buried IL/TiO$_2$ interface. As water is evacuated from the system, the molecular adsorbed water eventually desorbs from the surface, and the peak associated with the [BF$_4$]$^-$ anion begins to decrease.

Cammarata et al [36] showed, using attenuated total reflectance infrared spectroscopy, that water interacts with the [BF$_4$]$^-$ anion via hydrogen bonding, both in imidazolium- and non-imidazolium-based ILs. This finding was also corroborated by Baldelli's group [37] using the more surface sensitive technique of sum frequency generation spectroscopy, who examined the interactions and surface orientation of [C$_4$C$_1$Im][BF$_4$] and water. Ridings et al [16] used neutral impact collision ion scattering spectroscopy to show that small amounts of water in an imidazolium-based IL (1-hexyl-3-methylimidazolium chloride, [C$_6$C$_1$Im][Cl],) can influence the composition of the IL surface. They found that at higher water concentrations the anion showed an increased presence at the IL surface, with the alkyl chains of the cation moving towards the bulk. Hence, as the water content is increased the charge at the surface becomes more negative. They attribute this behaviour to the influence of water on the hydrogen-bonding network in the IL, specifically hydrogen bonding between the anions and water. While we do not see any evidence of bonding between the water and the [BF$_4$]$^-$ ions in the F 1s spectra, we do observe a relative intensity change that suggests a rearrangement of the anion preferentially towards the IL/water interface. This somewhat corroborates the idea that water adsorbed on the IL influences the composition of the surface ions, bringing the anion and imidazolium ring toward the IL/water interface.

3.4.4 Discussion

The ordering at the topmost surface undoubtedly plays a role in the sorption mechanics of ILs, but questions remain as to what kind of interactions occur at the IL/water interface. As mentioned previously, water molecules are known to interact with imidazolium-based ILs via dipole-dipole interactions and hydrogen bonding [14]. In that study, water was allowed to stabilise in a bulk IL, so the interactions and adsorption mechanisms at the IL/water interface were not studied directly. Our study, using an ultrathin film rather than bulk IL, shows that the cations of the water-miscible $[C_4C_1Im][BF_4]$ experience an interaction with water molecules at the IL/water interface, possibly through hydrogen bonding and dipole-dipole forces with the imidazolium groups. However, there appears to be no reaction with the imidazolium N atoms (see Figure 3.12). The interaction appears instead to influence a reorganisation of the molecules at the IL surface, where the imidazolium ring becomes more prominent. An in situ XPS study carried out by Broderick et al [35] investigated the interactions between water and a different water-miscible IL with the same cation. They also suggest that a rearrangement of ions occurs, but rather alkyl chains become more prevalent in the IL/water interfacial region at a water mole fraction of 0.6. However, the system in question was arguably a bulk film, able to absorb and stabilise a relatively large quantity of water in the bulk liquid. Numerous theoretical studies have been conducted into the interactions between $[C_4C_1Im][BF_4]$ [38, 39], and many of its analogues [40, 41], with water; and while local structuring within the bulk liquid has been considered carefully, few have probed the structure and interactions that take place at the IL/water interface upon adsorption.

It may be the case that the $[C_4C_1Im][BF_4]$ deposition investigated here was sufficiently thin to not have allowed the water molecules at the interface to be absorbed and stabilise between the layers. In a recent study by Buckley et al [42] of the interactions with water and $[C_8C_1Im][BF_4]$, it was found that more than 68 water molecules could be stabilised per IL pair due to long-range interactions with IL ions. This finding supports the idea that water is interacting with, and possibly even being stabilised by, the ultrathin IL film examined here. However, the ability for an IL thin film to adsorb water for a significant period may have a negative impact on IL thin film catalysis applications (such as SILP

and SCILL). If the surface structure determines how gases are ad/absorbed into ILs, the presence of water could therefore alter the surface ordering of the IL thin films in these systems. This could then inhibit the reaction kinetics through inhibition of sorption of gaseous reactants and products. As a result, this could diminish the reaction rate and furthermore, diminish the efficiency of these systems.

3.5 Conclusion

The interaction of water with IL multilayers, and water-induced reordering in an ultrathin film of the IL $[C_4C_1Im][BF_4]$ have been observed using near-ambient pressure X-ray photoelectron spectroscopy. Similar behaviour is seen in both the IL multilayer and IL ultrathin film. The results indicate that water is adsorbed on the ultrathin IL surface, involving an interaction between water and the cations, which leads to a reorganisation of the ions at the surface. Reorganisation is observed for both the IL multilayer and IL ultrathin film system, but is more pronounced for the ultrathin IL film. When the IL/anatase TiO_2 (101) system is exposed to water, the ad/absorbed water peak in the O 1s region is much more prominent than the adsorbed water peak in the O 1s region recorded for the ultrathin IL film at 70% RH. It is seen for the water/IL on rutile TiO_2 (110) system that water initially remains trapped on the IL surface even as water vapour is pumped out of the near-ambient pressure cell. The water eventually desorbs from the IL ultrathin film when the cell has been under UHV for some time. The combination of water-induced reordering of the ions at the IL surface and the prolonged presence of molecular water under vacuum conditions could have negative implications for IL thin film catalysis. This insight into the behaviour at the interface provides some understanding of the interaction of water with ILs under realistic conditions, and provides a basis for understanding adsorption and absorption mechanisms found in SCILL/SILP catalysis and gas capture/separation applications.

Chapter 3 References

[1] J. Dupont, R.F. de Souza, P.A. Suarez, *Ionic Liquid (Molten Salt) Phase Organometallic Catalysis*, Chemical Reviews, 102 (2002) 3667-3692, D.O.I.: 10.1021/cr010338r

[2] D. Zhao, M. Wu, Y. Kou, E. Min, *Ionic Liquids: Applications in Catalysis*, Catalysis Today, 74 (2002) 157-189, D.O.I.: 10.1016/S0920-5861(01)00541-7

[3] T. Cremer, M. Stark, A. Deyko, H.-P. Steinrück, F. Maier, *Liquid/Solid Interface of Ultrathin Ionic Liquid Films:[C1C1Im][Tf2N] and [C8C1Im][Tf2N] on Au (111)*, Langmuir, 27 (2011) 3662-3671, D.O.I.: 10.1021/la105007c

[4] H.-P. Steinrück, *Recent Developments in the Study of Ionic Liquid Interfaces Using X-Ray Photoelectron Spectroscopy and Potential Future Directions*, Physical Chemistry Chemical Physics, 14 (2012) 5010-5029, D.O.I.: 10.1039/C2CP24087D

[5] C.P. Mehnert, R.A. Cook, N.C. Dispenziere, M. Afeworki, *Supported Ionic Liquid Catalysis - a New Concept for Homogeneous Hydroformylation Catalysis*, Journal of the American Chemical Society, 124 (2002) 12932-12933, D.O.I.: 10.1021/ja0279242

[6] J. Arras, M. Steffan, Y. Shayeghi, D. Ruppert, P. Claus, *Regioselective Catalytic Hydrogenation of Citral with Ionic Liquids as Reaction Modifiers*, Green Chemistry, 11 (2009) 716-723, D.O.I.: 10.1039/B822992A

[7] T. Cremer, L. Wibmer, S.K. Calderón, A. Deyko, F. Maier, H.-P. Steinrück, *Interfaces of Ionic Liquids and Transition Metal Surfaces—Adsorption, Growth, and Thermal Reactions of Ultrathin [C 1 C 1 Im][Tf 2 N] Films on Metallic and Oxidised Ni (111) Surfaces*, Physical Chemistry Chemical Physics, 14 (2012) 5153-5163, D.O.I.: 10.1039/C2CP40278E

[8] T.J. Gannon, G. Law, P.R. Watson, A.J. Carmichael, K.R. Seddon, *First Observation of Molecular Composition and Orientation at the Surface of a Room-Temperature Ionic Liquid*, Langmuir, 15 (1999) 8429-8434, D.O.I.: 10.1021/la990589j

[9] V. Lockett, R. Sedev, C. Bassell, J. Ralston, *Angle-Resolved X-Ray Photoelectron Spectroscopy of the Surface of Imidazolium Ionic Liquids*, Physical Chemistry Chemical Physics, 10 (2008) 1330-1335, D.O.I.: 10.1039/b713584j

[10] Y. Jeon, J. Sung, W. Bu, D. Vaknin, Y. Ouchi, D. Kim, *Interfacial Restructuring of Ionic Liquids Determined by Sum-Frequency Generation Spectroscopy and X-Ray Reflectivity*, Journal of Physical Chemistry C, 112 (2008) 19649-19654, D.O.I.: 10.1021/jp807873j

[11] R.M. Lynden-Bell, M. Del Popolo, *Simulation of the Surface Structure of Butylmethylimidazolium Ionic Liquids*, Physical Chemistry Chemical Physics, 8 (2006) 949-954, D.O.I.: 10.1039/b514848k

[12] Y. Lauw, M.D. Horne, T. Rodopoulos, N.A.S. Webster, B. Minofar, A. Nelson, *X-Ray Reflectometry Studies on the Effect of Water on the Surface Structure of [C(4)mpyr][NTf2] Ionic Liquid*, Physical Chemistry Chemical Physics, 11 (2009) 11507-11514, D.O.I.: 10.1039/b916046a

[13] H. Xu, Z. Han, D.J. Zhang, J.H. Zhan, *Interface Behaviors of Acetylene and Ethylene Molecules with 1-Butyl-3-Methylimidazolium Acetate Ionic Liquid: A Combined Quantum Chemistry Calculation and Molecular Dynamics Simulation Study*, Acs Applied Materials & Interfaces, 4 (2012) 6646-6653, D.O.I.: 10.1021/am301796w

[14] S. Rivera-Rubero, S. Baldelli, *Influence of Water on the Surface of Hydrophilic and Hydrophobic Room-Temperature Ionic Liquids*, Journal of the American Chemical Society, 126 (2004) 11788-11789, D.O.I.: 10.1021/ja0464894

[15] L.E. Ficke, J.F. Brennecke, *Interactions of Ionic Liquids and Water*, Journal of Physical Chemistry B, 114 (2010) 10496-10501, D.O.I.: 10.1021/jp1012736

[16] C. Ridings, V. Lockett, G. Andersson, *Significant Changes of the Charge Distribution at the Surface of an Ionic Liquid Due to the Presence of Small Amounts of Water*, Physical Chemistry Chemical Physics, 13 (2011) 21301-21307, D.O.I.: 10.1039/c1cp22551k

[17] M. Mezger, S. Schramm, H. Schröder, H. Reichert, M. Deutsch, E.J. De Souza, J.S. Okasinski, B.M. Ocko, V. Honkimäki, H. Dosch, *Layering of [BMIM]+-Based Ionic Liquids at a Charged Sapphire Interface*, Journal of Chemical Physics, 131 (2009) 094701, D.O.I.: 10.1063/1.3212613

[18] M.P. Seah, *An Accurate and Simple Universal Curve for the Energy-Dependent Electron Inelastic Mean Free Path*, Surface and Interface Analysis, 44 (2012) 497-503, D.O.I.: 10.1002/sia.4816

[19] M. Wagstaffe, M.J. Jackman, K.L. Syres, A. Generalov, A.G. Thomas, *Ionic Liquid Ordering at an Oxide Surface*, Chemphyschem, 17 (2016) 3430-3434, D.O.I.: 10.1002/cphc.201600774

[20] M.B. Hugenschmidt, L. Gamble, C.T. Campbell, *The Interaction of H2O with a TiO2(110) Surface*, Surface Science, 302 (1994) 329-340, D.O.I.: 10.1016/0039-6028(94)90837-0

[21] A.C. Papageorgiou, G. Cabailh, Q. Chen, A. Resta, E. Lundgren, J.N. Andersen, G. Thornton, *Growth and Reactivity of Titanium Oxide Ultrathin Films on Ni(110)*, Journal of Physical Chemistry C, 111 (2007) 7704-7710, D.O.I.: 10.1021/jp067802m

[22] K.L. Syres, A.G. Thomas, W.R. Flavell, B.F. Spencer, F. Bondino, M. Malvestuto, A. Preobrajenski, M. Grätzel, *Adsorbate-Induced Modification of Surface Electronic Structure: Pyrocatechol Adsorption on the Anatase TiO2 (101) and Rutile TiO2 (110) Surfaces*, Journal of Physical Chemistry C, 116 (2012) 23515-23525, D.O.I.: 10.1021/jp308614k

[23] L.-Q. Wang, D.R. Baer, M.H. Engelhard, A.N. Shultz, *The Adsorption of Liquid and Vapor Water on TiO2(110) Surfaces: The Role of Defects*, Surface Science, 344 (1995) 237-250, D.O.I.: 10.1016/0039-6028(95)00859-4

[24] S. Yamamoto, H. Bluhm, K. Andersson, G. Ketteler, H. Ogasawara, M. Salmeron, A. Nilsson, *In Situ X-Ray Photoelectron Spectroscopy Studies of Water on Metals and Oxides at Ambient Conditions*, Journal of Physics-Condensed Matter, 20 (2008) 184025, D.O.I.: 10.1088/0953-8984/20/18/184025

[25] G. Ketteler, S. Yamamoto, H. Bluhm, K. Andersson, D.E. Starr, D.F. Ogletree, H. Ogasawara, A. Nilsson, M. Salmeron, *The Nature of Water Nucleation Sites on TiO2 (110) Surfaces Revealed by Ambient Pressure X-Ray Photoelectron Spectroscopy*, Journal of Physical Chemistry C, 111 (2007) 8278-8282, D.O.I.: 10.1021/jp068606i

[26] L. Walle, A. Borg, P. Uvdal, A. Sandell, *Probing the Influence from Residual Ti Interstitials on Water Adsorption on TiO2 (110)*, Physical Review B, 86 (2012) 205415, D.O.I.: 10.1103/PhysRevB.86.205415

[27] K. Lovelock, C. Kolbeck, T. Cremer, N. Paape, P. Schulz, P. Wasserscheid, F. Maier, H.-P. Steinruck, *Influence of Different Substituents on the Surface Composition of Ionic Liquids Studied Using ARXPS*, The Journal of Physical Chemistry B, 113 (2009) 2854-2864, D.O.I.: 10.1021/jp810637d

[28] I.J. Villar-Garcia, E.F. Smith, A.W. Taylor, F.L. Qiu, K.R.J. Lovelock, R.G. Jones, P. Licence, *Charging of Ionic Liquid Surfaces under X-Ray Irradiation: The Measurement of Absolute Binding Energies by XPS*, Physical Chemistry Chemical Physics, 13 (2011) 2797-2808, D.O.I.: 10.1039/C0cp01587c

[29] M. Sobota, I. Nikiforidis, W. Hieringer, N. Paape, M. Happel, H.P. Steinruck, A. Gorling, P. Wasserscheid, M. Laurin, J. Libuda, *Toward Ionic-Liquid-Based Model Catalysis: Growth, Orientation, Conformation, and Interaction Mechanism of the [Tf2N](-) Anion in [BMIM][Tf2N] Thin Films on a Well-Ordered Alumina Surface*, Langmuir, 26 (2010) 7199-7207, D.O.I.: 10.1021/la904319h

[30] E.F. Smith, F.J. Rutten, I.J. Villar-Garcia, D. Briggs, P. Licence, *Ionic Liquids in Vacuo: Analysis of Liquid Surfaces Using Ultra-High-Vacuum Techniques*, Langmuir, 22 (2006) 9386-9392, D.O.I.: 10.1021/la061248q

[31] H. Hashimoto, A. Ohno, K. Nakajima, M. Suzuki, H. Tsuji, K. Kimura, *Surface Characterization of Imidazolium Ionic Liquids by High-Resolution Rutherford Backscattering Spectroscopy and X-Ray Photoelectron Spectroscopy*, Surface Science, 604 (2010) 464-469, D.O.I.: 10.1016/j.susc.2009.12.023

[32] K.R.J. Lovelock, E.F. Smith, A. Deyko, I.J. Villar-Garcia, P. Licence, R.G. Jones, *Water Adsorption on a Liquid Surface*, Chemical Communications, (2007) 4866-4868, D.O.I.: 10.1039/B711680B

[33] A. Deyko, T. Cremer, F. Rietzler, S. Perkin, L. Crowhurst, T. Welton, H.-P. Steinrück, F. Maier, *Interfacial Behavior of Thin Ionic Liquid Films on Mica*, Journal of Physical Chemistry C, 117 (2013) 5101-5111, D.O.I.: 10.1021/jp3115397

[34] A. Deyko, R.G. Jones, *Adsorption, Absorption and Desorption of Gases at Liquid Surfaces: Water on [C 8 C 1 Im][BF 4] and [C 2 C 1 Im][Tf 2 N]*, Faraday Discussions, 154 (2012) 265-288, D.O.I.: 10.1039/C1FD00062D

[35] A. Broderick, Y. Khalifa, M.B. Shiflett, J.T. Newberg, *Water at the Ionic Liquid–Gas Interface Examined by Ambient Pressure X-Ray Photoelectron Spectroscopy*, Journal of Physical Chemistry C, 121 (2017) 7337-7343, D.O.I.: 10.1021/acs.jpcc.7b00775

[36] L. Cammarata, S.G. Kazarian, P.A. Salter, T. Welton, *Molecular States of Water in Room Temperature Ionic Liquids*, Physical Chemistry Chemical Physics, 3 (2001) 5192-5200, D.O.I.: 10.1039/b106900d

[37] S. Rivera-Rubero, S. Baldelli, *Influence of Water on the Surface of the Water-Miscible Ionic Liquid 1-Butyl-3-Methylimidazolium Tetrafluoroborate: A Sum Frequency Generation Analysis*, Journal of Physical Chemistry B, 110 (2006) 15499-15505, D.O.I.: 10.1021/jp062694p

[38] J. Carrete, T. Mendez-Morales, O. Cabeza, R.M. Lynden-Bell, L.J. Gallego, L.M. Varela, *Investigation of the Local Structure of Mixtures of an Ionic Liquid with Polar Molecular Species through Molecular Dynamics: Cluster Formation and Angular Distributions*, Journal of Physical Chemistry B, 116 (2012) 5941-5950, D.O.I.: 10.1021/jp301309s

[39] J. Gao, N.J. Wagner, *Water Nanocluster Formation in the Ionic Liquid 1-Butyl-3-Methylimidazolium Tetrafluoroborate ([C4mim][BF4])–D2O Mixtures*, Langmuir, 32 (2016) 5078-5084, D.O.I.: 10.1021/acs.langmuir.6b00494

[40] S. Feng, G.A. Voth, *Molecular Dynamics Simulations of Imidazolium-Based Ionic Liquid/Water Mixtures: Alkyl Side Chain Length and Anion Effects*, Fluid Phase Equilibria, 294 (2010) 148-156, D.O.I.: 10.1016/j.fluid.2010.02.034

[41] T. Méndez-Morales, J. Carrete, O. Cabeza, L.J. Gallego, L.M. Varela, *Molecular Dynamics Simulation of the Structure and Dynamics of Water–1-Alkyl-3-Methylimidazolium Ionic Liquid Mixtures*, Journal of Physical Chemistry B, 115 (2011) 6995-7008, D.O.I.: 10.1021/jp202692g

[42] M. Buckley, K.L. Syres, R.G. Jones, *Interactions and Stabilisation of Acetone, Sulfur Dioxide and Water with 1-Octyl-3-Methylimidazolium Tetrafluoroborate at Low Temperatures*, Faraday Discussions, 206 (2017) 475-495, D.O.I.: 10.1039/C7FD00146K

4 Reversible CO$_2$ Reaction with a Superbasic Ionic Liquid

Ionic liquids (ILs) have emerged in recent years as potential CO$_2$ capture agents, since they display good CO$_2$ capacity, and are known for their capabilities in gas selectivity. Functionalisation of ILs can be useful for a number of applications, including CO$_2$ capture and uptake, but can sometimes lead to complications. In the case of amine-functionalised ILs, they display improved CO$_2$ capacity over ILs, but struggle with physicochemical changes, in particular their viscosity, which ultimately hinder their ability to uptake CO$_2$.

Within the last five years, superbasic ILs have presented superior CO$_2$ uptake, with negligible changes in viscosity. However, superbasic ILs have shown a decreased capacity in the presence of water, which is problematic when real-life applications in CO$_2$ capture involve mixed gases that contain water vapour.

Recent developments allow the surface-sensitive technique, X-ray photoelectron spectroscopy, to be used under near-ambient pressure conditions, allowing for further investigation into the interactions between ILs and gases. Presented in this Chapter is a near-ambient pressure X-ray photoelectron spectroscopy investigation into the interactions between a superbasic IL and various gases: CO$_2$, water vapour, and mixtures of both.

4.1 Introduction

International commitments to a reduction in global CO$_2$ emissions could be in part met by CO$_2$ sequestration and storage, or utilisation [1-3]. As a result, there is a pressing desire to identify stable, practical and economically viable methods to achieve this. Currently, the most widely used industrial solution is monoethanolamine (MEA) [4, 5]. When MEA reacts with CO$_2$, it forms a carbamate species (COO$^-$) and a protonated MEA species (see Scheme 4.1). MEA is relatively cheap as a bulk solvent, but is extremely corrosive and requires a relatively large amount of energy to regenerate it following CO$_2$

capture [6]. Both of these factors contribute to increased costs where CO_2 is required to be removed.

Ionic liquids (ILs) have been widely investigated as potential CO_2 capture agents due to their advantageous properties, including ultra-low vapour pressures and excellent thermal stability. They are relatively easy to handle, and the regeneration of ILs after CO_2 capture is a relatively low energy process [6, 7]. ILs can capture CO_2 via chemisorption or physisorption, and in previous years, attempts to improve the CO_2 capture capabilities of ILs have been successful with the addition of amine functional groups [8]. These react with CO_2 in much the same way as MEA (see Scheme 4.1). However, a problematic repercussion of CO_2 absorption in amine-functionalised ILs is an increase in their viscosity, which tends to inhibit further CO_2 absorption.

Scheme 4.1: Reaction between amine and CO_2 to form carbamate (R-NHCOO$^-$) and an ammonium (R-NH3$^+$) species. In the case of MEA, the group R represents ethanol (CH_2CH_2OH), and in the case of amine-functionalised ILs, the group R can represent either a cationic or an anionic substituent.

Current research also suggests that the presence of water in the gas stream can assist or hinder the ability of an IL to capture CO_2, depending on the constituent IL ions and the concentration of water. While the addition of water in amine-functionalised ILs reduces their viscosity, it also results in a decrease in CO_2 uptake [9]. The decrease in CO_2 uptake is attributed to protonation of the pyridine-like N group, which reduces the number of available sites for CO_2 to chemically bind [9]. The addition of small amounts of water has shown to improve the CO_2 capture capabilities of some ILs. Phenolate-based ILs, for example, capture CO_2 through chemisorption, and the addition of 2 wt% H_2O almost doubled the molar CO_2 absorption [10]. For acetate-based ILs, which capture CO_2 through physisorption, the molar absorption increased eightfold with the addition of 0.35 mole fraction of H_2O [11].

In recent years, superbasic ILs have attracted particular interest. These ILs consist of an imidazolide anion (a deprotonated and negatively charged aromatic ion). Reaction with CO_2 leads to the exothermic formation of

carbamate at one or more of the deprotonated amine sites [6, 12]. Studies of superbasic ILs by various groups have shown an excellent capacity for CO_2 capture, with molar ratios (n_x) of up to 1.6:1 (n_{CO2}:n_{IL}) [6]. In addition, these superbasic ILs do not undergo a large increase in viscosity upon CO_2 saturation, which makes them potentially useful in large-scale applications. An experimental and theoretical study of superbasic ILs showed that the IL, trihexyl-tetradecylphosphonium benzimidazolide ([P_{66614}][benzim] - see Figure 4.1), was able to absorb equimolar quantities of CO_2 in the dry state, but exhibited a reduced capacity for CO_2 absorption if the IL was pre-wetted [6, 12]. This could be problematic if they are to be considered for CO_2 capture on an industrial scale, since industrial flue gases consist of a complex mixture of gas molecules, including CO_2 and H_2O.
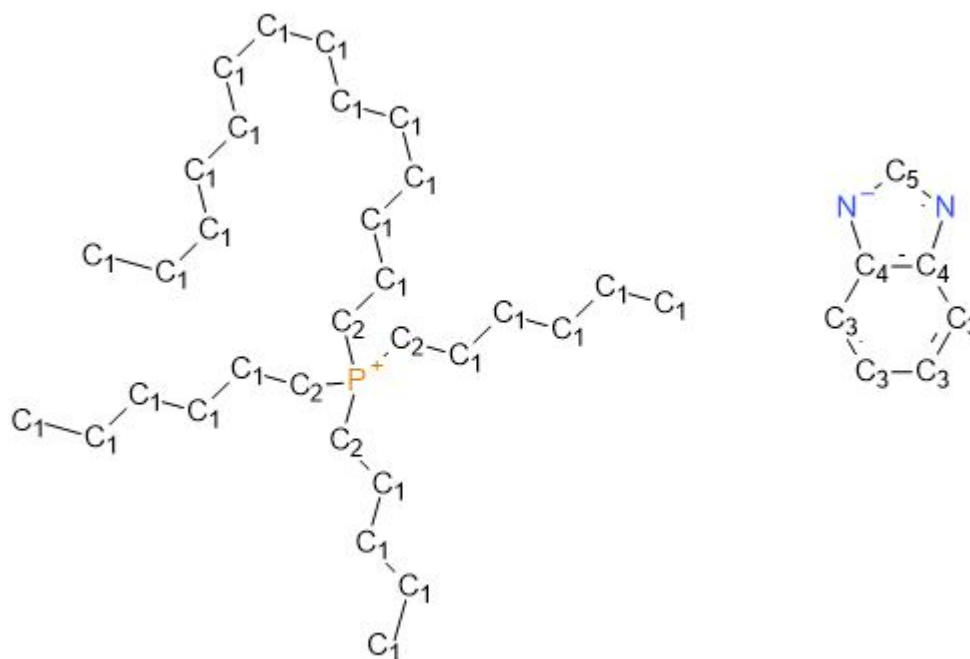
Figure 4.1: Chemical structure diagram of the superbasic IL, trihexyl-tetradecylphosphonium benzimidazolide, or [P_{66614}][benzim]. The labels C_1 to C_5 highlight the different carbon environments in the IL pair.

X-ray photoelectron spectroscopy (XPS) has been a useful tool in the analysis of surface reactions, and surface electronic structure of solids for many years [13, 14]. The extremely low vapour pressure of ILs has also meant that in recent years studies of liquid surfaces have been possible [15-18]. Interactions between gases and ILs have been studied using XPS, but at low temperatures. The gas and the IL need to be cooled together (which forms a glassy structure),

then gently heated to monitor gas desorption from the IL [19]. This process is necessary because, at the extremely low pressures required for XPS, gases often do not remain trapped or ad/absorbed in any appreciable amount at ambient temperatures. Rivera-Rubero and Baldelli, for example, showed that water can be removed from the IL 1-butyl-3-methylimidazolium tetrafluoroborate ($[C_4C_1Im][BF_4]$) at pressures of $<1\times10^{-5}$ mbar at room temperature [20]. The recent availability of near-ambient pressure XPS (NAPXPS) has opened up the possibility of measurements of liquid surfaces in gas pressures of up to a few tens of mbar [4, 8, 21-23]. Presented in this Chapter is a NAPXPS investigation into the reaction of the superbasic IL, $[P_{66614}][benzim]$, with CO_2, H_2O and two mixed CO_2/H_2O vapour regimes using NAPXPS.

4.2 Experimental section

The IL, $[P_{66614}][benzim]$ was prepared using a two-step synthesis described in previous work by Taylor et al [6], which is outlined in Appendix B of this thesis. The IL was dried under vacuum (0.01 mbar at 50°C) and then transferred to a vial sealed with a rubber septum in a dry argon-filled glovebox prior to use. Around 0.5 ml of IL was deposited dropwise by syringe onto a Ta sample plate in ambient laboratory conditions. The plate was transferred to a vacuum load lock and the load lock pumped down and left to reach $<1\times10^{-6}$ mbar before transferring to the near-ambient pressure (NAP) cell for analysis. During the preparation process, the sample was exposed to ambient lab atmosphere for around 5 minutes.

XPS analysis was carried out using the SPECS NAPXPS system at the University of Manchester (see Chapter 2.10.1 for equipment details). CO_2 (CK Gases, purity 99.9995%) was further purified by passing it through a scrubber (SAES Microtorr) to remove trace impurities, particularly of CO. Doubly distilled water was purified by repeated freeze-thaw-pump cycles until no gas bubbles were observed in the water under a vacuum of 1×10^{-6} mbar. Spectra were recorded with electron emission normal to the surface from the top edge of the IL film to minimise the possibility of sample charging. Normal emission and grazing emission XPS measurements were carried out in ultra-high vacuum (UHV) conditions (at a pressure of approximately 10^{-9} mbar) before being transferred to the NAP cell.
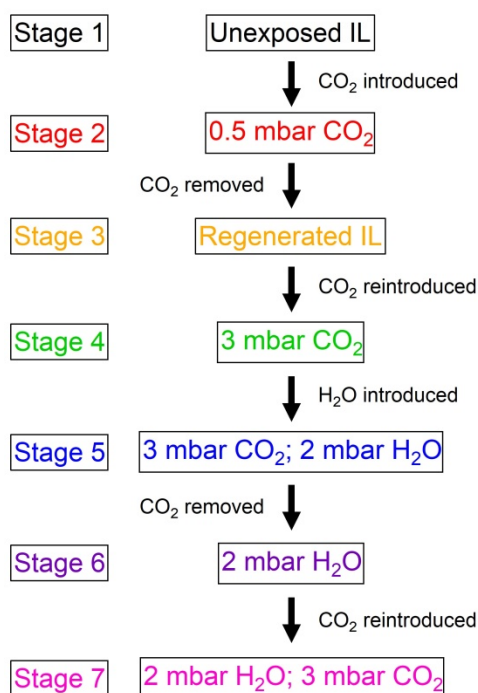
Scheme 4.2: Flow chart illustrating the stages of the experiment in the NAP cell, numbered 1 to 7. The annotations between the stages describe which gases are introduced or removed. Measurements were taken at each stage.

NAPXPS measurements were carried out over seven stages in the NAP cell, as outlined in Scheme 4.2. During Stage 1, measurements were recorded from the as-presented IL. In Stage 2, the IL was exposed to 0.5 mbar of CO_2. For Stage 3, the CO_2 was pumped out of the NAP cell and measurements were taken when the pressure had stabilised at approximately 10^{-8} mbar, i.e. the IL was under high-vacuum conditions once again. Measurements taken at Stages 1 through 3 were to determine whether or not the CO_2 capture by the IL was reversible through pressure reduction. In measurements taken after Stage 3, the IL is referred to as 'regenerated'. Stage 4 involved exposing the regenerated IL to 3 mbar of CO_2. In stage 5, 2 mbar H_2O vapour was introduced into the NAP cell, creating the first mixed-gas regime. During Stage 6, the CO_2 flow was turned off, leaving the IL exposed only to 2 mbar of H_2O vapour and measurements were taken when the pressure in the NAP cell had stabilised at 2 mbar. For the final stage, Stage 7, 3 mbar of CO_2 was reintroduced into the system giving a total CO_2 and water pressure of 5 mbar for the second mixed-gas regime.

Each NAPXPS spectrum was recorded from a different position on the sample surface to avoid damage due to prolonged X-ray exposure. Each measurement took approximately one hour, and all measurements were taken at room

temperature. Spectra are aligned on the binding energy (BE) scale relative to the alkyl C 1s signal at 285.0 eV [24], with all BEs quoted to ± 0.1 eV. XPS core level peak fitting was carried out using CasaXPS software with a linear background and 70:30 Gaussian:Lorentzian lineshapes [25].

4.3 Results and discussion

4.3.1 XPS of [P$_{66614}$][benzim] under UHV
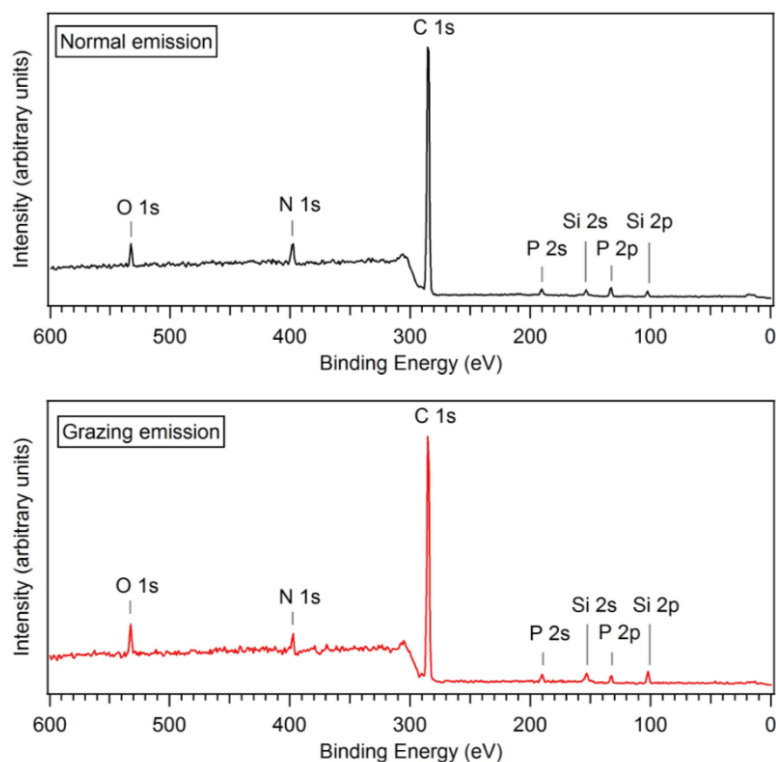
Figure 4.2: Survey spectra taken of the IL at normal emission (top, represented by a black line) and at a grazing emission angle of 60° (bottom, represented by a red line).

The XPS spectra for the IL, trihexyltetradecyl-phosphonium benzimidazolide ([P$_{66614}$][benzim]) in ultra-high vacuum (UHV) conditions (pressure approximately 10^{-9} mbar) are shown in Figure 4.2, at normal emission (NE, represented by a black line) and grazing emission (GE, at 60°, represented by a red line). All measurements were taken on the same part of the IL. The survey spectra are annotated with labels of the regions associated with the IL (C 1s, N 1s, and P 2p), as well as the O 1s region. Ta from the sample plate is not visible, indicating the IL layer is thicker than the sampling depth of XPS (> 100 Å). Also annotated are the Si 2s and Si 2p peaks. These are thought to be due to Si-based contamination from synthesis [26].
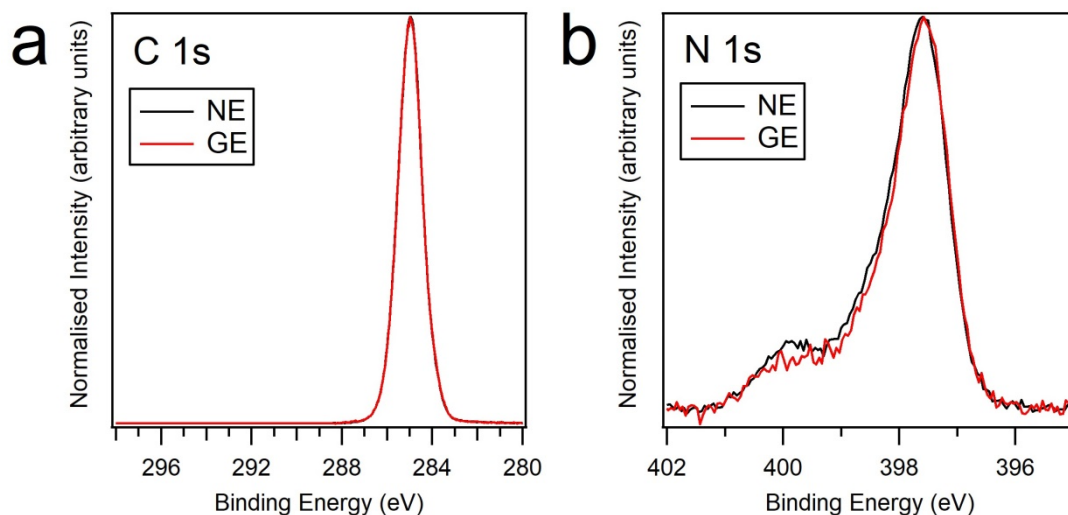
Figure 4.3: C 1s region (a) and N 1s region (b) recorded of the IL in UHV. The normal emission spectra (represented by black lines) and grazing emission spectra (represented by red lines) for each region are plotted on the same axes. Each spectrum is normalised to the height of the largest peak in the region.

Figure 4.3 shows the C 1s and N 1s, regions taken of the IL in UHV. The C 1s region (Figure 4.3a) does not significantly change shape at GE compared to NE. However, the N 1s appears to have a slightly different shape at GE. The N 1s region (Figure 4.3b) appears to have a more prominent feature at the higher BE edge at NE than at GE, which suggests the species responsible is present in the bulk of the IL rather than at the surface. The origin of these peaks is explored in more depth later in the discussion.
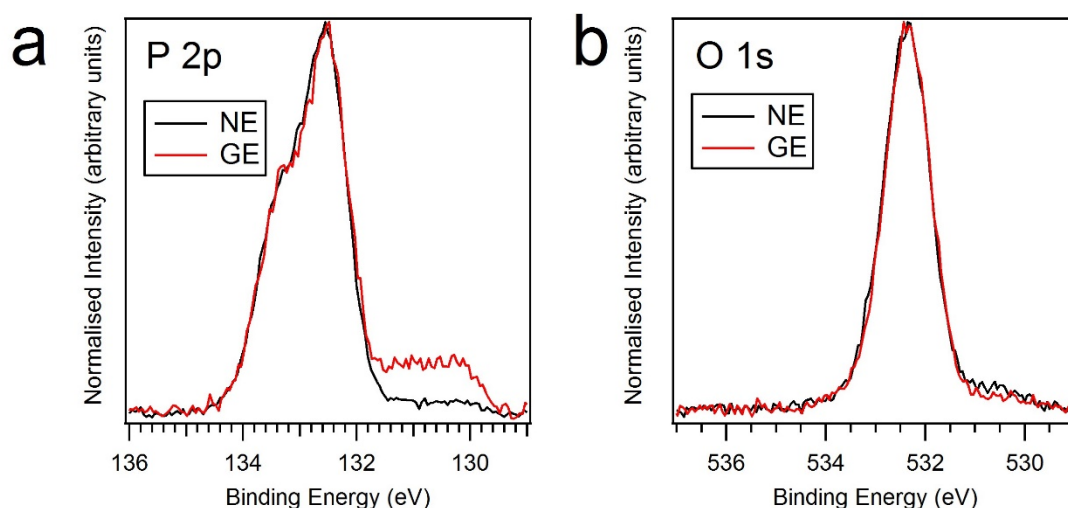
Figure 4.4: P 2p region (a) and O 1s region (b) recorded of the IL in UHV. The normal emission spectra (represented by black lines) and grazing emission spectra (represented by red lines) for each region are plotted on the same axes. Each spectrum is normalised to the height of the largest peak in the region.

Figure 4.4 displays the P 2p and O 1s regions recorded from [P$_{66614}$][benzim] under UHV conditions. The P 2p region (Figure 4.4a) demonstrates the most striking change at GE compared to NE. The main features at 132.5 eV and 133.4 eV are attributed to the P 2p$_{3/2}$ and P 2p$_{1/2}$ of the P 2p doublet originating from the [P$_{66614}$]$^+$ cation. There appears to be a shoulder at the lower BE edge of the region that is much more prevalent at GE than at NE. This is indicative of a P species located nearer to the surface of the IL. The exact nature of the species is not known, but it is speculated that it may be the result of X-ray beam damage. The UHV measurements were taken at the same position on the IL and were not rastered. In the O 1s region (Figure 4.4b), there appears to be one dominating signal at 532.4 eV. This feature is likely to be due, predominantly, to silicon grease. In the survey spectra, the O 1s feature is slightly more intense at GE than at NE, when compared to the N 1s peak in both cases. This is also the case for the Si 2s and Si 2p peaks. These observations corroborate the assignment of Si grease contamination, which is typically found at the surface of the IL rather than in the bulk [26]. While Si contamination at the surface of the IL may affect the rate of gas sorption, it is unlikely to influence the chemical reactions that take place in the IL. Its presence, however, overlaps significantly with peaks associated with hydroxyl groups and with water molecules adsorbed on ILs (see Chapters 3.3 and 3.4 for those BE assignments) and makes a definitive deconvolution of the region impossible.

4.3.2 NAPXPS: Stages 1 to 3
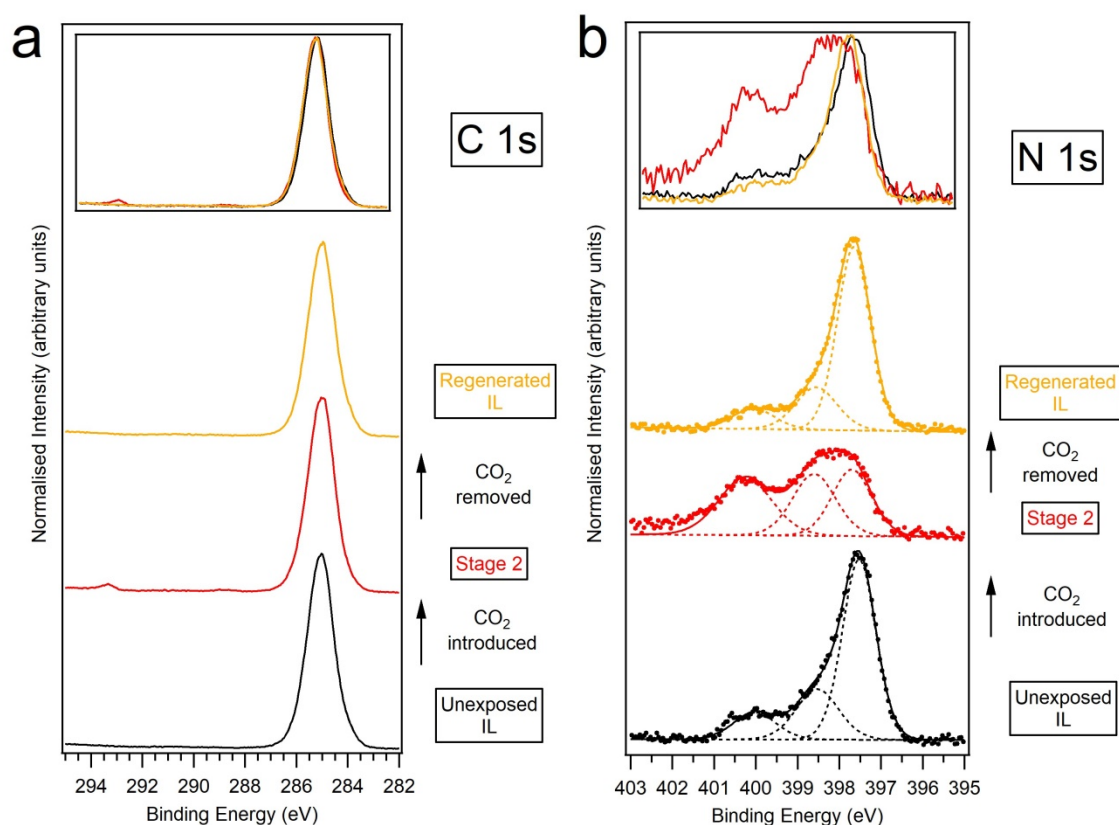
Figure 4.5: The C 1s region (a), and N 1s region (b) of the unexposed IL (Stage 1, black line), of the IL during exposure to 0.5 mbar of CO_2 (Stage 2, red line), and of the regenerated IL (Stage 3, amber line). Each N 1s spectrum has been normalised to the total area, and each C 1s spectrum has been normalised to the height of the IL carbon peak. The intensity of the spectra in the inset figures have been normalised to the most intense peak.

The C 1s and N 1s photoelectron spectra recorded from the IL during Stages 1 through 3 are shown in Figure 4.5, represented by the black, red and amber lines, respectively. In each region, the spectrum post-exposure is almost identical to the spectrum of the unexposed IL (see inset of Figure 4.5a and Figure 4.5b). This demonstrates that any interaction between the IL and CO_2 is reversible when the pressure in the NAP cell is reduced. Furthermore, these data suggest that the IL can be largely regenerated through a reduction in pressure. The C 1s shows very little discernible change upon exposure to 0.5 mbar CO_2 and following regeneration by evacuation of the gas cell (see inset of Figure 4.5a). The N 1s, however, shows more significant changes in the presence of the gas with a broadening of the peak near 397.5 eV and the growth of a second feature at around 400 eV. The peak at 397.5 eV, which dominates the spectrum recorded from the unexposed film, is attributed to the nitrogen atoms of the [benzim]⁻ anion. Due to resonance effects the two N

atoms in the [benzim]⁻ anion can be considered chemically equivalent [16, 17]. The small feature at around 400 eV has been attributed to the presence of protonated benzimidazole. The growth of this peak and the associated broadening of the lower binding energy feature on exposure to CO_2, coupled with the loss of these features on removal of CO_2, indicate these features are associated with the interaction with CO_2. In order to investigate the origin of these features the regenerated IL was exposed to CO_2 and H_2O in stages as described in Scheme 4.2.

4.3.3 NAPXPS: Stages 3 to 7
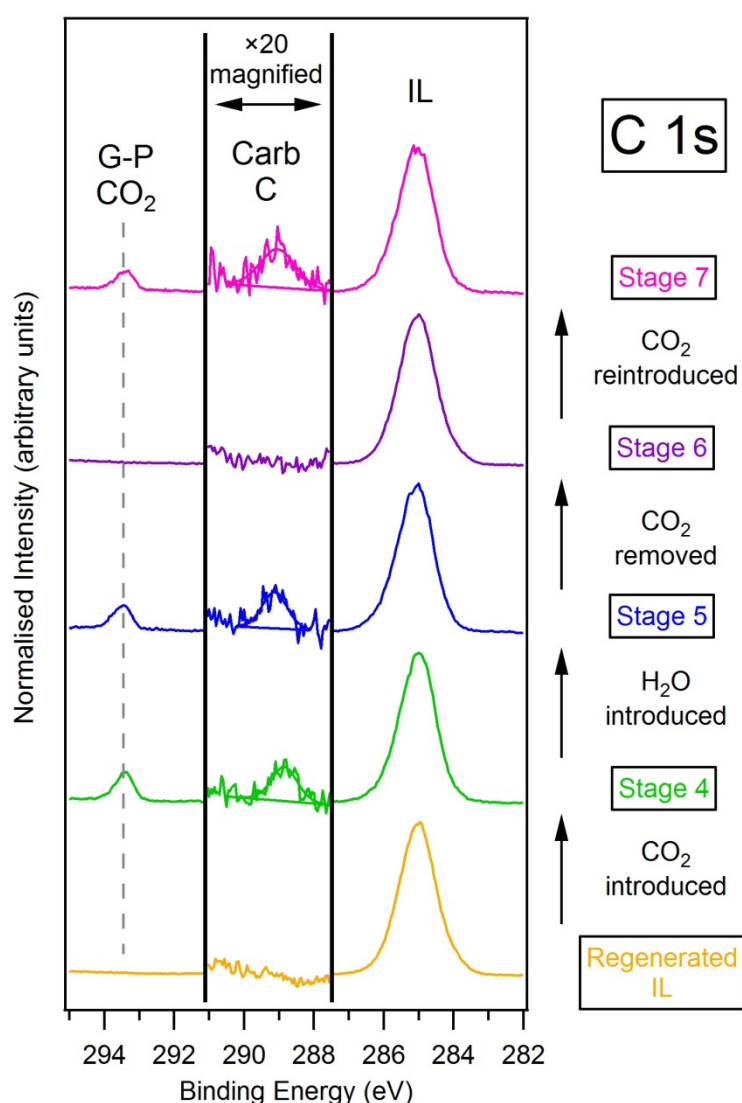
Figure 4.6: C 1s spectrum taken of the regenerated IL (Stage 3, amber line), of the IL during exposure to 3 mbar CO_2 (Stage 4, green line), during exposure to the first mixed-gas regime (Stage 5, blue line), during exposure to 2 mbar H_2O (Stage 6, violet line), and during exposure to the second mixed-gas regime (Stage 7, magenta line). The data between 291.0 eV and 287.5 eV is ×20 magnified. The term gas-phase is abbreviated to 'G-P', and carbamate is shortened to 'Carb'. Each spectrum has been normalised to the IL C peak at 285.0 eV.

Figure 4.6 shows the C 1s spectra recorded through Stages 3 to 7. All of the C 1s spectra feature a strong, slightly asymmetric signal at 285.0 eV. This signal is attributed to the carbon atoms in $[P_{66614}][benzim]$. Blundell and Licence [24] studied other ILs with the same cation using XPS. They resolved the asymmetrical peak associated with the $[P_{66614}]^+$ cation into two components: one attributed to the hetero (C-P) carbon, and one attributed to the alkyl (C-C) carbon (the hetero carbons and alkyl carbons are labelled as C_4 and C_5 respectively in Figure 4.1). The C 1s signal in this work will consist of contributions from these carbon environments, in addition to contributions from the aromatic carbon species of the anion (labelled C_1 to C_3 in Figure 4.1). However, none of the contributions from either the cation or the anion have been fitted here, since fitting any components to this peak would be speculative at best given the broad nature of the peak. Upon exposure to 3 mbar CO_2 (Stage 4, represented by the green line), two more signals appear in the region. The peak at a BE of 293.4 eV is attributed to gas phase CO_2 and the peak observed at a BE of approximately 289.0 eV is attributed to carbamate formation [27]. These peaks do not change significantly in shape upon exposure to water during the first mixed-gas regime (Stage 5, represented by the blue line), but there is a slight upward shift in BE for the carbamate peak from 288.8 eV to 289.1 eV. In numerous studies, the BE of peaks associated with ad/absorbed gas species tend to shift with increased coverage (in the case of adsorbates), or increased gas pressure [28-31]. Since the IL was subject to further CO_2 exposure during Stage 5, it is, therefore, likely that this shift is due to an increase in carbamate groups in the IL. During Stage 6 (2 mbar H_2O vapour only, represented by the violet line), the signal attributed to absorbed CO_2 is no longer present, indicating desorption of CO_2 from the IL. When 3 mbar of CO_2 is then reintroduced into the NAP cell (Stage 7, represented by the magenta line) the peak at ~289.0 eV returns with a similar intensity to that seen in Stage 5. The peak assignments are summarised in Table 4.1.

Table 4.1: Assignments and binding energies of all peaks in the C 1s and N 1s regions throughout the experiment.

Region	Binding Energy (eV) (±0.1 eV)	Assignment
C 1s	285.0	IL C
	289.0	Carbamate C
	293.4	Gas-phase CO_2
N 1s	397.5	Imidazolide N (N_{Im})
	298.5	Unreacted N (N_U)
	400.0	Reacted N (N_R)
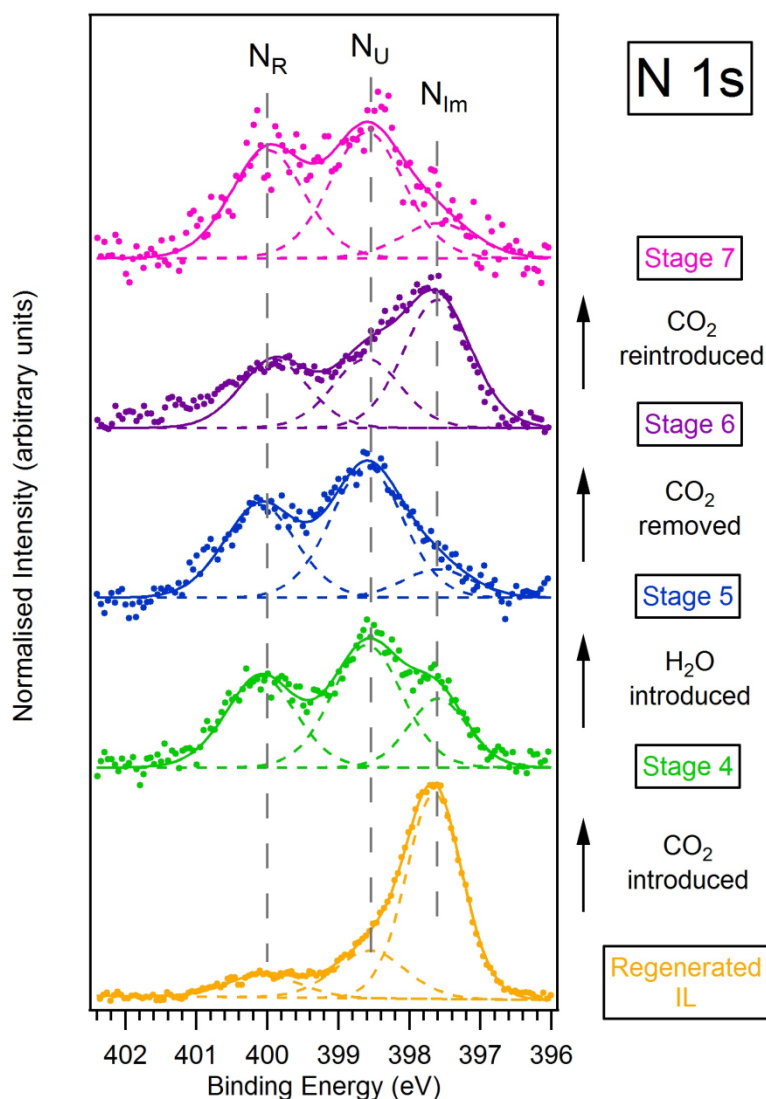
Figure 4.7: N 1s spectrum taken of the regenerated IL (Stage 3, amber line), of the IL during exposure to 3 mbar CO_2 (Stage 4, green line), during exposure to the first mixed-gas regime (Stage 5, blue line), during exposure to 2 mbar H_2O (Stage 6, violet line), and during exposure to the second mixed-gas regime (Stage 7, magenta line). The label N_{Im} refers to the imidazolide N. The labels N_U and N_R refer to the unreacted and reacted N respectively. Each spectrum has been normalised to the total area of the region.

Figure 4.7 shows the N 1s spectrum through Stages 3 to 7 of the experiment. The spectrum of the regenerated IL (amber line) can be fitted with three peaks at binding energies of 397.5 eV, 398.5 eV and 400.0 eV. The peak at 397.5 eV is assigned to the imidazolide N atoms, as described above. The two peaks at higher BE are seen to increase in intensity when the IL is exposed to 3 mbar of CO_2 in Stage 4 (green line). They are, therefore, attributed to the reaction between the IL and CO_2. The peak at 400 eV is attributed to the formation of carbamate, and has been labelled N_R, to mean 'reacted' N. Once a [benzim]$^-$ anion has reacted with CO_2, the N atoms in the anion can no longer be considered as chemically equivalent. The reaction of the imidazolide ion with CO_2 will also mean the two N atoms in the anion will have a different charge density and therefore a different BE. As a result, the signal at 398.5 eV is attributed to a BE shift in this 'unreacted' N atom in the [benzim]$^-$ anion that has reacted with CO_2 (labelled N_U in Figure 4.7).

When 2 mbar of H_2O is introduced to create the first mixed-gas regime (Stage 5, blue line), the N_U and N_R peaks continue to increase in intensity. This is likely to be due to continued reaction with CO_2, reaction between the IL and H_2O, or a combination of both. Imidazolide-based anions react with water to form an imidazole (protonated imidazolide) and a hydroxide anion ([OH]$^-$) [32] (see Scheme 4.3). This reaction is seen in ^{1}H NMR spectra of [P$_{66614}$][benzim]/H_2O mixtures, manifesting as a downward chemical shift [6]. Morales-Gil et al [33] reported, for mercaptobenzimidazole, a BE difference of 1.6 eV between pyridine-like (N) and the pyrrole-like (NH) nitrogen atoms. This BE difference is consistent with the BE difference between our N_U and N_R peaks. In addition, Tenney et al [4] showed only a small shift of 0.3 eV BE between the carbamate N and protonated N in an XPS study of 3-amino-1-propanol and CO_2. Therefore, on exposure to water we attribute the additional intensity of the N_U and N_R peaks to unreacted (non-protonated) N and reacted (protonated) N, respectively, as a result of the reaction between the IL and H_2O. To clarify, the N_R peak is attributed to a combination of N-COO$^-$ and NH signals, and the N_U peak is attributed to the unreacted N atom in the ring of a 'reacted' anion.
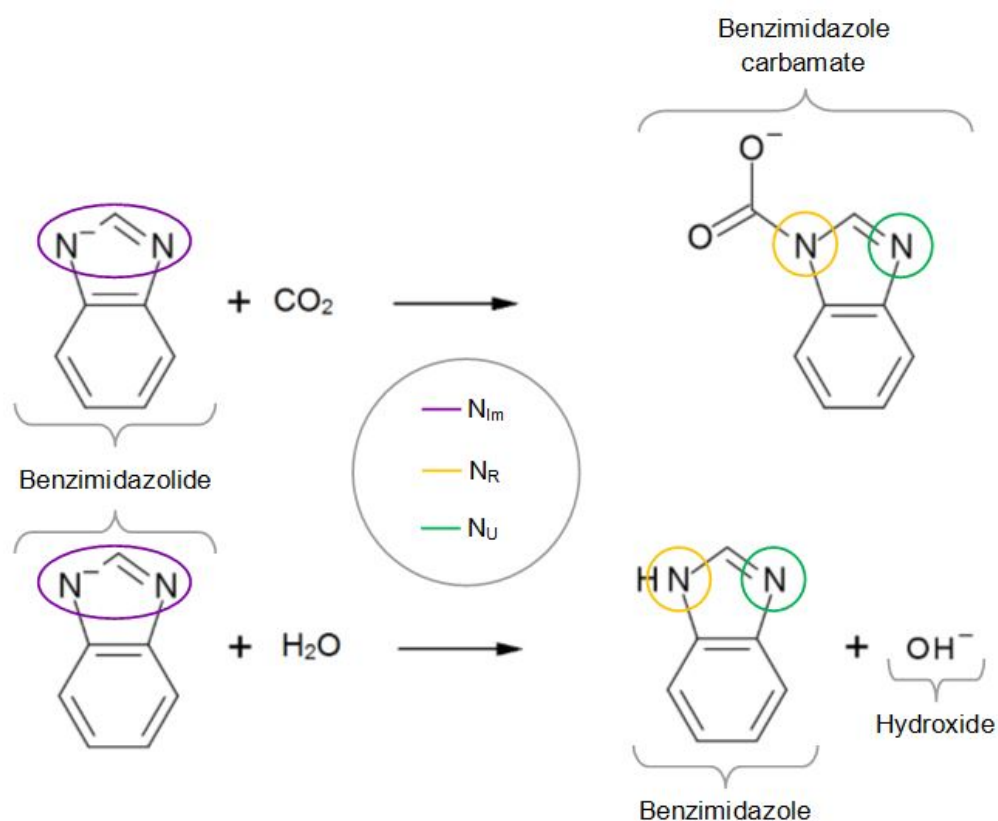
Scheme 4.3: Proposed reaction between a benzimidazolide ([benzim]$^-$) anion and CO_2 (top), generating a carbamate group bound to the previously negatively-charged N, forming benzimidazole carbamate. The proposed reaction between a benzimidazolide anion and H_2O is shown (bottom), where the anion is protonated (forming imidazole) and generates a hydroxide anion. The violet circles highlight the imidazolide N (labelled N_{Im}), the amber circles highlight the reacted N of both the carbamate and imidazole (labelled N_R), and the green circles highlight the unreacted N of both reactions (labelled N_U).

When the IL is exposed to only 2 mbar H_2O (Stage 6), the N_U and N_R peaks both decrease in intensity. This further supports the theory that the IL can be regenerated through a reduction in surrounding CO_2 partial pressure. The intensities of these peaks, however, do not completely return to the same values as those from the regenerated IL, confirming that there is an interaction between the IL and H_2O vapour. Since the N_U and N_R peaks are much less intense when only exposed to H_2O, this seems to indicate a preferential reaction with CO_2 over H_2O. During the second mixed-gas regime (Stage 7), when the IL is exposed to 2 mbar H_2O and 3 mbar CO_2 once again, the N_U and N_R peaks increase in intensity, with similar peak area ratios as those in Stage 5. From the assignments above one would expect that the N_R and N_U peaks should have a roughly equal intensity.
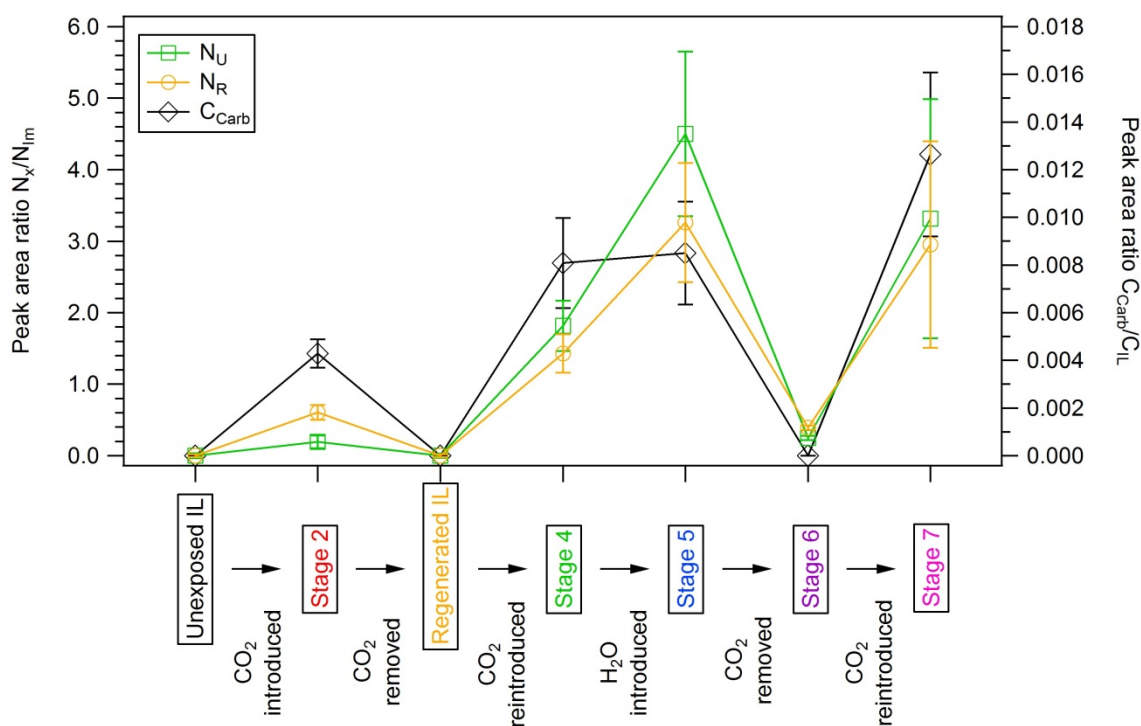
Figure 4.8: Displayed on the left axis: peak area ratios of N_U/N_{Im} (green squares) and N_R/N_{Im} (amber circles), where N_U refers to unreacted nitrogen, N_R refers to reacted nitrogen, and N_{Im} refers to imidazolide nitrogen. Displayed on the right axis: the peak area ratio of C_{Carb}/C_{IL} (black diamonds), where C_{Carb} refers to carbamate carbon and C_{IL} refers to IL carbon.

Figure 4.8 shows the peak area ratios of N_U/N_{Im} and N_R/N_{Im} for each stage of experiment. The peak area ratios were calculated by dividing the area of the N_U or N_R peak by the area of the N_{Im} peak at each stage. The N_U and N_R peaks in the N 1s spectra for the unexposed IL and the regenerated IL have been accounted for in the calculations for the ratios calculated for Stages 2, and Stages 4 to 7. Specifically, the areas of the N_U and N_R peaks from the unexposed IL and the regenerated IL have been subtracted from the areas of the N_U and N_R peaks from later stages. Through Stages 3 to 7, it can be seen that $N_U/N_{Im} > N_R/N_{Im}$. This means the area of the N_U peak is consistently greater than that of N_R throughout these stages, which means a peak area ratio of 1:1 is not maintained. The reasons for this are unclear. One possibility is that some of the absorbed CO_2, rather than forming a carbamate group, weakly interacts with the benzimidazolide anion, causing a shift in the imidazolide N peak to a higher BE. This could account for the consistently greater intensity of N_U compared to N_R, since increased gas exposure would lead to more CO_2 absorption (via both physisorption and chemisorption) and a greater number of these weak interactions between the anion and CO_2 molecules. It is possible

153

that X-ray beam damage occurs, although this is usually indicated by the presence of a feature at low binding energy (~397 eV) [16]. From the data here, it is not possible to unambiguously identify the origin of this apparent discrepancy. Further work utilising angle resolved photoemission (to vary the depth) and near edge X-ray absorption fine structure (see Chapter 7) may prove useful in elucidating the source of the increased intensity. The peak area ratio C_{Carb}/C_{IL} at each stage of the experiment is shown on the right axis of Figure 4.8. The C 1s peak intensities are normalised to the IL carbon peak, allowing for comparison of changes in the carbamate carbon peak intensity throughout the experiment. This ratio describes the change in intensity of the carbamate signal only, while both of the ratios of N_U/N_{Im} and N_R/N_{Im} describe intensity changes associated with both carbamate formation and benzimidazole formation. C_{Carb}/C_{IL} does not increase as significantly as N_U/N_{Im} or N_R/N_{Im} when the IL is exposed to H_2O in the first mixed gas regime (Stage 5). This confirms that the increase in N_U and N_R from Stage 4 to Stage 5 is largely due to the reaction with water. C_{Carb}/C_{IL} decreases significantly when the IL is exposed to only H_2O (Stage 6), which reflects the trend displayed by both N_U/N_{Im} and N_R/N_{Im}. Once the IL is exposed to the second mixed-gas regime (Stage 7), C_{Carb}/C_{IL} increases, again reflecting the trend displayed by both N_U/N_{Im} and N_R/N_{Im}. This supports the idea that the IL continues to react with CO_2 despite initially exposing the IL to H_2O vapour.
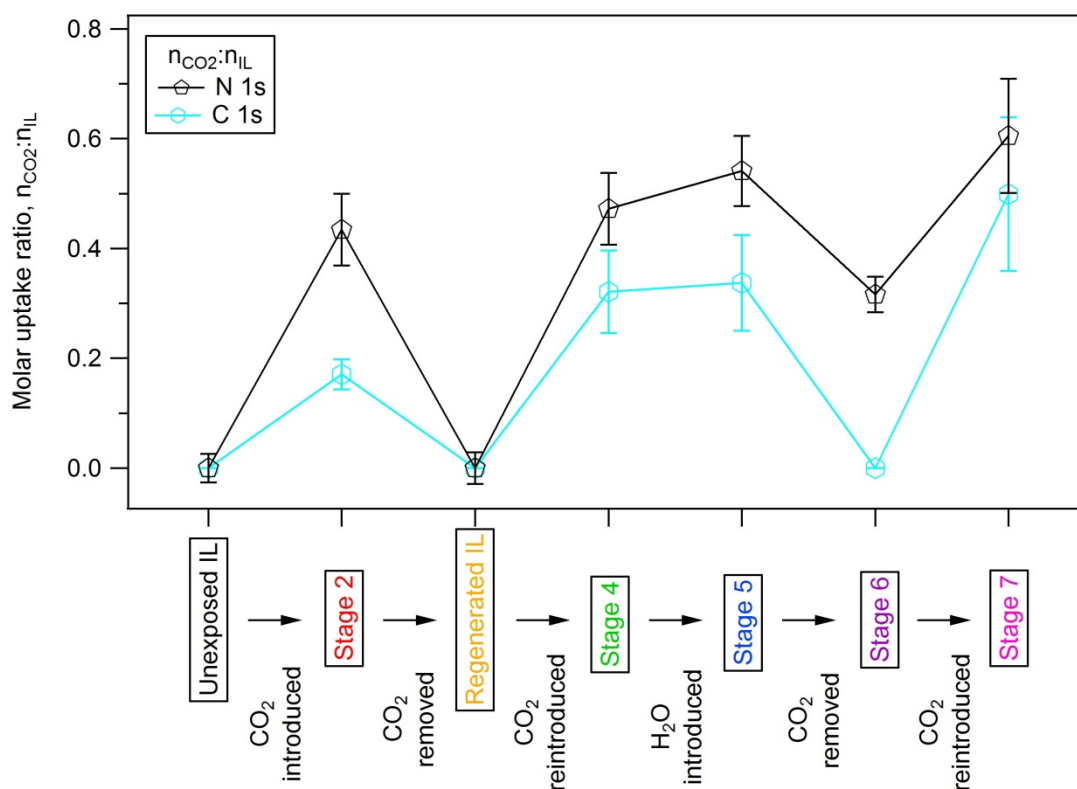
Figure 4.9: Molar uptake ratio, $n_{CO2}:n_{IL}$, at each stage of the experiment, calculated using the N 1s region (black pentagons) and the C 1s region (cyan hexagons).

The molar uptake ratio, $n_{CO2}:n_{IL}$ was calculated using the area of the N_R peak in the N 1s region, and the area of the whole N 1s region. For comparison, a separate value for the molar uptake ratio was calculated using the area of the carbamate peak and the area of the whole C 1s region (excluding gas-phase signals). Similarly to the N 1s area ratios, the N_U and N_R peaks from the unexposed IL and regenerated IL have been accounted for in the calculation of the molar uptake ratio at each Stage. These values of $n_{CO2}:n_{IL}$ at each stage have been plotted in Figure 4.9. In the study by Taylor et al [6], the molar uptake ratio of CO_2 in dry [P_{66614}][benzim] (at saturation) was calculated to be 1.2:1. It is likely that the chemisorption of CO_2 occurs at a ratio of 1:1, but can exceed capacity by 'trapping' physisorbed CO_2. It was found the addition of water reduced the molar uptake ratio of CO_2 to 1:1, which indicates saturation of the IL with water diminishes its capacity for physisorbed CO_2. Throughout all stages of our experiment the ratio $n_{CO2}:n_{IL}$ is always <1 which is expected since the imidazolide signal is always present in the N 1s region, and therefore some unreacted anions remain in the IL. The molar uptake ratio calculated using these regions follow a similar trend, but $n_{CO2}:n_{IL}$ for the C 1s region is always

less than that calculated using the N 1s region at every stage (with the exception of Stages 1 and 3, where the corrections to N_U and N_R mean the ratio is zero). There are two reasons for this. Firstly, the reaction with H_2O leads to an increase in the intensity of the N_R peak. As a result, the molar uptake ratio calculated using the N 1s region is overestimated. Secondly, the presence of any contaminant C at the surface, likely as a part of silicon grease (see Section 4.3.1), has not been taken into account [34, 35]. The signal would overlap with that of the IL, and so would contribute to the intensity of the IL carbon peak. This intensity inflation consequently reduces the apparent relative intensity of the carbamate peak, causing the molar uptake ratio calculated using the C 1s region to be underestimated.

The values of n_{CO2}:n_{IL} calculated using the N 1s region averages at ~0.5, irrespective of CO_2 partial pressure. A consistent uptake ratio may be explained by the existence of a threshold of 'surface saturation', where reacted species move to the bulk of the IL, and a portion of unreacted species are present at the surface. An XPS investigation into the reaction between a solution of MEA and CO_2 by Lewis et al [36] demonstrated that the concentration of reacted species was greater in the bulk of the solution, whereas the concentration of the unreacted MEA was greater at the surface. The IL film studied here is greater than the sampling depth of XPS, and is therefore considered a bulk system. It may be the case for [P_{66614}][benzim] that the anions that have reacted with CO_2 move to the bulk of the IL, and unreacted anions become more prevalent at the surface of the IL. If a portion of unreacted species consistently populates the IL/CO_2 interface, this would facilitate continuous reaction between the IL and CO_2 until saturation. However, [P_{66614}][benzim] is significantly more viscous than MEA [6, 37, 38], which is likely to hinder transport of reacted species in the IL. In previous studies, the IL was subject to saturation of CO_2/H_2O [6], but at these pressures, we are predominantly investigating absorption phenomena via chemisorption due to changes in the N 1s following reaction between CO_2 and the IL. While physisorption of CO_2 cannot be ruled out, the C 1s and O 1s spectra recorded in this work cannot be deconvoluted sufficiently to determine the presence of physisorbed or absorbed CO_2.

It is evident from the signals attributed to carbamate formation in both the C 1s and N 1s regions that IL continues to react with CO_2, irrespective of whether it

is exposed to CO_2 or H_2O vapour first. This demonstrates that its ability to react is not significantly inhibited by exposure to H_2O vapour. As mentioned previously, in the study by Taylor et al [6], the capacity for chemisorbed CO_2 was maintained (i.e. 1:1 ratio of CO_2 molecules to IL pairs), but the capacity for physisorbed CO_2 ('trapped' CO_2, the remaining 0.2 of the dry IL molar uptake ratio) was reduced. This is also reflected in our data, whereby the molar uptake ratio (which is likely to be dominated by chemisorption) is a similar value in both mixed-gas regimes, demonstrating that the capacity for chemisorption, under these conditions, was not significantly affected by initial exposure to H_2O vapour. The peak area ratios N_U/N_{Im}, N_R/N_{Im}, and C_{Carb}/C_{IL} in the second mixed-gas regime (Stage 7) are consistent with those in the first mixed-gas regime (Stage 5). This means that the IL reacts with CO_2 and forms a similar proportion of carbamate groups irrespective of whether the IL has been exposed initially to H_2O vapour or CO_2 gas. The idea that a similar number of carbamate groups formed in Stages 5 and 7 suggests that H_2O does not displace CO_2, but CO_2 molecules do displace the hydrogen bonds formed via the reaction between the IL and H_2O.

In previous work, the superbasic ILs were regenerated through heating to 80°C, and removing the desorbed CO_2 under a flow of N_2 [6]. The measurements discussed here have shown that $[P_{66614}][benzim]$ can be regenerated by reducing the CO_2 partial pressure surrounding it. This might also suggest that when working at such low pressures (compared to those employed by Taylor et al) the IL is more easily deprotonated allowing the reaction with CO_2 to proceed. The measurements here clearly demonstrate that the CO_2 capture capabilities of superbasic ILs are not diminished after regeneration for both dry and pre-wetted superbasic ILs.

4.4 Conclusion

In summary, the reaction of CO_2 with $[P_{66614}][benzim]$ has been studied by NAPXPS and indicates reaction between the CO_2 and benzimidazolide N atoms to form a carbamate species. The results obtained during exposure to both H_2O vapour and CO_2 indicate that the ability of the IL to react with CO_2 is not inhibited significantly by the presence of H_2O, and that CO_2 appears to preferentially bind to the IL, even after exposure to H_2O vapour. The upper limit

of the molar uptake ratio, $n_{CO2}:n_{IL}$, is calculated to be approximately 0.5. Additionally, the CO_2 reaction with the anion appears to be reversible simply by reducing the surrounding CO_2 pressure, showing that $[P_{66614}][benzim]$ can be regenerated in situ.

Chapter 4 References

[1] R.S. Haszeldine, *Carbon Capture and Storage: How Green Can Black Be?*, Science, 325 (2009) 1647-1652, D.O.I.: 10.1126/science.1172246

[2] N. MacDowell, N. Florin, A. Buchard, J. Hallett, A. Galindo, G. Jackson, C.S. Adjiman, C.K. Williams, N. Shah, P. Fennell, *An Overview of CO2 Capture Technologies*, Energy & Environmental Science, 3 (2010) 1645-1669, D.O.I.: 10.1039/C004106H

[3] K.M.K. Yu, I. Curcic, J. Gabriel, S.C.E. Tsang, *Recent Advances in CO2 Capture and Utilization*, ChemSusChem, 1 (2008) 893-899, D.O.I.: 10.1002/cssc.200800169

[4] S.A. Tenney, D. Lu, F. He, N. Levy, U.G.E. Perera, D.E. Starr, K. Müller, H. Bluhm, P. Sutter, *Key Structure–Property Relationships in CO2 Capture by Supported Alkanolamines*, Journal of Physical Chemistry C, 118 (2014) 19252-19258, D.O.I.: 10.1021/jp507205t

[5] G.T. Rochelle, *Amine Scrubbing for CO2 Capture*, Science, 325 (2009) 1652-1654, D.O.I.: 10.1126/science.1176731

[6] S.F.R. Taylor, C. McCrellis, C. McStay, J. Jacquemin, C. Hardacre, M. Mercy, R.G. Bell, N.H. de Leeuw, *CO2 Capture in Wet and Dry Superbase Ionic Liquids*, Journal of Solution Chemistry, 44 (2015) 511-527, D.O.I.: 10.1007/s10953-015-0319-z

[7] L.A. Blanchard, D. Hancu, E.J. Beckman, J.F. Brennecke, *Green Processing Using Ionic Liquids and CO2*, Nature, 399 (1999) 28-29, D.O.I.: 10.1038/19887

[8] I. Niedermaier, M. Bahlmann, C. Papp, C. Kolbeck, W. Wei, S. Krick Calderón, M. Grabau, P.S. Schulz, P. Wasserscheid, H.-P. Steinrück, *Carbon Dioxide Capture by an Amine Functionalized Ionic Liquid: Fundamental Differences of Surface and Bulk Behavior*, Journal of the American Chemical Society, 136 (2013) 436-441, D.O.I.: 10.1021/ja410745a

[9] B.F. Goodrich, J.C. de la Fuente, B.E. Gurkan, Z.K. Lopez, E.A. Price, Y. Huang, J.F. Brennecke, *Effect of Water and Temperature on Absorption of CO2 by Amine-Functionalized Anion-Tethered Ionic Liquids*, Journal of Physical Chemistry B, 115 (2011) 9140-9150, D.O.I.: 10.1021/jp2015534

[10] S. Stevanovic, A. Podgorsek, L. Moura, C. Santini, A.A. Padua, M.C. Gomes, *Absorption of Carbon Dioxide by Ionic Liquids with Carboxylate Anions*,

International Journal of Greenhouse Gas Control, 17 (2013) 78-88, D.O.I.: 10.1016/j.ijggc.2013.04.017

[11] C. Wang, H. Luo, H. Li, X. Zhu, B. Yu, S. Dai, *Tuning the Physicochemical Properties of Diverse Phenolic Ionic Liquids for Equimolar CO2 Capture by the Substituent on the Anion*, Chemistry–A European Journal, 18 (2012) 2153-2160, D.O.I.: 10.1002/chem.201103092

[12] M. Mercy, S.F.R. Taylor, J. Jacquemin, C. Hardacre, R.G. Bell, N.H. De Leeuw, *The Addition of CO2 to Four Superbase Ionic Liquids: A DFT Study*, Physical Chemistry Chemical Physics, 17 (2015) 28674-28682, D.O.I.: 10.1039/C5CP05153C

[13] F. Reinert, S. Hüfner, *Photoemission Spectroscopy—from Early Days to Recent Applications*, New Journal of Physics, 7 (2005) 97, D.O.I.: 10.1088/1367-2630/7/1/097

[14] A. Damascelli, *Probing the Electronic Structure of Complex Systems by ARPES*, Physica Scripta, 2004 (2004) 61-74, D.O.I.: 10.1238/Physica.Topical.109a00061

[15] V. Lockett, R. Sedev, C. Bassell, J. Ralston, *Angle-Resolved X-Ray Photoelectron Spectroscopy of the Surface of Imidazolium Ionic Liquids*, Physical Chemistry Chemical Physics, 10 (2008) 1330-1335, D.O.I.: 10.1039/b713584j

[16] K.R.J. Lovelock, E.F. Smith, A. Deyko, I.J. Villar-Garcia, P. Licence, R.G. Jones, *Water Adsorption on a Liquid Surface*, Chemical Communications, (2007) 4866-4868, D.O.I.: 10.1039/B711680B

[17] I.J. Villar-Garcia, E.F. Smith, A.W. Taylor, F.L. Qiu, K.R.J. Lovelock, R.G. Jones, P. Licence, *Charging of Ionic Liquid Surfaces under X-Ray Irradiation: The Measurement of Absolute Binding Energies by XPS*, Physical Chemistry Chemical Physics, 13 (2011) 2797-2808, D.O.I.: 10.1039/C0cp01587c

[18] M. Wagstaffe, M.J. Jackman, K.L. Syres, A. Generalov, A.G. Thomas, *Ionic Liquid Ordering at an Oxide Surface*, Chemphyschem, 17 (2016) 3430-3434, D.O.I.: 10.1002/cphc.201600774

[19] K.L. Syres, R.G. Jones, *Adsorption, Desorption, and Reaction of 1-Octyl-3-Methylimidazolium Tetrafluoroborate, [C8C1Im][BF4], Ionic Liquid Multilayers on Cu (111)*, Langmuir, 31 (2015) 9799-9808, D.O.I.: 10.1021/acs.langmuir.5b02932

[20] S. Rivera-Rubero, S. Baldelli, *Influence of Water on the Surface of the Water-Miscible Ionic Liquid 1-Butyl-3-Methylimidazolium Tetrafluoroborate: A Sum Frequency Generation Analysis*, Journal of Physical Chemistry B, 110 (2006) 15499-15505, D.O.I.: 10.1021/jp062694p

[21] M.J. Jackman, A.G. Thomas, C. Muryn, *Photoelectron Spectroscopy Study of Stoichiometric and Reduced Anatase TiO2(101) Surfaces: The Effect of Subsurface Defects on Water Adsorption at Near-Ambient Pressures*, Journal of Physical Chemistry C, 119 (2015) 13682–13690, D.O.I.: 10.1021/acs.jpcc.5b02732

[22] D.E. Starr, Z. Liu, M. Havecker, A. Knop-Gericke, H. Bluhm, *Investigation of Solid/Vapor Interfaces Using Ambient Pressure X-Ray Photoelectron Spectroscopy*, Chemical Society Reviews, 42 (2013) 5833-5857, D.O.I.: 10.1039/C3CS60057B

[23] K.A. Stoerzinger, W.T. Hong, E.J. Crumlin, H. Bluhm, Y. Shao-Horn, *Insights into Electrochemical Reactions from Ambient Pressure Photoelectron Spectroscopy*, Accounts of Chemical Research, 48 (2015) 2976-2983, D.O.I.: 10.1021/acs.accounts.5b00275

[24] R.K. Blundell, P. Licence, *Quaternary Ammonium and Phosphonium Based Ionic Liquids: A Comparison of Common Anions*, Physical Chemistry Chemical Physics, 16 (2014) 15278-15288, D.O.I.: 10.1039/C4CP01901F

[25] N. Fairley, *CasaXPS Manual 2.3.15 Introduction to XPS and AES*, Casa Software, (2009).

[26] K.R.J. Lovelock, I.J. Villar-Garcia, F. Maier, H.-P. Steinrück, P. Licence, *Photoelectron Spectroscopy of Ionic Liquid-Based Interfaces*, Chemical reviews, 110 (2010) 5158-5190, D.O.I.: 10.1021/cr100114t

[27] D.P. Bezerra, F.W. da Silva, P.A. de Moura, A.G. Sousa, R.S. Vieira, E. Rodriguez-Castellon, D.C. Azevedo, *CO2 Adsorption in Amine-Grafted Zeolite 13x*, Applied Surface Science, 314 (2014) 314-321, D.O.I.: 10.1016/j.apsusc.2014.06.164

[28] B. Eren, C. Heine, H. Bluhm, G.A. Somorjai, M. Salmeron, *Catalyst Chemical State During Co Oxidation Reaction on Cu (111) Studied with Ambient-Pressure X-Ray Photoelectron Spectroscopy and near Edge X-Ray Adsorption Fine Structure Spectroscopy*, Journal of the American Chemical Society, 137 (2015) 11186-11190, D.O.I.: 10.1021/jacs.5b07451

[29] L. Walle, A. Borg, P. Uvdal, A. Sandell, *Probing the Influence from Residual Ti Interstitials on Water Adsorption on TiO2 (110)*, Physical Review B, 86 (2012) 205415, D.O.I.: 10.1103/PhysRevB.86.205415

[30] G. Ketteler, S. Yamamoto, H. Bluhm, K. Andersson, D.E. Starr, D.F. Ogletree, H. Ogasawara, A. Nilsson, M. Salmeron, *The Nature of Water Nucleation Sites on TiO2 (110) Surfaces Revealed by Ambient Pressure X-Ray Photoelectron Spectroscopy*, Journal of Physical Chemistry C, 111 (2007) 8278-8282, D.O.I.: 10.1021/jp068606i

[31] T.H. Seyller, D. Borgmann, G. Wedler, *Interaction of CO2 with Cs-Promoted Fe (110) as Compared to Fe (110)/K+ CO2*, Surface Science, 400 (1998) 63-79, D.O.I.: 10.1016/S0039-6028(97)00842-X

[32] R.L. Thompson, W. Shi, E. Albenze, V.A. Kusuma, D. Hopkinson, K. Damodaran, A.S. Lee, J.R. Kitchin, D.R. Luebke, H. Nulwala, *Probing the Effect of Electron Donation on CO2 Absorbing 1, 2, 3-Triazolide Ionic Liquids*, RSC Advances, 4 (2014) 12748-12755, D.O.I.: 10.1039/C3RA47097K

[33] P. Morales-Gil, M. Walczak, R. Cottis, J. Romero, R. Lindsay, *Corrosion Inhibitor Binding in an Acidic Medium: Interaction of 2-Mercaptobenizmidazole with Carbon-Steel in Hydrochloric Acid*, Corrosion Science, 85 (2014) 109-114, D.O.I.: 10.1016/j.corsci.2014.04.003

[34] H. Hashimoto, A. Ohno, K. Nakajima, M. Suzuki, H. Tsuji, K. Kimura, *Surface Characterization of Imidazolium Ionic Liquids by High-Resolution Rutherford Backscattering Spectroscopy and X-Ray Photoelectron Spectroscopy*, Surface Science, 604 (2010) 464-469, D.O.I.: 10.1016/j.susc.2009.12.023

[35] E.F. Smith, F.J. Rutten, I.J. Villar-Garcia, D. Briggs, P. Licence, *Ionic Liquids in Vacuo: Analysis of Liquid Surfaces Using Ultra-High-Vacuum Techniques*, Langmuir, 22 (2006) 9386-9392, D.O.I.: 10.1021/la061248q

[36] T. Lewis, M. Faubel, B. Winter, J.C. Hemminger, *CO2 Capture in Amine-Based Aqueous Solution: Role of the Gas–Solution Interface*, Angewandte Chemie International Edition, 50 (2011) 10178-10181, D.O.I.: 10.1002/anie.201101250

[37] R.M. DiGuilio, R.J. Lee, S.T. Schaeffer, L.L. Brasher, A.S. Teja, *Densities and Viscosities of the Ethanolamines*, Journal of Chemical and Engineering Data, 37 (1992) 239-242, D.O.I.: 10.1021/je00006a028

[38] Y. Maham, C.-N. Liew, A. Mather, *Viscosities and Excess Properties of Aqueous Solutions of Ethanolamines from 25 to 80°C*, Journal of Solution Chemistry, 31 (2002) 743-756, D.O.I.: 10.1023/A:10211330

5 Surface Phenomena and Thermal Stability of Ionic Liquid Multilayers on Polar and Nonpolar Zinc Oxide

Understanding how the constituent ions of ionic liquids (ILs) arrange themselves and interact with oxide surfaces is important for a wide variety of applications. Of particular relevance to the theme of this thesis are oxides as a part of photovoltaic (PV) systems and as catalysts.

The arrangement of IL ions on oxide surfaces is dependent on their size and shape, as well as the interactions they experience with the atoms at the oxide surface. The ordering and interactions of ionic liquids (ILs) have previously been investigated on a number of metal [1-3] and metal oxide [4-7] surfaces, but few studies exist that investigate their behaviour specifically on ZnO. Various groups have incorporated ILs into ZnO-based PV devices to improve performance [8, 9]. ILs have shown to be beneficial for various catalysis systems by improving selectivity [10], and avoid loss of solvent during reaction due to their low vapour pressures [11].

Presented in this chapter is a two-part study into the structure and interactions of two imidazolium-based ILs on ZnO. The first part investigates the ordering and interactions of an IL on two ZnO surfaces using a combination of X-ray photoelectron spectroscopy and near-edge X-ray absorption fine structure spectroscopy with a view toward PV applications. The second investigates the thermal stability of an IL on ZnO using X-ray photoelectron spectroscopy, with a view toward catalysis applications.

5.1 Introduction

Zinc oxide (ZnO) is an inorganic semiconductor material with a wide band gap of ~ 3.3 eV, and has a hexagonal-wurtzite structure (see Figure 5.1). The low-index surfaces of ZnO can be categorised into two types: polar and non-polar. These are differentiated by the concentration of Zn^{2+} and O^{2-} ions at the free

surface: specifically, non-polar surfaces have an equal number of Zn^{2+} and O^{2-} ions, while polar surfaces are dominated by either Zn^{2+} or O^{2-}, and are referred to as being either Zn-terminated or O-terminated respectively. The concentration of surface ions results in differing chemical properties between the polar and non-polar surfaces of ZnO.
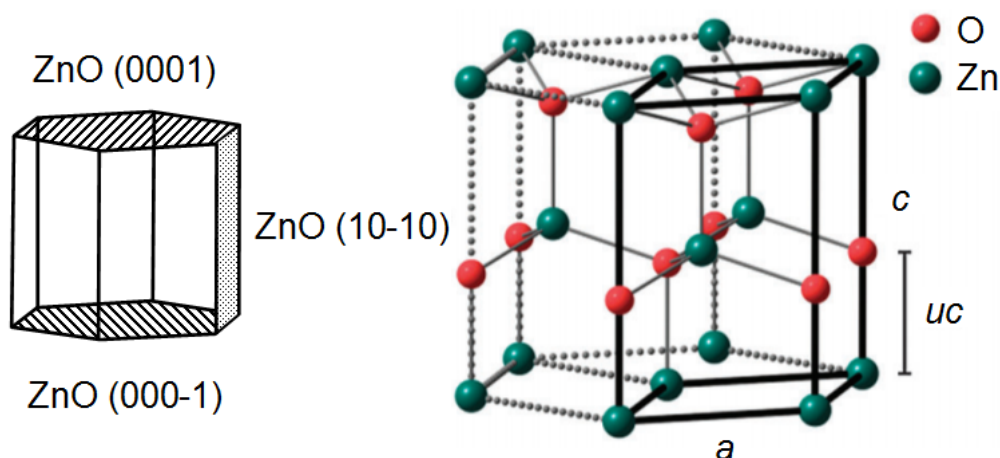
Figure 5.1: Diagram of the wurtzite crystal structure of ZnO, where the ZnO (0001), ZnO (000-1) (polar faces), and ZnO (10-10) (non-polar face) terminations are highlighted. On the right shows the position of the Zn atoms (large green spheres) and the O atoms (small red spheres), and the unit cell with lattice parameters a (3.3 Å) and c (5.2 Å). The dimension u is an internal constant that describes the Zn-O displacement along c, which, for a perfect ZnO unit cell, is 3/8. Figure adapted from [12].

ZnO is a desirable candidate material for photovoltaic applications due to its good electrical and optical properties, whilst also being stable, non-toxic and relatively cheap to manufacture in bulk quantities [13, 14]. ZnO catalysts consist of ZnO in its nanoparticulate form, and can be utilised for a variety of applications, including methanol synthesis [15], water treatment [16] and H_2O/CO_2 splitting [17].

In PV systems, charge transfer between composite layers is of vital importance to their efficiency. For organic-based PV in particular, challenge lies in lowering the charge transfer barrier between the active layer (where current is photogenerated in a photovoltaic cell) and the metal oxide layer. This is done through engineering the energy difference between the conduction band of the metal oxide and the LUMO of the active layer. This can be done using an organic electrolyte, located between the metal oxide and the active layer, to enhance charge transfer. Charge transfer across an interface is closely linked to the arrangement of atoms or molecules at the interface in question. Lee et al [8] used a monolayer of IL electrolyte (specifically 1-benzyl-3-methylimidazolium

chloride) to enhance the performance of hybrid organic-inorganic solar cells, containing ZnO for the metal oxide layer and 'Super Yellow' as the active layer. The IL ions arranged themselves preferentially, with the Cl anions located at the ZnO surface, and the 1-benzyl-3-methylimidazolium cations at the active layer. This dipole arrangement shifted the band edge of ZnO closer to that of the active layer, subsequently causing a decrease in the ZnO work function and the charge transfer barrier. The self-assembling ionic nature of ILs provides an advantage for their potential use in PV systems over other organic electrolytes.

In catalysis systems such as supported ionic liquid phase (SILP) and solid catalyst with ionic liquid layer (SCILL), the addition of IL exists to enhance the catalysts' selectivity of reactants and thus, in theory, improve the efficiency of these systems, but interactions with the IL and the catalyst itself could alter the adsorption and/or reaction properties of the catalyst. Sobota et al [18, 19] conducted a combined IR absorption and X-ray photoelectron spectroscopy (XPS) study into the effects of 1-butyl-3-methylimidazolium bis(trifluoromethylsulphonyl)imide ($[C_4C_1Im][Tf_2N]$) on CO adsorption of Pd nanoparticles immobilised on an Al_2O_3 support. The addition of IL to the system reduced CO adsorption at bridge sites on the catalyst, but stabilised adsorption on the hollow sites of facet features on the catalyst. More pertinently, they found that the IL decomposed when the system was heated, and the products of the decomposition blocked the majority of the CO adsorption sites on the Pd catalysts. The XPS revealed that the decomposition species (which were cation-derived) were preferentially located on the catalysts, and not on the Al_2O_3 support. By blocking adsorption sites for reactants, the presence of decomposition species is likely to have a negative impact on rate of reaction and reaction kinetics.
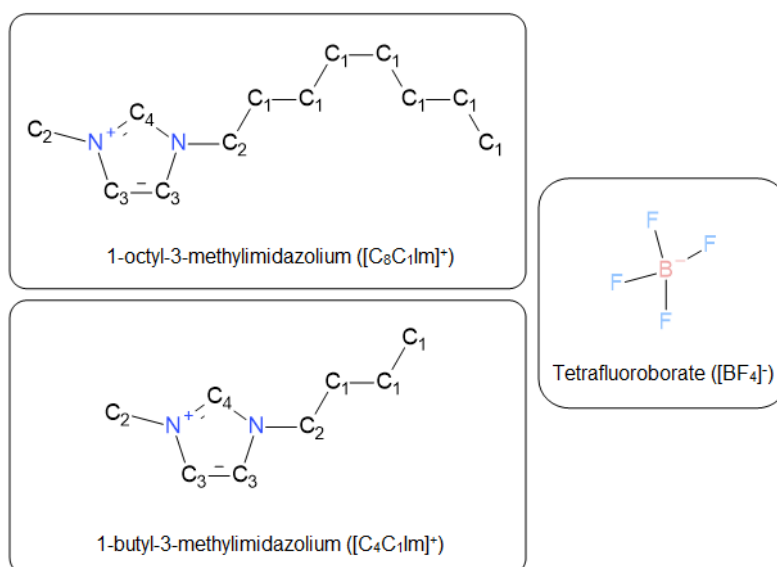
Figure 5.2: Chemical structures of the $[C_8C_1Im]^+$ and $[C_4C_1Im]^+$ cations, and of the $[BF_4]^-$ anion.

Presented here is an investigation into the structure and ordering of 1-octyl-3-methylimidazolium tetrafluoroborate ($[C_8C_1Im][BF_4]$) on ZnO (0001) and ZnO (10-10), followed by an investigation into the thermal stability of the analogous 1-butyl-3-methylimidazolium tetrafluoroborate $[C_4C_1Im][BF_4]$ on ZnO (0001).

5.2 Experimental section

5.2.1 $[C_8C_1Im][BF_4]$ on ZnO (0001) and ZnO (10-10)
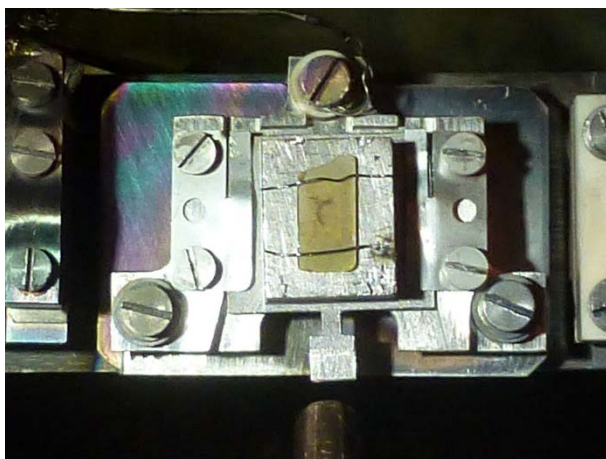
Figure 5.3: ZnO (0001) crystal mounted onto the Ta sample plate with Ta wire at the ANTARES beamline at Soleil. The ZnO (10-10) crystal, of the same dimensions, was mounted in a similar fashion.

The ZnO (0001) and (10-10) single crystal surfaces (5 mm × 10 mm, PI-KEM) were mounted onto Ta sample plates and fixed into place with Ta wire (see Figure 5.3). They were cleaned via several Ar$^+$ sputter-anneal cycles (sputtering

at 1 keV for 15 minutes and annealing at 700°C for 20 minutes) with a final anneal in 10^{-6} mbar O_2 for five minutes. The cleanliness of the surfaces was then determined by X-ray photoelectron spectroscopy (XPS) scans (see Figure 5.5 for these spectra). Additionally, a low-energy electron diffraction (LEED) pattern was acquired for the ZnO (0001) surface (using an incident energy of 74.0 eV) to confirm the cleanliness of the surface, as well as check for the correct pattern for the (0001) termination. The LEED pattern was not heavily obscured by background noise, indicating a smooth (0001) surface with few defects (see Figure 5.4).
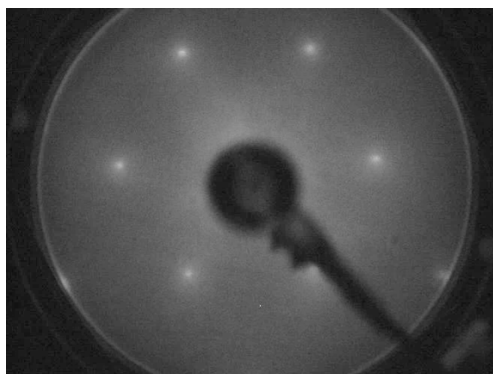
Figure 5.4: LEED pattern taken from the clean ZnO (0001) surface at 74.0 eV. The hexagonal-shaped pattern shows that the surface has the correct surface termination.

The IL, 1-octyl-3-methylimidazolium tetrafluoroborate ($[C_8C_1Im][BF_4]$, Sigma Aldrich, >97%, chemical structure shown in Figure 5.2) was degassed in a modified Knudsen cell at 120°C for approximately 3 hours to remove water and impurities. The IL was heated to ~350°C for deposition. The deposition time was 20 minutes for the ZnO (0001) substrate, and 420 minutes for the ZnO (10-10) substrate. The dosing time needed to be increased due to the experimental setup used on the beamline. The substrate was cooled to ~-150°C to prevent beam damage. For IL/ZnO (0001), the substrate was cooled after IL deposition; and for IL/ZnO (10-10), the substrate was cooled prior to IL deposition.
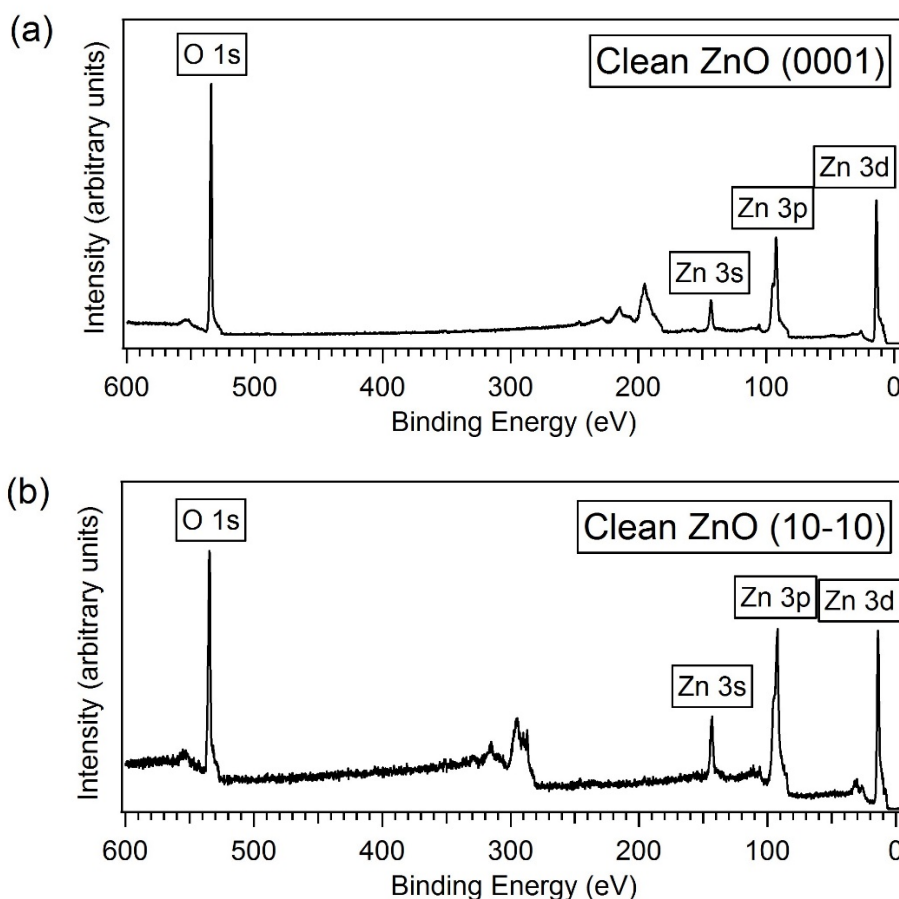
Figure 5.5: XPS surveys of clean ZnO (0001) (photon energy, $h\nu$ = 700 eV) (a), and of clean ZnO (10-10) ($h\nu$ = 800 eV) (b).

XPS and N K-edge near-edge X-ray absorption fine structure (NEXAFS) measurements were taken at the ANTARES beamline at the SOLEIL synchrotron in France. All XPS measurements were taken at normal emission (photoelectron emission 90° relative to sample surface) and have been calibrated on the BE scale to the O 1s region at 530.0 eV [20]. All core level XPS BEs are quoted to ±0.1 eV. On the ZnO crystals, each XPS spectrum was taken at a new position on the sample surface. The same procedure was carried out for the N K-edge NEXAFS spectra. A set of seven scans were taken, each with 0.5 eV steps, scanning the N absorption edge with a total range of 390 eV to 430.5 eV. The seven spectra were then merged, and produced a spectrum spanning 390 eV to 430.5 eV, with a step size of 0.1 eV. The NEXAFS spectra were recorded by monitoring the N auger peak at a kinetic energy of 375 eV; with the beam at normal incidence (NI, beam at 90° relative to the sample surface) and grazing incidence (GI, beam 30° relative to the sample surface). An additional NEXAFS spectrum was recorded for the IL/ZnO (0001) system with the beam at an angle of 50° relative to the surface. The XPS

and NEXAFS spectra were recorded at different positions on the surface in order to prevent sample beam damage. XPS spectra of the clean ZnO (0001) and ZnO (10-10) surfaces are shown in Figure 5.5, with peaks associated with the substrate labelled. An O KLL Auger feature appears at ~200 eV in the ZnO (0001) survey, and at ~300 eV in the ZnO (10-10) survey. Table 5.1 outlines the photon energies used in acquiring the XPS spectra.

Table 5.1: Photon energies used in acquiring the XPS spectra on the ANTARES beamline

Region	Photon energy, $h\nu$ (eV)
C 1s	700
O 1s	700
N 1s	700
F 1s	800
B 1s	300

5.2.2 [C$_4$C$_1$Im][BF$_4$] on ZnO (0001)

The ZnO (0001) single crystal substrate (5 mm × 5 mm, PI-KEM) was mounted onto a Ta sample plate, held in place using Ta strips that were spot-welded into place. The substrate was prepared via two Ar$^+$ sputter-anneal cycles (sputtering at 1 keV for 15 minutes and annealing at 700°C for 20 minutes). The final anneal was carried out in ~10^{-6} mbar O$_2$ for five minutes. Similar to the ZnO substrates in the previous section, a LEED pattern was acquired for the ZnO (0001) crystal at an energy of 71.3 eV (see Figure 5.6). The LEED pattern shows that the ZnO (0001) has the correct surface termination, and its sharpness confirms that the surface has few defects.
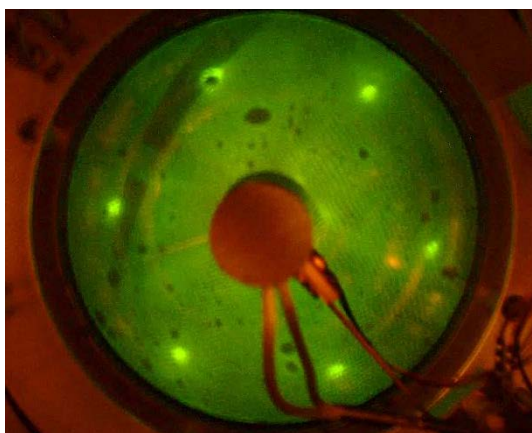
Figure 5.6: LEED pattern taken from the clean ZnO (0001) surface at 71.3 eV. The hexagonal-shaped pattern shows that the surface has the correct surface termination.

The IL, 1-butyl-3-methylimidazolium tetrafluoroborate ($[C_4C_1Im][BF_4]$, Sigma Aldrich, >97%, see Figure 5.2 for the chemical structure) was degassed in a modified Knudsen cell at ~120°C for three hours to remove water and impurities, during which time the ZnO (0001) substrate was cooled to -150°C. The IL was then heated to 180°C for physical vapour deposition under ultra-high vacuum (UHV) conditions for 25 minutes. XPS measurements were taken at the AU-MATline beamline of the ASTRID storage ring at the Danish synchrotron facility, ISA.

XPS spectra were recorded as the sample was heated from -150°C, through the glass transition temperature of $[C_4C_1Im][BF_4]$ (-97°C [21]), up to 200°C. At each temperature, spectra were taken at normal emission (NE, with photoelectron emission angle at 90° relative to the sample surface), and at grazing emission (GE, with photoelectron emission angle 45° relative to the sample surface). Measurements at these angles possess approximate sampling depths of 1.5 nm and 1.0 nm respectively (using a derivation of the Beer-Lambert law [22]), and thus the GE spectra are more surface-sensitive. Binding energies of all core level XPS peaks are quoted to ±0.1 eV and have been calibrated to the Zn $3p_{3/2}$ peak at 88.6 eV [23]. Table 5.2 outlines the photon energies used in acquiring the XPS spectra.

Table 5.2: Photon energies used in acquiring the XPS spectra on the AU-MATline beamline

Region	Photon energy, $h\nu$ (eV)
C 1s	370
O 1s	610
F 1s	770
B 1s	270

5.3 Results

The ordering and interactions of $[C_8C_1Im][BF_4]$ on polar and nonpolar ZnO were investigated using XPS and N K-edge NEXAFS. The C 1s XPS spectrum for $[C_8C_1Im][BF_4]$ on ZnO (0001) is shown in Figure 5.7a(i) (red line). The C 1s region for $[C_8C_1Im][BF_4]$ on ZnO (0001) possesses the characteristic two-peak shape, with a dominating feature at 284.8 eV, which is attributed to the alkyl chains of the IL cations. The BE of this feature is in correlation with literature values [24]. The shoulder at approximately 286.0 eV is therefore attributed to the amalgamation of signals arising from the carbon in the imidazolium ring of

171

the cation. The C 1s region recorded for $[C_8C_1Im][BF_4]$ on ZnO (10-10) is shown in Figure 5.7a(ii), also represented by a red line. The signal does not have the characteristic two-peak shape, but instead has a more asymmetrical line shape. This could indicate the presence of carbon species in addition to the IL carbon, all of which produce signals that overlap one another. This may be due to decomposition of the IL during deposition.
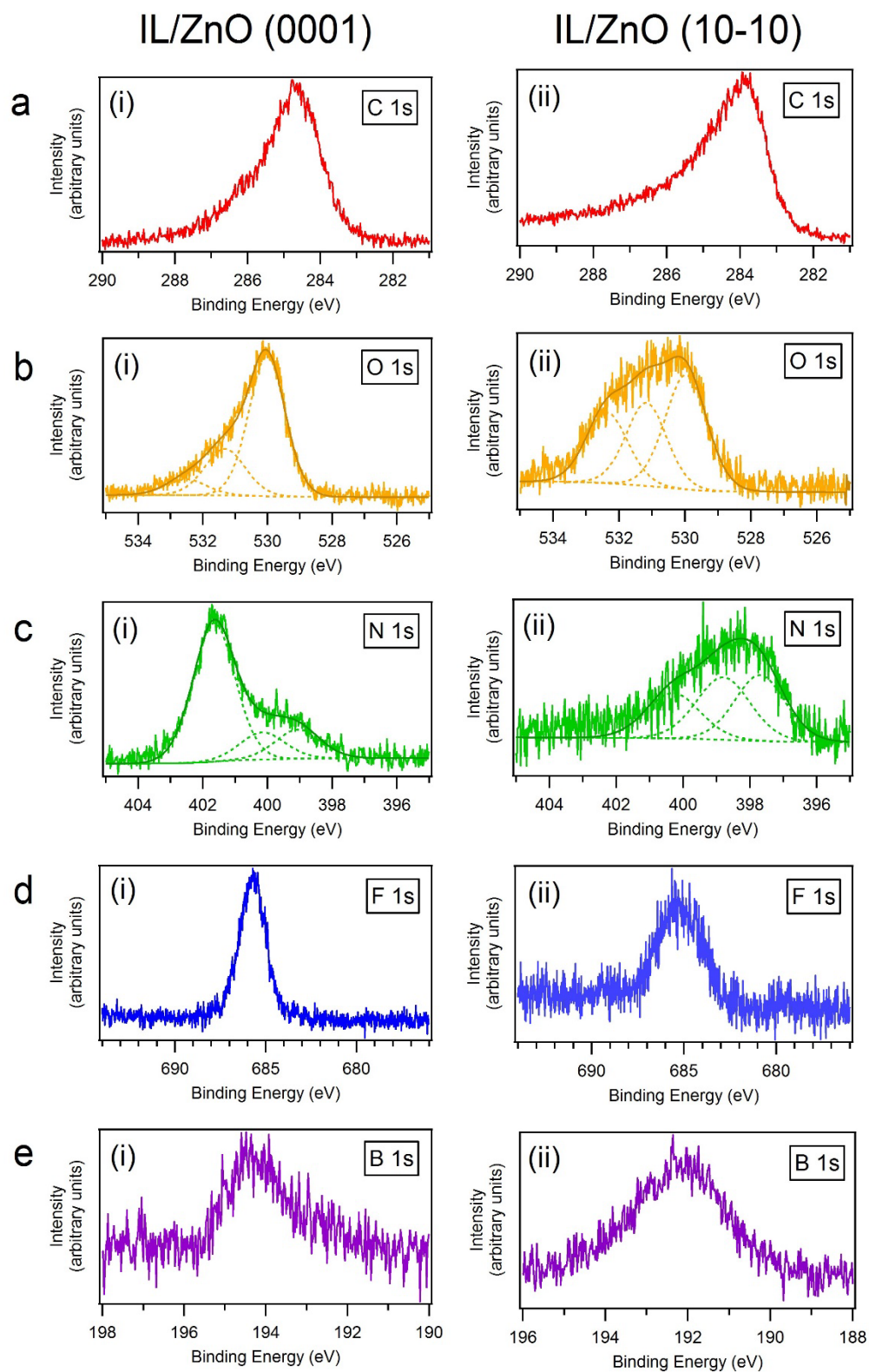
Figure 5.7: Core level XPS spectra of [C$_8$C$_1$Im][BF$_4$] on ZnO (0001) (i), and of [C$_8$C$_1$Im][BF$_4$] on ZnO (10-10) (ii). A summary of binding energies and assignments of peaks is featured in Table 5.3.

The O 1s spectrum of the IL on ZnO (0001) is shown in Figure 5.7b(i), represented by the amber line. This spectrum has been fitted with three peaks (a summary of binding energies and assignments of peaks is featured in Table 5.3). The first, at ~530 eV, is attributed to the lattice O peak of the substrate [20]. The second, at approximately 531.3 eV is attributed to surface hydroxyl groups, the presence of which are typical for the polar surfaces of ZnO [25-27]. The BE of the third peak (~532.5 eV) is consistent with that of molecular adsorbed water [28]. Water may have adsorbed on the surface of either the IL, the ZnO, or both when the substrate was cooled after IL deposition. The adsorption of water on the ZnO surface may have also contributed to the existence of hydroxyl groups via dissociation [27]. Babucci et al [29] investigated the interactions between the analogous IL $[C_4C_1Im][BF_4]$ and a variety of oxides, including ZnO, using Fourier transform infrared (FTIR) spectroscopy. The study revealed that CH at the C_4 position in the imidazolium ring interacts and bonds with with O^{2-} in the ZnO surface- a mechanism supported by other works [30]. This kind of interaction is likely to manifest a peak in the O 1s region at a higher BE than the lattice O, as the bond formation will cause a change in electron density. Therefore, a portion of the signal at ~532.5 eV is attributed to the interaction between the C_4 carbon of the cation and O^{2-} at the ZnO surface. Scanning tunnelling microscopy (STM) investigations into the ZnO (0001) surface by Diebold's group [25, 27] revealed that the (0001) surface termination possesses a nanoscale roughness that culminates from a large number of small, irregularly spaced, triangular holes. The surface maintains the 1×1 periodicity, and therefore still generates the expected LEED pattern for the (0001) termination [27]. The ZnO (0001) surface itself is Zn-terminated, but step edges on the ZnO (0001) surface are O-terminated. Because there are many of these O-terminated step edges, it is likely that interaction between the IL cation and the substrate occurs at these sites. The O 1s region for $[C_8C_1Im][BF_4]$ on ZnO (10-10) is shown in Figure 5.7b(ii). This region has also been fitted with three composite peaks, with those at higher BEs displaying a greater intensity than those in the O 1s region for the same IL on ZnO (0001). The signal at approximately 530 eV is assigned to the lattice O of the substrate. The peak at ~531.3 eV has been attributed to surface hydroxyl groups. STM investigations of stoichiometric ZnO (10-10) surfaces [25] show that they are made up of flat, well-defined terraces, consisting of an equal

174

number of Zn and O atoms per unit area. This therefore means that interactions between the cation and the substrate could theoretically take place anywhere on the crystal surface, rather than specifically at step edges. Similarly to IL/ZnO (0001), the BE of the signal at 532.5 eV is consistent with that of adsorbed water [28], and thus may contain a contribution from water molecules that have adsorbed on the surface. It may be the case that that the presence of hydroxyl groups and adsorbed water is greater for IL/ZnO (10-10) than for IL/ZnO (0001), due to the substrate being cooled prior to IL deposition. Because of this, water from the background vacuum is likely to have condensed on the ZnO crystal surface and facilitated the formation of hydroxyl species via water dissociation at O-vacancy sites [27], as well as adsorbed as molecular water on the surface [31]. Conversely, for IL/ZnO (0001), the IL was deposited onto the substrate at room temperature, and then the whole sample was cooled. In that case, IL film may have subsequently 'protected' the ZnO (0001) surface from water molecules, and resulted in less hydroxyl formation. While it is possible that there may be a greater concentration of surface hydroxyl groups on the ZnO (10-10) surface, there may not necessarily be a mutually greater concentration of adsorbed water. The strength of the signal at ~532.5 eV could also be explained by a greater intensity of the signal associated with cation-substrate interaction [5]. This would be the case if the IL deposition on the ZnO (10-10) substrate was an ultrathin film, whereby the interaction between the IL and the substrate would be more 'visible', and not obscured beneath multilayers, leading to a more intense signal associated with that interaction. Using a combination of the TPP-2M calculation for the inelastic mean free path for organic materials [32], and the Beer-Lambert relation for photoelectron attenuation in thin films [22], the thicknesses of the deposited IL layers on ZnO (0001) and ZnO (10-10) were calculated. The IL deposition on ZnO (0001) was found to be approximately (11.26 ± 0.08) Å, corresponding to an estimated 1.6 IL layers, assuming the 'thickness' of one $[C_8C_1Im][BF_4]$ pair to be ~7 Å [33]. Meanwhile, the deposition on ZnO (10-10) was found to be almost half the thickness of the deposition on ZnO (0001), at approximately (6.30 ± 0.08) Å (the calculation for IL deposition thickness can be found in Appendix A). This corresponds to approximately 0.9 IL layers, suggesting a sub-monolayer coverage. The presence of adsorbed water in both cases may cause a more

intense O 1s signal, which would lead to an underestimation in the calculation for the thickness of the IL films.
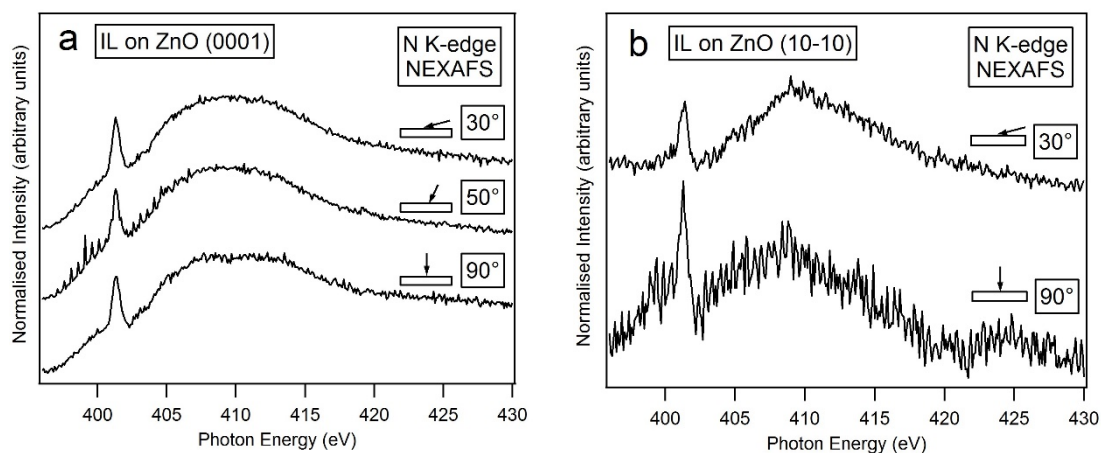
Figure 5.8: N K-edge NEXAFS spectra recorded for [C_8C_1Im][BF_4] on ZnO (0001) (a), and for [C_8C_1Im][BF_4] on ZnO (10-10) (b). The schematic diagrams to the left of the angle labels indicate the beam's incidence on the sample surface.

X-ray absorption techniques are particularly sensitive to molecular ordering, and while they (at the very least) can be used to affirm the existence of ordered thin films of ILs (as opposed to thicker IL films where molecular ordering is lost), X-ray absorption can be used to determine the orientation of any composite resonant structures. The N K-edge NEXAFS spectra for [C_8C_1Im][BF_4] on ZnO (0001) at incidence angles of 30°, 50°, and 90° are shown on in Figure 5.8a. The N K-edge NEXAFS spectra at incidence angles of 30° and 90° for [C_8C_1Im][BF_4] on ZnO (10-10) is shown in Figure 5.8b. The π^* feature in the NEXAFS spectrum for the IL on ZnO (0001) does not change significantly in intensity relative to the σ^* feature at 30°, 50° or 90°. The lack of change in intensity indicates that there is no ordering at the surface, and is therefore indicative of a thicker IL deposition [5]. However, for IL/ZnO (10-10), the π^* feature is more intense than the σ^* feature when the incident beam is 90° to the surface. Conversely, when the beam is incident at the grazing angle of 30° relative to the surface, the π^* feature is smaller than the σ^* feature. This indicates a preferential orientation of the imidazolium ring of the cation on the ZnO (10-10) surface, and thus indicates the existence of a thin and ordered IL layer. This supports the assessment of the O 1s XPS data and the calculations made for the thicknesses of the respective IL layers. Furthermore, in Figure 5.8b, the greater intensity of the π^* feature with the beam at normal incidence would indicate that the imidazolium ring of the cation is oriented at an angle that

is closer to the surface normal (and therefore more 'upright' relative to the surface), rather than oriented at an angle that is closer to the surface itself. In order to ascertain a more precise orientation, more higher-quality X-ray absorption spectra at a greater variety of angles would need to be recorded. Evidence suggesting the imidazolium ring orientates in a more 'upright' position on ZnO (10-10) would offer an interesting contrast to that observed for thin depositions of $[C_4C_1Im][BF_4]$ on TiO_2 (101) [5], where the imidazolium ring orients at an angle of ~32° to the surface.

The N 1s spectrum of the IL on ZnO (0001), represented by the green line, is shown in Figure 5.7c(i). While the $[C_8C_1Im]^+$ cation consists of two nitrogen atoms, they can be considered chemically equivalent due to resonance effects [24], and thus produce one signal in the N 1s region. The N 1s spectrum in Figure 5.7c(i) has been fitted with three peaks. The peak at ~401.6 eV is attributed to the nitrogen in the $[C_8C_1Im]^+$ cation [5, 24]. The other two signals, at ~400.0 eV and 399.0 eV respectively are likely to be the result of beam damage. The appearance of beam damage peaks in the N 1s region is reported in numerous works involving ILs [2, 5, 34]. Furthermore, ANTARES is a powerful undulator beamline, and it is likely that the flux of the beam was great enough to cause some damage to the IL films despite changing positions on the sample after every scan and cooling the substrate. The N 1s region for IL/ZnO (10-10) (Figure 5.7c(ii)) displays a different shape to that of IL/ZnO (0001), and features associated with beam damage are more intense than for IL/ZnO (0001). Despite the same raster process being applied to the spectra as for IL/ZnO (0001), it appears that significant damage due to prolonged X-ray exposure has been sustained by this system. This behaviour is consistent with that of a thin IL film, which are known to be more susceptible to beam damage than thicker films of IL [2, 34].

The F 1s spectrum of the IL on ZnO (0001), shown in Figure 5.7d(i), is represented by the blue line and is composed of just one signal. The BE of this peak is consistent with that of the $[BF_4]^-$ anion, and is therefore attributed to $[BF_4]^-$. In an XPS study of the same IL on a Cu (111) substrate by Syres and Jones [35], the $[BF_4]^-$ anion reacted with the Cu, forming chemisorbed fluorine (Cu-F) and boron trifluoride (BF_3). The gaseous BF_3 simply desorbed, leaving a single F species on the Cu substrate. While there may be weak interaction

between the anion and ZnO substrate, previous works investigating the interactions between [BF$_4$]$^-$-containing ILs and ZnO do not seem to suggest any kind of chemisorption of F or B [29]. The F 1s spectrum for [C$_8$C$_1$Im][BF$_4$] on ZnO (10-10) is shown in Figure 5.7d(ii), and is slightly broader than that shown in Figure 5.7d(i). This may indicate the presence of a second peak alongside that associated with [BF$_4$]$^-$, but is difficult to resolve, and cannot be fitted without ambiguity. Babucci et al [29] suggested that the interaction between the cation and O^{2-} of ZnO weakened the cation-anion interactions, which subsequently strengthened the B-F bonds in the anion. It is difficult to de-convolute the C 1s region, and thus it cannot be determined whether the cation interacts differently with ZnO (0001) than ZnO (10-10) (or vice versa). It may be the case, however, that a stronger cation-substrate interaction would lead to a weaker cation-anion interaction, and thus lead to a strengthening of the B-F bonds of the anion. This would then result in the peaks associated with the anion shifting to a higher BE. It can be seen for both the F 1s and B 1s regions that there is a clear difference in BE between each system. When compared to the F 1s signal from IL/ZnO (0001), the F 1s signal from IL/ZnO (10-10) is shifted to a lower BE by approximately 1 eV. Similarly, the B 1s signal for the IL on ZnO (10-10) (Figure 5.7e(ii)) is shifted to a lower BE by approximately 2 eV compared to the IL on ZnO (0001) (Figure 5.7e(i)). Slight shifts are also seen in the regions associated with the cation. The C 1s and N 1s signals both appear to be shifted to a lower BE than those for IL/ZnO (0001), by approximately 0.5-1.0 eV. Under the assumption made above, this would mean the cation is interacting more strongly with the (0001) surface than with the (10-10). In order to investigate whether or not the cation experiences a stronger interaction with the (0001) surface, theoretical calculations could be undertaken to explore any differences in binding energies of IL/substrate bonds.

Table 5.3: Summary of fitted peak assignments of $[C_8C_1Im][BF_4]$ on ZnO (0001) and on ZnO (10-10), together with their respective binding energy (BE) values.

Substrate	Region	BE (eV) (±0.1 eV)	Assignment
ZnO (0001)	O 1s	530.0	O_2^- of ZnO
		531.3	OH groups
		532.5	H_2O, cation-substrate interactions
	N 1s	401.6	Imidazolium N of $[C_8C_1Im]^+$ cation
		400.0	Beam damage species
		399.0	Beam damage species
	F 1s	685.7	F of $[BF_4]^-$ anion
ZnO (10-10)	O 1s	530.0	O_2^- of ZnO
		531.3	OH groups
		532.5	H_2O, cation-substrate interactions
	N 1s	401.6	Imidazolium N of $[C_8C_1Im]^+$ cation
		400.0	Beam damage species
		399.0	Beam damage species
	F 1s	685.3	F of $[BF_4]^-$ anion

Babucci et al [29] investigated the thermal stability of the analogous IL $[C_4C_1Im][BF_4]$ on ZnO as well as other transition metals, using thermogravimetric analysis (TGA) and FTIR spectroscopy. They found that the decomposition of the IL starts with the weakening of the bond between the cation and the substrate. This subsequently influences the interactions between the imidazolium ring and the butyl group, as well as affecting the bonds within the ring itself. Furthermore, they suggest that the weakened cation-substrate interaction has a knock-on effect on the cation-anion interactions, whereby anion-substrate interactions develop, resulting in a structural loss of the IL.

As previously mentioned, cation-substrate interactions may influence the strength of the bonds within the $[BF_4]^-$ anion, leading to an upward shift in XPS core level binding energies in the F 1s and B 1s region. Furthermore, were cation-substrate interactions to weaken, it follows that the subsequent influence on the cation-anion interactions would also cause the B-F bonding in the anion to weaken. This could then cause a shift in the F 1s and B 1s core XPS regions toward lower binding energies.

The thermal stability of $[C_4C_1Im][BF_4]$, and its subsequent effects on IL/substrate interactions, was investigated on the polar surface ZnO (0001) using XPS. The C 1s region at NE and GE at each temperature are shown in Figure 5.9. The shape of the region should be similar to that of the analogous

[C_8C_1Im][BF_4], where superimposed signals create the characteristic two-peak shape of the region. Because the [C_4C_1Im]$^+$ cation has a shorter alkyl chain, the lowest BE peak is smaller in relative intensity [24, 36]. At -150°C, four peaks can be fitted to the NE and GE spectra (a summary of binding energies and assignments of peaks is featured in Table 5.4). The peak at 284.4 eV is, assigned to the alkyl chain of the IL in corroboration with literature [5, 24]. The peak at 286.2 eV arises from a combination of signals attributed to the carbon atoms just outside the imidazolium ring (denoted C_2 in Figure 5.2 of the structure of the [C_4C_1Im]$^+$ cation), and the carbon atoms, C_3, inside the imidazolium ring. The peaks attributed to the C_2 and C_3 carbons are close in BE (typical separation of 0.2 eV - 0.4 eV [5, 24]; and to illustrate BE fluctuations in later spectra, it can be fitted with one, slightly wider, peak (full width at half maximum of this peak at -150°C ~ 1.6 eV). The peak at 287.0 eV is attributed to the C_4 carbon, between the two N atoms inside the imidazolium ring. A shoulder is also present at ~288.4 eV in both the NE and GE C 1s spectra, but is more prevalent at NE. This indicates an extra C species, which likely to be beneath the IL rather than on the surface since the NE spectra are more sensitive to signals from deeper within the sample than GE. This signal could be due to adsorbed contaminant CO on the ZnO surface, as CO tends to adsorb onto oxide surfaces at very low temperatures (<-120°C) [37, 38]. This feature was not seen in the C 1s spectrum for [C_8C_1Im][BF_4]/ZnO (0001), but the [C_8C_1Im][BF_4]/ZnO (0001) sample was cooled after IL deposition. It is difficult to determine whether or not this feature is present in the C 1s region for [C_8C_1Im][BF4]/ZnO (10-10). The deposition of [C_8C_1Im][BF_4] is considered ultrathin, and thus a C 1s signal arising from CO absorbed on the ZnO (10-10) surface would be, in all likelihood, intense enough to be resolved. This does not appear to be the case, which may indicate that there was some contaminant species in the background vacuum of the analysis chamber on the AU-MATline beamline, and minimal contamination from the background vacuum of the analysis chamber on the ANTARES beamline. The shoulder disappears when the sample is heated to -80°C, which could be indicative of CO desorption from the ZnO surface.
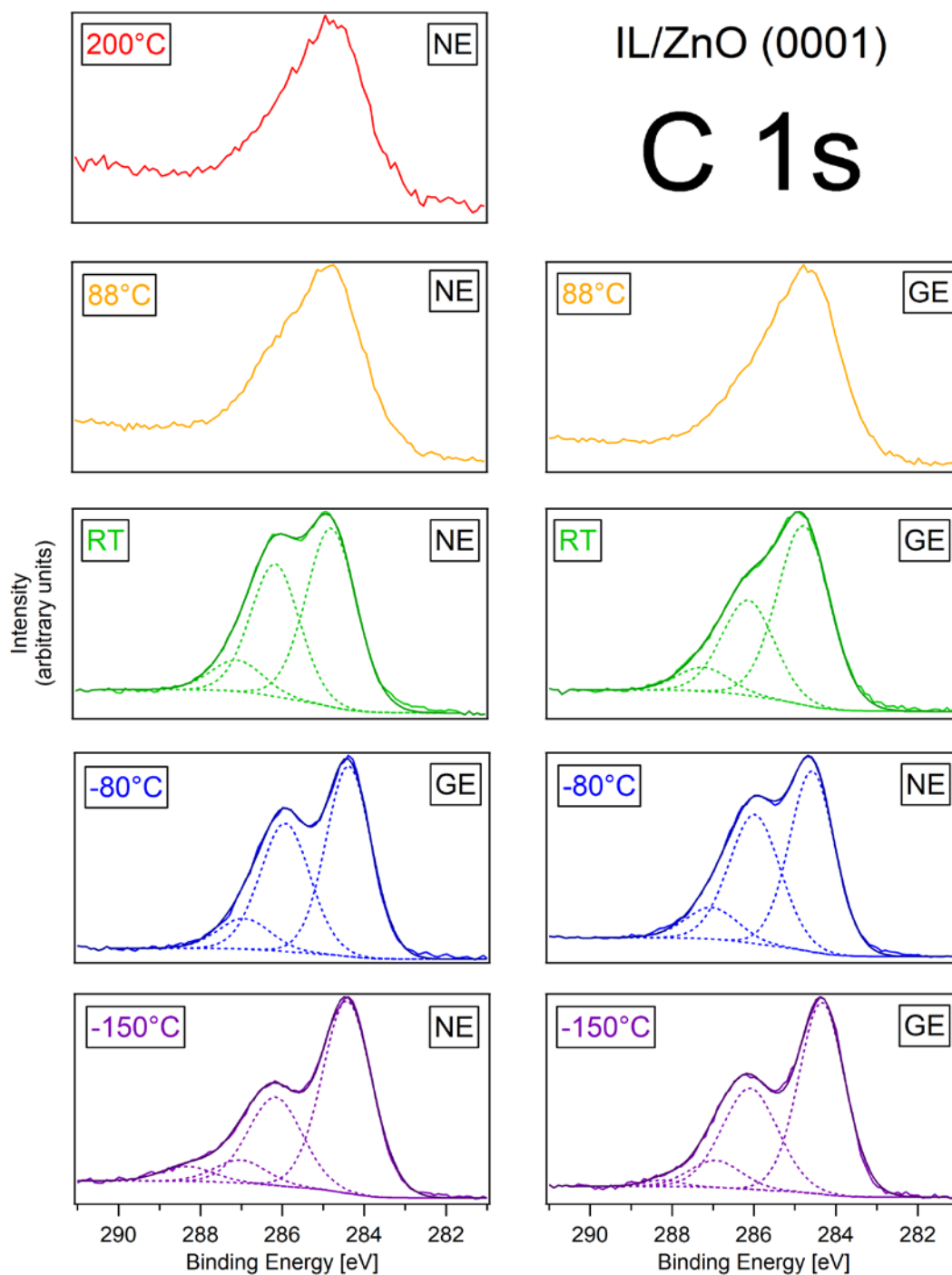
Figure 5.9: C 1s spectra recorded at normal emission (NE, left) and at grazing emission (GE, right) for [C_4C_1Im][BF_4] on ZnO (0001); for temperatures ranging from -150°C (bottom, shown in purple), to 200°C (top, shown in red).

At RT, the separation between the alkyl peak at 284.4 eV and the C_2+C_3 peak at 286.2 eV in the NE spectrum decreases by approximately 0.4 eV. The evident shift could be indicative of a phase transition of the IL; from a glassy solid to a liquid. Evidence of this kind of phase transition in an imidazolium-based IL in XP spectra has been seen previously on a metal surface [35]. Throughout the increase in temperature from -150°C to RT, the peak associated

with the alkyl chain is consistently dominant, particularly in the GE spectra, indicating the preferential orientation of the alkyl chain out towards vacuum (a phenomenon seen previously in this IL [39-42]) even at low temperatures.

As the sample is heated to 88°C, there is a change in the shape of the C 1s region, and devolves from two distinct peaks (the intensity of the alkyl peak approximately twice that of the peak associated with the imidazolium ring carbons) to one asymmetrical peak at ~284.6 eV. This indicates BE shifts of existing peaks and/or development of new peaks in the region, both associated with changes in bonding within the cation and the formation of other carbon species. This could therefore indicate decomposition of the IL on the ZnO (0001) surface. Babucci et al [29] demonstrated that $[C_4C_1Im][BF_4]$ on ZnO decomposes when the system is kept at a constant temperature of 250°C for periods of 6, 10, and 24 hours; displaying more advanced decomposition for longer time periods. In that study, powder-form ZnO was used, which will have contained a variety of surface terminations [43-46]. It can, therefore, be assumed that in their study, interactions between the IL and the ZnO would have taken place on many different terminations of ZnO. It may be the case that certain terminations of ZnO reduce the thermal stability limits of ILs more than others, and the findings of Babucci et al are averaged from various ZnO surface terminations. Therefore, it may be possible that the ZnO (0001) termination acts like a catalyst, reducing the thermal stability limit to below 100°C. This catalytic effect on the thermal stability limits may have also influenced decomposition of $[C_8C_1Im][BF_4]$/ZnO.

The change in the shape of the C 1s region continues to 200°C. One possible decomposition mechanism for $[C_4C_1Im][BF_4]$ is C-N bond cleavage on the alkyl side of the imidazolium ring (see Scheme 5.1a), which causes the IL to break down into a variety of hydrocarbon species [47]. Combined with decomposition of the anion, various alkylfluoride species (such as 2-propylfluoride and 1-fluorobutane) could also be formed [48]. This kind of decomposition would manifest itself as a shift in the binding energy in the F 1s and B 1s spectra as well as forming new peaks in the C 1s, and thus changing the shape with further degradation of the IL. The F 1s and B 1s spectra are discussed later in this chapter. The change in shape of the C 1s region is consistent with the idea that the IL is breaking at the alkyl-side C-N bond, forming, at least, various

hydrocarbon species. However, the emergence of extra species means the C 1s cannot be de-convoluted without ambiguity.
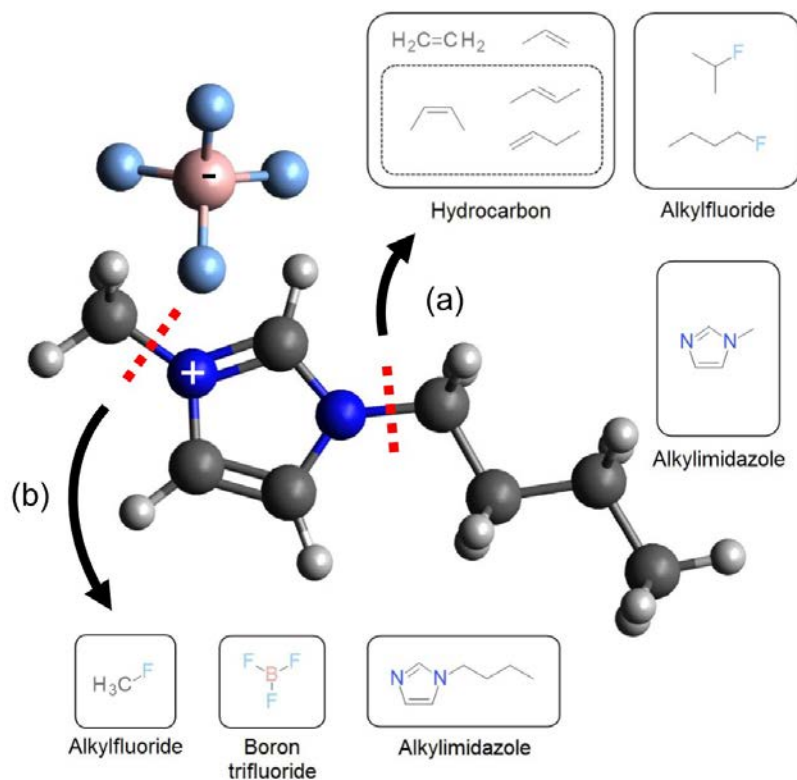
Scheme 5.1: Diagram showing decomposition pathways of $[C_4C_1Im][BF_4]$ via cleavage of the alkyl chain (a), or via cleavage of the methyl group (b). As described in the text, a variety of hydrocarbon species (a), some alkylfluoride species (a and b), some alkylimidazole species (a and b), and boron trifluoride (b) may form as a result of decomposition.
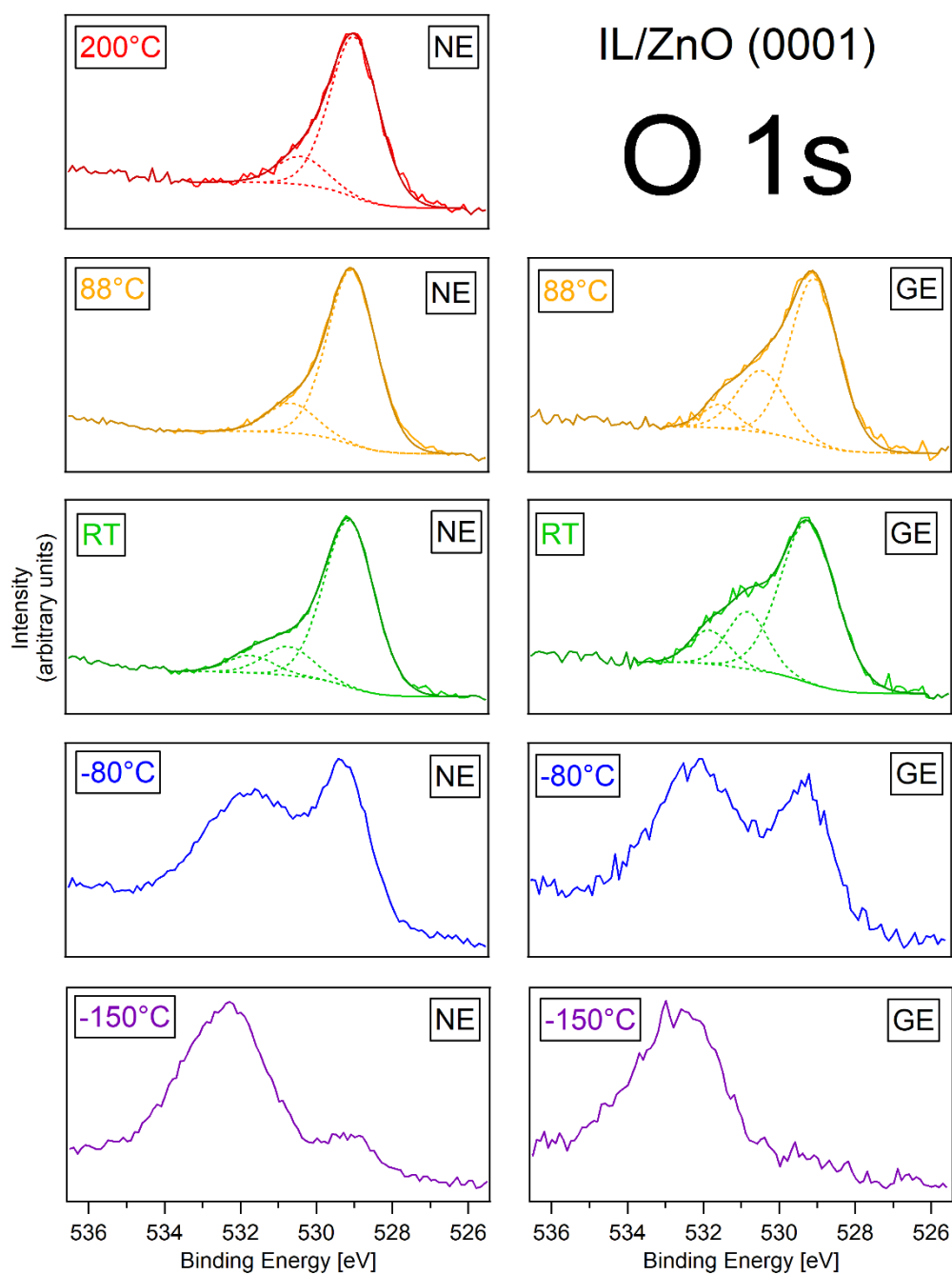
Figure 5.10: O 1s spectra recorded at normal emission (NE, left) and at grazing emission (GE, right) for [C$_4$C$_1$Im][BF$_4$] on ZnO (0001); for temperatures ranging from -150°C (bottom, shown in purple), to 200°C (top, shown in red).

Figure 5.10 shows the O 1s spectra at each temperature, for both NE (left) and GE (right). At -150°C, the region is distinctly different to that of [C$_8$C$_1$Im][BF$_4$]/ZnO (0001). There are two peaks in the region: a large peak at ~532.3 eV, and a smaller peak at 529.1 eV. The peak at 529.1 eV is assigned to O in the ZnO substrate [20, 49, 50]. The larger peak is likely to be made up of multiple signals arising from various species adsorbed on both the ZnO and IL surfaces, and possibly trapped between the IL layers. The peak at 532.3 eV

spans a large BE range, which is attributed to a combination of multiple overlapped composite peaks (and thus resulting in a peak that is of a greater relative intensity than the substrate O peak), and broadening due to sample charging. Sample charging is known to occur for ILs below their glass transition temperature, since the phase change from a liquid to a glassy solid results in the IL behaving more like an insulator than a conductor [51]. There exists some discrepancy in assignments of O 1s composite peaks to non-metal oxide species on ZnO surfaces. The peak at 532.3 eV is likely to include a signal from adsorbed water from the background vacuum due to the substrate being cooled prior to IL deposition. Water molecules could have adsorbed at the ZnO surface prior to IL deposition [28, 52]. Water could also have co-adsorbed during IL deposition, or adsorbed on top of the IL after deposition. It is also likely that there are hydroxyl (OH) groups present at the ZnO surface, which tend to manifest as peaks at ~1.4 eV-1.6 eV greater than the substrate O [28, 49, 50, 53]- also seen for $[C_8C_1Im][BF_4]$/ZnO (0001). As mentioned earlier, in the discussion of the C 1s region at this temperature, there may be some contribution from CO adsorbed on the surface, as peaks associated with CO typically appear at the higher BE edge of the O 1s region [54-56]. Additionally, in the discussion for the O 1s region of $[C_8C_1Im][BF_4]$ on ZnO (0001) and ZnO (10-10), we postulated that there may also be a signal originating from cation-substrate interactions, which could manifest at a BE that falls within the range of the peak. However, a signal associated with this interaction cannot be resolved without ambiguity from the other signals at this temperature.

As the sample is heated to -80°C, the O 1s region begins to change shape: the peak at ~532.3 eV appears to decrease in relative intensity, while the peak at ~529.1 eV appears to increase in relative intensity. Similarly to the C 1s region, these changes support the idea of CO desorbing from the ZnO surface. Water multilayers are also likely to desorb from the IL surface at this temperature, which could be contributing to the shape change in the O 1s spectra [34, 52]. Multilayers of water have been found to desorb from an imidazolium-based IL at low temperatures (approximately -90°C), leaving only a monolayer that eventually desorbs at a higher temperature (approximately -30°C)[34]. Desorption of both CO and water multilayers are consistent with the apparent shift of the larger peak by ~0.4 eV toward lower BE, and would account for its decrease in relative intensity in both the NE and GE spectra at this temperature.

The peaks attributed to hydroxyl groups, water, and cation-substrate interactions are likely to still remain at this temperature, but again, these peaks cannot be resolved unambiguously.

As the sample is heated to RT, the peak associated with O in the ZnO substrate dominates, and the shoulder at the higher binding energy edge may be resolved, with composite peaks attributed to hydroxyl groups and molecular water at 530.7 eV and 531.7 eV respectively [28]. These features are of a greater intensity at GE than at NE, indicating they are located nearer to the surface of the sample. This is consistent with the presence of water within the IL multilayers. Water adsorbed on an imidazolium-based IL at low temperatures has been seen to absorb into the bulk at approximately -30°C [52], and is thought to stabilise in the bulk through interactions with the imidazolium groups [57, 58]. This corroborates with the assignment made for the peak at 531.7 eV to water from the background vacuum. The signals associated with hydroxyl groups and cation-anion interactions are likely to remain as the sample is heated beyond RT, but small amounts of water in IL can be removed from ILs by heating to ~60-80°C under vacuum [57, 58]. When the sample is heated to 88°C, the peak at 531.3 eV decreases in relative intensity. The peak has disappeared from the spectra recorded at NE, and only makes up approximately 6.8% of the region at GE. This supports the idea that water trapped within the multilayers has largely desorbed, and it is possible that the peak at 531.3 eV mainly arises due to cation-substrate interaction at this temperature. Investigating monolayer to multilayer coverage of ILs on surfaces using XPS at different photoelectron emission angles has shown that signals associated with IL-substrate interaction decrease significantly with additional IL layers. For example, Wagstaffe et al [5] investigated the interactions of approximately monolayer coverage of $[C_4C_1Im][BF_4]$ on anatase TiO_2 (101) using XPS. They found that the F in the anion interacted with the Ti in the TiO_2 substrate, which manifested as a signal in the F 1s region. The same feature was seen in the work discussed in Chapter 3, of $[C_4C_1Im][BF_4]$ on rutile TiO_2 (110) with a thicker deposition (approximately three layers). In that case, the peak associated with the Ti-F interaction was much less intense because of the increased IL layer thickness, causing greater attenuation of the photoelectrons emitted from atoms involved in those bonds. Using a combination of the TPP-2M calculation for the inelastic mean free path for organic materials [32], and

the Beer-Lambert relation for photoelectron attenuation in thin films [22], the thickness of the deposition of $[C_4C_1Im][BF_4]$ on ZnO (0001) was calculated (the calculation for IL deposition thickness can be found in Appendix A). It was found to be approximately (15.2 ± 0.3)Å, which is more than twice the thickness of the deposition of $[C_8C_1Im][BF_4]$ on ZnO (10-10). It therefore stands to reason that the peak associated with cation-substrate interaction is much less intense for this system, and would be easily obscured by adsorption of any other contaminate species. However, in the C 1s region, there was evidence of decomposition at this temperature and therefore the signal attributed to cation-substrate interactions may be less intense due to some IL decomposition at the surface of the ZnO (0001). Heating through to 200°C, the peak at 531.3 eV disappears from the GE spectrum entirely- indicating further decomposition/desorption of the IL.
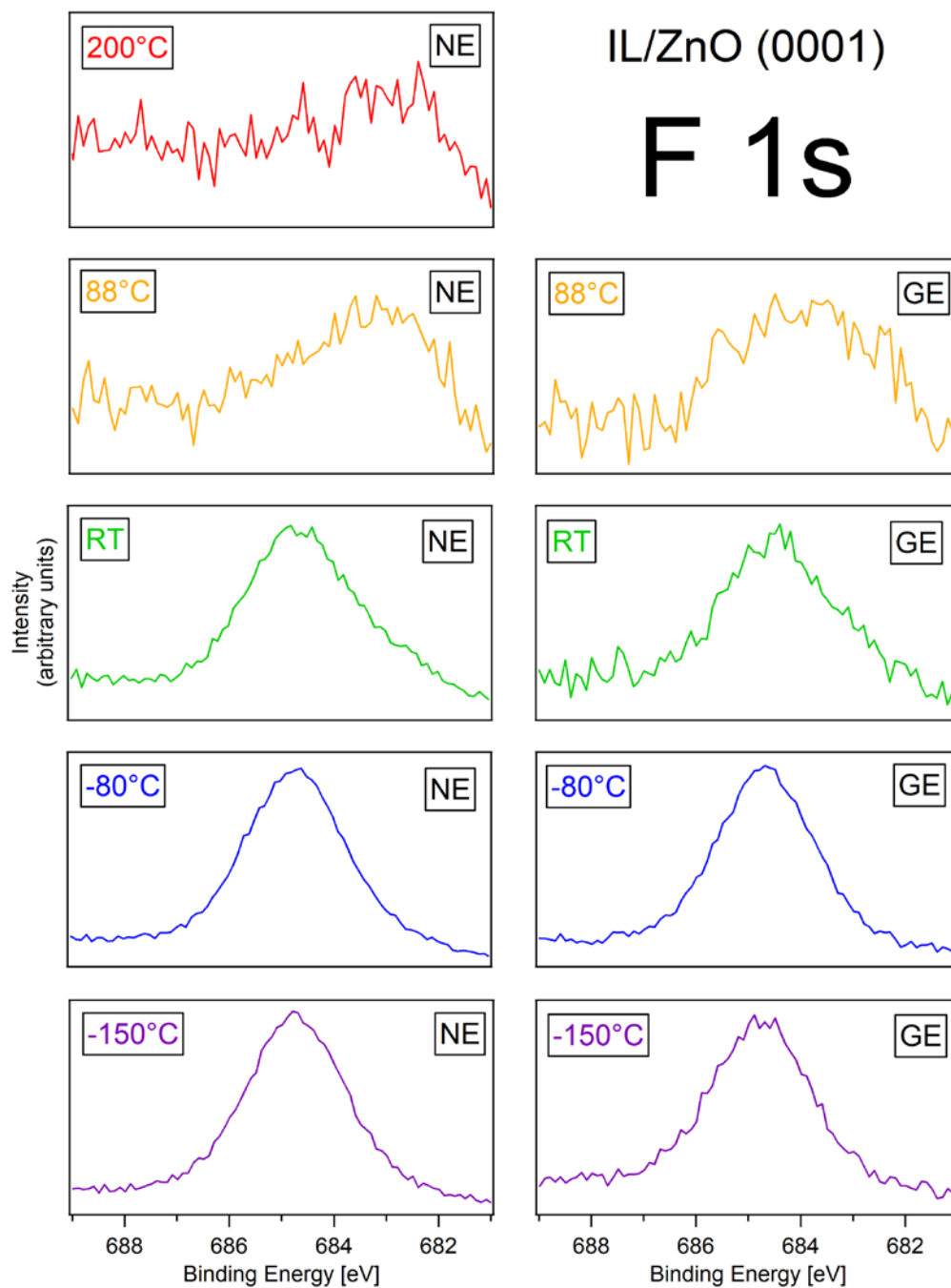
Figure 5.11: F 1s spectra recorded at normal emission (NE, left) and at grazing emission (GE, right) for [C₄C₁Im][BF₄] on ZnO (0001); for temperatures ranging from -150°C (bottom, shown in purple), to 200°C (top, shown in red).

The F 1s region is shown in Figure 5.11 at NE from -150°C to 200°C (left) and at GE from -150°C to 88°C (right). At -150°C and -80°C, the region is populated by only one symmetrical peak at 684.7 eV. This is attributed to the F in the [BF₄]⁻ anion [24]. As the system is heated through to RT, the peak at 684.7 becomes less symmetrical, indicating the emergence of a second peak. There does not appear to be much difference in the relative intensity of this peak between NE and GE, indicating that it is a species present at both the surface

and in the bulk. In the discussion of $[C_8C_1Im][BF_4]$ on polar and nonpolar ZnO, we theorised that the change in the cation-substrate interactions could influence the cation-anion interactions, and subsequently affect the B-F bonding in the anion. Therefore, a weakening of the cation-substrate interactions would lead to a strengthening of the cation-anion interactions, and a weakening of the B-F bonds in the anion. It may be possible that the asymmetrical nature of the F 1s region in Figure 5.11 at RT may be due to the nature of those B-F bonds weakening, causing a shift toward lower BE.

As the sample is heated to 88°C, the F 1s region drastically changes shape. Rather than being entirely due to a continuing change in cation-substrate interactions, this altering shape may be due to IL decomposition, causing other F species to form. This would therefore produce another peak or multiple peaks, and consequently change the shape of the region. Numerous fluorine species can be formed from thermal decomposition of $[C_4C_1Im][BF_4]$ [47, 48]. These include: 2-propylfluoride and 1-fluorobutane (Scheme 5.1a, box labelled alkylfluoride, top and bottom molecules respectively) from cleavage of the alkyl-side C-N bond; and methyl fluororide (Scheme 5.1b, box labelled alkylfluoride) and boron trifluoride (BF_3, also in Scheme 5.1b) from cleavage of the methyl-side C-N bond [48]. Alkylfluoride species are more likely to manifest as a peak at a lower BE than $[BF_4]^-$ in the F 1s region due to an overall reduced electronegativity, which could explain the appearance of a peak at lower BE.

As the sample is heated to 200°C, the F 1s region continues to change, and becomes much less intense than that recorded at 88°C. As shown in Scheme 5.1, one of the species formed from cleavage of the methyl-side C-N bond is BF_3. Syres and Jones [35] found that $[C_8C_1Im][BF_4]$ decomposed on Cu (111), forming and desorbing BF_3 in the process. The formation of BF_3 would account for the shift in the F 1s region at this temperature (since another F species would be formed in conjunction with the formation of BF_3) as well as account for the reduction of the overall F 1s signal intensity, as BF_3 would desorb from the surface.
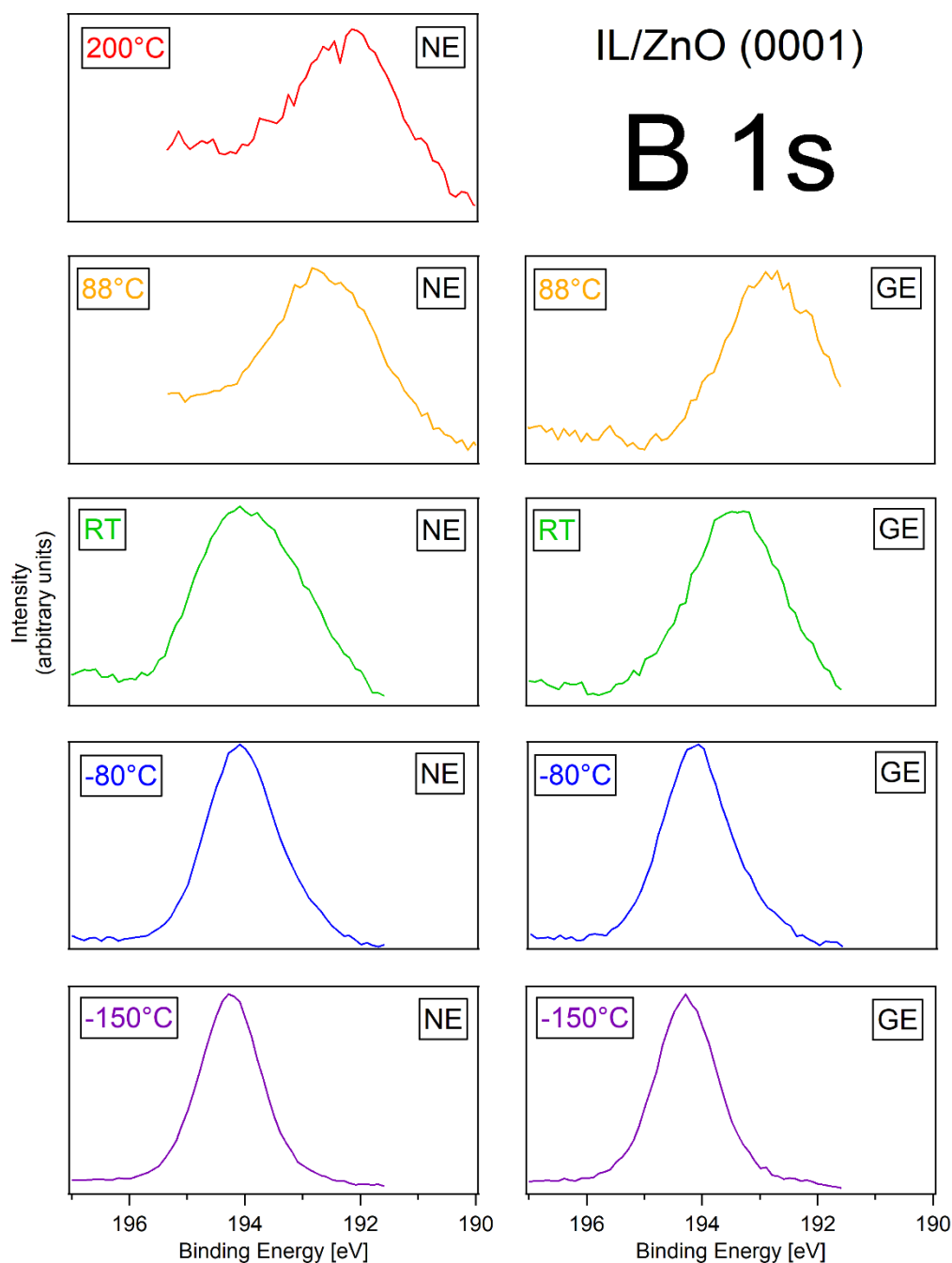
Figure 5.12: B 1s spectra recorded at normal emission (NE, left) and at grazing emission (GE, right) for [C$_4$C$_1$Im][BF$_4$] on ZnO (0001); for temperatures ranging from -150°C (bottom, shown in purple), to 200°C (top, shown in red).

The changes seen in the F 1s region are corroborated by the B 1s region, but with even more extreme BE shifts at temperatures in excess of RT. Figure 5.12 shows the B 1s region at NE from -150°C to 200°C (left) and at GE from -150°C to 88°C (right). At -150°C, the region consists of a single symmetric peak at 194.3 eV, which is attributed to B in the [BF$_4$]$^-$ anion [24]. The region begins to change shape at -80°C: the peak at 194.3 eV is no longer symmetrical, and has shifted to lower BE in both the NE and GE spectra by approximately 0.3 eV.

This change could be the result of a phase change of the IL. If the transition from glassy solid to liquid changes the nature of the cation-anion interactions, this change in shape may be a consequence of that change in the interactions. Conversely, there does not appear to be as significant a change in the F 1s region compared to the B 1s region. The peak appears to shift and become more asymmetrical as the sample is heated to RT. As postulated for the changes in the F 1s region, it may be the case that the nature of the cation-substrate interactions is causing the change in shape of the B 1s region.

Heating the sample through 88°C results in an even greater shift toward lower BE in the B 1s region, by approximately 1.5 eV compared to the spectrum recorded at RT. As was suggested for the F 1s region, these changes could be due to IL decomposition. If decomposition of the anion results in BF_3 and separate F species only (i.e. no other B species), the intensity of the B 1s signal would continue to decrease until the IL completely decomposed. There is a decrease in the intensity in the B 1s region at higher temperatures, with the intensity at 200°C much less than that recorded at 88°C, and this is attributed to the formation and desorption of BF_3. A peak still remains in the B 1s region, which indicates that the IL does not decompose completely. This asymmetrical peak is therefore still attributed to the $[BF_4]^-$ anion, but the shift of this peak toward lower BE is attributed to IL decomposition and its subsequent effects on cation-anion interactions.

Table 5.4: Summary of fitted peak assignments of $[C_4C_1Im][BF_4]$ on ZnO (0001), together with their respective binding energy (BE) values.

Region	BE (eV) (±0.1 eV)	Assignment
C 1s	284.4	C_1 of $[C_4C_1Im][BF_4]$*
	286.2	$C_2 + C_3$ of $[C_4C_1Im][BF_4]$*
	287.0	C_4 of $[C_4C_1Im][BF_4]$*
	288.4	Contaminant CO**
O 1s	529.1	O_2^- of ZnO[†]
	530.7	OH groups[†]
	531.7	H_2O, cation-substrate bonding[†]

* BE at -150°C
** Feature in NE/GE spectra at -150°C condition only
[†] BE at RT

5.4 Discussion

Many of the early studies into the decomposition of ILs used fast-scanning thermogravimetric analysis (TGA) to determine the temperature of onset of decomposition. These methods involved a fast ramp-up in temperature (in excess of 10°C/min), heating the ILs to high temperatures for relatively short periods of time [21, 59-61]. Therefore, the temperatures at which ILs decompose in those conditions are sometimes referred to in the literature as the onset temperature, or T_{onset} [62]. This value is seen as an overestimate of their thermal stability in the context of heat-transfer applications; where ILs are exposed to lower temperatures than their onset temperature, but for extended periods of time. In reality, ILs can undergo significant decomposition if they are kept at lower temperatures than T_{onset} for longer periods. This phenomenon is referred to as the long-term thermal stability. The long-term thermal stability of an IL will change depending on the desired working temperature for the IL (i.e. the temperature at which the IL will be kept for long periods of time), and the time for which the IL is kept at that temperature [60, 63, 64]. The rate at which the IL is heated will also affect its long-term thermal stability [60]. One property often reported to quantify the long-term thermal stability of ILs is $T_{0.01/10h}$. It is defined as the temperature at which 1% of the IL mass is lost over a period of 10h. Studies into the long-term thermal stability of 1-alkyl-*n*-imidazolium tetrafluoroborate ILs have reported a significant difference between T_{onset} and $T_{0.01/10h}$, but are still considered very thermally stable since both temperature values are high. Cao et al [65] found that for $[C_8C_1Im][BF_4]$, the difference between T_{onset} and $T_{0.01/10h}$ was 198°C, with its value for $T_{0.01/10h}$ at 199°C. For the purposes of physical vapour deposition (PVD) in UHV, the IL will need to be heated to an appropriate temperature between $T_{0.01/10h}$ and T_{onset}. This way, the IL is heated to a point where it will vaporise and then be carried through the pressure gradient to be deposited as ion pairs on the substrate [66, 67]. For PVD, the IL should not be heated to such a temperature that the IL begins to decompose. Van Valkenburg et al [63] investigated the decomposition rate (in %mass/min) of two analogous ILs with the same anion, $[C_2C_1Im][BF_4]$ and $[C_4C_1Im][BF_4]$, at isotherms of 250°C to 450°C. They found that the ILs showed significant decomposition when heated to, and held at, a temperature of 350°C. Furthermore, they calculated the decomposition rate of $[C_2C_1Im][BF_4]$ to be

~0.47%/min at 350°C- almost twice that of $[C_4C_1Im][BF_4]$ at 0.24%/min at the same temperature. For the investigation into $[C_8C_1Im][BF_4]$ on polar and non-polar ZnO, the IL was heated with a temperature gradient of ~22°C/min to ~350°C prior to the deposition on ZnO (0001), and was at ~350°C for approximately 20 minutes. For the deposition on ZnO (10-10), however, the deposition time was ~420 minutes. When kept at the evaporation temperature for several hours (which was the case for the deposition on ZnO (10-10)), decomposition of the IL may take place, and therefore may not deposit IL pairs intact. This may account for the asymmetrical line shape of the C 1s region for $[C_8C_1Im][BF_4]$ on ZnO (10-10).

The polar ZnO (0001) surface has shown to catalyse the decomposition of methanol and formic acid [68, 69], and ZnO-based catalysts are used in methanol synthesis [70]. As mentioned earlier, the step edges of the ZnO (0001) surface are O-terminated. These step edges are thought to be connected to the reactivity of the surface, and therefore connected to the reactions that take place at the surface. As evidenced by Babucci et al [29], which is supported by our investigation of $[C_4C_1Im][BF_4]$ multilayers on ZnO (0001), the thermal stability limits are significantly reduced when 1-alkyl-*n*-imidazolium tetrafluoroborate ILs are deposited on ZnO. It is also possible that multilayers of IL could be more sensitive to temperature changes than bulk IL, and the accelerated decomposition of $[C_4C_1Im][BF_4]$ could actually be due to a combination of these factors. Babucci et al [29] investigated the short-term thermal stability limits of $[C_4C_1Im][BF_4]$ on ZnO compared to values for bulk $[C_4C_1Im][BF_4]$ from literature (i.e. heating at 10°C/min from room temperature to 600°C and recording the temperature of the onset of decomposition). For bulk IL, the thermal stability limit was reported in the literature to be approximately 400°C, while Babucci et al found in the presence of ZnO it was 333°C. Additionally, the approximate thickness of the IL layer on ZnO in their work was of a similar order of magnitude as the data discussed here, at a value of 12.4 Å. They ruled out the effects of coverage on their findings since the T_{onset} value they measured for one of the thinnest layers of IL was one of the largest values, and thus attributed the decrease in thermal stability to the nature of the oxide surface, specifically its basicity. It is evident from our data that the polar ZnO (0001) surface reduced the thermal stability of $[C_4C_1Im][BF_4]$ to even lower temperatures than those observed by Babucci et al, which would support the

theory that different terminations of ZnO will reduce the thermal stability of IL multilayers to varying degrees. It may be the case that the polar terminations reduce the thermal stability more than the non-polar terminations. In order to investigate this, XPS spectra at NE and GE could be recorded for a multilayer deposition of $[C_4C_1Im][BF_4]$ on ZnO (10-10) under similar temperature conditions for comparison with those recorded here.

The ordering and interactions of an IL on oxide surfaces has significant consequences for potential applications involving ILs and oxides, such as IL-based catalysis, and photovoltaic systems with IL electrolytes. Therefore, a large reduction of the thermal stability of 1-alkyl-n-imidazolium tetrafluoroborate ILs on ZnO may have a negative impact on the effectiveness of ZnO-based catalysts used in systems (such as SILP and SCILL) at higher temperatures.

5.5 Conclusion

The structure and ordering of $[C_8C_1Im][BF_4]$ on polar and nonpolar ZnO surfaces was studied using XPS and N K-edge NEXAFS. The XPS revealed interactions between $[C_8C_1Im][BF_4]$ and the ZnO substrate, characterised by a peak at higher BE in the O 1s region. This interaction is suggested to occur specifically with the C_4 carbon in the imidazolium ring of the cation. Peaks in the regions associated with the anion, F 1s and B 1s, were shifted to a higher BE for the IL deposition on ZnO (0001) compared to the IL deposition on ZnO (10-10), inferring a stronger interaction between the IL and the ZnO (0001) substrate. The $[C_8C_1Im][BF_4]$ deposition on the ZnO (10-10) substrate was found to be approximately (6.30 ± 0.08) Å, just over half the thickness of that calculated for ZnO (0001), which was (11.26 ± 0.08) Å. The N K-edge NEXAFS for the deposition on ZnO (10-10) revealed a preferential orientation of the imidazolium ring, displaying evidence of an ultrathin ordered layer, and simultaneously supports the estimation made of the thickness of the IL layer. The N K-edge NEXAFS for $[C_8C_1Im][BF_4]$/ZnO (0001) did not appear to change with angle- indicative of a thicker, and more disordered IL layer.

Additionally, the thermal stability of $[C_4C_1Im][BF_4]$ on the polar ZnO (0001) surface was investigated using XPS at normal and grazing photoemission angles. At low temperatures, the glassy IL appeared to be insulating, behaviour which manifested as broadening of XPS core level peaks, but as it was heated

to room temperature, shifts in BE indicate a change in phase from a glassy solid to a liquid. As the IL was heated to temperatures in excess of 80°C, the IL began to decompose, manifesting as additional peaks in the C 1s and F 1s regions, and shifts in the B 1s spectra. The feature associated with cation-substrate interactions in the O 1s region decreased in relative intensity with increasing temperature, indicating desorption of the IL from the ZnO (0001) surface. The long-term thermal stability limit of the same IL with powdered ZnO is quoted in the literature to be ~300°C, while the IL began to show signs of significant decomposition at a much lower temperature. This kind of extreme reduction in thermal stability may have negative consequences for the use of ZnO catalysts in IL-based catalysis systems such as SILP and SCILL, and for the use of $[C_4C_1Im][BF_4]$ in ZnO-based photovoltaic systems under extreme solar heating.

Chapter 5 References

[1] R. Atkin, S.Z. El Abedin, R. Hayes, L.H.S. Gasparotto, N. Borisenko, F. Endres, *AFM and STM Studies on the Surface Interaction of [BMP]TFSA and [EMIm]TFSA Ionic Liquids with Au(111)*, Journal of Physical Chemistry C, 113 (2009) 13266-13272, D.O.I.: 10.1021/jp9026755

[2] T. Cremer, M. Stark, A. Deyko, H.-P. Steinrück, F. Maier, *Liquid/Solid Interface of Ultrathin Ionic Liquid Films:[C1C1Im][Tf2N] and [C8C1Im][Tf2N] on Au (111)*, Langmuir, 27 (2011) 3662-3671, D.O.I.: 10.1021/la105007c

[3] V.O. Santos, M.B. Alves, M.S. Carvalho, P.A.Z. Suarez, J.C. Rubim, *Surface-Enhanced Raman Scattering at the Silver Electrode/Ionic Liquid (BMIPF6) Interface*, Journal of Physical Chemistry B, 110 (2006) 20379-20385, D.O.I.: 10.1021/jp0643348

[4] M. Mezger, S. Schramm, H. Schröder, H. Reichert, M. Deutsch, E.J. De Souza, J.S. Okasinski, B.M. Ocko, V. Honkimäki, H. Dosch, *Layering of [BMIM]+-Based Ionic Liquids at a Charged Sapphire Interface*, Journal of Chemical Physics, 131 (2009) 094701, D.O.I.: 10.1063/1.3212613

[5] M. Wagstaffe, M.J. Jackman, K.L. Syres, A. Generalov, A.G. Thomas, *Ionic Liquid Ordering at an Oxide Surface*, Chemphyschem, 17 (2016) 3430-3434, D.O.I.: 10.1002/cphc.201600774

[6] A. Deyko, T. Cremer, F. Rietzler, S. Perkin, L. Crowhurst, T. Welton, H.-P. Steinrück, F. Maier, *Interfacial Behavior of Thin Ionic Liquid Films on Mica*, Journal of Physical Chemistry C, 117 (2013) 5101-5111, D.O.I.: 10.1021/jp3115397

[7] T. Cremer, L. Wibmer, S.K. Calderón, A. Deyko, F. Maier, H.-P. Steinrück, *Interfaces of Ionic Liquids and Transition Metal Surfaces—Adsorption, Growth, and Thermal Reactions of Ultrathin [C 1 C 1 Im][Tf 2 N] Films on Metallic and Oxidised Ni (111) Surfaces*, Physical Chemistry Chemical Physics, 14 (2012) 5153-5163, D.O.I.: 10.1039/C2CP40278E

[8] B.R. Lee, H. Choi, J. SunPark, H.J. Lee, S.O. Kim, J.Y. Kim, M.H. Song, *Surface Modification of Metal Oxide Using Ionic Liquid Molecules in Hybrid Organic-Inorganic Optoelectronic Devices*, Journal of Materials Chemistry, 21 (2011) 2051-2053, D.O.I.: 10.1039/c0jm03688a

[9] W. Yu, L. Huang, D. Yang, P. Fu, L. Zhou, J. Zhang, C. Li, *Efficiency Exceeding 10% for Inverted Polymer Solar Cells with a ZnO/Ionic Liquid*

Combined Cathode Interfacial Layer, Journal of Materials Chemistry A, 3 (2015) 10660-10665, D.O.I.: 10.1039/C5TA00930H

[10] M. Babucci, C.-Y. Fang, A.S. Hoffman, S.R. Bare, B.C. Gates, A. Uzun, *Tuning the Selectivity of Single-Site Supported Metal Catalysts with Ionic Liquids*, ACS Catalysis, 7 (2017) 6969-6972, D.O.I.: 10.1021/acscatal.7b02429

[11] H.P. Steinrück, J. Libuda, P. Wasserscheid, T. Cremer, C. Kolbeck, M. Laurin, F. Maier, M. Sobota, P. Schulz, M. Stark, *Surface Science and Model Catalysis with Ionic Liquid-Modified Materials*, Advanced Materials, 23 (2011) 2571-2587, D.O.I.: 10.1002/adma.201100211

[12] M. Niskanen, M. Kuisma, O. Cramariuc, V. Golovanov, T.I. Hukka, N. Tkachenko, T.T. Rantala, *Porphyrin Adsorbed on the (10$\overline{1}$0) Surface of the Wurtzite Structure of ZnO – Conformation Induced Effects on the Electron Transfer Characteristics*, Physical Chemistry Chemical Physics, 15 (2013) 17408-17418, D.O.I.: 10.1039/C3CP51685G

[13] Ü. Özgür, Y.I. Alivov, C. Liu, A. Teke, M.A. Reshchikov, S. Doğan, V. Avrutin, S.J. Cho, H. Morkoç, *A Comprehensive Review of ZnO Materials and Devices*, Journal of Applied Physics, 98 (2005) 041301, D.O.I.: 10.1063/1.1992666

[14] J. Huang, Z. Yin, Q. Zheng, *Applications of ZnO in Organic and Hybrid Solar Cells*, Energy & Environmental Science, 4 (2011) 3861-3877, D.O.I.: 10.1039/C1EE01873F

[15] Y. Choi, K. Futagami, T. Fujitani, J. Nakamura, *The Role of ZnO in Cu/ZnO Methanol Synthesis Catalysts — Morphology Effect or Active Site Model?*, Applied Catalysis A: General, 208 (2001) 163-167, D.O.I.: 10.1016/S0926-860X(00)00712-2

[16] K.M. Lee, C.W. Lai, K.S. Ngai, J.C. Juan, *Recent Developments of Zinc Oxide Based Photocatalyst in Water Treatment Technology: A Review*, Water Research, 88 (2016) 428-448, D.O.I.: 10.1016/j.watres.2015.09.045

[17] P.G. Loutzenhiser, A. Meier, A. Steinfeld, *Review of the Two-Step H2O/CO2-Splitting Solar Thermochemical Cycle Based on Zn/ZnO Redox Reactions*, Materials, 3 (2010), D.O.I.: 10.3390/ma3114922

[18] M. Sobota, M. Schmid, M. Happel, M. Amende, F. Maier, H.-P. Steinrück, N. Paape, P. Wasserscheid, M. Laurin, J.M. Gottfried, J. Libuda, *Ionic Liquid Based Model Catalysis: Interaction of [BMIM][Tf2N] with Pd Nanoparticles*

Supported on an Ordered Alumina Film, Physical Chemistry Chemical Physics, 12 (2010) 10610-10621, D.O.I.: 10.1039/C003753B

[19] M. Sobota, M. Happel, M. Amende, N. Paape, P. Wasserscheid, M. Laurin, J. Libuda, *Ligand Effects in SCILL Model Systems: Site-Specific Interactions with Pt and Pd Nanoparticles*, Advanced Materials, 23 (2011) 2617-2621, D.O.I.: 10.1002/adma.201004064

[20] M. Valtiner, S. Borodin, G. Grundmeier, *Preparation and Characterisation of Hydroxide Stabilised ZnO(0001)–Zn–OH Surfaces*, Physical Chemistry Chemical Physics, 9 (2007) 2406-2412, D.O.I.: 10.1039/B617600C

[21] J.G. Huddleston, A.E. Visser, W.M. Reichert, H.D. Willauer, G.A. Broker, R.D. Rogers, *Characterization and Comparison of Hydrophilic and Hydrophobic Room Temperature Ionic Liquids Incorporating the Imidazolium Cation*, Green Chemistry, 3 (2001) 156-164, D.O.I.: 10.1039/B103275P

[22] J.F. Watts, J. Wolstenholme, *An Introduction to Surface Analysis by XPS and AES*, John Wiley & Sons, (2003).

[23] P. Parhi, V. Manivannan, *Novel Microwave Initiated Synthesis of Zn2 SiO4 and MCrO4 (M= Ca, Sr, Ba, Pb)*, Journal of Alloys and Compounds, 469 (2009) 558-564, D.O.I.: 10.1016/j.jallcom.2008.02.010

[24] I.J. Villar-Garcia, E.F. Smith, A.W. Taylor, F.L. Qiu, K.R.J. Lovelock, R.G. Jones, P. Licence, *Charging of Ionic Liquid Surfaces under X-Ray Irradiation: The Measurement of Absolute Binding Energies by XPS*, Physical Chemistry Chemical Physics, 13 (2011) 2797-2808, D.O.I.: 10.1039/C0cp01587c

[25] O. Dulub, L.A. Boatner, U. Diebold, *STM Study of the Geometric and Electronic Structure of ZnO (0001)-Zn,(0001)-O,(1010), and (1120) Surfaces*, Surface Science, 519 (2002) 201-217, D.O.I.: 10.1016/S0039-6028(02)02211-2

[26] O. Dulub, U. Diebold, G. Kresse, *Novel Stabilization Mechanism on Polar Surfaces: ZnO(0001)-Zn*, Physical Review Letters, 90 (2003) 016102, D.O.I.: 10.1103/PhysRevLett.90.016102

[27] B. Meyer, D. Marx, O. Dulub, U. Diebold, M. Kunat, D. Langenberg, C. Wöll, *Partial Dissociation of Water Leads to Stable Superstructures on the Surface of Zinc Oxide*, Angewandte Chemie International Edition, 43 (2004) 6641-6645, D.O.I.: 10.1002/anie.200461696

[28] R. Heinhold, G. Williams, S. Cooil, D. Evans, M. Allen, *Influence of Polarity and Hydroxyl Termination on the Band Bending at ZnO Surfaces*, Physical Review B, 88 (2013) 235315, D.O.I.: 10.1103/PhysRevB.88.235315

[29] M. Babucci, V. Balci, A. Akçay, A. Uzun, *Interactions of [BMIM][BF4] with Metal Oxides and Their Consequences on Stability Limits*, Journal of Physical Chemistry C, 120 (2016) 20089-20102, D.O.I.: 10.1021/acs.jpcc.6b03975

[30] L. Wang, L. Chang, B. Zhao, Z. Yuan, G. Shao, W. Zheng, *Systematic Investigation on Morphologies, Forming Mechanism, Photocatalytic and Photoluminescent Properties of ZnO Nanostructures Constructed in Ionic Liquids*, Inorganic Chemistry, 47 (2008) 1443-1452, D.O.I.: 10.1021/ic701094a

[31] J.T. Newberg, C. Goodwin, C. Arble, Y. Khalifa, J.A. Boscoboinik, S. Rani, *ZnO(10$\bar{1}$0) Surface Hydroxylation under Ambient Water Vapor*, The Journal of Physical Chemistry B, 122 (2018) 472-478, D.O.I.: 10.1021/acs.jpcb.7b03335

[32] M.P. Seah, *An Accurate and Simple Universal Curve for the Energy-Dependent Electron Inelastic Mean Free Path*, Surface and Interface Analysis, 44 (2012) 497-503, D.O.I.: 10.1002/sia.4816

[33] B. McLean, H. Li, R. Stefanovic, R.J. Wood, G.B. Webber, K. Ueno, M. Watanabe, G.G. Warr, A. Page, R. Atkin, *Nanostructure of [Li(G4)] TFSI and [Li(G4)] NO3 Solvate Ionic Liquids at HOPG and Au(111) Electrode Interfaces as a Function of Potential*, Physical Chemistry Chemical Physics, 17 (2015) 325-333, D.O.I.: 10.1039/C4CP04522J

[34] K.R.J. Lovelock, E.F. Smith, A. Deyko, I.J. Villar-Garcia, P. Licence, R.G. Jones, *Water Adsorption on a Liquid Surface*, Chemical Communications, (2007) 4866-4868, D.O.I.: 10.1039/B711680B

[35] K.L. Syres, R.G. Jones, *Adsorption, Desorption, and Reaction of 1-Octyl-3-Methylimidazolium Tetrafluoroborate, [C8C1Im][BF4], Ionic Liquid Multilayers on Cu (111)*, Langmuir, 31 (2015) 9799-9808, D.O.I.: 10.1021/acs.langmuir.5b02932

[36] E.F. Smith, F.J. Rutten, I.J. Villar-Garcia, D. Briggs, P. Licence, *Ionic Liquids in Vacuo: Analysis of Liquid Surfaces Using Ultra-High-Vacuum Techniques*, Langmuir, 22 (2006) 9386-9392, D.O.I.: 10.1021/la061248q

[37] R. Dorn, H. Lüth, *The Adsorption of Oxygen and Carbon Monoxide on Cleaved Polar and Nonpolar ZnO Surfaces Studied by Electron Energy Loss Spectroscopy*, Surface Science, 68 (1977) 385-391, D.O.I.: 10.1016/0039-6028(77)90226-6

[38] G. Raupp, J. Dumesic, *Adsorption of Carbon Monoxide, Carbon Dioxide, Hydrogen, and Water on Titania Surfaces with Different Oxidation States*, The

Journal of Physical Chemistry, 89 (1985) 5240-5246, D.O.I.: 10.1021/j100270a024

[39] V. Lockett, R. Sedev, C. Bassell, J. Ralston, *Angle-Resolved X-Ray Photoelectron Spectroscopy of the Surface of Imidazolium Ionic Liquids*, Physical Chemistry Chemical Physics, 10 (2008) 1330-1335, D.O.I.: 10.1039/b713584j

[40] T.J. Gannon, G. Law, P.R. Watson, A.J. Carmichael, K.R. Seddon, *First Observation of Molecular Composition and Orientation at the Surface of a Room-Temperature Ionic Liquid*, Langmuir, 15 (1999) 8429-8434, D.O.I.: 10.1021/la990589j

[41] Y. Jeon, J. Sung, W. Bu, D. Vaknin, Y. Ouchi, D. Kim, *Interfacial Restructuring of Ionic Liquids Determined by Sum-Frequency Generation Spectroscopy and X-Ray Reflectivity*, Journal of Physical Chemistry C, 112 (2008) 19649-19654, D.O.I.: 10.1021/jp807873j

[42] R.M. Lynden-Bell, M. Del Popolo, *Simulation of the Surface Structure of Butylmethylimidazolium Ionic Liquids*, Physical Chemistry Chemical Physics, 8 (2006) 949-954, D.O.I.: 10.1039/b514848k

[43] X. Shen, Y. Liang, Y. Zhai, Z. Ning, *Shape-Controllable Synthesis of Ultrafine ZnO Powders of Different Morphologies*, Journal of Materials Science & Technology, 29 (2013) 44-48, D.O.I.: 10.1016/j.jmst.2012.11.004

[44] C. Wu, Y.C. Zhang, Q. Huang, *Solvothermal Synthesis of N-Doped ZnO Microcrystals from Commercial ZnO Powder with Visible Light-Driven Photocatalytic Activity*, Materials Letters, 119 (2014) 104-106, D.O.I.: 10.1016/j.matlet.2013.12.111

[45] Z.W. Pan, Z.R. Dai, Z.L. Wang, *Nanobelts of Semiconducting Oxides*, Science, 291 (2001) 1947, D.O.I.: 10.1126/science.1058120

[46] T. Ohira, O. Yamamoto, Y. Iida, Z.-e. Nakagawa, *Antibacterial Activity of ZnO Powder with Crystallographic Orientation*, Journal of Materials Science: Materials in Medicine, 19 (2008) 1407-1412, D.O.I.: 10.1007/s10856-007-3246-8

[47] H. Ohtani, S. Ishimura, M. Kumai, *Thermal Decomposition Behaviors of Imidazolium-Type Ionic Liquids Studied by Pyrolysis-Gas Chromatography*, Analytical Sciences, 24 (2008) 1335-1340, D.O.I.: 10.2116/analsci.24.1335

[48] M.C. Kroon, W. Buijs, C.J. Peters, G.J. Witkamp, *Quantum Chemical Aided Prediction of the Thermal Decomposition Mechanisms and Temperatures of*

Ionic Liquids, Thermochimica Acta, 465 (2007) 40-47, D.O.I.: 10.1016/j.tca.2007.09.003

[49] B. Coppa, R. Davis, R. Nemanich, *Gold Schottky Contacts on Oxygen Plasma-Treated, n-Type ZnO (0001)*, Applied Physics Letters, 82 (2003) 400-402, D.O.I.: 10.1063/1.1536264

[50] N. Asakuma, T. Fukui, M. Toki, K. Awazu, H. Imai, *Photoinduced Hydroxylation at ZnO Surface*, Thin Solid Films, 445 (2003) 284-287, D.O.I.: 10.1016/S0040-6090(03)01162-3

[51] S. Krischok, M. Eremtchenko, M. Himmerlich, P. Lorenz, J. Uhlig, A. Neumann, R. Öttking, W. Beenken, O. Höfft, S. Bahr, *Temperature-Dependent Electronic and Vibrational Structure of the 1-Ethyl-3-Methylimidazolium Bis (Trifluoromethylsulfonyl) Amide Room-Temperature Ionic Liquid Surface: A Study with XPS, UPS, MIES, and HREELS*, Journal of Physical Chemistry B, 111 (2007) 4801-4806, D.O.I.: 10.1021/jp067136p

[52] A. Deyko, R.G. Jones, *Adsorption, Absorption and Desorption of Gases at Liquid Surfaces: Water on [C 8 C 1 Im][BF 4] and [C 2 C 1 Im][Tf 2 N]*, Faraday Discussions, 154 (2012) 265-288, D.O.I.: 10.1039/C1FD00062D

[53] M. Allen, D. Zemlyanov, G. Waterhouse, J. Metson, T.D. Veal, C.F. McConville, S. Durbin, *Polarity Effects in the X-Ray Photoemission of ZnO and Other Wurtzite Semiconductors*, Applied Physics Letters, 98 (2011) 101906, D.O.I.: 10.1063/1.3562308

[54] T.H. Becker, M. Kunat, C. Boas, U. Burghaus, C. Wöll, *Adsorption Dynamics of CO on the Polar Surfaces of ZnO*, Journal of Chemical Physics, 113 (2000) 6334-6343, D.O.I.: 10.1063/1.1309131

[55] C.T. Au, W. Hirsch, W. Hirschwald, *Adsorption and Interaction of Carbon Dioxide, Formic Acid and Hydrogen/Carbon Dioxide Mixtures on (1010) Zinc Oxide Surfaces Studied by Photoelectron Spectroscopy (XPS and UPS)*, Surface Science, 199 (1988) 507-517, D.O.I.: 10.1016/0039-6028(88)90918-1

[56] A.T. Vai, V.L. Kuznetsov, J.R. Dilworth, P.P. Edwards, *Uv-Induced Improvement in ZnO Thin Film Conductivity: A New in Situ Approach*, Journal of Materials Chemistry C, 2 (2014) 9643-9652, D.O.I.: 10.1039/C4TC01749H

[57] S. Rivera-Rubero, S. Baldelli, *Influence of Water on the Surface of Hydrophilic and Hydrophobic Room-Temperature Ionic Liquids*, Journal of the American Chemical Society, 126 (2004) 11788-11789, D.O.I.: 10.1021/ja0464894

[58] S. Rivera-Rubero, S. Baldelli, *Influence of Water on the Surface of the Water-Miscible Ionic Liquid 1-Butyl-3-Methylimidazolium Tetrafluoroborate: A Sum Frequency Generation Analysis*, Journal of Physical Chemistry B, 110 (2006) 15499-15505, D.O.I.: 10.1021/jp062694p

[59] J. D. Holbrey, K. R. Seddon, *The Phase Behaviour of 1-Alkyl-3-Methylimidazolium Tetrafluoroborates; Ionic Liquids and Ionic Liquid Crystals*, Journal of the Chemical Society, Dalton Transactions, (1999) 2133-2140, D.O.I.: 10.1039/A902818H

[60] D.M. Fox, J.W. Gilman, H.C. De Long, P.C. Trulove, *TGA Decomposition Kinetics of 1-Butyl-2,3-Dimethylimidazolium Tetrafluoroborate and the Thermal Effects of Contaminants*, Journal of Chemical Thermodynamics, 37 (2005) 900-905, D.O.I.: 10.1016/j.jct.2005.04.020

[61] H.L. Ngo, K. LeCompte, L. Hargens, A.B. McEwen, *Thermal Properties of Imidazolium Ionic Liquids*, Thermochimica Acta, 357-358 (2000) 97-102, D.O.I.: 10.1016/S0040-6031(00)00373-7

[62] C. Maton, N. De Vos, C.V. Stevens, *Ionic Liquid Thermal Stabilities: Decomposition Mechanisms and Analysis Tools*, Chemical Society Reviews, 42 (2013) 5963-5977, D.O.I.: 10.1039/C3CS60071H

[63] M.E. Van Valkenburg, R.L. Vaughn, M. Williams, J.S. Wilkes, *Thermochemistry of Ionic Liquid Heat-Transfer Fluids*, Thermochimica Acta, 425 (2005) 181-188, D.O.I.: 10.1016/j.tca.2004.11.013

[64] M. Kosmulski, J. Gustafsson, J.B. Rosenholm, *Thermal Stability of Low Temperature Ionic Liquids Revisited*, Thermochimica Acta, 412 (2004) 47-53, D.O.I.: 10.1016/j.tca.2003.08.022

[65] Y. Cao, T. Mu, *Comprehensive Investigation on the Thermal Stability of 66 Ionic Liquids by Thermogravimetric Analysis*, Industrial & Engineering Chemistry Research, 53 (2014) 8651-8664, D.O.I.: 10.1021/ie5009597

[66] A. Deyko, K.R.J. Lovelock, P. Licence, R.G. Jones, *The Vapour of Imidazolium-Based Ionic Liquids: A Mass Spectrometry Study*, Physical Chemistry Chemical Physics, 13 (2011) 16841-16850, D.O.I.: 10.1039/C1CP21821B

[67] K.R.J. Lovelock, A. Deyko, P. Licence, R.G. Jones, *Vaporisation of an Ionic Liquid near Room Temperature*, Physical Chemistry Chemical Physics, 12 (2010) 8893-8901, D.O.I.: 10.1039/C004197A

[68] J. Vohs, M. Barteau, *Conversion of Methanol, Formaldehyde and Formic Acid on the Polar Faces of Zinc Oxide*, Surface Science, 176 (1986) 91-114, D.O.I.: 10.1016/0039-6028(86)90165-2

[69] G. Zwicker, K. Jacobil, J. Cunningham, *Temperature Programmed Desorption of Polar Adsorbates from (1010),(0001) and (0001) ZnO Surfaces*, International Journal of Mass Spectrometry and Ion Processes, 60 (1984) 213-223, D.O.I.: 10.1016/0168-1176(84)80089-0

[70] J. Strunk, K. Kähler, X. Xia, M. Muhler, *The Surface Chemistry of ZnO Nanoparticles Applied as Heterogeneous Catalysts in Methanol Synthesis*, Surface Science, 603 (2009) 1776-1783, D.O.I.: 10.1016/j.susc.2008.09.063

6 Electrochemical Synthesis of Titanium Dioxide Nanotubes using an Ionic Liquid Electrolyte

Titanium dioxide (TiO_2) nanotubes, since they were first grown in 1999, have shown particular promise for numerous potential applications, including batteries and capacitors [1], self-cleaning coatings [2], drug delivery [3] and photocatalytic water splitting [4]. One of the more popular methods to synthesise TiO_2 nanotubes is electrochemically via anodization of Ti. The reason for its increasing popularity is its ease of use, as well as its precise control over the structure and dimensions of the synthesised nanotubes.

Numerous groups have used ionic liquids (ILs) as electrolytes in anodization of Ti to produce TiO_2 nanotubes. They provide simultaneous benefits that organic electrolytes provide, including intact nanotube morphology, and diverse customisation of the physicochemical properties of the electrolyte. The physicochemical properties of the electrolyte, such as conductivity, viscosity and chemical composition, has an impact on the morphology of the nanotubes. The anodization conditions, such as applied potential, also influence the morphology. Within this chapter is a study exploring the effects of the IL electrolyte composition and applied anodization potential on nanotubes prepared via anodization of Ti.

6.1 Introduction

The properties of TiO_2 nanotubes, including physicochemical, optical and electrical properties, are dependent on their morphology. As well as their size and shape, morphology also encompasses the crystallographic structure and any defects of the nanotubes. The morphology of TiO_2 nanotubes is therefore of vital importance to their applications, As a result, there is great scientific interest, not only into how their morphology affects the properties of nanotubes, but also how to control the morphology to synthesise nanotubes of specific dimensions for specific properties.

TiO$_2$ nanotube preparation methods include sol-gel synthesis, hydrothermal synthesis, and vapour deposition [5], but one of the more favourable ways is electrochemical synthesis via anodization of Ti. Synthesis through anodization is becoming increasingly popular due to its simplicity and precise control over the pore size, length, and wall thickness of the nanotubes. This is particularly important for photocatalytic water splitting applications, since those dimensions have a direct effect on the optical properties of the nanotubes [6], and will therefore impact how well the nanotubes absorb light and, subsequently, their catalytic performance.

Anodization of Ti involves applying a potential between a sample of pure Ti, (which is the anode- hence anodization of Ti) and a counter electrode, often consisting of a noble metal such as platinum or gold. The anode and counter electrode are submerged in an electrolyte. The anodization process begins with the formation of a compact oxide, where Ti^{4+} cations (formed by the applied potential) combine with oxygen from the addition of water to form TiO$_2$ [7]:

$$Ti \rightarrow 4e + Ti^{4+} \qquad (1)$$

$$Ti^{4+} + 2H_2O \rightarrow TiO_2 + 4H^+ \qquad (2)$$

Typical electrolytes contain fluorine, which is crucial to the next part of the anodization process. Fluorine is required for the formation of so-called 'pits', which are pores that are created when the fluorine reacts with the TiO$_2$ layer (via chemical dissolution), releasing water-soluble titanium hexafluoride and water. This leads to the creation of porous/nanotubular TiO$_2$ [7]:

$$TiO_2 + 4H^+ + 6F^- \rightarrow [TiF_6]^{2-} + 2H_2O \qquad (3)i$$
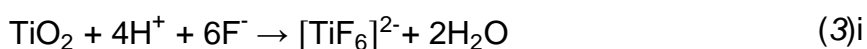
The electrolyte that is used in the anodization of Ti also has an impact on the morphology of the nanotubes. Much of the early work into the technique utilised aqueous electrolytes that incorporated fluorine through addition of hydrofluoric acid (HF) [8, 9]. The resultant nanotubes were approximately 0.5 µm in length, while those synthesised using less acidic media (such as diluted fluorinated salts) were grown up to 4 µm in length [10].
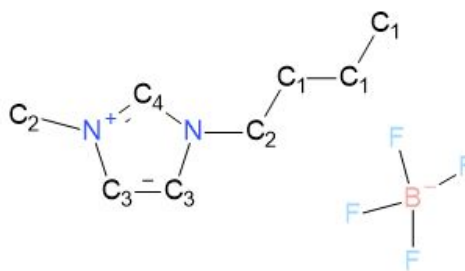
Figure 6.1: Chemical structure of the IL, 1-butyl-3-methylimidazolium tetrafluoroborate ($[C_4C_1Im][BF_4]$). The carbon environments have been labelled C_1 to C_4.

In more recent years, the use of organic electrolytes have produced nanotubes with lengths of the order of hundreds of μm, and with fewer defects (such as wall-cracking) [11, 12]. Electrolytes showing particular promise for TiO_2 nanotube synthesis are ionic liquids (ILs), particularly imidazolium based ILs, which have produced nanotubes of varying lengths, diameters, and tube thicknesses. The fluorine content in IL-based electrolytes arises from fluorinated anions, such as tetrafluoroborate ($[BF_4]^-$) or hexfluorophosphate ($[PF_6]^-$).

One of the first groups to demonstrate TiO_2 nanotube synthesis via anodization using an IL electrolyte was the Schmuki group [13], who anodized Ti foils using applied potentials in the range of 3 V to 10 V. They used two IL electrolytes: one composed of 1-butyl-3-methylimidazolium tetrafluoroborate, or $[C_4C_1Im][BF_4]$ (see Figure 6.1 for a chemical structure diagram); and another composed of 1-butyl-3-methylimidazolium hexafluorophosphate ($[C_4C_1Im][PF_6]$). They demonstrated the effects of both anodization potential and water content on the resultant nanotube arrays. At lower potentials in $[C_4C_1Im][BF_4]$, porous TiO_2 was produced, but at potentials of ~10 V, nanotube arrays were produced. Li et al [14] also synthesised TiO_2 nanotubes using IL-based electrolytes at much higher anodization potentials (up to 50 V) for shorter time periods, producing well-separated nanotubes. These were compared to nanotubes grown in an ethylene glycol-based electrolyte, which contained more defects than those produced using an IL-based electrolyte. Li et al also demonstrated that a 'debris'-layer, or barrier layer builds up over time during the anodization process, which needs to be cleaved, typically using an adhesive tape (such as Scotch tape), to allow for further nanotube growth [14].

Mazierski et al [15] proposed that the fluorinated anions react with the TiO_2 via the following:

$$TiO_2 + 4H^+ + 6BF_4^- \rightarrow \left[Ti(BF_4)_6\right]^{2-} + 2H_2O \qquad \text{(3)ii}$$
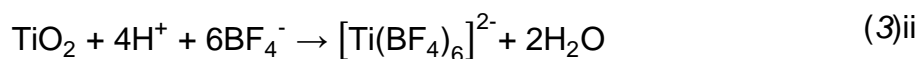
They also proposed that some electrochemical decomposition of the IL may occur, where small amounts of boron and nitrogen are incorporated into the nanotubes. For investigations into synthesised nanostructures, the ability to gain topographical information is vital. Scanning electron microscopy (SEM) is particularly favoured for simple acquisition of sub-µm length scale images of nanostructures, including TiO_2 nanotubes [7, 13-17]. Often coupled with SEM is energy dispersive X-ray spectroscopy (EDX), which is used to determine the elemental composition of samples. For surface-sensitive information, X-ray photoelectron spectroscopy (XPS) is usually employed, and is immeasurably useful for probing chemical environments at surfaces and interfaces. XPS has been used to investigate a range of TiO_2 nanostructures [18-20], including nanotubes [15, 21, 22]. However, there is little research utilising this technique for IL-synthesised TiO_2 nanotubes, particularly for those synthesised using low-voltage anodization processes. Presented here is a combined SEM/EDX and XPS study into the effects of electrolyte composition and applied potential on the electrochemical synthesis of TiO_2 nanotubes via anodization of Ti. While water is known to be important for TiO_2 nanotube synthesis [7, 23], the combination of morphological and surface-sensitive chemical analysis of the resultant nanostructures should provide more insight into the role that water plays in these systems.

6.2 Experimental section

Prior to anodization, 1.5cm × 6cm strips of Ti foil (99.99%, 50 mm × 50 mm, Sigma Aldrich) were cleaned via sonication in acetone. The anodization process involved directly applying a voltage between the Ti foil (anode) and a Pt wire mesh counter electrode (99.9%, 25 × 25 mm, Alfa Aesar) while submerged in IL-based electrolyte (consisting of 1-butyl-3-methylimidazolium tetrafluoroborate, $[C_4C_1Im][BF_4]$, >97%, Sigma Aldrich). This was done using a custom-design electrochemical cell (see Figure 6.2). A reference electrode was not required to grow nanotubes, as determined by previous studies such as Li et al [14].
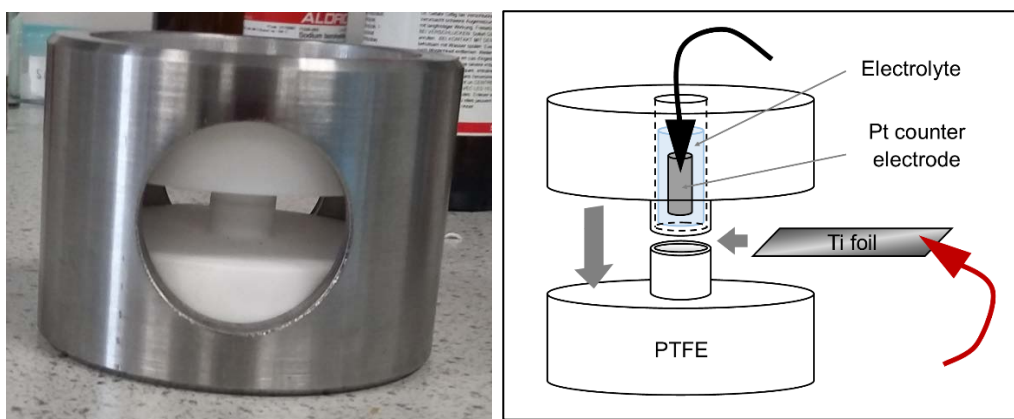
Figure 6.2: A photograph of the custom-built electrochemical cell (left). A schematic diagram of the electrochemical cell is shown on the right, and shows how the components of the cell fit together. The PTFE halves are housed in a stainless steel casing, as shown in the photograph on the left. The black and red crocodile clips in the diagram (attached to the Pt counter electrode and the Ti foil anode respectively) connect to the power supply.

Inside the cell, a strip of Ti foil was sandwiched between two halves of polytetrafluoroethylene (PTFE). Approximately 1 ml of the IL-based electrolyte was injected via pipette into the well (on top of the Ti). The anodization was a two-step process. The Pt electrode was submerged in the electrolyte, and a voltage was applied between the Ti anode and the Pt counter electrode. After some time (see Table 6.1 for details on sample conditions), the cell was disassembled and the Ti anode was removed for cleaning with acetone and 'stripping'. The surface of the Ti anode was 'stripped' using adhesive tape [14]. The anode was washed with acetone to remove adhesive residue. The cell and anode were reassembled with fresh electrolyte for the second (and final) growth stage. This process was repeated for a number of samples using different voltages and electrolyte compositions, which are featured in Table 6.1. Samples b and c were both anodized at 10 V, while samples a and d were anodized at 5 V and 20 V respectively. Samples designated a, b and d were anodized in pure $[C_4C_1Im][BF_4]$ (see Figure 6.1 for a chemical structure diagram of $[C_4C_1Im][BF_4]$). Sample c was anodized in an electrolyte consisting of $[C_4C_1Im][BF_4]$ and 2.6 wt% of H_2O.

Table 6.1: Summary of experimental conditions of each sample.

Sample designation	Anodization potential (V)	Electrolyte used	Anodization time (hours)	
			Stage 1	Stage 2
a	5	Pure IL	3	3.5
b	10	Pure IL	12	2.5
c	10	IL + 2.6 wt% H_2O	2	10.5
d	20	Pure IL	1	2.5

Post-anodization, scanning electron microscopy images were taken of each sample surface (using a Zeiss SIGMA VP FEG-SEM, and an acceleration voltage between 5 kV and 20 kV) to determine whether any nanostructures were present, and an estimate of their diameter. Additionally, energy dispersive X-ray (EDX) spectra were recorded using a FEI Quanta 200 series SEM with Genesis EDX for sample composition analysis. To gain a better understanding of the surface composition, X-ray photoelectron spectroscopy (XPS) was employed using a Kratos system at the University of Manchester equipped with an Al kα X-ray source (hv = 1486.6 eV). The binding energy (BE) scale of all XPS spectra have been calibrated to the C 1s peak at 285.0 eV, and BE values are quoted to ±0.1 eV. All XPS core level peaks have been fitted using CasaXPS software, with 70:30 Gaussian:Lorentzian (Voigt) lineshapes and a Shirley background.

6.3 Results

Photographs of the four samples were taken after the second growth stage and are shown in Figure 6.3. Each sample was chromatically unique, which implies a difference in surface chemistry between the samples. Sample a was a coppery-brown colour with a darker patch located off centre. Sample b was purple in colour, and consistent across the surface. Sample c was an off-white/grey with a slight pearlescent pink colouration. Sample d had a central vivid blue patch surrounded by light yellow discolouration. Sample c had a colouration closest to that of crystalline or powder TiO_2. Nanostructural TiO_2 can sometimes display a blue/purple colouration depending on the size of the nanostructures produced [24]. This possibility is explored in the SEM/EDX analysis.
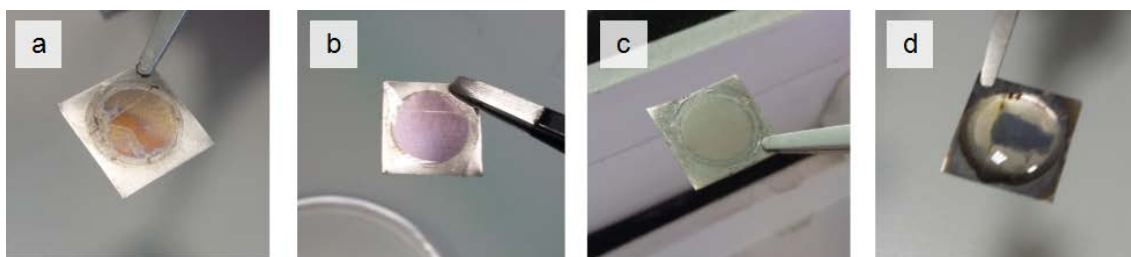
Figure 6.3: Photographs of samples a, b, c, and d taken after the final anodization.

6.3.1 SEM/EDX analysis
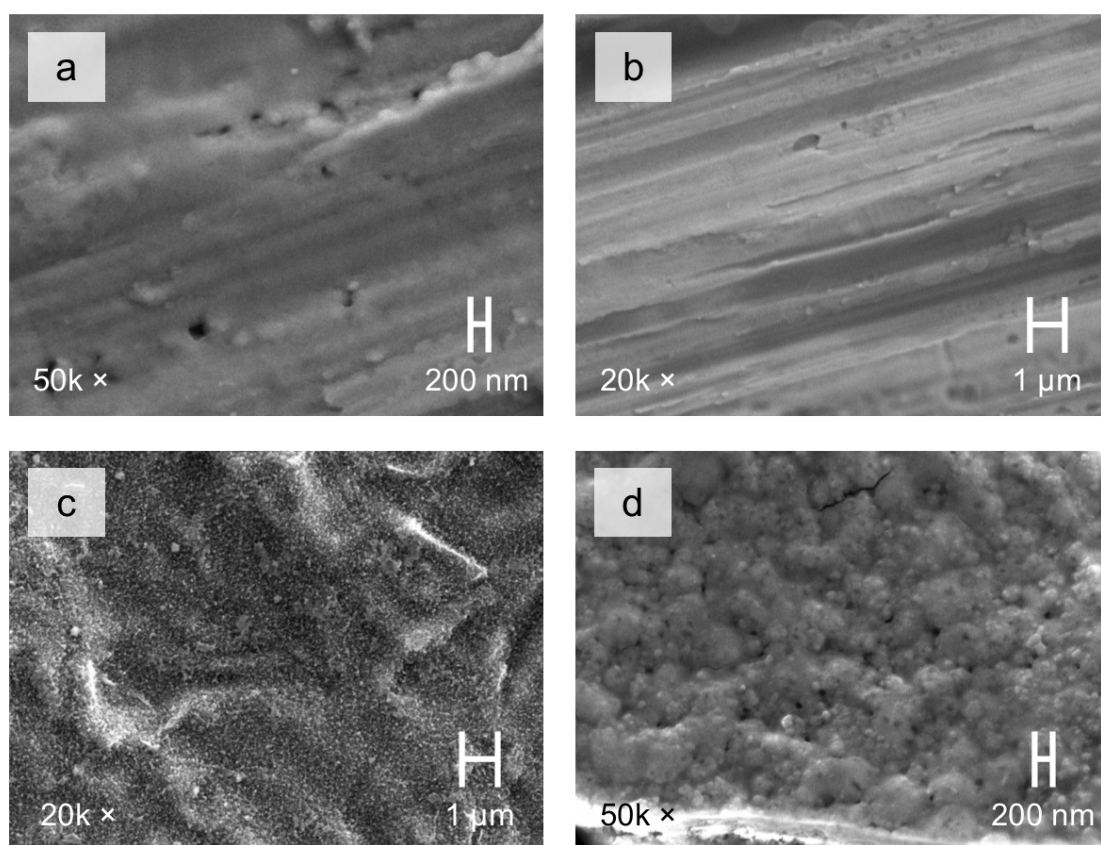
Figure 6.4: SEM images taken of samples a (top left), b (top right), c (bottom left), and d (bottom right). The magnification of each image is shown in the bottom left corner of each image.

The SEM images taken of all samples are shown in Figure 6.4. It can be seen with a relatively weak SEM magnification (20k ×) that there are structures on the surface of sample c. While there appear to be no structures present on the surface of sample a or b, each resemble that of an oxide film [14, 25]. The SEM image taken from the surface of sample d is quite different, and resembles a nanoporous film [14]. It is likely that TiO_2 nanotubes have not grown on the surfaces of samples a, b, or d due to the lack of available oxygen in the process to create TiO_2 nanotubes, requiring a small amount of water to be added to the electrolyte [23]. Figure 6.5 shows two sets of two SEM images: the first set (Figure 6.5(i) and Figure 6.5(ii)) are of sample c, and the second set (Figure 6.5(iii) and Figure 6.5(iv)) are of sample d. Both sets are of a greater magnification than those taken in Figure 6.4. Using the scale bar in Figure 6.5(ii), the average diameter of the nanotubes grown on sample c is approximately 50 nm. Figure 6.5(iii) shows a part of the surface of sample d that looks similar to the surfaces of sample a and b, but at a greater magnification.

This indicates only partial formation of a nanoporous film on the surface of sample d. Using the scale bar in Figure 6.5(iv), the average diameter of the pores of the partially-porous surface of sample d is approximately 75 nm. From the data presented here, it is not possible to determine the length of the TiO_2 nanotubes of sample c, but an approximation of the average length could be determined using SEM at more grazing angles. Paramasivam et al [13] synthesised TiO_2 nanotubes of similar dimensions using the same IL at a similar anodization potential (7 V). However, the group also successfully synthesised the nanotubes using an IL-only electrolyte, with a reported water content of ~1446 ppm. This approximately corresponds to ~0.01 wt% water content, which is significantly less than that used in this work.
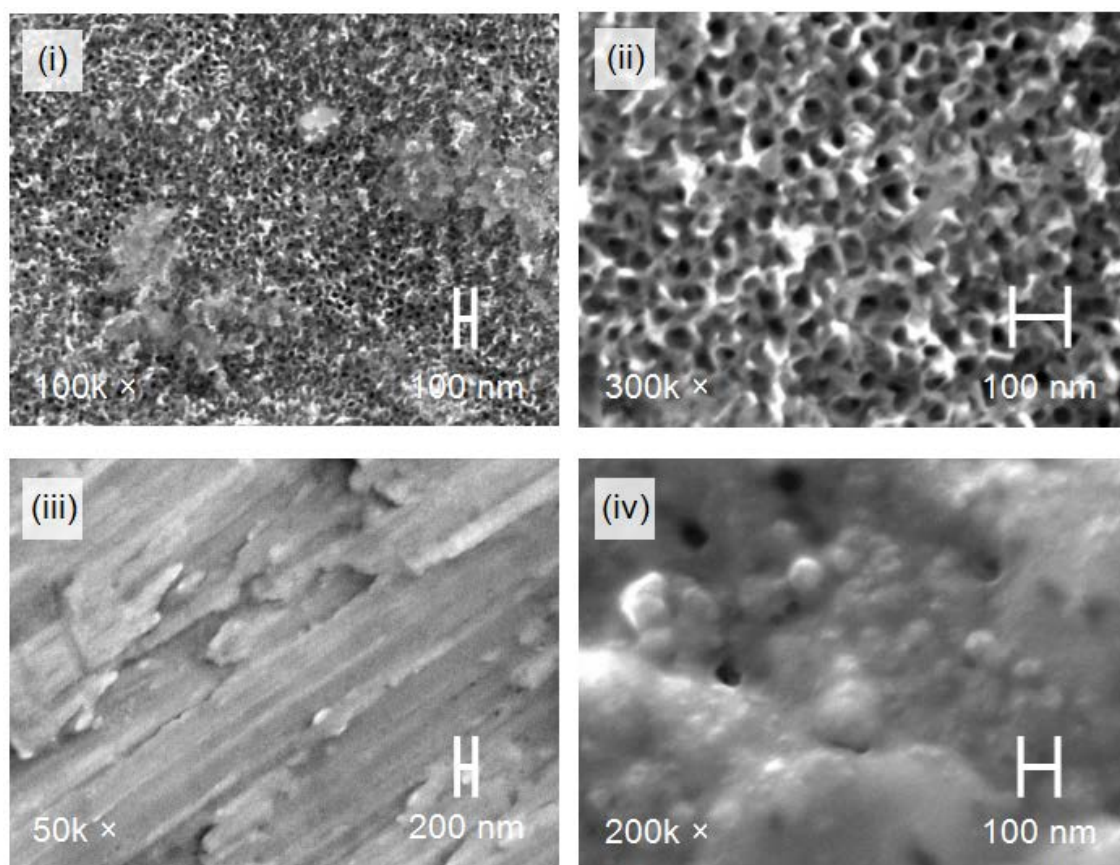
Figure 6.5: SEM images of sample c ((i) and (ii)), and of sample d ((iii) and (iv)). Magnifications are shown in the bottom left corner of each image.

From Figure 6.5(i), there are patches on the surface of sample c where nanotubes have not grown. It has been shown by Li et al [14] and others [26-28] that a 'debris layer' tends to grow atop of TiO_2 nanotube arrays that are synthesised under similar conditions. This layer subsequently requires mechanical removal via the Scotch tape method. The patches on the surface of

sample c may be parts where this layer was not successfully removed, and may even retain some residual adhesive from the tape used to 'strip' the surface between the first and final anodization stages.

The EDX spectra of all samples are shown in Figure 6.6. The titanium K_α transition peak is seen in all four spectra (~4.51 keV), with additional features at lower transition energies (<1.0 keV) that are thought to arise from the K_α transitions of carbon, nitrogen, oxygen and fluorine. The K_α transitions of these elements occur at 0.277 keV, 0.392 keV, 0.523 keV, and 0.677 keV respectively. Features corresponding to transitions at low ex citation energies are difficult to resolve with the system used, making quantitative EDX analysis of organic materials, including ILs, difficult [29]. However, from inspection of the low-energy data displayed in the inset figures in Figure 6.6, we can say qualitatively there are differences in composition between the samples.
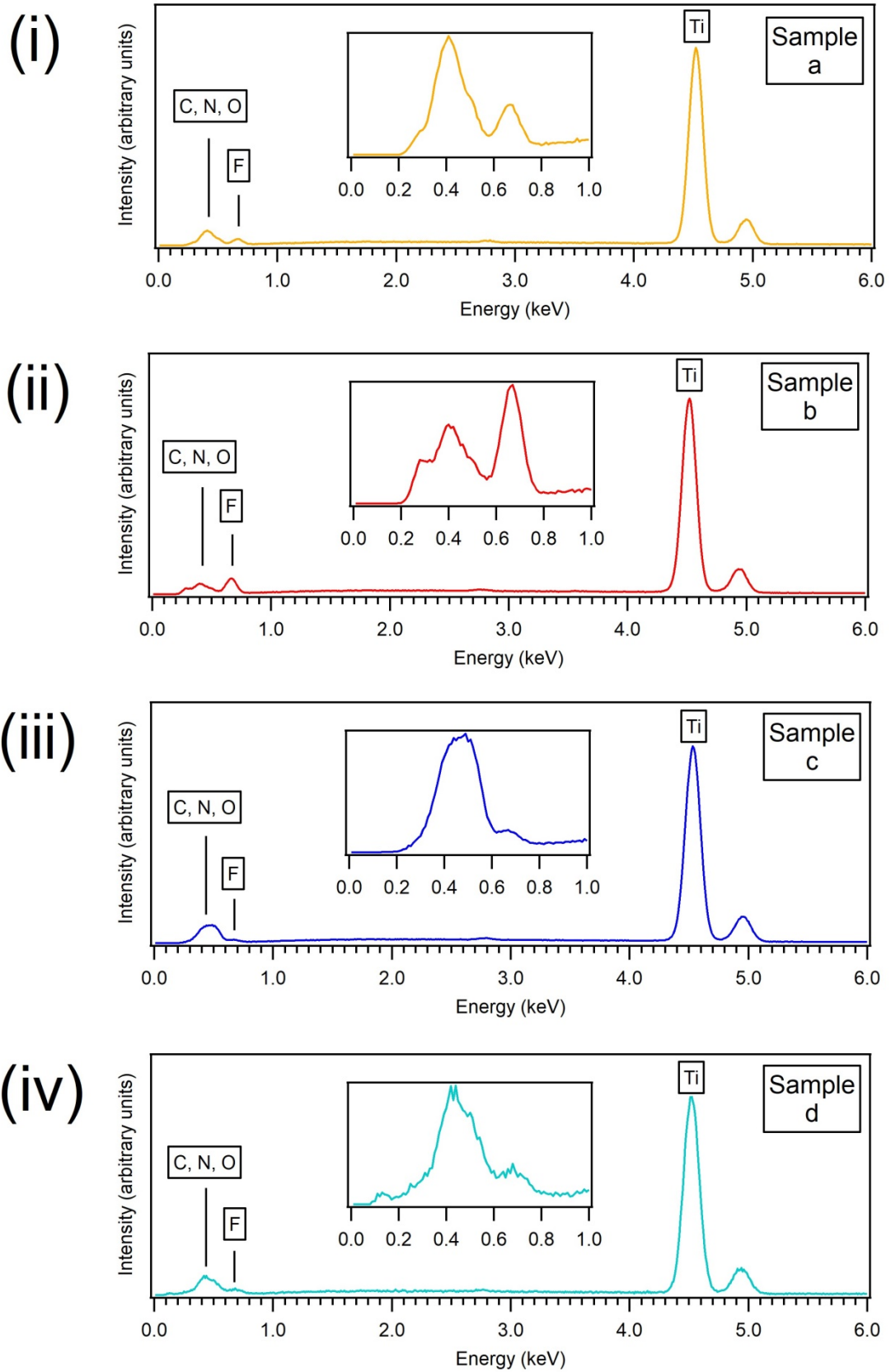
Figure 6.6: EDX spectra of samples a (amber line in (i)), b (red line in (ii)), c (blue line in (iii)) and d (cyan line in (iv)). All inset figures show the data between 0 and 1 keV.

6.3.2 XPS analysis

All four samples were analysed using XPS, and spectra were recorded of the following core level regions: C 1s, F 1s, N 1s, O 1s, and Ti 2p. Survey spectra were also recorded (see Figure 6.7). The aforementioned core level peaks are labelled in the survey spectra.
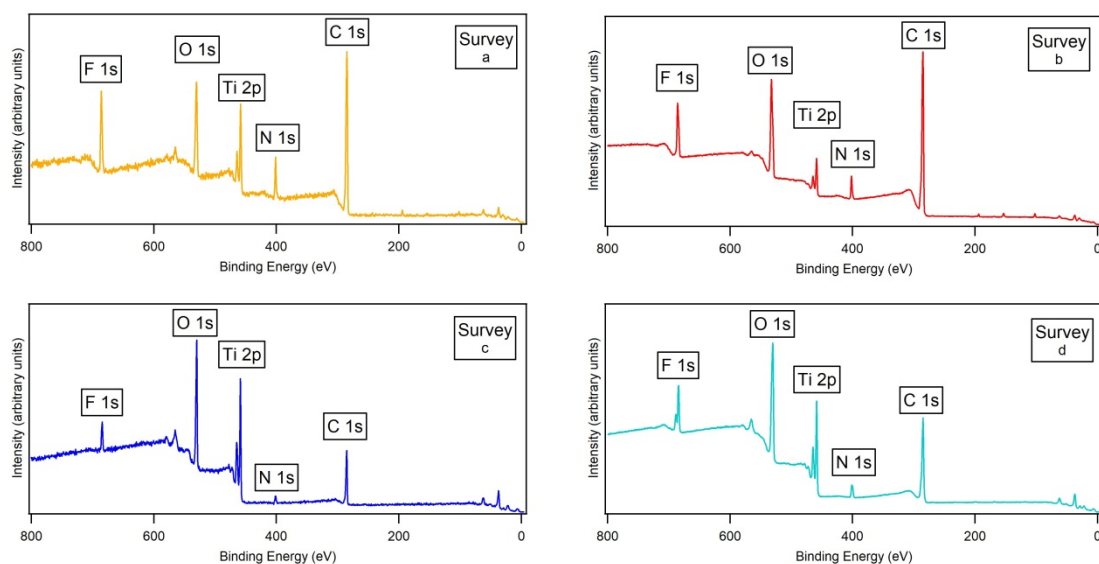
Figure 6.7: Survey XPS spectra of sample a (amber line, top left), sample b (red line, top right), sample c (blue line, bottom left), and sample d (cyan line, bottom right). Significant peaks are labelled.

For ease, comparisons are made between the spectra recorded for different electrolyte compositions (pure IL electrolyte and IL-based electrolyte), and for the different anodization potentials (5 V, 10 V, and 20 V with pure IL electrolyte).
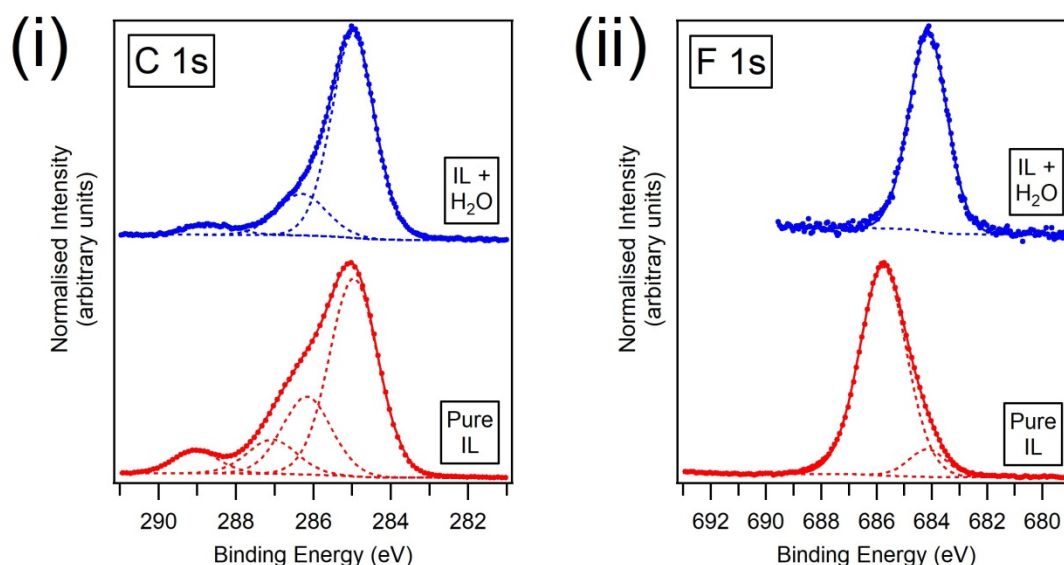
Figure 6.8: C 1s (i) and F 1s (ii) spectra of sample b (anodized in pure IL, red line) and sample c (anodized in electrolyte composed of IL and 2.6 wt% H_2O, blue line), both anodized at 10 V.

Figure 6.8 displays the C 1s and F 1s spectra of samples b and c, which were anodized at the same potential of 10 V, but in different electrolytes. The red lines represent the spectra recorded for sample b (which was anodized in a pure IL electrolyte). Spectra recorded for sample c (which was anodized in an electrolyte consisting of IL with 2.6 wt% H_2O) are represented by the blue lines.

The C 1s spectrum for sample c (Figure 6.8(i)) has been fitted with three peaks: one at 285.0 eV, one at 286.3 eV and one at 288.7 eV. A summary of binding energies and assignments of peaks is featured in Table 6.2. The lowest BE peak, at 285.0 eV, is attributed to C=C/C-C bonding, and could have multiple sources. C-C bonds are present in the alkyl chains of $[C_4C_1Im]^+$ cations (see Figure 6.1, where the alkyl chain carbons are labelled C_1), and therefore a portion of this peak may arise from physisorbed/chemisorbed cations. The peak at 285.0 eV may also contain a contribution from adventitious carbon, which is typically composed of singly-bonded (C-C) or doubly-bonded (C=C) carbon. Numerous XPS studies into TiO_2 nanotube synthesis have reported high carbon content in the resultant nanotubes, regardless of the electrolyte composition. Regonini et al [21], who used an inorganic electrolyte composed of sodium fluoride and sodium sulphate (NaF/Na_2SO_4) to synthesise TiO_2 nanotubes, attributed most of the C 1s signal to residual isopropyl alcohol (from washing post-anodization) bonding to the nanotubes. Mazierski et al [15], who

synthesised TiO$_2$ nanotubes using various imidazolium-based IL electrolytes, report a similar carbon content, which they attribute to generic aliphatic (C-C) carbon. The samples in the work in this chapter were anodized in an IL-based electrolyte and were washed with acetone post-anodization, which has a similar structure to isopropyl alcohol, but contains a doubly-bonded oxygen atom rather than a hydroxyl group. A portion of the signal at 285.0 eV could be attributed to C-C bonding in residual acetone. Similarly, some of the signal at 286.3 eV in the C 1s region for sample c could be attributed to C=O bonding in residual acetone. In addition, 'stripping' the samples between the two anodization stages may have left residue on the surface despite washing in acetone afterward. Typical adhesives on tapes such as Scotch tape are made up of polymer materials containing C-OH/C=O groups. It is possible that some of the adhesive remained on the surface where the debris layer was not removed (see SEM image of sample c in Figure 6.5(i)), contributing to the intensity of the peak associated with C-OH/C=O. Another contributing factor could be exposure of the sample to atmosphere, which could increase coverage of hydroxyl (OH) groups. The peak at ~288.7 eV is consistent with that of carboxyl (COOH) and carboxylate (COO) groups on TiO$_2$ [30, 31], which are also present in the adhesives used in adhesive tapes. The peak at ~288.7 eV may be due to cation-substrate bonding. Mazierski et al [15] detected a signal in the C 1s region at a similar BE of 288.9 eV. They attributed this peak to cation-substrate bonding, specifically the imidazolium ring bonded to TiO$_2$ via the CH group at the C$_4$ carbon position (see Figure 6.1 for the chemical structure of [C$_4$C$_1$Im][BF$_4$] with carbon positions labelled). This kind of interaction has been observed in other studies involving nanoparticulate TiO$_2$ [32]. Therefore, the peak at 288.7 eV is tentatively assigned to bonding between IL cations and TiO$_2$ of the nanotubes.

The C 1s spectrum for sample b (Figure 6.8(i), red line) is fitted with 4 peaks: one at 285.0 eV, one at 286.2 eV, one at 287.1 eV, and one at 289.0 eV. Much like sample c, the peaks at 285.0 eV and 286.2 eV could be attributed to C=C/C-C bonding and C=O/C-OH bonding respectively. The BE of the peak at 287.1 eV is in line with that of the C$_4$ carbon in the IL cation [33, 34]. Similarly, the peak at 286.2 eV has a BE in line with that of the C$_2$ and C$_3$ carbons in the [C$_4$C$_1$Im]$^+$ cation [33, 34]. Therefore, a portion of the peak at 286.2 eV is attributed to C$_2$/C$_3$ carbons in the [C$_4$C$_1$Im]$^+$ cation, and the peak at 287.1 eV is

attributed to C_4 carbon in $[C_4C_1Im]^+$ cation. The signal arising at 286.2 eV is more intense for sample b than for sample c. This could be the case for multiple reasons. Sample b was exposed to atmosphere for a greater period of time (>24 hours) than sample c (<10 minutes) between anodization stages, which would contribute to signals associated with adventitious species. There may also be residual adhesive still present on the sample (that is not visible in the SEM images) despite washing in acetone, which would also contribute to the peak at 286.2 eV.

The nature of the fluorine detected by EDX can be explored in more depth in the F 1s XPS spectra. The F 1s spectrum for sample c (Figure 6.8(ii)) is fitted with a single peak at 684.1 eV. The BE of this peak is consistent with that of Ti-F bonding [34]. A similar feature was observed for $[C_4C_1Im][BF_4]$ on rutile TiO_2 in Chapter 3 of this thesis. Two peaks are fitted for the F 1s spectrum for sample b: one at 685.8 eV and one at 684.2 eV. The most intense F 1s peak for sample b is at a BE of 685.8 eV, which is more in line with XPS peaks attributed to the $[BF_4]^-$ anion of adsorbed $[C_4C_1Im][BF_4]$ on TiO_2 [34], which is also seen in Chapter 3 of this thesis. The peak at 684.2 eV is at a BE consistent with Ti-F bonding. While nanostructures did not form on the surface of sample b, Ti-F bonds may still have formed for a number of reasons. The experiment took place under ambient conditions, so a small amount of water will have been present in the IL due to its hygroscopic nature. This small amount of water will contribute to the formation of oxide (see reaction *(1)*), and therefore may allow some chemical dissolution to take place. This chemical dissolution results in $[TiF_6]^{2-}$ and consequently Ti-F bond formation (see reactions *(2)* and *(3)*). Furthermore, evidence of Ti-F bonds has been seen previously in XPS studies of $[C_4C_1Im][BF_4]$ on TiO_2 [15, 16], and should no oxide have formed through reaction *(1)* on the surface of sample b, there may be some natural oxide from exposure to air [35], allowing for anion-substrate interaction, and thus some Ti-F bond formation.
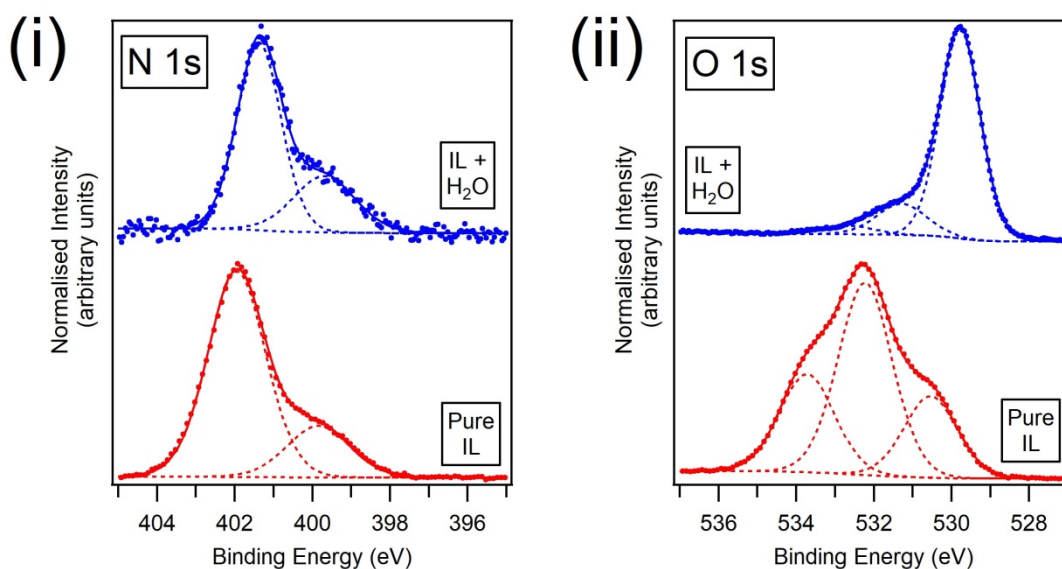
Figure 6.9: N 1s (i) and O 1s (ii) spectra of samples b (anodized in pure IL, red line) and c (anodized in electrolyte composed of IL and 2.6 wt% H_2O, blue line).

Figure 6.9(i) shows the N 1s region for samples b and c (represented by red and blue lines respectively). The shapes of the regions are similar to one another, and have both been fitted with two peaks. In the N 1s region for sample c, the higher BE peak in the N 1s region is situated at 401.4 eV, and the lower BE peak is situated at 399.7 eV. The peak at 401.4 eV is at a BE that is more in line with adsorbed IL on TiO_2 [34]. With regard to the lower BE peak, a number of XPS studies into the composition of TiO_2 nanotubes synthesised via anodization using IL-based electrolytes have reported peaks ~400.0 eV in the N 1s region, which are typically attributed to Ti-O-N interactions [15, 22]. However, signals around this BE have also been reported in works using an electrolyte void of nitrogen entirely, such as Regonini et al [21]. They attributed an N signal at ~400.0 eV to combined contamination from distilled water in the electrolyte and exposure to atmosphere. Mazierski et al [15], when they synthesised TiO_2 nanotubes using a $[C_2C_1Im][BF_4]$-based electrolyte discovered two N signals in the N 1s region: one at approximately 400.0 eV, and one at a higher BE of 401.7 eV. They attributed the higher BE peak to positively-charged N, which is likely to originate from adsorbed IL. Secondly, they attribute the peak at 400.0 eV to Ti-O-N interactions, and also comment that peaks associated with both pyrrole- and pyridine-type N manifest around this BE. The peaks in the data presented here, at 401.7 eV and 400.0 eV, are tentatively attributed to physisorbed IL and Ti-O-N interactions respectively. The peaks at ~401.9 eV and ~399.8 eV in the N 1s region for sample b are of a

218

similar BE separation and have similar full width at half-maximum (FWHM) values, and are, therefore, attributed to the same sources as those in the region for sample c.

The O 1s region for samples b and c are shown in Figure 6.9(ii), and display very different line shapes. The O 1s region for sample c (blue line) has been fitted with three peaks. The first peak, at 529.8 eV, dominates the region, and is attributed to lattice O of the TiO_2 nanotubes [15]. The second peak, at 531.3 eV, has a BE consistent with hydroxyl groups on Ti (Ti-OH) [15, 21], which are likely to have originated from exposure of the nanotubes to atmosphere. The third signal, at 532.6 eV, is attributed to organic hydroxyl groups (C-OH) or C=O [21]. To reiterate, C=O/C-OH groups may be present due to a combination of exposure to atmosphere, use of acetone in post-anodization cleaning, and residual adhesive. Ti-O-N interactions may appear at ~532.0 eV, in conjunction with the C-OH/C=O peak [36-38], so a portion of the signal at 532.6 eV is tentatively also attributed to Ti-O-N interactions. The region for sample b has also been fitted with three peaks: one at 530.5 eV, one at 532.2 eV, and one at 533.7 eV. The peak at 530.5 eV is attributed to O in TiO_2. The peak at 532.2 eV is attributed to Ti-OH groups. Since features associated with Ti-O-N interactions can appear at 532.0 eV, a portion of this peak is additionally attributed to Ti-O-N interactions. Finally the peak at 533.7 eV is attributed to C=O/C-OH. Sample b consists of a greater contribution from Ti-OH and C-OH/C=O, which may indicate more significant contamination.

Table 6.2: Summary of peak assignments of samples b and c, together with their respective binding energy (BE) values

Sample	Region	BE (eV) (± 0.1 eV)	Assignment
b	C 1s	285.0	C-C/C=C
		286.2	C=O/C-OH; C_2/C_3 of cation
		287.1	C_4 of cation
		289.0	IL-substrate interactions*
	F 1s	685.8	F ($[BF_4]^-$)
		684.2	Ti-F
	N 1s	401.9	N ($[C_4C_1Im]^+$)
		399.8	Ti-O-N*
	O 1s	530.5	TiO_2
		532.2	Ti-OH
		533.7	C=O/C-OH; Ti-O-N
c	C 1s	285.0	C-C/C=C
		286.3	C=O/C-OH
		288.7	IL-substrate interactions*
	F 1s	684.1	Ti-F
	N 1s	401.4	N ($[C_4C_1Im]^+$)
		399.7	Ti-O-N*
	O 1s	529.8	TiO_2
		531.3	Ti-OH
		532.6	C=O/C-OH; Ti-O-N

* Assignment debated in Discussion section

Anodization potential: 5 V, 10 V, and 20 V with pure IL electrolyte

Figure 6.10 shows the core level XPS spectra recorded from samples which were all anodized in pure IL electrolyte, but at different anodization potentials. Sample a (amber line) was anodized at 5 V, sample b (red line) was anodized at 10 V, and sample d (cyan line) was anodized at 20 V. The spectra are plotted in Figure 6.10 in order of anodization potential; with spectra recorded from sample a at the bottom, and spectra recorded from sample d at the top. A summary of binding energies and assignments of peaks is featured in Table 6.3.
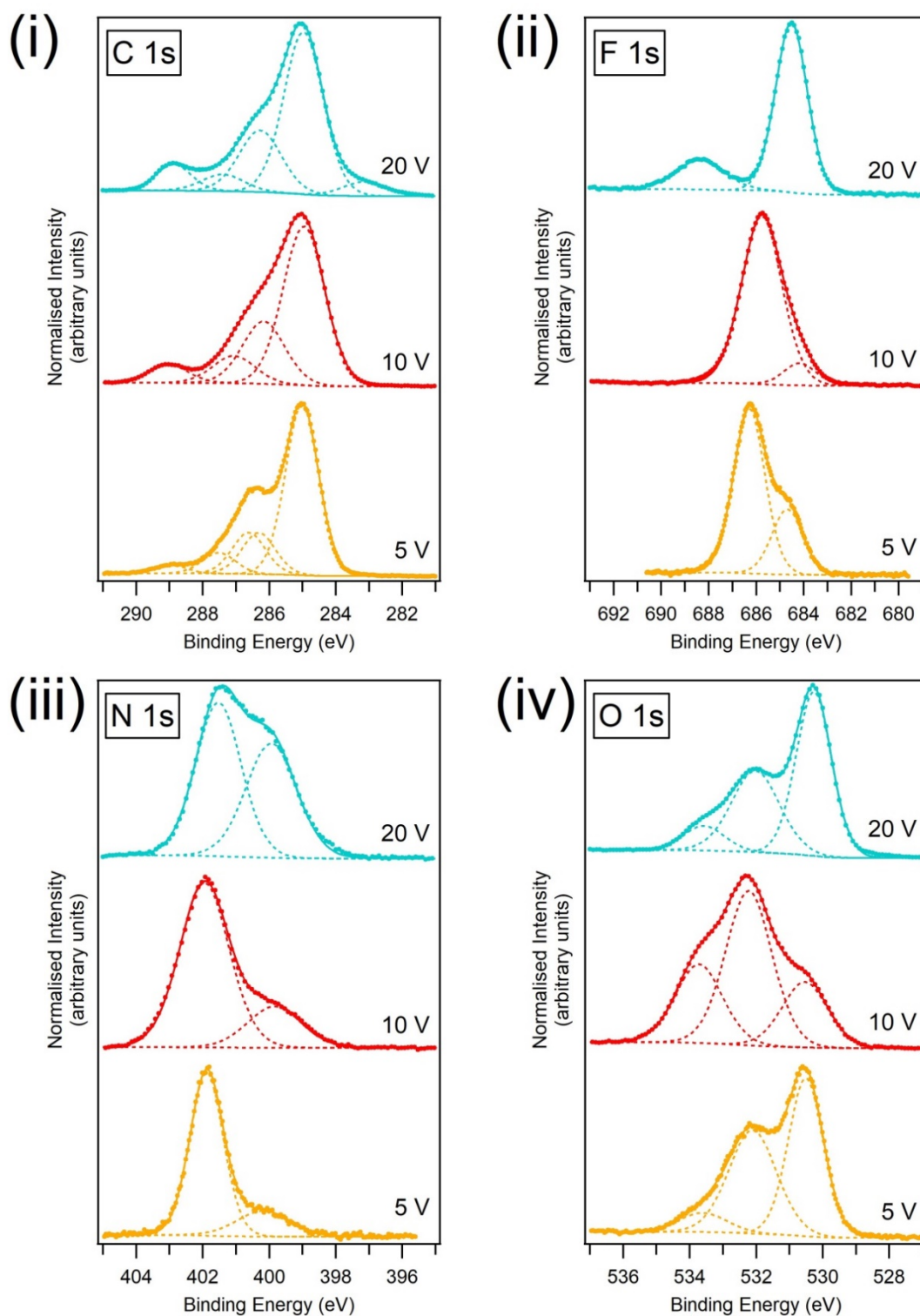
Figure 6.10: Core level XP spectra of samples a (anodized at 5 V, amber line), b (anodized at 1V, red line), and d (anodized at 20 V, cyan line).

The C 1s spectra taken for samples a, b, and d are shown in Figure 6.10(i) (represented by red, amber and cyan lines respectively). The C 1s spectrum for sample a (Figure 6.10(i), amber line) has been fitted with 5 peaks. The peak at 285.0 eV is attributed to C=C/C-C bonding. The majority of the C 1s region for sample a resembles that of an ultrathin IL film on TiO_2 [34]. Therefore, the

peaks situated at 286.3 eV and 286.6 eV are attributed to the C_2 and C_3 carbon atoms of the $[C_4C_1Im]^+$ cation, and the peak situated at 287.5 eV is attributed to the C_3 carbon atom of the $[C_4C_1Im]^+$ cation. The peak at 289.0 eV is attributed to IL-substrate interactions. The C 1s region for sample d (Figure 6.10(i), cyan line) is also fitted with five peaks, but has a very different shape to that of sample a. The peak at 285.0 eV is attributed to C-C/C=C bonding. The peaks at 286.3 eV and 287.4 eV could arise from adsorbed IL on the nanoporous surface. The peak at 286.3 eV could also contain a contribution from contaminant species. Similar to the other C 1s spectra, the region for sample d displays a feature at 288.9 eV, which is also attributed to IL-substrate interactions. A small shoulder is present at the lower BE edge, at 283.1 eV. The origin of this peak is not known, but may be the result of electrochemical decomposition of the IL- a topic explored in more depth in the discussion section.

The peak that appears at ~289.0 eV for all samples increases in relative intensity with increasing anodization potential (see Figure 6.11(i) for all C 1s spectra overlaid). Earlier, this peak was tentatively assigned to cation-substrate interactions, but is at a higher BE than those associated with intact IL cations. This suggests that a carbon-containing species, separate from any cationic or contaminant species, is more prominent on samples anodized at higher potentials. It is also interesting to note that the relative intensity of this peak is smaller for sample c than it is for sample b. Since both samples b and c were anodized at 10 V, this difference in relative intensity suggests that the presence of water may inhibit the production of the species generating this peak.

The F 1s spectrum recorded from sample a (Figure 6.10(ii), amber line) is fitted with two peaks: one at 686.3 eV, which is at a BE consistent with the $[BF_4]^-$ anion. The other peak is at 684.7 eV, which is at a BE that is consistent with Ti-F bonding. The region has a shape that is much like that recorded for sample b, but with a more intense signal attributed to Ti-F. The F 1s spectrum for sample d (Figure 6.10(ii), cyan line) is the most unique of all four samples, displaying two very distinct peaks, one at 684.5 eV, correlating with the BE of peaks associated with Ti-F bonding; and one slightly broad peak (FWHM ~2.4 eV) at ~688.3 eV. The BE of this peak in the F 1s region is consistent with CF_x groups [33, 39], but C 1s signals attributed to CF_x typically appear in the BE range of

291 eV to 293 eV [33, 39]. No peaks appear in the C 1s region of any sample at >291.0 eV (C 1s region with extended BE range is features in Figure 6.11(i)).
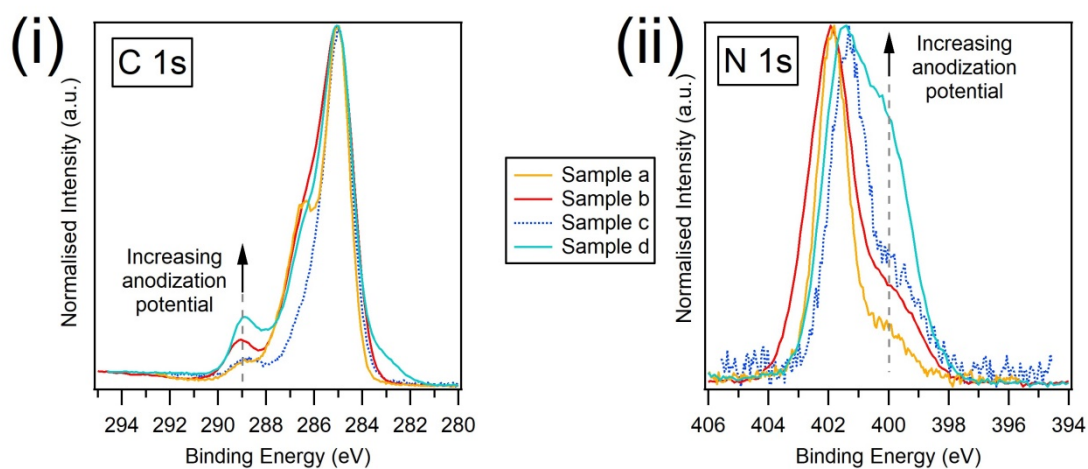
Figure 6.11: C 1s (i) and N 1s (ii) regions of all samples overlaid. The peaks that change in intensity with increasing anodization potential for samples a, b, and d have been highlighted. The same regions for sample c have been included (represented by a blue dotted line) to serve as a comparison.

In the N 1s region for samples a and d (Figure 6.10(iii), amber and cyan lines respectively) have been fitted with two peaks, much like that of sample b. The N 1s region for sample a consists of a dominating peak at 401.9 eV, consistent with that of the N of $[C_4C_1Im]^+$ cations, as well as a shoulder at 400.2 eV. The N 1s region for sample d features a dominating feature at 401.5 eV, which is also attributed to N in the IL cations, and a shoulder at 399.9 eV. For all samples, regardless of electrolyte composition, it appears that the intensity of the peak at ~400.0 eV increases relative to the peak at ~401.7 eV, with increasing anodization potential (see Figure 6.11(ii) for all N 1s spectra overlaid). This indicates that the relative intensity of this peak is solely dependent on anodization potential, and is not significantly affected by the addition of small amounts of water to the electrolyte. As suggested previously, the peak at ~400.0 eV has been attributed to Ti-O-N interactions. The increased intensity of this peak relative to the peak at ~401.7 eV could indicate that the increase in anodization voltage results in more cation/substrate interactions.

The O 1s region for samples a and d are similar in shape to one another (Figure 6.10(iv), amber line and cyan line respectively), but differ very much from that recorded for sample b. The O 1s region for samples a and d both display a dominating feature: at 530.5 eV for sample a and at 530.2 eV for sample d. The BE values of both of these peaks are in line with those in literature for lattice O

of TiO_2 [21, 34, 40]. The region for both samples feature a peak at ~532.0 eV, which is consistent with the assignment made for both samples b and c of Ti-OH groups. Similar to the O 1s region recorded for samples b and c, a peak appears in the O 1s region for samples a and d at 533.6 eV. These are also attributed to C-OH/C=O contaminant species. The O 1s region for sample a appears to have a more intense signal at ~532.0 eV (relative to the lattice O peak) than sample d; while the O 1s region for sample d has a more intense signal at 533.6 eV, relative to the lattice O peak, than sample a. The time that elapsed between the first and second anodization stages for sample a was >24 hours, while for sample d it was <10 minutes, which may contribute to a greater intensity of the peak attributed to Ti-OH groups for sample a than sample d. The peak attributed C-OH/C=O groups may be more intense for sample d than for sample a due to more solvent adsorbed and/or more adhesive residue on the sample surface that is not visible in the SEM images.

Table 6.3: Summary of all peak assignments of samples a, b, and d, together with their respective binding energy (BE) values

Sample	Region	BE (eV) (± 0.1 eV)	Assignment
a	C 1s	285.0	C-C (C_1 of cation)/C=C bonding
		286.3	C_2 of cation
		286.6	C_3 of cation
		287.5	C_4 of cation
		289.0	IL-substrate interactions*
	F 1s	686.3	F ($[BF_4]^-$)
		684.7	Ti-F
	N 1s	401.9	N ($[C_4C_1Im]^+$)
		400.2	Ti-O-N*
	O 1s	530.5	TiO_2
		532.1	Ti-OH
		533.6	C=O/C-OH; Ti-O-N
b	C 1s	285.0	C-C/C=C
		286.2	C=O/C-OH; C_2/C_3 of cation
		287.1	C_4 of cation
		289.0	IL-substrate interactions*
	F 1s	685.8	F ($[BF_4]^-$)
		684.2	Ti-F
	N 1s	401.9	N ($[C_4C_1Im]+$)
		399.8	Ti-O-N*
	O 1s	530.5	TiO_2
		532.2	Ti-OH
		533.7	C=O/C-OH; Ti-O-N
d	C 1s	283.1	Species from electrochemical decomposition
		285.0	C-C/C=C

		286.3	C=O/C-OH; C_2/C_3 of cation
		287.4	C_4 of cation
		288.9	IL-substrate interactions*
	F 1s	684.5	Ti-F
		688.3	CF_x*
	N 1s	401.5	N ($[C_4C_1Im]^+$)
		399.9	Ti-O-N*
	O 1s	530.2	TiO_2
		532.0	Ti-OH
		533.6	C=O/C-OH; Ti-O-N

* Assignment debated in Discussion section

6.4 Discussion

When synthesising TiO_2 nanotubes via anodization, various groups have subjected IL-based electrolytes to potentials in excess of 50 V for relatively short periods of time (<1 hour) [14, 15, 22]. However, subjecting ILs to potentials outside of their electrochemical stability window for significantly long periods (>1 hour) can result in decomposition: a strong negative potential causes oxidation of the anion, and a strong positive potential causes reduction of the cation. Theoretical calculations are useful for predicting the electrochemical decomposition products of an IL. In a combined theoretical and experimental study, it was found that, for $[C_4C_1Im][BF_4]$, reduction of the cation occurs via formation of radicals (Scheme 6.1, reaction *(4)*), where the unpaired electron is located at the CH group at the C^4 carbon position (see Figure 6.1 for chemical structure of $[C_4C_1Im][BF_4]$) [41]. Subsequently, two radicals can react (radical coupling) and form a dimer (Scheme 6.1, reaction *(5)*i), or undergo disproportionation through 'picking up' a hydrogen atom from another radical (Scheme 6.1, reaction *(5)*ii). Disproportionation results in neutral 1-butyl-3-methylimidazole (which has the same structure as $[C_4C_1Im]^+$, but the methyl-side nitrogen is no longer doubly bound to the C^4 carbon, and is neutral), and zwitterionic 1-butyl-3-methylimidazole (same structure as $[C_4C_1Im]^+$, but contains both positive and negative charge, but overall neutral). In the zwitterionic molecule, the positive charge is on the butyl-side N atom (rather than the methyl-side N atom typical of $[C_4C_1Im]^+$ cations), and the negative charge is on the C^4 carbon.
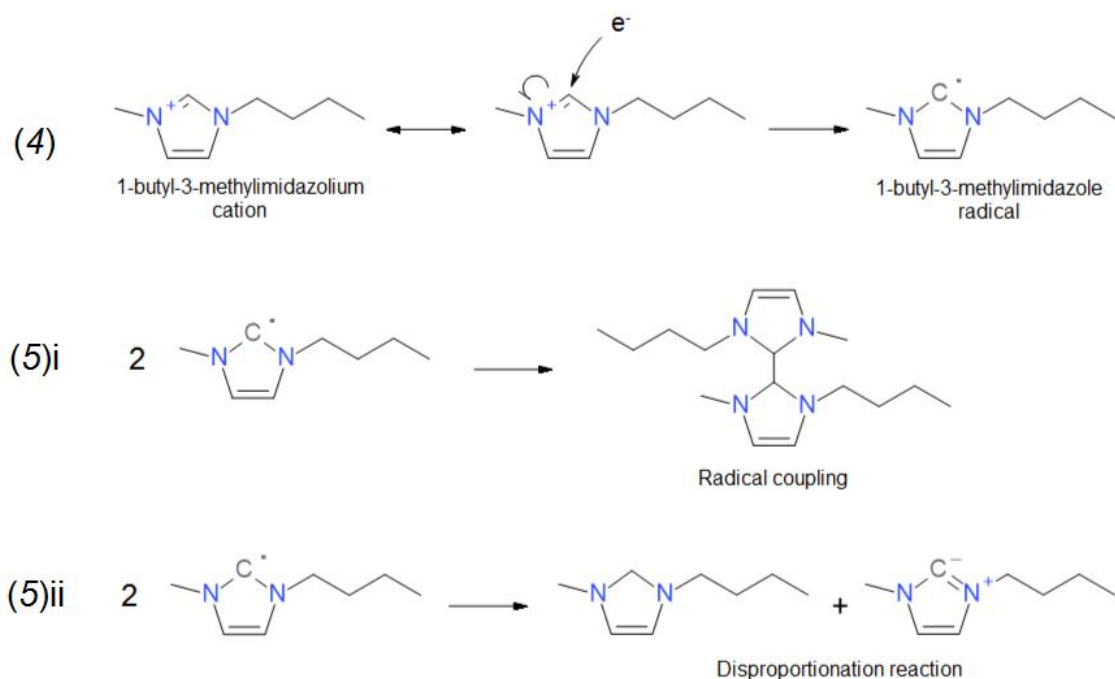
Scheme 6.1: Electrochemical decomposition of the $[C_4C_1Im]^+$ cation, starting with the formation of a 1-butyl-3-methylimidazole radical in *(4)*, followed by either dimerization (radical coupling) in *(5)*i, or disproportionation in *(5)*ii. Based on the schemes featured in [41].

In the N 1s spectra for all samples, the shoulder at ~400.0 eV was attributed to Ti-O-N interactions. This shoulder increased in relative intensity with anodization potential, seemingly irrespective of electrolyte composition. This suggests the peak, and by proxy the species responsible for it, shares a relationship with the anodization potential. Since all the samples were subjected to anodization potentials beyond the upper limit of the IL's electrochemical stability for significant periods, the peak at ~400.0 eV in the N 1s region of each sample may be related to decomposition products of the IL. Whether these decomposition species exist as dimers, or as the products of disproportionation, it follows that they would manifest peaks somewhere in the N 1s region, separate from, but possibly overlapping with, the peak attributed to adsorbed IL cations. As seen in Chapter 3 of this thesis and in other XPS studies [42], evidence of beam damage of ILs can manifest peaks around 400.0 eV in the N 1s region. Ultrathin depositions of IL are prone to damage from prolonged X-ray exposure (see Chapter 3.4.1). For sample a in particular, which may be supporting such an ultrathin film, this could explain the intensity of the shoulder at 400.0 eV, and thus may actually be beam damage rather than Ti-O-N interactions.

Samples a and d were anodized for similar periods for the first and second anodization stages, where each stage was between 2 hours and 3.5 hours. However, the peak at ~400.0 eV is more prominent in the N 1s region for sample d than for sample a. Moreover, sample b was subject to a longer initial anodization stage (12 hours), while sample c was subject to a longer second anodization stage (10.5 hours), but the peak at ~400.0 eV is of a similar relative intensity for both samples b and c. These observations support the assessment that the relative intensity of the peak is strongly related to anodization potential rather than anodization time. It could also be associated with electrochemical decomposition of the IL. This means the peak at ~400.0 eV may not necessarily originate entirely from Ti-O-N interactions, but may include a contribution from electrochemically decomposed IL.
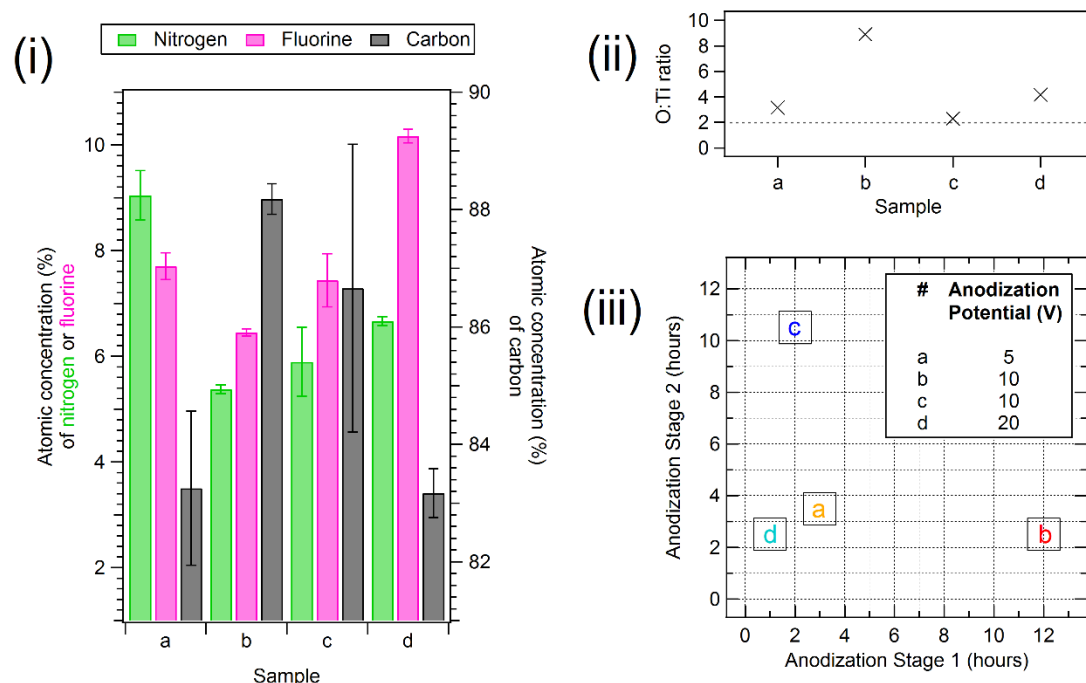
Figure 6.12: Atomic concentration (%) of N, F, and C of all samples acquired from the XPS data (i); and the O/Ti atomic ratio of all samples (ii). The dashed line in (ii) represents the stoichiometric O/Ti atomic ratio = 2. For reference, the time taken for each anodization stage for each sample is illustrated in (iii) with an inset table displaying their respective anodization potentials.

The atomic concentrations of nitrogen, fluorine, and carbon in each of the samples are shown in Figure 6.12(i), and were calculated using the total areas of the N 1s, F 1s, and C 1s regions, and their respective relative sensitivity factors (RSFs). Figure 6.12(ii) displays the O/Ti atomic ratio of each sample. Due to the existence of multiple peaks in the O 1s regions of all samples (and by proxy multiple O species on the surface of all samples), the atomic

concentration of O calculated from these data is likely to be an overestimate of varying degrees. For sample c, the intensities of the peaks at 531.3 eV and 532.6 eV, relative to the lattice O peak at 529.8 eV, are small, and therefore the atomic concentration of O for sample c is only a slight overestimate. On the other hand, the atomic concentration of O for sample b is likely to be overestimated to the greatest degree due to the peaks in the O 1s region at 532.2 eV and 533.7 eV being so intense relative to the peak attributed to lattice O. Sample c has the closest atomic O/Ti ratio (of 2.27) to the stoichiometric value (of 2.0) than any other sample, but is still higher than the stoichiometric value due to the presence of contaminant O species. As expected, sample b has the highest atomic O/Ti ratio (of 8.93) due to significant contamination compared to the other samples. It is expected of successfully synthesised nanotubes to possess stoichiometry close to that of pristine TiO_2, but always contain contaminants; some of which, depending on the source of contamination, can skew the calculation of the concentration of O at the surface [15, 21, 22].

The probing depth of XPS is calculated to be of the order of 60 Å for TiO_2 (using an inelastic mean free path predicted by TPP-2M equation [43] of approximately 20 Å in TiO_2). The thickness of the oxide layer will be of vital importance when calculating the O/Ti ratio. Nanotubes were successfully synthesised on sample c, and a nanoporous TiO_2 layer was synthesised on sample d, but neither samples a or b display any TiO_2 nanostructures. The O/Ti ratio for sample c is very close to that of stoichiometric TiO_2, we can assume that the XPS is probing only TiO_2. It also follows that the length of the nanotubes can be considered to be greater than that of the sampling depth of XPS, thus applying a lower limit on their length of ~6 nm.

The atomic concentrations (Figure 6.12(i)) were calculated without contribution from the Ti 2p or O 1s regions in order to allow a proper comparison of nitrogen, fluorine, and carbon without any skewing of the concentrations from the substrate peaks. Sample b has the lowest concentration of nitrogen and fluorine on the surface, but has the greatest concentration of carbon. Sample a has the greatest concentration of nitrogen, but has one of the lowest concentrations of carbon, alongside sample d. A large concentration of nitrogen at the surface of sample a corroborates the shape and fit of the C 1s region recorded for sample

a, closely resembling an ultrathin IL film on TiO_2. Sample d has the greatest concentration of fluorine at the surface. The concentration of nitrogen, fluorine, and carbon at the surface of sample c have relatively large uncertainties because of their concentration when factoring in the substrate peaks. When the contribution from the O 1s and Ti 2p regions is taken into account in the concentration of all five elements (N, F, C, O, and Ti), sample c has the lowest concentration of nitrogen, fluorine and carbon.

The O 1s and Ti 2p spectra are shown for all samples (and are overlaid) in Figure 6.13(i) and Figure 6.13(ii) respectively. The incorporation of nitrogen into TiO_2 has been shown to lower the BE of the O 1s and Ti 2p regions [37, 44] up to as much as 2 eV compared to undoped TiO_2 [45]. The BE differences between each of the O 1s (fitted lattice O) signals, and for each of the Ti $2p_{3/2}$ signals, are similar (the BE values of these peaks are shown in Figure 6.13(i) and Figure 6.13(ii)). The O 1s and Ti 2p regions for sample a are shifted the most toward higher BE, despite having the highest atomic concentration of N at 9.0%. This corroborates the idea that some IL remains on the surface of the sample from the anodization process. Interestingly, the O 1s and Ti 2p regions for sample c are shifted the most toward lower BE. This would indicate a greater concentration of chemisorbed N (i.e. Ti-O-N interactions) than all the other samples, despite possessing the second lowest atomic concentration of N. The Ti 2p region (Figure 6.13(ii)) for sample b looks different to that of samples a, c, and d. The region for sample b appears to be somewhat broader, and a shoulder feature appears at the lower BE end of the region. The shape of the region for the other samples is consistent with that of majority Ti^{4+} ions in TiO_2, but the region for sample b may have contributions from Ti^{3+} as well as Ti^{4+}, hence the appearance of the lower BE shoulder feature. The Ti^{3+} features are typical of oxygen vacancies of a defective surface [34], but defects can also cause BE shifts of all regions to lower BEs [46]. This will affect the calibration, and could also be contributing to various BE differences between sample spectra.
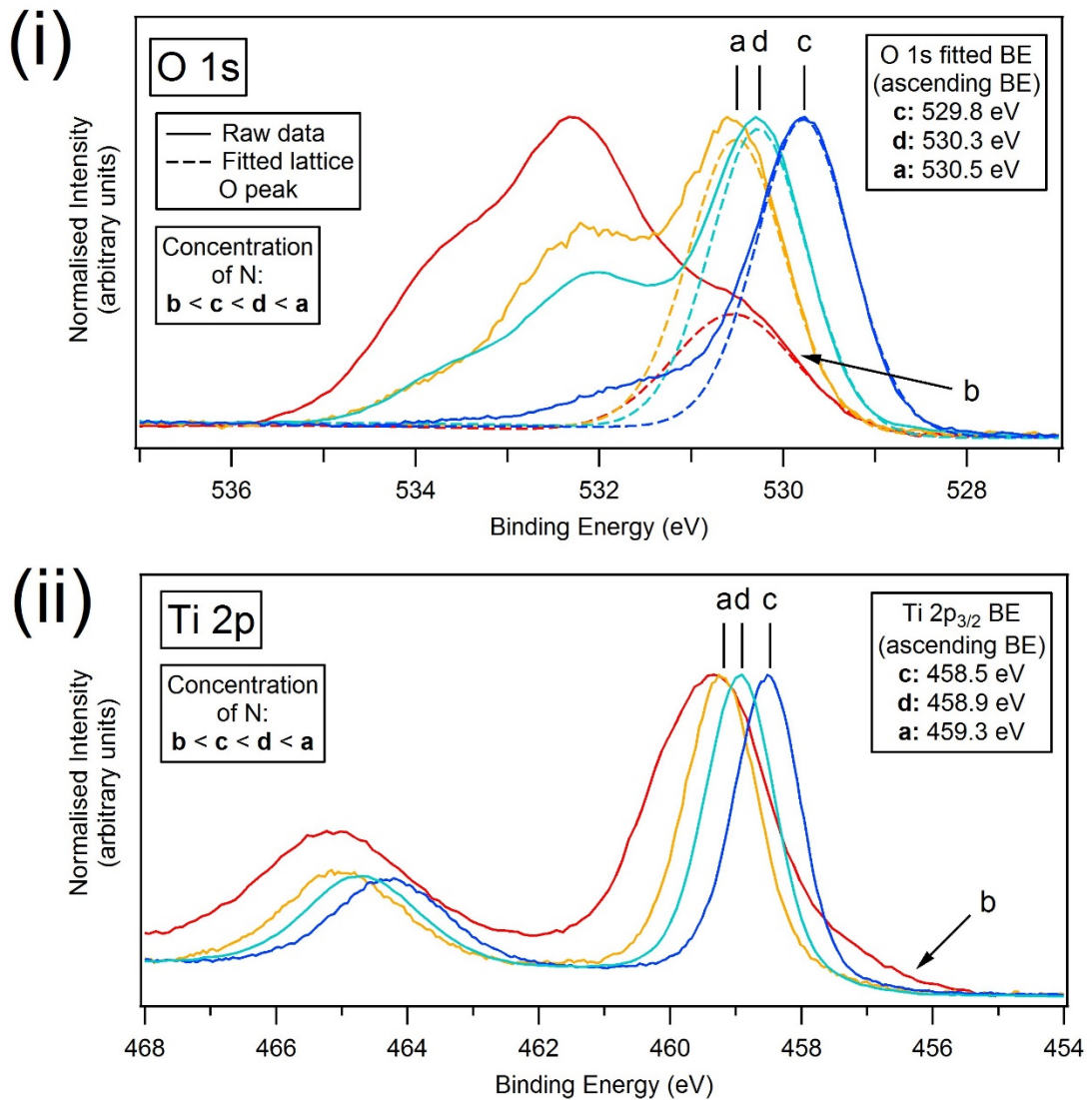
Figure 6.13: O 1s (i) and Ti 2p (ii) regions of all samples overlaid. Each spectrum is annotated with the associated sample designation. The binding energy values of the fitted lattice O peak in the O 1s for samples a, c, and d are shown on the right in (i). The binding energy values of the Ti 2p$_{3/2}$ peak for samples a, c and d are shown on the right in (ii). On the left side of each spectrum describes the order of samples in atomic concentration of N (determined quantitatively from the XPS), from sample b (with the least concentration) to sample a (with the greatest concentration).

As described in Chapter 2, XPS is inherently more surface-sensitive due to the mean free path of photoelectrons, while EDX can detect X-rays emitted from as deep as several μm, so is considered, in this case, to be more bulk-sensitive. Therefore, EDX provides insight into the bulk composition, while XPS provides insight into the surface composition. Oxygen was unable to be detected in any of the samples by the SEM/EDX system used (corresponding to a concentration of <0.01%), which suggests that the nanotubes grown are much less than μm in length. This actually corroborates with literature, where low voltage anodization

(between 5 and 10 V) how shown to produce nanotubes with lengths < 700 nm [13].

The surface atomic concentration of fluorine, as determined by XPS, does not appear to correlate with either anodization time (of either stage, or total) or anodization potential. One possibility is that the concentration of F is dependent on the morphology of the surface. As mentioned previously, TiO_2 nanotubes that have been synthesised via anodization using comparable potentials can have lengths in the μm range, which means XPS will only probe the nanotube layer. As mentioned earlier, this is likely to be the case for sample c since the ratio of O/Ti is close to the stoichiometric value, indicating that XPS is probing TiO_2 only. For samples where nanotubes have not been synthesised, a small amount of oxide may have formed at the surface, or have a naturally occurring oxide from exposure to atmosphere. Should there be sufficient oxide for dissolution to take place (occurring via reaction *(3)* between the IL and the TiO_2), pits may form. This process is likely to have been the mechanism for the formation of the nanoporous TiO_2 on sample d. So while nanotubes were not formed due to insufficient amounts of available oxygen, the initial pits may have been synthesised, and the fluorine environments within them detected by XPS. This could provide insight into these initial pits, and the chemistry at the root of TiO_2 nanotubes synthesised via anodization of Ti.

The reaction that creates the initial pits is thought to be responsible for the creation and maintenance of the tube structure of the nanotubes [7]. While fluorine is necessary for the TiO_2 nanotube formation, its presence in the resultant nanotube array could be seen as contamination, since it will alter physicochemical properties of the nanotubes and therefore have an effect on their function for particular applications. In particular, it could have negative consequences such as diminished absorption of dye in dye-sensitised solar cells [47, 48], or diminished hydrogen production rate in photocatalytic water splitting [49]. However, the concentration of contaminant species (which includes N, F, and C) is significantly reduced when TiO_2 nanotubes are annealed after synthesis [21]. This is the case for TiO_2 synthesised via anodization using either IL-based [22] or non-IL-based electrolytes [21]. While the nitrogen, fluorine and carbon content of sample c was the lowest of all

samples, it would be interesting to compare the present composition with the composition after an annealing at 400°C.

Based on this work, it would be interesting to compare the resultant compositions via XPS of samples subject to similar anodization potentials (namely 5 V and 20 V) whilst also including a small addition of water to all electrolytes. The addition of water is the key factor as to whether or not nanotubes can be synthesised under these low-potential (≤20 V) conditions. It would be interesting to explore whether the addition of water to the electrolyte would decrease the fluorine, nitrogen, and carbon contents of any synthesised structures at these potentials, and how the concentrations of carbon, nitrogen and fluorine at the surface would compare to those of the nanotubes of sample c. Furthermore, it could be determined whether or not the XPS features that currently adhere to the trend of increasing relative intensity with increasing anodization potential would still do so with the addition of water.

Another interesting avenue of study involves using scattering techniques, such as such as grazing incidence small angle X-ray scattering (GISAXS), to gain structural information of the nanotubes during anodization. GISAXS is a surface sensitive X-ray scattering technique that has been used to study a variety of nanostructures [50-52], including TiO_2 nanotubes [53-55]. In the case of TiO_2 nanotubes, measurements were only taken of arrays that have already been synthesised via anodization of Ti. One of the benefits of GISAXS is that can be used in situ, which means it can be employed both under ambient conditions, and without needing to remove the electrolyte from the electrochemical cell. Because GISAXS measurements can be taken under ambient conditions, there is no requirement for a specialist vacuum-safe electrochemical cell. Furthermore, since GISAXS can be conducted without needing to remove the IL electrolyte, measurements can be taken throughout the anodization process, not just after completion. This could provide a unique insight into the structural progression of the TiO_2 nanotubes during synthesis, which (to the best of our knowledge) has not been reported with this technique before.

6.5 Conclusion

In order to investigate the effect of anodization potential and electrolyte composition on the synthesis of TiO_2 nanostructures, four samples of Ti were

subject to a two-step anodization method under various anodization conditions in a custom-built electrochemical cell. These samples were designated letters a to d. Their individual anodization conditions are listed below:

- Sample a: anodized at 5 V in pure $[C_4C_1Im][BF_4]$
- Sample b: anodized at 10 V in pure $[C_4C_1Im][BF_4]$
- Sample c: anodized at 10 V in an electrolyte composed of $[C_4C_1Im][BF_4]$ and 2.6 wt% H_2O
- Sample d: anodized at 20 V in pure $[C_4C_1Im][BF_4]$

The samples were then characterised using SEM/EDX and XPS. From the SEM analysis, only sample c displayed the presence of nanotube structures on the surface with an average inner diameter of 50 nm. Sample d appeared to have a partially-nanoporous surface, with average pore diameter of 75 nm. Samples a and b looked similar, but did not appear to support nanostructures. This observation demonstrates that the addition of water is essential for the successful synthesis of nanotubes. The ratio of O/Ti calculated for sample c was close to that of stoichiometric TiO_2, which defines a lower limit of 6 nm to the length of the nanotubes, equal to the sampling depth of XPS. The EDX analysis revealed differences in the composition of the samples, which was explored in more depth in the XPS analysis. The XPS revealed trends with anodization potential in the C 1s and N 1s regions for all samples. A peak at ~288.9 eV in the C 1s region increased in relative intensity with anodization potential, but was of a smaller intensity for sample c, displaying an additional relationship with electrolyte composition. A peak at ~399.9 eV in the N 1s region, however, increased irrespective of electrolyte composition. These peaks are thought to be related to electrochemical decomposition of the IL, but warrant further study with the electrolyte composition as used for sample c. Further study could also include GISAXS to monitor structural progress during anodization, which to the best of our knowledge has not yet been reported.

Chapter 6 References

[1] W.-J. Lee, M. Alhoshan, W.H. Smyrl, *Titanium Dioxide Nanotube Arrays Fabricated by Anodizing Processes Electrochemical Properties*, Journal of the Electrochemical Society, 153 (2006) B499-B505, D.O.I.: 10.1149/1.2347098

[2] R. Wang, K. Hashimoto, A. Fujishima, M. Chikuni, E. Kojima, A. Kitamura, M. Shimohigoshi, T. Watanabe, *Light-Induced Amphiphilic Surfaces*, Nature, 388 (1997) 431-432, D.O.I.: 10.1038/41233

[3] K.C. Popat, M. Eltgroth, T.J. LaTempa, C.A. Grimes, T.A. Desai, *Titania Nanotubes: A Novel Platform for Drug-Eluting Coatings for Medical Implants?*, Small, 3 (2007) 1878-1881, D.O.I.: 10.1002/smll.200700412

[4] S.K. Mohapatra, M. Misra, V.K. Mahajan, K.S. Raja, *A Novel Method for the Synthesis of Titania Nanotubes Using Sonoelectrochemical Method and Its Application for Photoelectrochemical Splitting of Water*, Journal of Catalysis, 246 (2007) 362-369, D.O.I.: 10.1016/j.jcat.2006.12.020

[5] X. Chen, S.S. Mao, *Titanium Dioxide Nanomaterials: Synthesis, Properties, Modifications, and Applications*, Chemical Reviews, 107 (2007) 2891-2959, D.O.I.: 10.1021/cr0500535

[6] C.A. Grimes, *Synthesis and Application of Highly Ordered Arrays of TiO2 Nanotubes*, Journal of Materials Chemistry, 17 (2007) 1451-1457, D.O.I.: 10.1039/B701168G

[7] P. Roy, S. Berger, P. Schmuki, *TiO2 Nanotubes: Synthesis and Applications*, Angewandte Chemie-International Edition, 50 (2011) 2904-2939, D.O.I.: 10.1002/anie.201001374

[8] D. Gong, C.A. Grimes, O.K. Varghese, W. Hu, R. Singh, Z. Chen, E.C. Dickey, *Titanium Oxide Nanotube Arrays Prepared by Anodic Oxidation*, Journal of Materials Research, 16 (2001) 3331-3334, D.O.I.: 10.1557/JMR.2001.0457

[9] O.K. Varghese, D. Gong, M. Paulose, C.A. Grimes, E.C. Dickey, *Crystallization and High-Temperature Structural Stability of Titanium Oxide Nanotube Arrays*, Journal of Materials Research, 18 (2003) 156-165, D.O.I.: 10.1557/JMR.2003.0022

[10] J.M. Macak, L.V. Taveira, H. Tsuchiya, K. Sirotna, J. Macak, P. Schmuki, *Influence of Different Fluoride Containing Electrolytes on the Formation of Self-*

Organized Titania Nanotubes by Ti Anodization, Journal of Electroceramics, 16 (2006) 29-34, D.O.I.: 10.1007/s10832-006-3904-0

[11] S.P. Albu, A. Ghicov, S. Aldabergenova, P. Drechsel, D. LeClere, G.E. Thompson, J.M. Macak, P. Schmuki, *Formation of Double-Walled TiO2 Nanotubes and Robust Anatase Membranes*, Advanced Materials, 20 (2008) 4135-4139, D.O.I.: 10.1002/adma.200801189

[12] S.P. Albu, P. Schmuki, *TiO2 Nanotubes Grown in Different Organic Electrolytes: Two-Size Self-Organization, Single Vs. Double-Walled Tubes, and Giant Diameters*, Physica Status Solidi-Rapid Research Letters, 4 (2010) 215-217, D.O.I.: 10.1002/pssr.201004244

[13] I. Paramasivam, J. Macak, T. Selvam, P. Schmuki, *Electrochemical Synthesis of Self-Organized TiO 2 Nanotubular Structures Using an Ionic Liquid (BMIM-BF 4)*, Electrochimica Acta, 54 (2008) 643-648, D.O.I.: 10.1016/j.electacta.2008.07.031

[14] H.Q. Li, J. Qu, Q.Z. Cui, H.B. Xu, H.M. Luo, M.F. Chi, R.A. Meisner, W. Wang, S. Dai, *TiO2 Nanotube Arrays Grown in Ionic Liquids: High-Efficiency in Photocatalysis and Pore-Widening*, Journal of Materials Chemistry, 21 (2011) 9487-9490, D.O.I.: 10.1039/c1jm11540e

[15] P. Mazierski, J. Łuczak, W. Lisowski, M.J. Winiarski, T. Klimczuk, A. Zaleska-Medynska, *The ILs-Assisted Electrochemical Synthesis of TiO2 Nanotubes: The Effect of Ionic Liquids on Morphology and Photoactivity*, Applied Catalysis B: Environmental, 214 (2017) 100-113, D.O.I.: 10.1016/j.apcatb.2017.05.005

[16] D. Regonini, C.R. Bowen, A. Jaroenworaluck, R. Stevens, *A Review of Growth Mechanism, Structure and Crystallinity of Anodized TiO2 Nanotubes*, Materials Science and Engineering: R: Reports, 74 (2013) 377-406, D.O.I.: 10.1016/j.mser.2013.10.001

[17] J. Tian, Z. Zhao, A. Kumar, R.I. Boughton, H. Liu, *Recent Progress in Design, Synthesis, and Applications of One-Dimensional TiO2 Nanostructured Surface Heterostructures: A Review*, Chemical Society Reviews, 43 (2014) 6920-6937, D.O.I.: 10.1039/C4CS00180J

[18] Z. Zhang, Z. Zhou, S. Nie, H. Wang, H. Peng, G. Li, K. Chen, *Flower-Like Hydrogenated TiO2(B) Nanostructures as Anode Materials for High-Performance Lithium Ion Batteries*, Journal of Power Sources, 267 (2014) 388-393, D.O.I.: 10.1016/j.jpowsour.2014.05.121

[19] Y. Liu, J.H. Wei, R. Xiong, C.X. Pan, J. Shi, *Enhanced Visible Light Photocatalytic Properties of Fe-Doped TiO2 Nanorod Clusters and Monodispersed Nanoparticles*, Applied Surface Science, 257 (2011) 8121-8126, D.O.I.: 10.1016/j.apsusc.2011.04.121

[20] Z. Song, J. Hrbek, R. Osgood, *Formation of TiO2 Nanoparticles by Reactive-Layer-Assisted Deposition and Characterization by XPS and STM*, Nano Letters, 5 (2005) 1327-1332, D.O.I.: 10.1021/nl0505703

[21] D. Regonini, A. Jaroenworaluck, R. Stevens, C.R. Bowen, *Effect of Heat Treatment on the Properties and Structure of TiO2 Nanotubes: Phase Composition and Chemical Composition*, Surface and Interface Analysis, 42 (2010) 139-144, D.O.I.: 10.1002/sia.3183

[22] Y. Liu, K. Mu, G. Yang, H. Peng, F. Shen, L. Wang, S. Deng, X. Zhang, Y. Zhang, *Fabrication of a Coral/Double-Wall TiO2 Nanotube Array Film Electrode with Higher Photoelectrocatalytic Activity under Sunlight*, New Journal of Chemistry, 39 (2015) 3923-3928, D.O.I.: 10.1039/C5NJ00340G

[23] K.S. Raja, T. Gandhi, M. Misra, *Effect of Water Content of Ethylene Glycol as Electrolyte for Synthesis of Ordered Titania Nanotubes*, Electrochemistry Communications, 9 (2007) 1069-1076, D.O.I.: 10.1016/j.elecom.2006.12.024

[24] I. Paramasivam, J.M. Macak, A. Ghicov, P. Schmuki, *Enhanced Photochromism of Ag Loaded Self-Organized TiO2 Nanotube Layers*, Chemical Physics Letters, 445 (2007) 233-237, D.O.I.: 10.1016/j.cplett.2007.07.107

[25] W. Zhang, W. Liu, C. Wang, *Tribological Behavior of Sol–Gel TiO2 Films on Glass*, Wear, 253 (2002) 377-384, D.O.I.: 10.1016/S0043-1648(02)00139-4

[26] Y. Shin, S. Lee, *Self-Organized Regular Arrays of Anodic TiO2 Nanotubes*, Nano Letters, 8 (2008) 3171-3173, D.O.I.: 10.1021/nl801422w

[27] Y. Yang, X. Wang, L. Li, *Synthesis and Growth Mechanism of Graded TiO2 Nanotube Arrays by Two-Step Anodization*, Materials Science and Engineering: B, 149 (2008) 58-62, D.O.I.: 10.1016/j.mseb.2007.12.006

[28] J. Macak, S. Albu, D. Kim, I. Paramasivam, S. Aldabergerova, P. Schmuki, *Multilayer TiO2–Nanotube Formation by Two-Step Anodization*, Electrochemical and Solid-State Letters, 10 (2007) K28-K31, D.O.I.: 10.1149/1.2737544

[29] D.E. Newbury, N.W.M. Ritchie, *Is Scanning Electron Microscopy/Energy Dispersive X-Ray Spectrometry (SEM/EDS) Quantitative?*, Scanning, 35 (2013) 141-168, D.O.I.: 10.1002/sca.21041

[30] K.L. Syres, A.G. Thomas, D.M. Graham, B.F. Spencer, W.R. Flavell, M.J. Jackman, V.R. Dhanak, *Adsorption and Stability of Malonic Acid on Rutile TiO2 (110), Studied by Near Edge X-Ray Absorption Fine Structure and Photoelectron Spectroscopy*, Surface Science, 626 (2014) 14-20, D.O.I.: 10.1016/j.susc.2014.03.015

[31] J.N. Wilson, R.M. Dowler, H. Idriss, *Adsorption and Reaction of Glycine on the Rutile TiO2(011) Single Crystal Surface*, Surface Science, 605 (2011) 206-213, D.O.I.: 10.1016/j.susc.2010.10.020

[32] M. Babucci, V. Balci, A. Akçay, A. Uzun, *Interactions of [BMIM][BF4] with Metal Oxides and Their Consequences on Stability Limits*, Journal of Physical Chemistry C, 120 (2016) 20089-20102, D.O.I.: 10.1021/acs.jpcc.6b03975

[33] I.J. Villar-Garcia, E.F. Smith, A.W. Taylor, F.L. Qiu, K.R.J. Lovelock, R.G. Jones, P. Licence, *Charging of Ionic Liquid Surfaces under X-Ray Irradiation: The Measurement of Absolute Binding Energies by XPS*, Physical Chemistry Chemical Physics, 13 (2011) 2797-2808, D.O.I.: 10.1039/C0cp01587c

[34] M. Wagstaffe, M.J. Jackman, K.L. Syres, A. Generalov, A.G. Thomas, *Ionic Liquid Ordering at an Oxide Surface*, Chemphyschem, 17 (2016) 3430-3434, D.O.I.: 10.1002/cphc.201600774

[35] G. Lu, S.L. Bernasek, J. Schwartz, *Oxidation of a Polycrystalline Titanium Surface by Oxygen and Water*, Surface Science, 458 (2000) 80-90, D.O.I.: 10.1016/S0039-6028(00)00420-9

[36] M. Bellardita, M. Addamo, A. Di Paola, L. Palmisano, A.M. Venezia, *Preparation of N-Doped TiO2: Characterization and Photocatalytic Performance under UV and Visible Light*, Physical Chemistry Chemical Physics, 11 (2009) 4084-4093, D.O.I.: 10.1039/B816708G

[37] X. Chen, C. Burda, *Photoelectron Spectroscopic Investigation of Nitrogen-Doped Titania Nanoparticles*, The Journal of Physical Chemistry B, 108 (2004) 15446-15449, D.O.I.: 10.1021/jp0469160

[38] D. Wu, L. Wang, *Low-Temperature Synthesis of Anatase C-N-TiO2 Photocatalyst with Enhanced Visible-Light-Induced Photocatalytic Activity*, Applied Surface Science, 271 (2013) 357-361, D.O.I.: 10.1016/j.apsusc.2013.01.202

[39] S. Men, K.R.J. Lovelock, P. Licence, *X-Ray Photoelectron Spectroscopy of Pyrrolidinium-Based Ionic Liquids: Cation–Anion Interactions and a Comparison*

to Imidazolium-Based Analogues, Physical Chemistry Chemical Physics, 13 (2011) 15244-15255, D.O.I.: 10.1039/C1CP21053J

[40] K.L. Syres, A.G. Thomas, W.R. Flavell, B.F. Spencer, F. Bondino, M. Malvestuto, A. Preobrajenski, M. Grätzel, *Adsorbate-Induced Modification of Surface Electronic Structure: Pyrocatechol Adsorption on the Anatase TiO2 (101) and Rutile TiO2 (110) Surfaces*, Journal of Physical Chemistry C, 116 (2012) 23515-23525, D.O.I.: 10.1021/jp308614k

[41] M.C. Kroon, W. Buijs, C.J. Peters, G.-J. Witkamp, *Decomposition of Ionic Liquids in Electrochemical Processing*, Green Chemistry, 8 (2006) 241-245, D.O.I.: 10.1039/B512724F

[42] K.R.J. Lovelock, E.F. Smith, A. Deyko, I.J. Villar-Garcia, P. Licence, R.G. Jones, *Water Adsorption on a Liquid Surface*, Chemical Communications, (2007) 4866-4868, D.O.I.: 10.1039/B711680B

[43] S. Tanuma, C.J. Powell, D.R. Penn, *Calculation of Electron Inelastic Mean Free Paths (IMFPs) VII. Reliability of the TPP-2M IMFP Predictive Equation*, Surface and Interface Analysis, 35 (2003) 268-275, D.O.I.: 10.1002/sia.1526

[44] M.-S. Wong, H. Pang Chou, T.-S. Yang, *Reactively Sputtered N-Doped Titanium Oxide Films as Visible-Light Photocatalyst*, Thin Solid Films, 494 (2006) 244-249, D.O.I.: 10.1016/j.tsf.2005.08.132

[45] F. Peng, L. Cai, H. Yu, H. Wang, J. Yang, *Synthesis and Characterization of Substitutional and Interstitial Nitrogen-Doped Titanium Dioxides with Visible Light Photocatalytic Activity*, Journal of Solid State Chemistry, 181 (2008) 130-136, D.O.I.: 10.1016/j.jssc.2007.11.012

[46] U. Diebold, *The Surface Science of Titanium Dioxide*, Surface Science Reports, 48 (2003) 53-229, D.O.I.: 10.1016/S0167-5729(02)00100-0

[47] H. Rensmo, K. Westermark, S. Södergren, O. Kohle, P. Persson, S. Lunell, H. Siegbahn, *XPS Studies of Ru-Polypyridine Complexes for Solar Cell Applications*, Journal of Chemical Physics, 111 (1999) 2744-2750, D.O.I.: 10.1063/1.479551

[48] J. Singh, A. Gusain, V. Saxena, A.K. Chauhan, P. Veerender, S.P. Koiry, P. Jha, A. Jain, D.K. Aswal, S.K. Gupta, *XPS, UV–Vis, FTIR, and EXAFS Studies to Investigate the Binding Mechanism of N719 Dye onto Oxalic Acid Treated TiO2 and Its Implication on Photovoltaic Properties*, Journal of Physical Chemistry C, 117 (2013) 21096-21104, D.O.I.: 10.1021/jp4062994

[49] J.M. Macak, S. Aldabergerova, A. Ghicov, P. Schmuki, *Smooth Anodic TiO2 Nanotubes: Annealing and Structure*, Physica Status Solidi (a), 203 (2006) R67-R69, D.O.I.: 10.1002/pssa.200622214

[50] F. Pietra, F.T. Rabouw, W.H. Evers, D.V. Byelov, A.V. Petukhov, C. de Mello Donegá, D. Vanmaekelbergh, *Semiconductor Nanorod Self-Assembly at the Liquid/Air Interface Studied by in Situ GISAXS and Ex Situ TEM*, Nano Letters, 12 (2012) 5515-5523, D.O.I.: 10.1021/nl302360u

[51] M.-A. Cha, C. Shin, D. Kannaiyan, Y.H. Jang, S.T. Kochuveedu, D.Y. Ryu, D.H. Kim, *A Versatile Approach to the Fabrication of TiO2 Nanostructures with Reverse Morphology and Mesoporous Ag/TiO2 Thin Films Via Cooperative PS-B-PEO Self-Assembly and a Sol-Gel Process*, Journal of Materials Chemistry, 19 (2009) 7245-7250, D.O.I.: 10.1039/B907922J

[52] S. Das, Q. Wu, R.K. Garlapalli, S. Nagpure, J. Strzalka, Z. Jiang, S.E. Rankin, *In-Situ GISAXS Investigation of Pore Orientation Effects on the Thermal Transformation Mechanism in Mesoporous Titania Thin Films*, Journal of Physical Chemistry C, 118 (2014) 968-976, D.O.I.: 10.1021/jp406165v

[53] M. Einollahzadeh-Samadi, R. Dariani, A. Paul, *Tailoring Morphology, Structure and Photoluminescence Properties of Anodic TiO2 Nanotubes*, Journal of Applied Crystallography, 50 (2017) 1133-1143, D.O.I.: 10.1107/S1600576717007968

[54] E.C. Giraud, P. Mokarian-Tabari, D.T.W. Toolan, T. Arnold, A.J. Smith, J.R. Howse, P.D. Topham, M.A. Morris, *Highly Ordered Titanium Dioxide Nanostructures Via a Simple One-Step Vapor-Inclusion Method in Block Copolymer Films*, ACS Applied Nano Materials, 1 (2018) 3426-3434, D.O.I.: 10.1021/acsanm.8b00632

[55] N. Paul, J. Brumbarov, A. Paul, Y. Chen, J.-F. Moulin, P. Mueller-Buschbaum, J. Kunze-Liebhäuser, R. Gilles, *GISAXS and TOF-GISANS Studies on Surface and Depth Morphology of Self-Organized TiO2 Nanotube Arrays: Model Anode Material in Li-Ion Batteries*, Journal of Applied Crystallography, 48 (2015) 444-454, D.O.I.: 10.1107/S1600576715002204

7 Conclusions and further work

7.1 Conclusions

Presented in this thesis were four studies that were conducted into the structure and interactions of ionic liquids (ILs) at gaseous and oxide interfaces, each with a view toward energy applications.

In Chapter 3, the interface between 1-butyl-3-methylimidazolium tetrafluoroborate ($[C_4C_1Im][BF_4]$) and water vapour was investigated using both IL multilayers and an ultrathin IL film, with near-ambient pressure X-ray photoelectron spectroscopy. The IL multilayer system (approximately 27 layers), deposited onto an anatase TiO_2 (101) substrate, was exposed to water vapour at 20% relative humidity (RH) and 60% relative humidity. The ad/absorption of water was more evident at 60% RH than at 20% RH, and relative intensity changes in the C 1s region indicate possible rearrangement of the cations at the surface. These changes were more apparent in the C 1s region for the ultrathin IL film. The ultrathin film (approximately 3 layers), was deposited onto a rutile TiO_2 (110) substrate and exposed to water vapour at 70% RH. Multiple measurements were taken after the water vapour was closed off from the near-ambient pressure cell. Water appeared to remain adsorbed on the ultrathin IL film for some time after exposure to water vapour. The intensity changes in the C 1s region continued even after the water vapour was closed off from the near-ambient pressure cell, which could indicate water-induced ionic rearrangement at the IL/water interface. The system eventually reversed to its original orientation once the surrounding pressure returned to UHV. The prolonged presence of water could be problematic for systems requiring dry IL for superior ad/absorption of gaseous reactants for catalysis, for example. As the presence of adsorbed water affects the structure of the outermost surface of ILs, it will also influence ad/absorption kinetics and how the IL interacts with the target gas. This could, therefore, have a negative impact on thin-film catalysis systems.

The IL/water interfacial region was also investigated in Chapter 4, alongside that of IL/CO_2 and IL/(CO_2/H_2O mixture), with the superbasic IL trihexyltetradecylphosphonium benzimidazolide, or [P_{66614}][benzim]. The interactions in the interfacial region were investigated using near-ambient pressure X-ray photoelectron spectroscopy. The reaction between the [P_{66614}][benzim] and CO_2 forms a carbamate bond, which was shown to be reversible via a reduction in the surrounding gas pressure. The anion of the superbasic IL also reacts with water to form benzimidazole and a hydroxide anion. Under the conditions investigated, the capability of [P_{66614}][benzim] to react with CO_2 was not hindered by preliminary exposure to H_2O vapour, and the molar uptake ratio, n_{CO2}/n_{IL}, was calculated to have an upper limit of 0.5, regardless of initial exposure to either CO_2 or H_2O vapour. This suggests that the superbasic IL preferentially reacts with CO_2, resulting in a consistent uptake ratio in both mixed-gas regimes. This property may be useful for gas separation applications under humid conditions. This study also demonstrates that NAPXPS is a powerful tool for investigating gas uptake in ILs and learning more about the interfacial behaviour.

In Chapter 5, the interactions between ZnO and multilayer depositions of the ILs 1-octyl-3-methylimidazolium tetrafluoroborate ([C_8C_1Im][BF_4]) and 1-butyl-3-methylimidazolium tetrafluoroborate ([C_4C_1Im][BF_4]) were studied. Using a combination of X-ray photoelectron spectroscopy (XPS) and N K-edge near-edge X-ray absorption fine structure (NEXAFS) spectroscopy, the interactions and ordering of [C_8C_1Im][BF_4] on polar and non-polar faces of ZnO were compared. The deposition of [C_8C_1Im][BF_4] on the polar ZnO was approximately double the thickness of the deposition on the non-polar ZnO, which resulted in a more disorganised IL film, showing no preferential orientation of the imidazolium ring in the N K-edge NEXAFS. However, the [C_8C_1Im][BF_4] deposition on non-polar ZnO displayed a preferential orientation of the imidazolium ring toward the surface normal. The orientation of molecules may influence charge transfer, and thus is important for optimising IL-incorporated optoelectric devices. It appears the IL interacts more strongly with the polar ZnO than the non-polar, possibly at the O-terminated step edges. In addition to this, the thermal stability of [C_4C_1Im][BF_4] was investigated on polar ZnO using XPS. It was found that [C_4C_1Im][BF_4] began to decompose when heated to temperatures in excess of 80°C, a much lower temperature than the

long-term thermal stability quoted in literature at ~300°C. This indicates that ZnO has a catalytic effect on the thermal decomposition of $[C_4C_1Im][BF_4]$. This may have a negative impact on potential use of ILs in photovoltaic ZnO-based applications for example, where thermal stability is crucial to device longevity.

Chapter 6 investigated the influence of IL-based electrolyte composition and anodization voltage on the electrochemical synthesis of TiO_2 nanotubes via anodization of Ti, by studying the morphology and chemical composition of the resultant nanostructures. Three of the four samples were anodized in an electrolyte composed solely of $[C_4C_1Im][BF_4]$ (at 5 V, 10 V and 20 V), and one was anodized in an electrolyte composed of $[C_4C_1Im][BF_4]$ with 2.6 wt% water (at 10 V). Nanotubes were synthesised on the sample anodized in $[C_4C_1Im][BF_4]$/water electrolyte, with an average diameter of 50 nm. On a sample which was anodized at 20 V with pure IL electrolyte, a nanoporous film was synthesised with average pore diameter of 75 nm. The three samples that were anodized in pure IL electrolyte at 5 V, 10 V and 20 V showed a trend with increasing anodization potential, manifesting as an increase in relative intensity of peaks in the C 1s and N 1s regions in the XPS data. The ratio of O/Ti was calculated using the Ti 2p and O 1s regions for the synthesised nanotubes, and was close to that of stoichiometric TiO_2, providing a lower limit for the length of the nanotubes at approximately 6 nm. Many factors can influence the outcome of electrochemical synthesis, and understanding the effects of electrolyte composition and applied anodization potential on subsequent nanotube morphology composition is vital for applications such as photocatalytic water splitting, where contamination can hinder the catalytic performance of the nanotubes.

7.2 Further work

A number of further studies have stemmed from the work presented in this thesis. We have taken near-edge X-ray absorption fine structure spectroscopy and X-ray photoelectron spectroscopy data of multilayer and ultrathin films of $[P_{66614}][benzim]$ on rutile TiO_2 under near-ambient pressures at a recent experiment at the B07 beamline of Diamond Light Source. These data will determine the structure and ordering at the interface with vacuum and with CO_2 gas. Also scheduled is an experiment on the HIPPIE beamline at MAX IV, which

aims to investigate the structure and ordering of ultrathin layers of [P_{66614}][benzim] on rutile TiO_2 in the presence of both CO_2 and H_2O. One of the most promising aspects of ILs is their potential for use in gas separation applications [1, 2]. Therefore, further work into the CO_2 capture and separation capabilities of superbasic ILs in the presence of gases such as SO_2 could be interesting and beneficial from an industrial perspective as well as academic.

It would be interesting to conduct investigations into the interactions of different ILs with ZnO; with nanoparticulate ZnO in particular. ZnO exists in numerous nanostructural forms, including nanowires, nanorods, and nano-'flowers' [3]. ILs have been used as solvents for ZnO nanostructure synthesis [4, 5], and since nanoparticulate ZnO has applications in dye-sensitised solar cell (DSSC) technology [6], it would be interesting to look into the thermal stability of a variety of ILs with nanoparticulate ZnO.

The composition of electrochemically synthesised TiO_2 nanotubes is currently being investigated further as part of a MPhys project using a similar method as in Chapter 6, but using entirely IL/water electrolytes. As an accompaniment to the data from Chapter 6, studies into electrochemical decomposition of ILs could be conducted in vacuo and studied using X-ray photoelectron spectroscopy [7, 8]. The development of nanotube structure during anodization of Ti is of interest from a fundamental perspective. Grazing incidence small-angle X-ray scattering [9] data was collected on a recent synchrotron experiment at the I07 beamline at Diamond Light Source, with measurements recorded in situ during nanotube growth. The analysis, to be done in collaboration with colleagues at Diamond Light Source and the European Synchrotron Radiation Facility (France), may shed light onto the degree of ordering taking place at the Ti surface during synthesis. Additionally, a variety of fluorine-containing, non-imidazolium based ILs could be investigated. Other interesting avenues of study include the use of mixed-IL electrolytes [10], and nanotube doping [11, 12].

Chapter 7 References

[1] J.E. Bara, S. Lessmann, C.J. Gabriel, E.S. Hatakeyama, R.D. Noble, D.L. Gin, *Synthesis and Performance of Polymerizable Room-Temperature Ionic Liquids as Gas Separation Membranes*, Industrial & Engineering Chemistry Research, 46 (2007) 5397-5404, D.O.I.: 10.1021/ie0704492

[2] Y.-Y. Jiang, Z. Zhou, Z. Jiao, L. Li, Y.-T. Wu, Z.-B. Zhang, *SO2 Gas Separation Using Supported Ionic Liquid Membranes*, The Journal of Physical Chemistry B, 111 (2007) 5058-5061, D.O.I.: 10.1021/jp071742i

[3] L. Schmidt-Mende, J.L. MacManus-Driscoll, *ZnO – Nanostructures, Defects, and Devices*, Materials Today, 10 (2007) 40-48, D.O.I.: 10.1016/S1369-7021(07)70078-0

[4] H. Zhu, J.-F. Huang, Z. Pan, S. Dai, *Ionothermal Synthesis of Hierarchical ZnO Nanostructures from Ionic-Liquid Precursors*, Chemistry of Materials, 18 (2006) 4473-4477, D.O.I.: 10.1021/cm060472y

[5] L. Wang, L. Chang, B. Zhao, Z. Yuan, G. Shao, W. Zheng, *Systematic Investigation on Morphologies, Forming Mechanism, Photocatalytic and Photoluminescent Properties of ZnO Nanostructures Constructed in Ionic Liquids*, Inorganic Chemistry, 47 (2008) 1443-1452, D.O.I.: 10.1021/ic701094a

[6] I. Gonzalez-Valls, M. Lira-Cantu, *Vertically-Aligned Nanostructures of ZnO for Excitonic Solar Cells: A Review*, Energy & Environmental Science, 2 (2009) 19-34, D.O.I.: 10.1039/B811536B

[7] P. Aydogan Gokturk, S.E. Donmez, B. Ulgut, Y.E. Türkmen, S. Suzer, *Optical and XPS Evidence for the Electrochemical Generation of an N-Heterocyclic Carbene and Its CS2 Adduct from the Ionic Liquid [bmim][PF6]*, New Journal of Chemistry, 41 (2017) 10299-10304, D.O.I.: 10.1039/C7NJ01996C

[8] P. Aydogan Gokturk, U. Salzner, L. Nyulászi, B. Ulgut, C. Kocabas, S. Suzer, *XPS-Evidence for in-Situ Electrochemically-Generated Carbene Formation*, Electrochimica Acta, 234 (2017) 37-42, D.O.I.: 10.1016/j.electacta.2017.03.053

[9] M. Einollahzadeh-Samadi, R. Dariani, A. Paul, *Tailoring Morphology, Structure and Photoluminescence Properties of Anodic TiO2 Nanotubes*, Journal of Applied Crystallography, 50 (2017) 1133-1143, D.O.I.: 10.1107/S1600576717007968

[10] H. Niedermeyer, J.P. Hallett, I.J. Villar-Garcia, P.A. Hunt, T. Welton, *Mixtures of Ionic Liquids*, Chemical Society Reviews, 41 (2012) 7780-7802, D.O.I.: 10.1039/C2CS35177C

[11] M.M. Momeni, Y. Ghayeb, *Photoelectrochemical Water Splitting on Chromium-Doped Titanium Dioxide Nanotube Photoanodes Prepared by Single-Step Anodizing*, Journal of Alloys and Compounds, 637 (2015) 393-400, D.O.I.: 10.1016/j.jallcom.2015.02.137

[12] Z. Dong, D. Ding, T. Li, C. Ning, *Ni-Doped TiO2 Nanotubes Photoanode for Enhanced Photoelectrochemical Water Splitting*, Applied Surface Science, 443 (2018) 321-328, D.O.I.: 10.1016/j.apsusc.2018.03.031

Appendix A: Calculation of inelastic mean free path and deposition thicknesses of ionic liquids

A.1 Inelastic mean free path of photoelectrons in ionic liquids

The calculation for the inelastic mean free path (IMFP) of photoelectrons in ionic liquids (ILs) uses the TPP-2M calculation, as given by Equation (*1*), for photoelectron IMFP in organic materials as formulated by Seah [1]:

$$\lambda_{IL} = \frac{(4 + 0.44 Z_{IL}^{0.5} + 0.104 E^{0.872})\, a_{IL}^{1.7}}{Z_{IL}^{0.3}} \tag{1}$$

where λ_{IL} is the IMFP of photoelectrons passing through the IL in nm, Z_{IL} is the average number of protons in one IL pair, E is the average kinetic energy of the photoelectrons of interest in eV, and a_{IL} is the cube root of the atomic volume of the IL (a_{IL} is sometimes known as the IL 'thickness' or IL 'length') in nm.

The average number of protons per IL pair, Z_{IL}, is calculated using Equation (1)i:

$$Z_{IL} = \frac{\sum (x_i\, Z_{Xi})}{\sum x_i} \tag{1}i$$

where the total number of protons in one IL pair (i.e. the sum of x number of atoms of element X, multiplied by the proton number Z for each element within the IL pair) is divided by the sum of the total number of atoms (as shown by the denominator). For example, in 1-butyl-3-methylimidazolium tetrafluoroborate ([C_4C_1Im][BF_4]), which has the chemical formula $C_8H_{15}BF_4N_2$, Z_{IL} for [C_4C_1Im][BF_4] is 3.9.

The average kinetic energy of photoelectrons through the IL layer, E, can be calculated using X-ray photoelectron spectroscopy (XPS) data. This is shown in Equation (*1*)ii:

$$E = h\nu - E_{BS} \qquad (1)\text{ii}$$

where $h\nu$ is the incident photon energy, and E_{BS} is the binding energy of the XPS core level feature used for comparison of the substrate before and after IL deposition. For example, using a standard Al K_α X-ray source ($h\nu \approx 1486$ eV), and E_{BS} of O 1s region in $TiO_2 \approx 530$ eV, the average kinetic energy from photoelectrons emitted from a TiO_2 substrate, $E \approx 956$ eV.

The molecular volume in nm^3, denoted a_{IL}^3, of an IL pair is dependent on the molar weight, M_{IL} (in g mol^{-1}), the density of the IL (in g cm^{-3}), and the total number of atoms within the IL, as described in Equation (1)iii below:

$$a_{IL}^3 = \frac{10^{21} \, M_{IL}}{\rho_{IL} \, N_A \, (\sum x_i)} \qquad (1)\text{iii}$$

where ρ_{IL} is the density of the IL and N_A is Avogadro's number. The cube root of a_{IL}^3 is also given by Equation (1.04) in Chapter 1.3.1 of this thesis (but is simply denoted by d in the context of monolayer IL depositions). Using $[C_4C_1Im][BF_4]$ as an example, the sum of the individual atomic weights of its elemental components gives a molar (molecular) weight of 226.02 g mol^{-1}. At room temperature, its density is approximately 1.21 g cm^{-3}, and gives an IL volume, a_{IL}^3, of approximately 0.0104 nm^3.

Combining all of the quantities calculated from Equations (1)i, (1)ii and (1)iii in Equation (1) gives an IMFP, λ_{IL}, of photoelectrons emitted from the O 1s levels in a TiO_2 substrate travelling through a deposition of $[C_4C_1Im][BF_4]$ to be approximately 2.60 nm.

A.1.1 Application of the TPP-2M equation to inorganic materials

A form of the TPP-2M equation (developed by Tanuma et al [2]) can be applied to inorganic materials (such as TiO_2) to predict the IMFP (denoted by λ_{In}, and is in Å) of photoelectrons in those materials:

$$\lambda_{In} = \frac{E}{E_p^2 \left[\beta \, \ln(\gamma \, E) - \left(\frac{C}{E}\right) - \left(\frac{D}{E^2}\right)\right]} \qquad (2)$$

where E is the kinetic energy of photoelectrons, and E_p, β, γ, C and D are represented by Equations (2)i, (2)ii, (2)iii, (2)iv and (2)v:

$$\beta = -0.10 + 0.944 \left(E_p^2 + E_g^2 \right)^{-0.5} + 0.069 \, \rho^{0.1} \tag{2)i}$$

$$\gamma = 0.191 \, \rho^{-0.5} \tag{2)ii}$$

$$C = 1.97 - 0.91 \left(\frac{E_p^2}{829.4} \right) \tag{2)iii}$$

$$D = 53.4 - 20.8 \left(\frac{E_p^2}{829.4} \right) \tag{2)iv}$$

and E_p is the free-electron plasmon energy (in eV), given by:

$$E_p = 28.8 \left(\frac{N_v \, \rho}{M} \right)^{0.5} \tag{2)v}$$

E_g in (2)ii is the band-gap energy (in eV), N_v in (2)v is the number of valence electrons per molecule, ρ is the density (in g cm^{-3}) and M in (2)v is the molecular weight (in g mol^{-1}). For example, TiO_2 has 16 valence electrons (4 from Ti, and 6 from each O), a molecular weight of 79.86 g mol^{-1}, a density value of approximately 4.2 g cm^{-3}, and a band gap of approximately 3 eV. Therefore, E_p for TiO_2 is approximately 26.5 eV, and gives an IMFP, λ_{In}, of approximately 20 Å for photoelectrons with kinetic energy, E, of 956 eV (using Equation (1)ii, and the same values as in the previous subsection). As described in Chapter 2.3.4, the IMFP can then be used to calculate the sampling depth. Therefore, in TiO_2, the sampling depth, $d = 3\lambda_{In} \approx 60$ Å.

A.2 Calculation for the thickness of an ionic liquid deposition

The thickness of an ionic liquid film on a solid substrate is given by Equation (3), which is based on the Beer-Lambert relation of the attenuation of photoelectrons in thin films [3]:

$$d_{IL} = -\lambda_{IL} \ln \left(\frac{I}{I_0} \right) \tag{3}$$

where d_{IL} is the thickness, or depth, of the IL deposition, λ_{IL} is the IMFP of photoelectrons traversing though the IL deposition, I_0 is the initial intensity of the substrate core level XPS peak (the intensity prior to IL deposition), and I is the attenuated intensity of the same core level XPS peak after deposition. It

follows from this calculation that a rough estimate can be made of the number of IL 'layers'. This done by dividing the thickness of the IL deposition (d_{IL}) by the thickness of one IL pair (a_{IL}).

Appendix A References

[1] M.P. Seah, *An Accurate and Simple Universal Curve for the Energy-Dependent Electron Inelastic Mean Free Path*, Surface and Interface Analysis, 44 (2012) 497-503, D.O.I.: 10.1002/sia.4816

[2] S. Tanuma, C.J. Powell, D.R. Penn, *Calculation of Electron Inelastic Mean Free Paths (IMFPs) VII. Reliability of the TPP-2M IMFP Predictive Equation*, Surface and Interface Analysis, 35 (2003) 268-275, D.O.I.: 10.1002/sia.1526

[3] J.F. Watts, J. Wolstenholme, *An Introduction to Surface Analysis by XPS and AES*, John Wiley & Sons, (2003).

Appendix B: Synthesis of trihexyl-tetradecylphosphonium benzimidazolide

The two step synthesis process to obtain the superbasic ionic liquid (IL), trihexyl-tetradecylphosphonium benzimidazolide, or $[P_{66614}]$[benzim] (see Chapter 4), was carried out by Dr S. F. R. Taylor of the School of Chemical Engineering and Analytical Science at the University of Manchester. This process is also outlined in [1].

The precursors, trihexyl-tetradecylphosphonium chloride ($[P_{66614}]$[Cl]) and benzimidazole were purchased from Cytec (97.7%) and Sigma Aldrich (98%) respectively. An ion exchange resin (Amberlite IRN-78, OH-form; Sigma Aldrich) was used to first synthesise trihexyl-tetradecylphosphonium hydroxide ($[P_{66614}]$[OH]), by pouring a solution of 35 g of $[P_{66614}]$[Cl] and 25 cm^3 of ethanol into a column containing the clean exchange resin (the resin itself was washed in absolute ethanol to remove air and impurities). The product containing $[P_{66614}]$[OH] was then poured into the column again. This was repeated three times to ensure complete ion exchange, converting $[P_{66614}]$[Cl] into $[P_{66614}]$[OH]. The product was then analysed using nuclear magnetic resonance spectroscopy to determine the amount of $[P_{66614}]$[OH] present. From there, a sufficient amount of benzimidazole was added to the product to form a 1:1 ratio of $[P_{66614}]$[OH] and benzimidazole. The solution was then stirred for 8 hours under rotary evaporation and high vacuum at 50°C to obtain pure and dry $[P_{66614}]$[benzim].

Appendix B References

[1] S.F.R. Taylor, C. McCrellis, C. McStay, J. Jacquemin, C. Hardacre, M. Mercy, R.G. Bell, N.H. de Leeuw, *CO2 Capture in Wet and Dry Superbase Ionic Liquids*, Journal of Solution Chemistry, 44 (2015) 511-527, D.O.I.: 10.1007/s10953-015-0319-z